1
2
3
4
5
6
7
8
9
10
11
12
13
14
15
16
17
18
19
20
21
22
23
24
25
26
27
28
29
30
31
32
33
34
35
36
37
38
39
40
41
42
43
44
45
46
47
48
49
50
51
52
53
54
55
56
57
58
59
60

Chapter 7: Energetic particle physics

M. Salewski[1], D.A. Spong[2], P. Aleynikov[3], R. Bilato[4],
B.N. Breizman[5], S. Briguglio[6], H. Cai[7], L. Chen[8], W. Chen[9],
V.N. Duarte[10], R.J. Dumont[11], M.V. Falessi[6,12,13],
M. Fitzgerald[14], E.D. Fredrickson[10], M. García-Muñoz[17],
N.N. Gorelenkov[10], T. Hayward-Schneider[4],
W.W. Heidbrink[8], M.J. Hole[16], Ye.O. Kazakov[17],
V.G. Kiptily[14], A. Könies[3], T. Kurki-Suonio[18], Ph. Lauber[4],
S.A. Lazerson[3,19], Z. Lin[8], A. Mishchenko[3], D. Moseev[3],
C.M. Muscatello[20], M. Nocente[21], M. Podestà[10,22],
A. Polevoi[23], M. Schneider[23], S.E. Sharapov[14],
A. Snicker[18,24], Y. Todo[25], Z. Qiu[26], G. Vlad[6], X. Wang[4],
D. Zarzoso[27], M.A. Van Zeeland[20], F. Zonca[6,12,26], and
S.D. Pinches[23]

[1] Department of Physics, Technical University of Denmark, Kgs. Lyngby,
Denmark
[2] Oak Ridge National Laboratory, 1 Bethel Valley Rd, Oak Ridge, TN 37830,
United States of America
[3] Max-Planck Institute for Plasma Physics, Wendelsteinstrasse 1, 17491
Greifswald, Germany
[4] Max-Planck Institute for Plasma Physics, Boltzmannstrasse 2, 85748
Garching, Germany
[5] Institute for Fusion Studies, The University of Texas, Austin, TX 78712,
United States of America
[6] ENEA, Nuclear Department, C.R. Frascati, Via E. Fermi 45, 00044 Frascati,
Italy
[7] School of Nuclear Science and Technology, University of Science and
Technology of China, Hefei 230026, People's Republic of China
[8] Department of Physics and Astronomy, University of California, Irvine,
California 92697-4574, USA
[9] Southwestern Institute of Physics, PO Box 432, Chengdu 610041, People's
Republic of China
[10] Princeton Plasma Physics Laboratory, Princeton University, Princeton, NJ
08543-0451, USA
[11] CEA, IRFM, F-13108 Saint-Paul-lez-Durance, France
[12] Center for Nonlinear Plasma Science and C.R. ENEA Frascati, C.P. 65, 00044
Frascati, Italy
[13] Istituto Nazionale di Fisica Nucleare (INFN), Sezione di Roma, Piazzale Aldo
Moro 2, Roma, Italy
[14] United Kingdom Atomic Energy Authority, Culham Campus, Abingdon,
Oxon OX14 3DB, UK
[15] University of Seville, 41012 Seville, Spain
[16] Australian National University, Canberra, ACT 0200, Australia
[17] Laboratory for Plasma Physics, LPP-ERM/KMS, Royal Military Academy,
Avenue de la Renaissance 30, B-1000 Brussels, Belgium
[18] Department of Applied Physics, Aalto University, FI-00076 AALTO, Finland
[19] Gauss Fusion GmbH, 85748 Garching, Germany [20] General Atomics, P.O.
Box 85608 San Diego, California 92186-5608, USA
[21] Department of Physics 'G. Occhialini', University of Milano-Bicocca, Piazza
della Scienza 3, 20126 Milano, Italy

1
2
3
4
5
6
7
8
9
10
11
12
13
14
15
16
17
18
19
20
21
22
23
24
25
26
27
28
29
30
31
32
33
34
35
36
37
38
39
40
41
42
43
44
45
46
47
48
49
50
51
52
53
54
55
56
57
58
59
60

[22] Ecole Polytechnique Fédérale de Lausanne, Swiss Plasma Center, CH-1015 Lausanne, Switzerland
[23] ITER Organization, Route de Vinon-sur-Verdon, 13115, St. Paul-lez-Durance, France
[24] VTT, PO Box 1000, FI-02044 VTT, Espoo, Finland
[25] National Institute for Fusion Science, National Institutes of Natural Sciences, Toki, 509-5292, Japan
[26] Institute for Fusion Theory and Simulation, School of Physics, Zhejiang University, Hangzhou 310027,People's Republic of China
[27] Aix-Marseille Université, CNRS, Centrale Med, M2P2, Marseille, France

E-mail: msal@dtu.dk

Abstract. We review the physics of energetic particles (EPs) in magnetically confined burning fusion plasmas with focus on advances since the last update of the ITER Physics Basis [A. Fasoli *et al.* 2007 Nucl. Fusion 47 S264]. Topics include basic EP physics, EP generation, diagnostics of EPs and instabilities, the interaction of EPs and thermal plasma instabilities, EP-driven instabilities, energetic particle modes (EPMs), and turbulence, linear and nonlinear stability and simulation of EP-driven instabilities and EPMs, 3D effects, scenario optimization strategies based on EP phase-space control, EPs in reduced field scenarios in ITER before DT, and the physics of runaway electrons. We describe the simulation and modelling of EPs in fusion plasmas, including instability drive and damping as well as EP transport, with a range of approaches from first-principles to reduced models, including gyrokinetic simulations, kinetic-MHD models, gyrofluid models, reduced models, and semi-analytical approaches.

2

Contents

1. Introduction

The era of fusion power generation is approaching with the construction of the ITER tokamak [1, 2]. A primary goal of the ITER project is to demonstrate a fusion power $P_{\mathrm{fus}} = 500\,\mathrm{MW}$ for an injected auxiliary heating power $P_{\mathrm{aux}} = 50\,\mathrm{MW}$, which gives a power amplification of $Q = P_{\mathrm{fus}}/P_{\mathrm{aux}} = 10$. A second primary mission goal is $Q = 5$ in a steady-state scenario. These mission goals in terms of Q directly imply necessary values for the α-particle heating

fraction η_α which indicates how much plasma heating originates from fusion reactions, leading towards a self-sustained system, and how much heating originates from auxiliary heating systems directly controlled from the outside. The α-particles from the deuterium-tritium (DT)‡ fusion reaction, $D + T \rightarrow \alpha + n$, receive $1/5$ of the released fusion energy due to energy and momentum conservation, so the α-particle heating power is $P_\alpha = P_{\text{fus}}/5 = QP_{\text{aux}}/5$. Hence, η_α is related to Q by

$$\eta_\alpha = \frac{P_\alpha}{P_\alpha + P_{\text{aux}}} = \frac{Q}{Q+5}, \tag{1}$$

as illustrated in figure 1. At ITER's mission goal $Q = 5$, we have $\eta_\alpha = 0.5$, so self-heating by energetic α-particles equals auxiliary heating ($P_\alpha = P_{\text{aux}}$), and at ITER's mission goal $Q = 10$, we have $\eta_\alpha = 0.67$, so the plasma is predominantly self-heated by energetic α-particles.
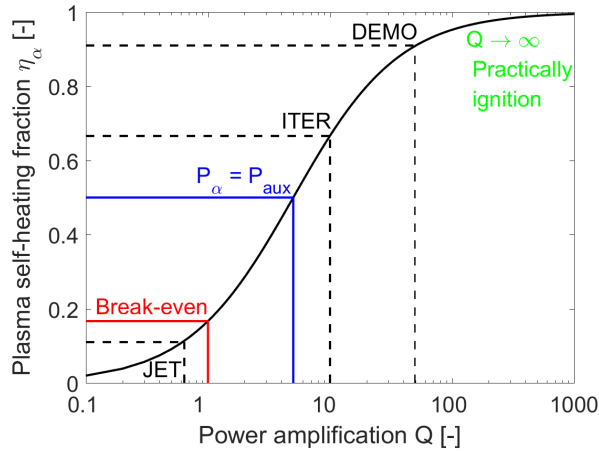
Figure 1. Plasma self-heating fraction as a function of the power amplification Q . Plasmas are predominantly heated by MeV-range alphas for $Q > 5$. Reproduced from [3].

In this review, we will focus on energetic particle (EP) physics in *burning plasmas* in magnetic confinement devices.§ We consider a plasma to be a *burning plasma* if the self-heating is larger than the auxiliary heating, leading to a high degree of self-sustainment and self-organization. Such self-organized plasmas constitute a new regime of EP physics. For

‡ We will introduce acronyms when they first appear but have also appended a complete list of acronyms.
§ Note by the ITER Organization: The progress on R&D described in this volume includes topics of relevance to ITER, as well as to burning plasmas more generally. In some cases, the underlying physics R&D activities were motivated by specific features of the ITER 2016 staged approach baseline [4] and ITR-2024-5 (final version) [5]. The new ITER baseline 2024 currently under elaboration proposes modifications to several of these features (e.g. first wall material, heating and current drive mix, etc.), as introduced in [6], which will require additional R&D beyond that described in this chapter.

burning plasmas, $P_\alpha > P_{\text{aux}}$, so $\eta_\alpha > 0.5$ and $Q > 5$. The highest achieved Q in magnetic confinement fusion to date is $Q = 0.64$, corresponding to $\eta_\alpha = 0.11$, which was achieved at JET in 1997 [7]. We denote such plasmas with significant fusion power but below the burn condition as *weakly burning plasmas*. Scientific break-even is defined by $Q = 1$, corresponding to $\eta_\alpha = 0.17$. *Reactor-grade burning plasmas* in the first power plants will require a much higher Q than our burn condition, $Q > 5$, to have a substantial net electricity output [8]. For example, various DEMO designs have $Q \sim 20$–50 and $\eta_\alpha \sim 0.8$–0.91. The *ideal burning plasma* is completely self-heated and has $Q \rightarrow \infty$ and $\eta_\alpha \rightarrow 1$. This is also called *ignition*. In recent years, several devices have been designed or are already being constructed, which currently aim at operating burning plasmas, among them SPARC [9], STEP [10, 11], CFETR [12], and BEST. The various burning plasma regimes and relevant magnetic confinement devices are summarized in table 1. Characteristics of burning fusion plasma devices are reviewed in chapter 1 of this volume [13].

ITER is currently scheduled to start low-power plasma operation in a few years and burning fusion plasma operation a few years later. Some of the privately and publicly funded fusion efforts may access the burning-plasma regime even earlier. The next phase of fusion power generation beyond ITER, hopefully early in the second half of this century, is the operation of reactor-grade burning plasmas in fusion power plants, delivering fusion power to the electricity grid for humankind to use. These long timescales make fusion research necessarily a multi-generational effort. The next generation of fusion scientists will base the operation of reactor-grade burning plasmas on the choices our generation is making now. This generation changeover will be well on its way even for the burning plasma operation in ITER. This aspect of fusion research is a primary motivation for the ITPA Topical Groups to periodically condense the knowledge and progress towards burning plasma operation achieved in recent years into a single volume to explain the rationale for the choices we have made [13–19]. We will refer the reader to these other 7 chapters of this volume where the referred topics are discussed from the perspective of the other ITPA Topical Groups.

The essential defining characteristic of a burning fusion plasma is the self-sustained heating by the energetic α-particles, which we will call alphas in the following. To ensure self-sustained heating, the alphas must be well-confined. The enhanced transport of alphas caused by 3D effects and instabilities must be minimized. This central role of alphas in any burning plasma system makes EP physics a core part of this volume.

	Q	η_α	Heating power	Devices
weakly burning plasma below break-even	$0 \ll Q < 1$	$0 \ll \eta_\alpha < 17\%$	$0 \ll P_{\text{fus}} < P_{\text{aux}}$	JET, TFTR
weakly burning plasma above break-even	$1 < Q < 5$	$17\% < \eta_\alpha < 50\%$	$P_\alpha < P_{\text{aux}} < P_{\text{fus}}$	ITER, STEP, BEST, SPARC, CFETR
burning plasma	$Q > 5$	$\eta_\alpha > 50\%$	$P_\alpha > P_{\text{aux}}$	ITER, STEP, BEST, SPARC, CFETR
reactor-grade burning plasma	$Q \gg 5$	$\eta_\alpha \gg 50\%$	$P_\alpha \gg P_{\text{aux}}$	DEMO, CFETR, STEP
ideal ignited plasma	$Q \to \infty$	$\eta_\alpha = 100\%$	$P_\alpha \gg P_{\text{aux}} = 0$	

Table 1. Burning plasma regimes in terms of power amplification, alpha heating fraction, and heating, and a selection of devices aiming to achieve these.

Here, we will review the most essential EP physics in burning plasmas in magnetic confinement devices. We consider a particle in a plasma to be energetic, if its energy $\mathcal{E}_{\text{f}}$ is significantly larger than the plasma temperature T (in eV), $\mathcal{E}_{\text{f}} \gg T$. EP populations consist of fusion-born alphas, fast ions from neutral beam injection (NBI), fast ions accelerated by electromagnetic wave heating in the ion cyclotron range of frequencies (ICRF), and finally the undesired runaway electrons that can get accelerated to MeV-range energies by parallel electric fields. While we will attempt to cover EP physics thoroughly and emphasize current results, the starting point and depth we have in mind will be appropriate to the non-specialist reader. We will focus on the progress achieved in the field of EP physics for burning plasmas since the last update of the ITER Physics Basis [20]. Most work of the ITPA Topical Group for Energetic Particle Physics has been done for ITER which will provide early experimental tests of our predictions on EP physics in a burning plasma. Furthermore, we will discuss implications for the fusion power plants currently being designed around the world. For further and in some areas more comprehensive information, we also point to the EP physics chapters in the earlier ITER Physics Bases [20, 21] as well as several reviews on EP physics [22–38]. We also highlight the recent JET DT experiments which allowed EP studies in mildly burning plasmas [39–53].

First, let us start by briefly reviewing the historical context of EP physics in magnetically confined fusion plasmas. Experimental investigations of EP physics began in the 1980s, when powerful NBI and ICRF heating technologies were developed and applied to toroidal plasmas. Initially favorable heating results were obtained. However, as scaling information accumulated over a range of devices and regimes, the negative effects of auxiliary heating power on confinement became recognized and were incorporated into empirical scaling laws.

On the theoretical front, new forms of global Alfvén waves susceptible to resonant destabilization by EPs were identified. These modes exist in frequency gaps of the shear Alfvén spectrum created by couplings across poloidal mode numbers [27]. Such couplings arise from the periodic variation of magnetic field strength in the poloidal direction and are analogous to the bandgaps between the Brillouin zones of lattices with periodically varying potential, as described in solid state physics. Also, modes such as the fishbone instability and the kinetic ballooning mode that involve interaction of EPs with low-frequency magnetohydrodynamic (MHD) activity were observed in experiments and analyzed. The DT operation of TFTR and JET in the 1990s motivated an intense search for alpha-driven instabilities. However, the significant EP population from NBI heating and the relatively dilute alpha population made it difficult to identify instabilities specifically driven by alphas, except for in brief intervals following the turn-off of the beams.

Fast forwarding to current times, a large zoology of Alfvén eigenmodes (AEs) has been identified, and carefully diagnosed in many toroidal devices, including imaging of two-dimensional mode structures and diagnosis of rapid frequency variations and nonlinear dynamics. Among these are the toroidicity-induced AE (TAE), reversed-shear AE (RSAE), ellipticity-induced (EAE), non-circular-triangularity-induced (NAE), global AE (GAE), compressional AE (CAE), beta-induced AE (BAE), and the beta-induced Alfvén-acoustic eigenmode (BAAE), see figure 26 in section 6. It is also known that these AEs can lead to substantial EP transport, removing up to 40 to 60% of the beam power that would normally be available for core plasma heating. Measurements and simulations of AEs can be very precise, leading to an often remarkable agreement between theory and simulation, which is one of the major quantitative successes of MHD in toroidal devices. We will discuss AEs from section 6.

In addition to energetic ions, tokamaks can also spontaneously create in-situ beams of relativistic electrons, known as runaway electrons. The runaway phenomenon is caused by the acceleration in toroidal electric fields present in tokamak plasmas, coupled with the decreasing collisional drag on electrons with increasing velocity. Such runaway beams can attain a sufficient intensity to cause damage to the vacuum vessel walls. Runaway electrons were first a concern in the early days of tokamak research due to their generation by the Ohmic electric field in the early breakdown phase of the discharge. More recently, it has been recognized that intense runaway generation can be possible due to avalanche phenomena and the large induced electric fields that will be driven by the current collapse phase of disruptive instabilities which sometimes terminate tokamak discharges. We will treat runaway electrons in section 12, and disruptions and runaway electrons are also treated in chapter 4 of this volume [16].

Understanding and predicting EP-driven instabilities requires both linear and nonlinear modeling. Linear modeling is important because EP-driven modes experience damping, resulting in thresholds that have to be surpassed before a mode can exist. Nonlinear modeling is important because observed EP-driven modes typically survive for many e-folding times, based on linear growth rates. Thus, the instabilities dynamically reach some balance between sources and sinks, i.e. drive strength vs. mitigating effects such as flattened regions in phase space, zonal flows and currents, and turbulent cascades. It has become recognized that EP-driven modes set limits on the profiles and parameters that can be achieved through critical-gradient behavior and enhanced transport. In current devices, enhanced EP transport can conveniently be characterized through the deuterium-deuterium (DD) neutron rate which is almost linearly related to the EP density since DD neutrons in existing devices are predominantly generated through beam-target reactions, i.e. reactions between slow ions and EPs. An observed neutron deficit indicates an EP density deficit and hence enhanced transport. Nonlinear EP physics remains an active area of experimental and theoretical research. The nonlinear effects of EP-driven instabilities can depend strongly on the q-profile, the mode classification, the mode frequency range, and the number of modes that are active concurrently.

A significant challenge arising in burning plasmas with high power amplification Q is that the temperature and density profiles are self-organized, i.e. self-consistently determined by self-heating from alphas rather than directly controlled from the outside by auxiliary heating. The physics and stability properties of plasma with self-sustained heating by alpha populations lead to a new regime of operation in ITER and future burning plasma devices. Several plasma characteristics are substantially different, such as the high degree of isotropy of energetic alpha populations compared to the highly anisotropic ions generated by auxiliary heating, the shape of the EP profile, the EP Larmor radius normalized by the minor radius, which is around $\rho_{\mathrm{Lf}}^* \sim 0.02$ in present devices and 0.04 in ITER, and the Alfvén Mach number (the ratio of EP speed and Alfvén speed), which often is 0.3 to 0.5 in present devices but will be 1 or above in ITER. EP-driven instabilities will have different characteristics compared to those seen in present experiments. They are most active around $k_\perp \delta_{\mathrm{f}} \sim 1$, where $k_\perp$ is the perpendicular wave number and δ_{f} is the drift orbit width, and will therefore predominantly exist at higher mode numbers and be more radially localized than in present experiments. This can lead to increased local transport and the potential for radial avalanches as compared to existing devices where radial wavelengths are typically 20 to 50% of the minor radius. This new regime of operation cannot be directly tested on non-burning, externally heated plasmas in present machines and forms a major part of the rationale for building ITER and other experimental burning plasma devices.

One might have hoped to tackle this change in parameters by a "wind-tunnel" approach, where we carefully diagnose the EP populations and instabilities in experiments on a sequence of smaller devices and develop scaling laws describing EP-related phenomena. However, since the resonant nature of EP-driven instabilities causes strong dependencies on the plasma profiles, such a "wind-tunnel" approach by itself cannot be relied on to predict the performance of reactor-grade fusion plasmas from present high-performance plasmas or even from weakly burning plasmas. Instead, our approach is to make predictions of experimental outcomes in present devices by modeling and simulation and test these predictions against the experimental data. The application of codes validated this way constitutes our best prediction of EP physics in burning fusion plasmas. To gain a full understanding of alpha heating and instabilities in burning plasmas, it will be crucial to test these predictions against experimental data at ITER and other burning plasma devices, both in the operation phases with and without burning fusion plasmas. Good diagnostic coverage at ITER and the other devices will therefore be essential. However, many existing diagnostic methods will not be available in the high neutron flux environment of burning plasmas.

Thus, in order to prepare for future plasma operation with significant alpha populations and self-sustained heating, EP physics research must support three main research areas, which comprise the main

topics of this paper:

(i) Experiments on existing devices,

(ii) Diagnostic development, and

(iii) Theory, modeling, and simulation.

Studies of EPs further need to consider the helium ash, i.e., alphas that have slowed down and delivered a major part of their energy to the bulk plasma. Whereas the high-energy alphas, which heat the plasma, are a cherished population for sustaining fusion power, the helium ash is an undesired impurity population, diluting the DT fuel mixture. If these thermalized alphas are not transported out of the plasma at a sufficient rate, the fuel dilution can lead to an extinction of the burning plasma state. The transport of helium ash is discussed comprehensively in chapter 2 of this volume [14]. The understanding of alpha physics must extend over a broad range of energies from the 3.5 MeV alpha birth energy to a few times the thermal plasma energy. Ideally, control mechanisms should be identified that rapidly transport alphas out of the plasma once they have deposited a large fraction of their energy in the thermal bulk plasma. These mechanisms could include EP-driven instabilities, externally driven radiofrequency (RF) waves, 3D fields, or MHD instabilities such as sawteeth or edge-localized modes (ELMs).

The physics of the helium ash regime has not attracted nearly as much attention as the effects related to the higher energy alphas. ITER will face this issue in an especially direct way since the pulse length significantly exceeds the slowing-down time of alphas. Dilution of the DT fuel by thermalized helium ash can threaten this mission goal for the pulse length of burning plasmas. The need to understand alpha transport over the whole energy range leads to an unusual bimodal challenge. At high energies, the alphas must have good confinement and instabilities suppressed; at low energies comparable to the thermal energy, alpha confinement should be degraded and instabilities excited if possible. ITER will offer a crucial experimental platform to consistently address both extremes of alpha physics. This motivates careful diagnostic and modeling over the full energy range of the alpha distribution function.

This paper is organized as follows. Section 2 reviews elementary EP physics in idealized plasmas, including drift orbit theory and associated frequencies, EP sources, plasma heating, confinement, and losses, which constitutes a basis for more complex physics discussed in later sections. Section 3 highlights recent developments in the area of ICRF heating, such as the efficient three-ion scheme, which opens new possibilities not known when ITER was designed. Furthermore, in the early operational phases of ITER

before DT, ICRF heating will be the only significant source of EPs. Section 4 describes the main diagnostics used to detect EPs and instabilities, in particular the diagnostics capable of working in the high neutron- and gamma-ray flux environment of burning plasmas. We focus on what physics can be diagnosed and refer to chapter 8 of this volume for the technical details of the diagnostics [19]. Section 5 describes the mutual interaction of EPs and thermal-plasma instabilities, i.e. instabilities typically not driven by EPs. In particular, we describe the interaction of EPs and neoclassical tearing modes, sawteeth, ballooning instabilities, resistive wall modes, and edge-localized modes, which are thought to have the strongest interaction with EPs. Section 6 discusses linear stability theory of EP-driven modes and EPMs, which remains a crucial theoretical framework to predict their existence. While section 6 can describe the existence of EP-driven modes and EPMs, section 7 deals with their evolution, requiring nonlinear theory and simulation. This field has grown substantially since the 2007 ITER Physics Basis [20], partially owing to the ever increasing computer power. Taking the fishbone instability as our starting point requiring nonlinear theory and simulation, we review various approaches to modeling. Gyrokinetic theory and simulation constitutes the most fundamental approach to EP simulations, requiring the fewest modeling assumptions. We then review various approaches relying on progressively more modeling throughout the section: kinetic-MHD models, gyrofluid models, reduced models, and semi-analytic approaches. Simulations using such reduced models are often more tracktable since they allow us to focus on the most essential nonlinear physics. Section 8 deals with 3D effects on EP confinement. 3D effects arise since plasmas in real magnetic fusion devices are never exactly axisymmetric, which would be required for a 2D treatment, due to the magnetic coil systems generating magnetic field ripples and due to the 3D structures of modes in the plasma. Section 9 considers multi-scale synergistic interactions between EP-driven modes, low-frequency perturbations, especially EP-driven geodesic acoustic modes (EGAMs), and turbulence, which are interactions where several phenomena are concurrently active. In section 10 we explore options to optimize plasma scenarios and to enhance the plasma performance through EPs by considering the EP phase space and possible actuators we have to control the EP phase space. section 11 deals with the EP physics in ITER plasmas before fusion power operation, where plasmas are heated by NBI and ICRF heating, but are not burning. Here we study EP physics in plasma scenarios with reduced magnetic fields, in which it is easier to access the H-mode. Finally, while runaway

electrons are considered throughout this review as a group of EPs, section 12 focuses on the physics of runaway electrons in particular. Section 13 concludes this review by highlighting the state-of-the-art of EP physics research and by pointing to possible future avenues of EP physics research in burning plasmas.

2. Basic physics of EPs: sources, plasma heating, confinement and losses

Most of the plasma in ITER will be in a state near local thermodynamic equilibrium. The thermal ions and electrons that comprise the bulk gyrate with Larmor orbits with radii ρ_{Li} and ρ_{Le} which are small when compared with the scales of the vessel, and they drift along magnetic field lines with small deviations δ_{i} and δ_{e} from the concentric flux surfaces on which the magnetic field lines lie. Typical characteristic speeds of phenomena in the bulk plasma include the thermal speeds of the ions $v_{\mathrm{th,i}} = \sqrt{T_{\mathrm{i}}/m_{\mathrm{i}}}$ and electrons $v_{\mathrm{th,e}} = \sqrt{T_{\mathrm{e}}/m_{\mathrm{e}}}$, the propagation speeds of Alfvén waves $v_{\mathrm{A}} = B/\sqrt{\mu_0 m_{\mathrm{i}} n_{\mathrm{i}}}$ and sound waves $c_{\mathrm{s}} = \sqrt{(T_{\mathrm{e}} + \Gamma_{\mathrm{i}} T_{\mathrm{i}})/m_{\mathrm{i}}}$ with Γ_{i} the adiabatic index, and the diamagnetic drift velocities of electrons $v_{*\mathrm{e}} = T_{\mathrm{e}}/(eB)\partial_r \log(p_{\mathrm{e}})$ and ions $v_{*\mathrm{i}} = T_{\mathrm{i}}/(Z_{\mathrm{i}}eB)\partial_r \log(p_{\mathrm{i}})$. Several thermal ion species will be present in burning plasmas, each with their own temperatures and velocities.

In order to sustain the thermal plasma at constant temperature, a steady source of bulk plasma heating must be provided by more energetic ions or electrons that are constantly generated or introduced into the plasma. They slow down due to collisional processes and gradually become thermalized. In addition to the plasma self-heating from 3.5 MeV alphas produced in the DT fusion reactions, also the auxiliary heating methods ICRF heating and NBI on ITER introduce MeV-range ions into the plasma. Electron cyclotron radio-frequency (ECRF) heating is another main auxiliary heating scheme, but it does not generate EPs.

Energetic ions reach speeds exceeding some of the important characteristic speeds of the bulk plasma processes, and the balance between ion creation and slowing-down produces energy distributions which deviate strongly from local thermal equilibrium distributions. The motion of fast ions is more complicated than the motion of thermal ions; in addition to the large free-streaming velocity $v_{\parallel \mathrm{L}}$ and perpendicular gyration $v_{\perp \mathrm{L}}$, the drift motion away from the magnetic field lines v_{D} can become significant as well. Importantly, the drift velocity depends not only on the particle energy, but also on the magnetic field strength and geometry. Confined fast ions will traverse ITER with these velocities, with the dimensions of ITER implying a corresponding set of timescales. For phenomena much slower than the ion

gyration and lengthscales larger than the gyroradius, it is sufficient to ignore the gyration and focus on the timescales associated with the gyro-averaged quantities $v_{\parallel}$ and v_{D}.

2.1. Equilibrium on the collisionless timescale

For magnetic fields with slow variations in space and time, and for sufficiently slow and weak electric fields, particles possess nearly invariant properties. The existence of these invariants guarantees that particles are confined to imaginary surfaces that can be labelled by the invariants [54]. When considering distributions of particles which are steady in time, confined particles belong to equilibrium distributions. The timescale of the equilibrium governs the form that the distribution must take [55]. For equilibrium on a longer timescale than a cyclotron period $2\pi/\omega_{\mathrm{c}}$, where $\omega_{\mathrm{c}} = ZeB/m$ is the cyclotron frequency, the particle distribution must be independent of gyroangle and expressible as

$$F = F(\boldsymbol{x}, \mathcal{E}, \mu, \sigma), \tag{2}$$

where $\sigma = \mathrm{sign}(v_{\parallel})$ and $\boldsymbol{x}$ is the position. The particle energy $\mathcal{E}$ is never changed by the magnetic field. The invariant μ associated with the gyration of the particle is given by the magnetic moment $\mu \approx m v_{\perp}^2/(2B)$, provided the magnetic field is nearly uniform on the scale of the gyration. The next fastest timescale is the time taken to follow a magnetic field line $L/v_{\parallel}$ for some typical distance L, meaning that equilibrium must be independent of distance along a magnetic field line, $\boldsymbol{B} \cdot \nabla F = 0$. If magnetic field lines are labeled with Clebsch-type coordinates α_{Cl} and β_{Cl} [56], so that $\boldsymbol{B} = \nabla \alpha_{\mathrm{Cl}} \times \nabla \beta_{\mathrm{Cl}}$, and a length coordinate along the field line is represented by s, then we will have the positional dependence on $\boldsymbol{x}$ replaced by

$$F = F(\alpha_{\mathrm{Cl}}, \beta_{\mathrm{Cl}}, \mathcal{E}, \mu, \sigma), \tag{3}$$

independent of s. For axisymmetric idealised tokamaks, the magnetic field lines lie within poloidal flux surfaces (constant poloidal flux ψ), and the magnetic field can be written in terms of ψ and toroidal angle ϕ as $\boldsymbol{B}_\theta = \nabla \psi \times \nabla \phi$. The poloidal flux is related to the magnetic vector potential according to $A_\phi = \psi/R$. For timescales shorter than $L/v_{\parallel}$, fast ions are approximately confined to those flux surfaces

$$F = F(\mathcal{E}, \mu, \psi, \sigma). \tag{4}$$

Eventually, the drift away from magnetic field lines becomes important for equilibrium on a timescale L/v_{D}, meaning that the surface traced by an invariant such as $J^{**} = \oint (v_{\parallel} + \frac{Ze}{m} A_{\parallel}) \mathrm{d}s$, where $A_{\parallel}$ is the parallel magnetic vector potential, (for almost closed field lines) defines the longer equilibrium

$$F = F(\mathcal{E}, \mu, J^{**}, \sigma) \tag{5}$$

9

with purely spatial position coordinates no longer appearing. If the field is exactly axisymmetric, then the canonical toroidal angular momentum $P_\phi = mRv_\phi + Ze\psi$ is an exact invariant providing perfect confinement with the equilibrium

$$F = F(\mathcal{E}, \mu, P_\phi, \sigma), \tag{6}$$

until collisions or other processes violate the symmetries underlying the constants of motion (COMs) [37]. Most notably, departures from axisymmetric magnetic fields violate the conditions for equilibrium because of the loss of the exact invariant P_ϕ.

Static or slowly time-varying perturbations to the magnetic field can each be decomposed into toroidal modes of the form

$$\delta \boldsymbol{B}(R, z, \phi, t) = \widetilde{\boldsymbol{B}}(R, z, t; n, \omega) \exp(i(n\phi - \omega t)), \tag{7}$$

where R is the major radius coordinate, z the vertical coordinate, ω is the angular frequency, and n is the toroidal mode number. For a particle interacting with this perturbation, the toroidal component of the Lorentz force changes the toroidal momentum in P_ϕ, whilst the perturbed vector potential changes the poloidal flux, so the canonical toroidal angular momentum changes at the rate

$$\frac{\mathrm{d}P_\phi}{\mathrm{d}t} = ZeR\hat{\boldsymbol{\phi}} \cdot \left(\delta \boldsymbol{E} + \boldsymbol{v} \times \delta \boldsymbol{B} + \frac{\mathrm{d}\delta \boldsymbol{A}}{\mathrm{d}t}\right)$$
$$= inZe(\delta \boldsymbol{A} \cdot \boldsymbol{v} - \delta \Phi), \tag{8}$$

where we have used Faraday's law to obtain the electric field $\delta \boldsymbol{E}$ from the vector and scalar potentials $\delta \boldsymbol{A}$ and $\delta \Phi$.

Important characteristic frequencies of the orbital motion of the ions are the transit frequencies in the toroidal and poloidal directions ω_ϕ and ω_θ, based on the gyro-averaged quantities $v_\parallel$ and v_D. If the time it takes a particle to complete a full revolution in the tokamak in the poloidal direction is denoted by τ_θ, these orbital frequencies are given by

$$\omega_\theta = 2\pi/\tau_\theta, \tag{9}$$

$$\omega_\phi = \frac{1}{\tau_\theta} \int_0^{\tau_\theta} \frac{\mathrm{d}\phi}{\mathrm{d}t} \mathrm{d}t \tag{10}$$

Any violation of equilibrium is most efficient when there is coherent synchronization between the orbital phase and the phase of the perturbation with frequency ω, leading to the resonance condition

$$\omega - n\omega_\phi - l\omega_\theta = 0, \tag{11}$$

where the integer l is arbitrary. The details of the orbit interaction with the 2D perturbation structure $\widetilde{\boldsymbol{B}}(R, z, t)$ governs the magnitude of the effect on the orbit for different values of l. Even when there is synchronization, the variation in the P_ϕ can be periodic and average to zero for sufficiently small $\delta B/B$. However, for orbits closest to being in resonance,

small deviations due to collisions or due to overlapping resonances can lead to chaotic motion. The number of orbits sensitive to this effect scales with the magnitude of the perturbation.

The slow time variation of the magnetic field of a single toroidal mode implies an induced electric field. This electric field does work on the particles and hence exchanges energy with the particle with a rate depending on the frequency according to

$$\frac{\mathrm{d}\mathcal{E}}{\mathrm{d}t} = Ze\left(\boldsymbol{v} \cdot \delta \boldsymbol{E} + \frac{\mathrm{d}\delta \Phi}{\mathrm{d}t}\right) = i\omega Ze(\delta \boldsymbol{A} \cdot \boldsymbol{v} - \delta \Phi). \tag{12}$$

The rates of change of the energy and the canonical toroidal angular momentum from each toroidal mode can be compared, giving immediately

$$n\Delta\mathcal{E} = \omega\Delta P_\phi. \tag{13}$$

This important equation can also be deduced from a quantum mechanical perspective if we imagined the perturbation of particles from toroidally propagating modes as the resonant absorption (or emission) of photons; for an incoming photon, the energy absorbed is $\Delta\mathcal{E} = \hbar\omega$ and the absorbed toroidal momentum is $\Delta P_\phi = R\hat{\boldsymbol{\phi}} \cdot \hbar\boldsymbol{k} = \hbar n$. An important consequence of equation (13) is that a particle undergoing radial excursion due to a perturbation will also experience a change in energy. This change in energy is the result of the induced electric field associated with the perturbation. For shear Alfvénic perturbations, this energy change is small, and vanishes entirely for magnetic perturbations approaching zero frequency and growth rate. For low-frequency large length-scale perturbations, the gyro-invariant is preserved, $\Delta\mu \approx 0$, giving together with equation (13) a complete description of how orbits are affected.

So far, we have only considered perturbations where the gyration of the particles plays no role in the coherent synchronization between the orbit and the waves. If the perturbations become narrow compared with the size of the gyration, or if the frequency of the perturbation becomes comparable to the gyrofrequency, considering only the resonance of guiding centres in equation (11) will not suffice and a general resonance condition is required [57]. Care must be taken to consider the coherent synchronization between the perturbation and the orbit-averaged poloidal, toroidal, and cyclotron frequencies. When these frequencies are well separated, such as on ITER, the resonant interaction can be taken as a local phenomenon giving

$$\omega = N\omega_\mathrm{c} + k_\parallel v_\parallel. \tag{14}$$

At high frequency, the changes in magnetic moment and the energy are no longer small, and a change in energy leads to a change in normalized magnetic

moment $\Lambda = \frac{\mu B_0}{\mathcal{E}}$, where B_0 is the toroidal magnetic field on axis, according to [58]

$$\Delta\Lambda = \left(\frac{N\omega_c}{\omega} - \Lambda\right)\frac{\Delta\mathcal{E}}{\mathcal{E}}, \tag{15}$$

or equivalently

$$\Delta\mu = \frac{N\omega_c}{\omega B_0}\Delta\mathcal{E}. \tag{16}$$

Note that the resonance condition in equation (14) applies when the particle interacts with the wave on a portion of its drift orbit, whereas the resonance condition in equation (11) applies when the particle experiences the same wave phase on multiple drift orbits. In addition to the resonances, efficient wave-particle energy transfer can occur when an EP encounters a constant phase during a single pass through an instability [59]. This phenomenon can cause AE-induced losses of fast ions that are born near the plasma edge [60].

2.2. Drift orbit approximations

For a perfectly confined particle, the drift velocity across magnetic field lines v_D is a periodic function, and the particles return to flux surfaces after a poloidal transit time $\tau_\theta = 2\pi/\omega_\theta$. The width of a drift orbit δ is then the distance traversed by v_D during half a poloidal transit time, which is the distance between the innermost and outermost flux surface the ion reaches. For realistic tokamak geometries, these characteristic frequency- and lengthscales can be computed using orbit-following codes, e.g. [61]. If $L/v_D \gg \tau_\theta$, we may neglect the orbit width in the equilibrium and take ψ to be invariant instead of P_ϕ. Under these conditions and for circular, large-aspect-ratio flux surfaces, we can estimate the orbital frequencies and widths. The toroidal and poloidal transit frequencies of strongly passing particles can be estimated as

$$\omega_{\phi,\mathrm{pa}} \approx \frac{v_\parallel}{R_0}, \tag{17}$$

$$\omega_{\theta,\mathrm{pa}} \approx \frac{v_\parallel}{qR_0}, \tag{18}$$

where R_0 is the major radius of the magnetic axis and

$$q \approx \frac{2\pi r^2 B_0}{\mu_0 I(r) R_0} \tag{19}$$

is the safety factor where r is the minor radius coordinate and $I(r)$ is the plasma current contained within the minor radius r. The safety factor q is the number of toroidal turns per poloidal turn of a magnetic field line around the torus. For trapped particles, orbits do not complete a circular transit, and ω_θ depends on a more complicated expression in terms of elliptic functions in analogy with the period for a pendulum [62]. As for a small amplitude pendulum,

deeply trapped particles approach a constant bounce period $\tau_{\theta,\mathrm{tr}} \approx 2\pi(\frac{2}{\epsilon})^{1/2}\frac{qR_0}{v}$ with the corresponding bounce frequency

$$\omega_{\theta,\mathrm{tr}} \approx \left(\frac{\epsilon}{2}\right)^{1/2}\frac{v}{qR_0}, \tag{20}$$

where $\epsilon = r/R_0$ is the inverse aspect ratio.

The parallel velocity of trapped particles changes sign, with inexact cancellation of toroidal motion over an orbit and a resulting precession with frequency $\omega_{\phi,\mathrm{tr}}$, which scales with the drift velocity according to $\omega_{\phi,\mathrm{tr}} = qv_D/r$. The drift velocity v_D is the sum of grad-B and curvature drifts. The grad-B drift depends on $v_\perp$ while the curvature drift depends on $v_\parallel$. A first approximation to the drift is again a constant value taken at the magnetic axis $v_D \approx \mu B_0/(mR_0\omega_c) + v_\parallel^2/(R_0\omega_c)$. Introducing the particle energy into the expression cancels the mass dependence giving

$$v_D \approx \frac{\mathcal{E}}{ZeB_0R_0}. \tag{21}$$

Hence, the drift velocity is proportional to the energy of the particle, where now the mass of the particle only enters through the energy. This cancellation of the mass dependence in the drift velocity implies the important result that electrons and ions at the same energy drift at the same speed. For deeply trapped particles, the toroidal precession frequency is thus in terms of energy

$$\omega_{\phi,\mathrm{tr}} \approx \frac{q\mathcal{E}}{ZeB_0R_0r}. \tag{22}$$

The precession frequency $\omega_{\phi,\mathrm{tr}}$ for trapped electrons and ions with a single charge is the same, but they drift in opposite directions. The maximum excursion of a strongly passing particle from a flux surface and the orbit width of deeply trapped particle δ can both also be estimated immediately using the drift velocity and bounce times, but a more accurate calculation based on P_ϕ conservation gives

$$\delta_{\mathrm{pa}} \approx 2q\rho_L, \tag{23}$$

$$\delta_{\mathrm{tr}} \approx 2q\rho_L\epsilon^{-1/2}, \tag{24}$$

showing that trapped particles drift further from flux surfaces than passing particles. The dependence on $q\rho_L$ makes clear that it is the poloidal Larmor radius which matters to the orbit width, which is not dependent on the toroidal field, but rather on the plasma current.

2.3. Equilibrium on the collisional timescale

The kinetic picture of fast-ion equilibrium presented above derives from ignoring collisional processes. Connection can be made with the neoclassical theory of transport (e.g: [63, 64]) by comparing the collision frequencies with the orbital frequencies of

collisionless motion. If collision frequencies are small when compared with orbital frequencies, as will be the case on ITER, equilibrium established on collisional timescales will be obtained in the 'banana limit' of the neoclassical theory. These equilibrium distribution functions, established over timescales exceeding the collision time, will not resemble Maxwellian distributions. The effect of Coulomb collisions on the equilibrium is modelled with a Fokker-Planck equation

$$\frac{\partial f_{\rm s}}{\partial t} + \boldsymbol{v} \cdot \frac{\partial f_{\rm s}}{\partial \boldsymbol{x}} + \frac{Z_{\rm s}e}{m_{\rm s}}\left(\boldsymbol{E} + \boldsymbol{v} \times \boldsymbol{B}\right) \cdot \frac{\partial f_{\rm s}}{\partial \boldsymbol{v}}$$
$$= Q[f_{\rm s}] + \sum_{\rm s'}\{C[f_{\rm s}, f_{\rm s'}] + S[f_{\rm s}, f_{\rm s'}]\} \tag{25}$$

where we have also included terms for the creation and loss of particles s and for the quasi-linear heating Q from rapidly varying electric fields that are not included in the left-hand side of the equation. The left-hand side of the equation represents the collisionless motion of particles including fast gyration and can be approximated by transformation to guiding-centre variables [65]. Solving the Fokker-Planck equation for timescales where $\frac{\partial}{\partial t} = 0$ gives the equilibrium distribution function expressible as $f_{\rm s} = F(\mathcal{E}, \mu, P_\phi, \sigma)$

Source and sink terms include the production and loss of fast ions in fusion reactions, the production and loss of charges in charge exchange reactions, or simply the external introduction of fast ion species.

2.4. EP sources

The main sources of energetic ions in fusion plasmas are fusion reactions, NBI and ICRF heating. We will discuss ICRF heating in section 3 and will here highlight certain aspects of alphas and other charged fusion products, EPs from NBI heating and energetic electrons generated by parallel electric fields. The heating systems at ITER are further described in chapter 6 of this volume [18].

The fusion reaction between a deuteron and a triton results in an alpha confined by the magnetic field and a neutron which escapes the plasma. The energy of the alpha in the center-of-mass frame of the fusion reaction is 3.52 MeV with no preferred velocity direction. The large energy and near isotropic distribution makes alpha physics difficult to imitate using ions produced by NBI or ICRF heating, which generate highly anisotropic distributions. Record fusion energy production, and equivalently the largest alpha population, was achieved in the recent JET DT campaign by injection a deuterium beam in tritium-rich plasma [39], but Q was lower than in the earlier experiments at JET and TFTR. A high $Q \approx 2.2$ at $P_\alpha = 1.8$ MW was achieved in an afterglow experiment, i.e. after the NBIs were switched off [47].

In presently operating tokamaks, NBI is the most reliable and commonly used method to heat the plasma to high temperatures relevant for fusion reactions to occur. ITER will have two 16.5 MW NBIs with energies up to 870 keV for hydrogen operation and 1 MeV for deuterium operation. In many present NBI sources, positive ions are brought up to energies in the range ∼20-180 keV in a particle accelerator and then neutralized by recombination reactions with electrons. In these positive-ion NBI sources, a mixture of ions and molecular ions, e.g. D^+, D_2^+, and D_3^+, is typically present when hydrogenic gas is ionized and accelerated in the voltage drop. The fast neutral molecules then dissociate into fast neutral atoms, dividing the energy of the molecule equally between the constituent atoms. The fast atoms entering the tokamak therefore have energies matching the full injection energy, half the injection energy, or one-third of the injection energy.

The resulting high-energy atoms are guided to the plasma through an NBI port, i.e. an opening in the vessel wall. The neutral atoms are not deflected by the magnetic field and move on straight paths, until they are ionized in the plasma. The beam of fast neutral atoms is highly directional and has a maximum energy chosen for optimal penetration into the core of the plasma before ionization and capture by the magnetic field. This ionization process corresponds to the source term S in the Fokker-Planck equation (25). After ionization, the ions proceed on a drift orbit dictated by the magnetic field. Subsequently, the energetic ions will heat the bulk plasma via Coulomb collisions and eventually become part of the thermal bulk plasma.

However, NBIs with typical energies of 100 kV cannot heat the plasma core in large machines with dense plasma such as ITER as most ionization already occurs in the plasma periphery. The penetration depth can be increased by increasing the particle energy, i.e., the acceleration voltage. But when the acceleration voltage is increased to significantly above 100 kV, the neutralization efficiency rapidly drops and is unacceptably low at energies required for ITER plasmas.

This problem can be circumvented by accelerating negative ions instead of positive ions. These two methods are referred to as negative-ion neutral beam injection (NNBI) and positive-ion neutral beam injection (PNBI). In NNBI, the additional electron is only loosely attached to the accelerated particle, so the neutralization efficiency is high. Since the ITER neutral beams will operate with 1 MeV energy, it is clear that NNBI is vastly superior to PNBI. NNBI has been experimentally demonstrated at the JT-60U tokamak and the LHD stellarator. NNBI do not inject neutrals at half- and one-third injection energy.

Also the orientation of the beams has to be

carefully considered, both to fully harness the potential of the beams and for safety reasons. Tangential injection, i.e. the beam path is tangent to some flux surface, produces a large fraction of ions on passing orbits, which drive current in the plasma. Therefore, neutral beam current drive (NBCD) is considered as a potential means for allowing non-inductive operation of tokamak plasmas [66]. In contrast, perpendicular injection produces energetic ions on trapped orbits that drive negligible current. We will discuss EP current drive in section 10.

An injected neutral that does not ionize in the plasma strikes the vacuum vessel wall of the inner column. When the plasma density is lower than the nominal design value, a large fraction of injected neutrals may traverse the plasma without ionizing, heating the wall materials instead of the plasma. This undesired wall heating is called "shinethrough". For ITER, plasma scenarios requiring extra care in this respect are the ramp-up and ramp-down phases in the beginning and end of the discharges, and in particular in scenarios with lower magnetic field strengths, such as in scenarios at $1/2$ and $1/3$ of the nominal magnetic field and plasma current foreseen in the early phases of ITER operations. Low magnetic fields lead to low plasma densities that promote shinethrough. The needed adjustments of the ITER beams in these plasma scenarios will be discussed in section 11.

Electrons in future burning plasmas are also anticipated to have energetic non-thermal populations. Heating and current drive of electrons can be achieved through exploiting electron cyclotron or lower hybrid wave resonances. Additionally, very large loop voltages can be induced in the plasma during a disruption, resulting in a population of runaway electrons whose drag due to collisions vanishes as they accelerate. These channels of relativistic electrons are highly directional and contain a large energy density since the energy gains of the runaway electrons are not balanced by energy losses due to collisions. These runaway electrons will be discussed in section 12.

2.5. Collisional energy transfer

Once EPs are introduced by the various sources, they slow down due to collisions, transferring energy to the thermal particles. Collisions between charged particles in a fully ionized plasma are dominated by the sum of many small angle collisions occurring within a Debye length [76]. The collisions are represented as an outflow of particles in velocity space

$$C\left[f_{\mathrm{s}}, f_{\mathrm{s'}}\right] = -\nabla_v \cdot \boldsymbol{j}_{\mathrm{s,s'}}. \tag{26}$$

The flow in velocity space depends in turn on the velocity gradients of the distribution:

$$\boldsymbol{j}_{\mathrm{s,s'}} \equiv -\boldsymbol{A}_{\mathrm{s'}} f_{\mathrm{s}} - \nabla_v \cdot \underline{\underline{\boldsymbol{D}}}_{\mathrm{s'}} f_{\mathrm{s}}. \tag{27}$$

The vector $\boldsymbol{A}_{\mathrm{s'}}$ represents a drag force slowing particles down, but not altering their directions. The tensor $\underline{\underline{\boldsymbol{D}}}_{\mathrm{s'}}$ represents the diffusion of particles. When considering any given fast ion, collisions with both electrons and ions must be accounted for. Due to the large mass difference between ions and electrons, diffusion is negligible for ions colliding with electrons. For fusion products and neutral beam heating, the equilibrium distribution is approximately solved by balancing the source rate S with the Coulomb collisions C.

In the range of energies typical for energetic ions in tokamaks, v_{f} always satisfies $v_{\mathrm{th,i}} \ll v_{\mathrm{f}} \ll v_{\mathrm{th,e}}$. In this case, analytic solutions to the Fokker-Planck equation for uniform plasmas are called slowing-down distribution functions [77, 78]. Since the Coulomb cross-section is determined by the relative velocity of the scattering particles, the scattering rate with electrons is determined by $v_{\mathrm{th,e}}$, while the scattering rate with thermal ions is determined by v_{f}, nearly independent of $v_{\mathrm{th,i}}$. The drag caused by thermal electrons (alone) leads deceleration of the particles with the associated Spitzer slowing-down time

$$\tau_{\mathrm{s}} = 6.27 \times 10^{14} \frac{A_{\mathrm{f}} T_{\mathrm{e}}^{3/2}}{Z_{\mathrm{f}}^2 n_{\mathrm{e}} \ln \Lambda} \frac{\mathrm{m}^{-3}}{\mathrm{eV}^{3/2}} \mathrm{s}, \tag{28}$$

where $\ln \Lambda$ is the Coulomb logarithm, T_{e} is the background electron temperature in eV, n_{e} is the density in m^{-3}, and A_{f} and Z_{f} the EP atomic mass and charge numbers. The relative importance of electron and ion friction depends upon both $v_{\mathrm{th,e}}$ and v_{f}. The fast ion energy at which the electron friction just balances the bulk ion friction is known as the critical energy $\mathcal{E}_{\mathrm{crit}}$ and is given by

$$\mathcal{E}_{\mathrm{crit}} \equiv 14.8 T_{\mathrm{e}} A_{\mathrm{f}} \left(\sum_i \frac{n_{\mathrm{i}} Z_{\mathrm{i}}^2}{n_{\mathrm{e}} A_{\mathrm{i}}} \right)^{2/3}, \tag{29}$$

where the sum is over the thermal-ion species. Above this critical energy, collisions with electrons dominate, leading to slowing down of the fast ions with little pitch angle scattering. Below the critical energy, collision with ions dominate, leading to slowing down of fast ions with significant pitch angle scattering. On ITER, the birth energies for fusion products and NNBI will exceed the critical energy and will, at first, be dominated by electron-ion drag collisions. Electron heating by alphas was directly observed in the recent JET DT campaign [45]. The Spitzer time describes the rate of change of the test particle velocity caused by the friction on background electrons, i.e. $\mathrm{d}v_{\mathrm{f}}/\mathrm{d}t = -v_{\mathrm{f}}/\tau_{\mathrm{se}}$ (assuming only electrons are involved in the slowing-down process). The thermalization time of a fast ion is related to the Spitzer slowing down time by $\tau_{\mathrm{th}} \equiv (\tau_{\mathrm{se}}/3) \ln(1 + (\mathcal{E}_{\mathrm{f}}/\mathcal{E}_{\mathrm{crit}})^{3/2})$.

For the fast ions to deposit their heat into the thermal electrons, the invariants of the motion must

	ITER	JET	NSTX	SPARC	STEP	DEMO	CFETR
	f_α	f_α	f_{NBI}	f_α	f_α	f_α	f_α
References	[31, 67]	[7, 67, 68]	[33, 69, 70]	[71, 72]	[11]	[8, 73]	[12, 74, 75]
a/R_0	0.32	0.33	0.76	0.31	0.56	0.3	0.31
$v_{\mathrm{f}}/v_{\mathrm{A}}$	1.91	1.68	3.34	1.55	4.17	1.46	1.66
$v_{\mathrm{A}}/v_{\mathrm{th,i}}$	4.70	4.74	2.19	6.08	2.26	5.34	4.48
$\rho_{\mathrm{L,f}}/a$	0.03	0.08	0.2	0.04	0.04	0.01	0.02
δ_{f}/a ∘	0.16	0.53	1.88	0.21	0.37	0.12	0.19
$\beta_{\mathrm{f}}(0)/\beta(0)$	0.15	0.13	0.15	0.13	0.58	0.4	0.16
Max $\delta B/B$ •	0.5%	0.08%	0.6%	0.15%	0.65%	0.3%	0.1%

Table 2. Non-dimensional parameters characterizing various EP effects.
∘ Orbit-width estimate modified to include ellipticity $\delta_{\mathrm{f}} \approx 2\rho_{\mathrm{L}}q/(\kappa\epsilon^{1/2})$
• Field ripple assumed as largest non-axisymmetric field

not vary much within a slowing down time. As we have already mentioned for low-frequency phenomena, the dominant loss of invariance occurs due to loss of axisymmetry. We therefore require that the variation in canonical momentum over an orbit $\Delta P_\phi/Ze(\psi_{\mathrm{edge}}-\psi_{\mathrm{core}})$ be much less than the number of orbits required to slow down $\tau_{\mathrm{s}}/\tau_\theta$.

2.6. Non-dimensional EP parameters

Several essential non-dimensional parameters characteristic for the size of various EP effects are given in Table 2. The larger the parameter, the stronger the EP effects will be. $v_{\mathrm{f}}/v_{\mathrm{A}}$ measures the EP ability to resonate with Alfvénic modes in the plasma, and $v_{\mathrm{A}}/v_{\mathrm{th,i}}$ measures if the Alfvénic modes will be dominated by EPs or by a combination of EP and thermal effects [79]. The normalized Larmor radius $\rho_{\mathrm{L,f}}/a$ is a fundamental measure of how strongly magnetized the plasma is, with ramifications for both stability and confinement of the EPs. The normalised orbit-width δ_{f}/a measures the deviation from flux surfaces, which relates to how well the asymmetric poloidal magnetic field is able to confine the EPs. The ratio $\beta_{\mathrm{f}}(0)/\beta(0)$ on axis with $\beta = 2\mu_0 p/B^2$ measures the relative sizes of the EP pressure and the plasma pressure. The EP pressure drives instabilities, and the plasma pressure results in damping. The perturbed magnetic field ripple $\delta B/B$ is responsible for the rate of momentum change $[1/Ze(\psi_{\mathrm{edge}} - \psi_{\mathrm{core}})]\mathrm{d}P_\phi/\mathrm{d}t$ which if sufficiently large will create chaotic orbits and result in radial transport.

3. EP generation and plasma heating by ICRF waves

3.1. Basic physics of ICRF heating

ICRF waves have been used early on in magnetic fusion research to generate EPs (see section 2.3 of [22] for a review). The thermal plasma is heated by two effects:

direct wave damping and collisional heating due to EPs accelerated by the ICRF waves. In the frequency range of ICRF waves ($f \approx 20 - 100\,\mathrm{MHz}$), part of the wave power is usually absorbed by the thermal particles. A physics description of RF heating therefore involves elements related to waves (propagation and damping) and to particles (e.g. wave-induced diffusion and collisional relaxation).

RF heating is described by the Fokker-Planck equation

$$\frac{\mathrm{d}f_{\mathrm{s}}}{\mathrm{d}t} = \hat{C}(f_{\mathrm{s}}) + \hat{Q}(f_{\mathrm{s}}) + S_{\mathrm{s}} - L_{\mathrm{s}}. \tag{30}$$

Here, f_{s} is the (quasilinearly time-space averaged) distribution function of ion species s, $\hat{C}$ is the collision operator, S_{s} is a particle source term, and L_{s} is a loss term. $\hat{Q}$ is the quasilinear operator representing the effect of waves interacting with species 's'. In quasilinear theory, this term takes the form of a diffusion or friction term and involves a quasilinear diffusion tensor, $\boldsymbol{D}_{\mathrm{ql}}$:

$$\hat{Q}(f_{\mathrm{s}}) \equiv \nabla_v \cdot (\boldsymbol{D}_{\mathrm{ql}} \cdot \nabla_v f_{\mathrm{s}}). \tag{31}$$

Depending on the level of sophistication of the description used, $\hat{Q}$ can have a rather complicated form. Important features of the quasilinear operator can nevertheless be illustrated by writing its components in the symbolic form

$$\boldsymbol{D}_{\mathrm{ql}} \equiv A \sum_n |\mathbf{d}^{(n)}(\boldsymbol{E})|^2 \delta(\omega - N\omega_{\mathrm{cs}} - k_\parallel v_\parallel). \tag{32}$$

Here, A is a constant, $\mathbf{d}^{(n)}(\boldsymbol{E})$ is a differential operator acting on the electromagnetic wave field, $k_\parallel$ is the component of the wave vector $\boldsymbol{k}$ along the local magnetic field, ω_{cs} is the cyclotron frequency of species 's'. The harmonic number N is any integer (including zero). The delta function $\delta(\omega - N\omega_{\mathrm{cs}} - k_\parallel v_\parallel)$ picks out the particles resonating with the wave, i.e. satisfying the wave-particle resonance condition equation (14).

A simplified representation of the process of plasma heating with ICRF waves appears in figure 2. The cold plasma dispersion relation in the ICRF

14

frequency range allows two plasma waves, the slow and the fast magnetosonic waves (SW and FW) [80] which are both excited by the ICRF antenna. Whereas the slow wave is evanescent, the fast wave can pass through a thin evanescence region to heat the core plasma through different branches illustrated in figure 2. In large-scale tokamaks such as ITER, the dominant branch is the generation of energetic ions rather than the mode-conversion branch.

However, other processes than those illustrated in figure 2 may play a significant role, too. For example, mode-converted waves (ion Bernstein waves and ion cyclotron waves) can also be absorbed by ions, and part of the fast-wave power can be directly absorbed by the thermal ions. Furthermore, it is possible to drive a small central electron current if part of the fast-wave power is directly absorbed by thermal electrons for an adequate toroidal antenna phasing [81, 82].
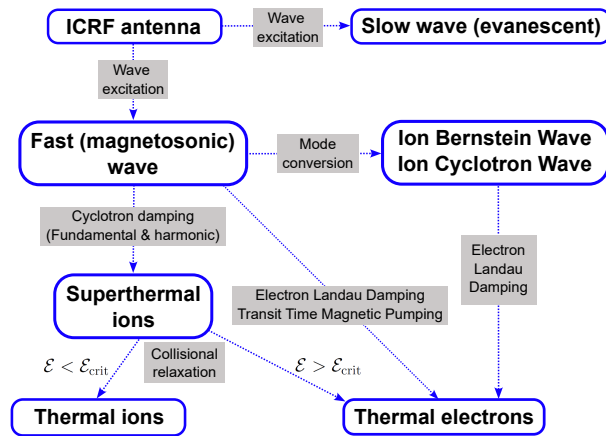

Figure 2. A simplified overview of fast-ion generation and plasma heating with ICRF waves.

3.1.1. Wave propagation and cyclotron damping. ICRF antennas typically consist of sets of metallic straps enclosed in boxes near the plasma edge. The currents in the straps can excite waves in the nearby plasma. In the ICRF frequency range, it is convenient to view the plasma and the antenna together as a global electrical circuit. In practical terms, the antenna needs to be adapted to the plasma by ensuring that the plasma and antenna impedances match [83, 84]. Indeed, the issue of ICRF power coupling to the plasma is a challenging problem requiring considerable effort.

The fast and slow magnetosonic waves are characterized by their refractive indeces $\boldsymbol{n} = \boldsymbol{k}c/\omega$. The parallel component of the refractive index with respect to the magnetic field, $n_\parallel$, is essentially determined by the antenna geometry, whereas the perpendicular component is determined by the dispersion relation. For conditions typical for the plasma edge in tokamaks, the slow wave is characterized by $n_{\perp,\mathrm{SW}}^2 \simeq -\omega_{\mathrm{pe}}^2/\omega_{\mathrm{ci}}^2$, where ω_{pe} is the electron plasma frequency and $\omega_{\mathrm{ci}} \equiv Z_{\mathrm{i}}eB/m_{\mathrm{i}}$ is the cyclotron frequency of the main ion species. Since the slow wave is evanescent ($n_{\perp,\mathrm{SW}}^2 < 0$) with a typical decay length of less then $1\,\mathrm{mm}$, it does not propagate to the regions far from the antenna and thus cannot heat the plasma core. However, the slow wave plays an important role in the problem of wave coupling and in the possible development of performance limiting electrical sheaths.

The propagation of the fast magnetosonic wave for a cold plasma is described by the dispersion relation [85]

$$n_{\perp,\mathrm{FW}}^2 \simeq \frac{\left(L - n_\parallel^2\right)\left(R - n_\parallel^2\right)}{S - n_\parallel^2}. \tag{33}$$

Here, S, L, and R are the components of the plasma dielectric tensor in the notation of Stix, with $S = 1 - \sum_{\mathrm{i}} \frac{\omega_{\mathrm{pi}}^2}{\omega^2 - \omega_{\mathrm{ci}}^2}$, $L = 1 - \sum_{\mathrm{i}} \frac{\omega_{\mathrm{pi}}^2}{\omega_{\mathrm{ci}}(\omega - \omega_{\mathrm{ci}})}$, and $R = 1 + \sum_{\mathrm{i}} \frac{\omega_{\mathrm{pi}}^2}{\omega_{\mathrm{ci}}(\omega + \omega_{\mathrm{ci}})}$. The fast-wave dispersion relation (equation 33) suggests quite complex behaviour, especially in plasmas with several ion species.

The presence of the right-hand cutoff, given by the condition $R = n_\parallel^2$, implies that the fast wave does not propagate below a certain density, $n_{\mathrm{e}} \lesssim 1 \times 10^{18}\,\mathrm{m}^{-3}$, which typically corresponds to a location in the plasma scrape-off layer. Therefore, the fast wave is evanescent near the plasma edge, too, just as the slow wave. However, since its decay length is typically on the order of 10 cm, a significant fraction of the fast-wave power can readily tunnel through the evanescence layer to reach the right-hand cutoff and propagate onward towards the plasma core. Part of the power reflected at the right-hand cutoff couples back to the antenna circuit, which leads to the requirement of adequate antenna-plasma matching.

In a single-ion plasma, the left-hand cutoff, $L = n_\parallel^2$, and the fast-wave resonance, $S = n_\parallel^2$, are reached at very low plasma densities, below the right-hand cutoff density. At the resonance layer, warm plasma effects (non-zero temperature) need to be taken into account, and the fast-wave resonance is bent into a confluence with a kinetic plasma mode. In plasmas with two or more ion species, both the left-hand cutoff and the fast-wave resonance can be located near the plasma core. In this case, the region bounded by this cutoff-resonance pair is often referred to as the ion-ion hybrid layer. For example, in plasmas with two ion species and for low $k_\parallel$, the ion-ion hybrid frequencies are given by

$$\omega_{\mathrm{S}} \approx \sqrt{\frac{\omega_{\mathrm{p1}}^2 \omega_{\mathrm{c2}}^2 + \omega_{\mathrm{p2}}^2 \omega_{\mathrm{c1}}^2}{\omega_{\mathrm{p1}}^2 + \omega_{\mathrm{p2}}^2}}, \tag{34}$$

$$\omega_{\mathrm{L}} \approx \frac{\omega_{\mathrm{p1}}^2 \omega_{\mathrm{c2}}^2 + \omega_{\mathrm{p2}}^2 \omega_{\mathrm{c1}}^2}{\omega_{\mathrm{p1}}^2 \omega_{\mathrm{c2}} + \omega_{\mathrm{p2}}^2 \omega_{\mathrm{c1}}}. \tag{35}$$

We always have $\omega_{\mathrm{S}} < \omega_{\mathrm{L}}$, and both ion-ion hybrid frequencies are in between the cyclotron frequencies ω_{c1} and ω_{c2}.

The dominant damping mechanism of the fast magnetosonic wave is cyclotron damping due to ions fulfilling the wave-particle resonance condition equation 14 [86]. $N = 1$ to $N = 3$ correspond to fundamental, 2nd harmonic, and 3rd harmonic ICRF heating at $\omega \approx \omega_{\mathrm{ci}}$, $2\omega_{\mathrm{ci}}$ and $3\omega_{\mathrm{ci}}$. Equation (14) is usually fulfilled in the vicinity of the ion cyclotron resonance layers, R_{IC}, where $\omega = N\omega_{\mathrm{ci}}$. The radial position of these layers in the plasma can be found considering on the $1/R$ radial dependence of the magnetic field in tokamaks by the handy formula,

$$R_{\mathrm{IC}} \approx R_0 \frac{N Z_{\mathrm{i}}}{A_{\mathrm{i}}} \frac{15.25 B_0}{f} \frac{\mathrm{MHz}}{\mathrm{T}} \tag{36}$$

where R_0 is the major radius, B_0 is the magnetic field on-axis in Tesla, and f is the RF frequency in MHz.

A simplified form of the quasilinear diffusion coefficient (equation 32) is given by

$$D_{\mathrm{ql}} = A \sum_N |E_+ J_{N-1}(k_\perp \rho_{\mathrm{Li}}) + E_- J_{N+1}(k_\perp \rho_{\mathrm{Li}})|^2$$
$$\times \, \delta(\omega - N\omega_{\mathrm{ci}} - k_\parallel v_\parallel), \tag{37}$$

where J_N is the Bessel function of order N, $k_\perp$ is the perpendicular wavenumber, and $\rho_{\mathrm{Li}} \equiv v_\perp / \omega_{\mathrm{ci}}$ is the heated ion Larmor radius. In equation (37), E_+ and E_- represent the left-hand and right-hand components of the RF electric field. For thermal and moderately energetic ions with energies of a few hundred keV, the argument of the Bessel functions is small, so we can approximate $J_0 \approx 1$ and $J_N(k_\perp \rho_{\mathrm{Li}}) \approx (k_\perp \rho_{\mathrm{Li}}/2)^N/N!$. As J_0 is the only Bessel function with an appreciable value at low $k_\perp \rho_{\mathrm{Li}}$, cyclotron damping at the fundamental frequency ($N = 1$) has a strong wave-particle interaction for thermal or fast ions, leading to potentially very effective heating (but not for single-ion plasmas as we will discuss below). For the harmonic ICRF heating ($N \geq 2$), the efficiency of the wave-particle interaction relies on the presence of higher-energy ions with a large Larmor radius, which is usually called the finite Larmor radius (FLR) effect.

Equation (37) also shows that the ion cyclotron damping is to lowest order determined by the left-hand component of the RF electric field, which rotates in the ion direction. However, the two components of the RF electric field are not independent. In fact, the local RF polarization (the ratio E_+/E_-) and its spatial distribution in the plasma volume is to a large extent determined by the plasma composition, rather than by the operational parameters of the RF system. For the fast wave, the RF polarization is given by

$$\frac{E_+}{E_-} \approx -\frac{R - n_\parallel^2}{L - n_\parallel^2}. \tag{38}$$

The combination of equations (33), (37) and (38) determines the characteristics of fast-wave propagation and ion cyclotron interaction in the plasma. The efficiency of the ICRF heating depends crucially on the plasma composition, i.e. the number of ion species with a different charge-to-mass ratio and their concentrations.

3.1.2. ICRF heating scenarios for fast-ion generation. It follows from equation (38) that, in a single-ion plasma, $E_+/E_- \approx (\omega - \omega_{\mathrm{ci}})/(\omega + \omega_{\mathrm{ci}})$. As the left-hand component of the RF electric field nearly vanishes for $\omega = \omega_{\mathrm{ci}}$, the fundamental cyclotron damping in single-ion species plasmas is weak. Since ICRF heating in metallic-wall machines is more dependent on adequate single-pass wave damping, this constraint limits the applicability of the fundamental ICRF heating in single-ion plasmas in both present-day and future tokamaks with metallic plasma-facing components.

To overcome this limitation, several methods have been developed [43, 85, 88–91], summarized in table 3. First, using harmonic resonances ($N = 2, 3, ...$) is an option, both for single-ion and multi-ion species plasmas. As outlined above, the harmonic damping is an FLR effect, requiring $k_\perp \rho_{\mathrm{Li}}$ to be large enough for efficient heating to occur. For this reason, harmonic ICRF heating is often applied in combination with NBI. Then the NBI system provides a seed of resonant fast ions with energies of about 50-100 keV that are accelerated to higher energies by ICRF heating. As fast ions reach MeV-range energies, the term for the right-hand component of the electric field $E_- J_{N+1}(k_\perp \rho_{\mathrm{Li}})$ in equation (37) becomes comparable or even larger than the term for the left-hand component $E_+ J_{N-1}(k_\perp \rho_{\mathrm{Li}})$. Eventually, a tail of fast ions is generated, with a maximum energy determined by the condition $D_{\mathrm{ql}} \approx 0$ [92]. The energy barrier scales approximately as B^2/n_{e} and usually reaches a few MeV. Being an efficient technique for generating MeV-range ions, the 3rd harmonic ICRF heating of D-beam ions is often used for fast-ion studies in D-D and D-^{3}He plasmas, see e.g. [93]. The form of the EP tail generated by 3rd harmonic ICRF heating simulated by the ASCOT-RFOF and the SPOT-RFOF codes was corroborated experimentally by velocity-space tomography (see section 4) based on NES and GRS measurements at JET as illustrated in figure 3 [87]. For this 3rd harmonic ICRF heating scheme, the coupling between the electromagnetic waves and the fast ions becomes weak at an energy of about 2 MeV which is corroborated by the measurement. Also

16

ICRF scenario	Resonant ion	Typical EP energies	Background plasma	Comments
$\omega = \omega_{ci}(H)$	H	A few hundred keV	D, T, DT mix, incl. 50%-50%	Efficient in the range $n_H/n_e \simeq 2-10\%$
$\omega = \omega_{ci}(^3He)$	^{3}He	A few hundred keV	D, T, DT mix, incl. 50%-50%	Efficient in the range $n_{^3He}/n_e \simeq 2-5\%$
$\omega = \omega_{ci}(D)$	D	A few hundred keV	T-rich plasma	Efficient in the range $n_D/n_e \simeq 5-15\%$
$\omega = 2\omega_{ci}(H)$	H	A few MeV	H, H-^{4}He mix, H-D mix	Often applied at low magnetic field
$\omega = 2\omega_{ci}(D)$	D	A few MeV	D, DT mix, incl. 50%-50%	Requires low n_H, typically $n_H/n_e \lesssim 2\%$, efficient in combination with NBI
$\omega = 2\omega_{ci}(T)$	T	A few MeV	T, DT mix, incl. 50%-50%	Efficient at $T_i \gtrsim 10\,\text{keV}$; main scenario for the flat-top plasma in ITER
$\omega = 3\omega_{ci}(D)$	D	A few MeV	D, D-^{3}He mix, DT mix, incl. 50%-50%	Efficient in combination with NBI
^{4}He-(^{3}He)-H, D-(^{3}He)-H	^{3}He	A few MeV	Mix H+~5-15% ^{4}He, mix H+~10-30% D	Three-ion scheme to generate MeV-range EPs in hydrogen majority plasmas
D-(D$_{NBI}$)-^{3}He	D	$\gtrsim 500\,\text{keV}$	D-^{3}He mix	Three-ion scheme to generate EPs (D and alphas) in D-^{3}He plasma

Table 3. Selected ICRF heating scenarios for EP generation in fusion plasmas. The first three rows are minority ICRF heating schemes, followed by the 2nd and the 3rd harmonic ICRF heating scenarios, and the three-ion ICRF heating schemes.
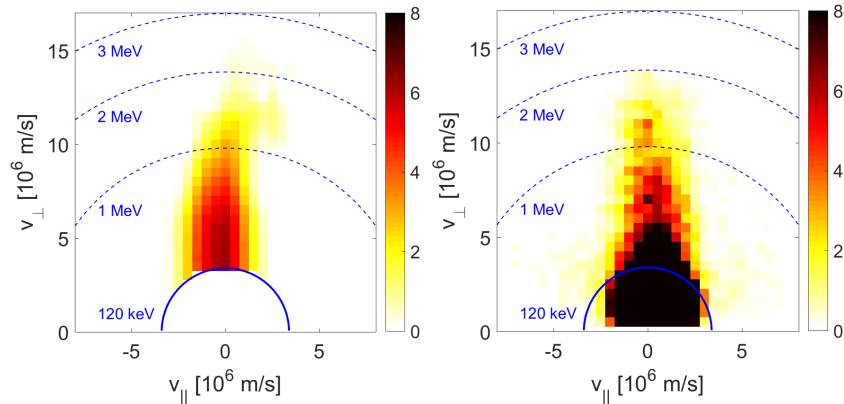

Figure 3. Measurement (left) and simulation (right) of a fast-ion velocity distribution function [a.u.] in the center of a plasma at JET heated by NBI and 3rd harmonic ICRF heating. The inversion was done for energies larger than 120 keV. Reproduced from [87].

the widths of the measured and simulated functions in $v_\perp$ direction agree well. A 3rd harmonic ICRF heating scheme was also used to generate an alpha tail by accelerating helium injected by NBI [94], which demonstrated the detection of alphas by gamma-ray spectroscopy (see section 4).

Nevertheless, the harmonic cyclotron interaction does not necessarily need a seed population of beam ions and can be an effective technique for plasma heating and fast-ion generation with ICRF heating alone [95]. For example, the 2nd harmonic heating of hydrogen ions, $\omega = 2\omega_{ci}(H)$ is routinely applied for heating JET hydrogen plasmas at $B_0 \approx 1.7\,\text{T}$. As discussed in [85], for harmonic absorption, the damping

rate scales with the ion beta as $\beta_i^{(N-1)}$, and therefore the wave absorptivity increases at lower magnetic fields. In general, in modern plasmas containing species with temperatures sufficiently large prior to the ICRF power application, harmonic heating has proven quite efficient, including during DT operation in TFTR [96, 97] and JET [98, 99]. The 2nd harmonic heating of tritium ions, $\omega = 2\omega_{ci}(T)$ is currently considered as the main scenario for ICRF heating of high-temperature DT plasmas in ITER [100].

A second possibility, referred to as minority heating [101], is to resort to fuel mixes containing only a small fraction of the targeted ion species. In this case, the RF frequency is tuned to the cyclotron frequency

of the minority ions, $\omega = \omega_{\mathrm{ci}}^{\mathrm{mino}}$, which usually have a concentration of a few percent ($n_{\mathrm{mino}}/n_{\mathrm{e}} \simeq 5\%$) [102]. In this case, the proximity of the left-hand cutoff and of the hybrid resonance results in the creation of a particular wave structure called the ion-ion resonance-cutoff pair. The practical consequence is that the wave polarization near the minority ion cyclotron layer is now dictated by the proximity of this structure, so that E_+ can remain significant close to the cyclotron resonance of minority ions. The minority heating scheme is efficient and robust with respect to changes in the features of the heated ion distribution function, since the corresponding leading term in equation (37) is independent of $k_\perp \rho_{\mathrm{Li}}$. The minority heating scheme has, therefore, been the main ICRF heating scenario in many fusion devices in operation until now. Minority heating of thermal and NBI-generated deuterons has been applied in recent JET DT experiments in T-rich plasmas, aiming to maximize beam-target fusion, and high performance DT hybrid plasmas [39, 43].
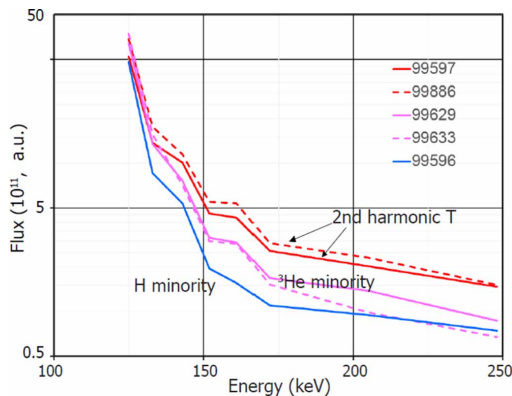

Figure 4. Energy spectra of neutral tritium fluxes measured by a neutral particle analyser in JET high performance DT hybrid plasmas with different ICRF heating schemes. The fluxes have been averaged over a one-second period (8-9 s) in each discharge. Reproduced from [43].

Figure 4 shows neutral particle analyzer measurements of tritium resolved in energy for high-performance DT hybrid discharges with 2$^{\mathrm{nd}}$ harmonic tritium ICRF heating and hydrogen and ^{3}He minority ICRF heating [43]. The neutral particle fluxes are largest for 2$^{\mathrm{nd}}$ harmonic tritium ICRF heating without ^{3}He gas injection. When ^{3}He is injected, the neutral particle fluxes of tritons decrease since less power is absorbed by triton ions when ^{3}He is present, leading to a less energetic triton population and lower neutral particle fluxes.

Finally, the recently proposed three-ion scheme has been successfully applied for plasma heating in several devices [104]. Whereas standard minority heating consists of introducing an ion species in a quantity suitable for the creation of the hybrid resonance-cutoff pair close to its own cyclotron layer,

the underlying principle of the three-ion scheme is to have two main ion species, characterized by mass and charge numbers A_1, Z_1 and A_2, Z_2, with a density ratio chosen to adequately locate the ion-ion resonance, typically near the magnetic axis, and introduce a third ion species (A_3, Z_3) in a small fraction with its cyclotron layer located close to the ion-ion resonance of the main ion species. This can be achieved by ensuring that the third species satisfies $Z_1/A_1 < Z_3/A_3 < Z_2/A_2$, which introduces a new ion-ion resonance layer in the plasma which benefits from the large $|E_+|$ component obtained at the ion cyclotron resonance of the minority ion. By separating the creation of a wave structure adequate for minority ion heating from the ion acceleration process at the cyclotron layer, the three-ion scheme achieves very good per-pass damping rate and effectively relaxes the stringent constraints on the minority ion concentration in the classical scheme. Alternatively, it is possible to choose a minority ion identical to one of the ion species already present in the plasma, but with a distribution function such that a substantial number of particles have a parallel velocity component $v_\parallel$ such that they are able to satisfy the resonance condition (equation 14) owing to their Doppler shift. In practice, this is achieved by targeting the NBI ions injected in the plasma, which has been demonstrated to yield efficient heating [38, 105]. Figure 5 illustrates that the power can be deposited in a small region close to the plasma core, as experimentally confirmed in the measured 2D neutron emission profile.

3.1.3. ICRF heating and collisional relaxation. Collisional relaxation during ICRF heating is more complex than for fusion alphas and NBI ions (section 2), since RF power continuously accelerates the targeted ions, counteracting the slowing-down process. Nevertheless, the RF power absorbed by superthermal ions is eventually transferred to the bulk plasma by collisional energy transfer. Accurately describing the process of ICRF heating requires solving the wave equation and the Fokker-Planck equation (30) self-consistently (see, e.g. Ref. [106]), now with a power source. The Fokker-Planck equation can be solved efficiently using, e.g., Monte Carlo methods, finite differences or finite elements.

Nevertheless, much insight into the relaxation process can be gained by examining the relaxation of a single test ion on the background plasma species outlined in section 2. The critical energy $\mathcal{E}_{\mathrm{crit}}$ suggest some flexibility of ICRF heating schemes to selectively heat predominantly electrons or ions. For example, in minority heating, targeting light ions at low concentrations (typically hydrogen) results in ions with energies $\mathcal{E} \gg \mathcal{E}_{\mathrm{crit}}$ and hence in dominant bulk
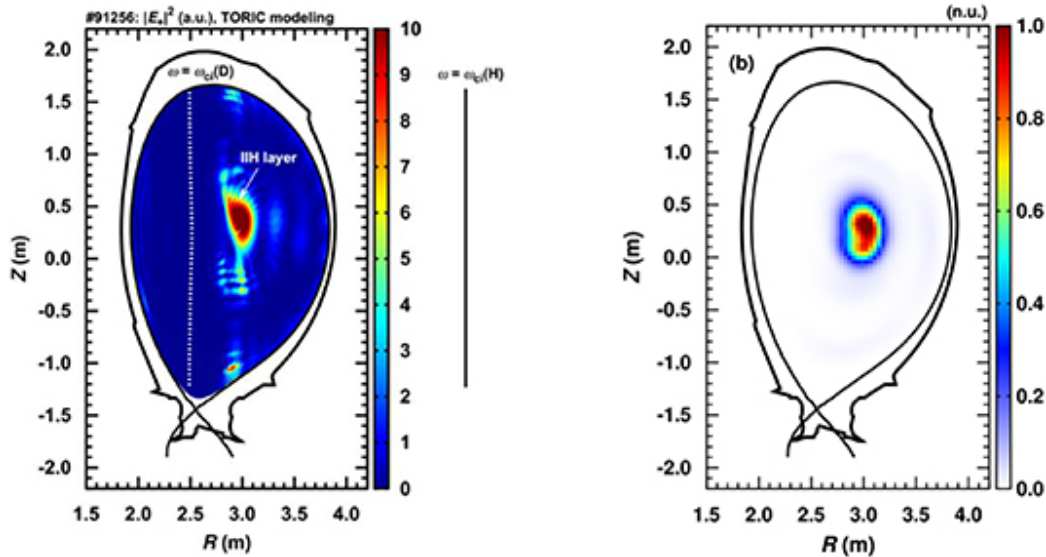
Figure 5. Illustration of the strong core localization of the RF power deposition and generation of energetic deuterium ions in JET pulse #91256 heated with the three-ion scheme. (a) Spatial distribution of $|E_+|^2$ (computed by the 2D full-wave code TORIC) exhibits the strong enhancement of $|E_+|^2$ at the ion-ion hybrid layer in the plasma core. (b) Tomographic reconstruction of neutron emission the neutron camera measurements. Reproduced from [103].

electron heating. Targeting heavier ions (such as ^{3}He) or larger concentrations of the minority species, or both, results in less energetic ions and hence promotes bulk ion heating. Finally, the three-ion scheme allows heavy intrinsic impurities to be targeted, and exhibits only weak dependence on the their concentration [107].

3.2. Application of ICRF heating for EP physics studies

3.2.1. Sawtooth dynamics. Controlling MHD events by external means has been an early priority in fusion research. Energetic ions have a stabilizing effect on various MHD instabilities, e.g. sawteeth [108–110]. By applying NBI or RF power, the sawtooth period can be increased, which appears to be an appealing idea at first sight, since a very hot core is formed. However, this leads to massive sawtooth crashes nicknamed "monster sawteeth" or "giant sawteeth", which can have deleterious outcomes. Monster sawtooth crashes can destabilize neoclassical tearing modes (NTMs), which are much more detrimental to the global confinement than the sawteeth themselves [111]. We will describe the physics of sawteeth and NTMs in detail in section 5. In addition to the possible modification of the sawtooth period, it has been recognized that sawteeth may sometimes be desirable as they eject heavy impurities from the plasma center to the periphery. Therefore, flexible tools capable of modulating the sawtooth activity are desirable. Such tools include ICRF and NBI heating to tailor the fast-ion population [112].

Initially, sawtooth destabilization has been at-

tributed to shear variations in the vicinity of the $q = 1$ surface. This has triggered the development of advanced schemes consisting of driving localized current by means of EC waves [113, 114] or IC waves, using the rather subtle ion cyclotron current drive (ICCD) effect [115]. ICCD requires asymmetric antenna phasing, which are more prone to operational difficulties than the more classical dipole phasing. More recently, however, it has been established that energetic ions themselves could have either a stabilizing or a destabilizing effect, depending on their distribution function [116,117]. This has relaxed some of the constraints on the asymmetric antenna phasing and allowed more classical ICRF heating conditions to be used to successfully control sawteeth [118,119].

3.2.2. AE destabilization. Fusion-born alphas in ITER and future fusion reactors are expected to destabilize a range of AEs. These instabilities could play a crucial role in a nonlinear impact of alphas on plasma heating and confinement in ITER. AE physics is described in sections 6 to 10. ICRF heating has been used to accelerate ions to velocities large enough to destabilize AEs and to study the impact of AEs on the plasma at different tokamaks. In particular, hydrogen minority heating was applied to destabilize TAEs and study mechanisms of their control on several devices [120–123]. 2nd and 3rd harmonic ICRF heating schemes were also efficient in destabilizing AEs in tokamak plasmas [124–126]. In JET experiments with 2nd harmonic deuterium ICRF heating, TAEs were shown to transport energetic deuterons with specific

energies away from the plasma core, thereby resulting in the formation of a local bump-on-tail distribution of fast ions in the plasma [127, 128].

TAEs and EAEs were regularly observed in fast-ion experiments with the three-ion ICRF heating scenarios on Alcator C-Mod, ASDEX Upgrade (AUG) and JET [107, 129–131]. Three-ion scheme ICRF heating scenarios efficiently generate large populations of passing fast ions at JET and can sustain plasmas with inverted q-profiles with $q_{\min} < 1$ [38, 132]. Consequently, this scenario provides necessary conditions for the destabilization of RSAEs, including high-frequency RSAEs [132]. Surprisingly, in most cases, the observed complex AE activity in fast-ion experiments with the three-ion ICRF heating scheme was not detrimental for plasma confinement. The improved thermal plasma confinement in the presence of a large population of MeV-range fast ions and AEs was observed at JET [133].

3.3. ICRF heating scenarios for EP and AE studies before DT operation in ITER

In the original ITER baseline, the plasma-facing components were planned to be beryllium for the first wall and tungsten for the divertor. Currently, the plan is to switch the material of the first wall to tungsten, too. As a result, a new ITER baseline plan is under development, accompanied by revisiting the ITER heating mix [134]. The ICRF system in ITER will operate in the frequency range 40-55 MHz [135]. A phased approach for increasing the ICRF power from 10 MW up to 20 MW during the later phases of ITER operations has been proposed.

A large variety of efficient ICRF heating scenarios can be applied at ITER, depending on the background plasma mix, the targeted species, and the magnetic field [136, 137]. The most promising ICRF heating scenarios for testing plasma heating and initial fast-ion studies in the plasma scenarios before DT operation in ITER include minority heating of hydrogen ions in deuterium plasma ($B_0 = 2.65$ T, $f \approx 40$ MHz), minority heating of ^{3}He ions in hydrogen plasma ($n_{3\text{He}}/n_{\text{e}} \approx 2$-$3\%$, $B_0 = 5.3$ T, $f \approx 53$ MHz) [138] and the three-ion ^{4}He-(^{3}He)-H scenario with a small amount of ^{3}He resonant ions in H-^{4}He plasmas ($n_{3\text{He}}/n_{\text{e}} < 0.5\%$, $B_0 = 5.3$ T, $f \approx 53$ MHz. (or 10-30% of deuterium ions)). This three-ion ^{4}He-(^{3}He)-H scenario was validated at JET and demonstrated robustness for both plasma heating and AE destabilization across a range of ^{4}He concentrations $n_{4\text{He}}/n_{\text{e}} \approx 5 - 15\%$ (which could be replaced by 10-30% of deuterium ions).

Because of a strongly increased RF power absorbed per resonant ion, which maximizes the generation of MeV-range fast ions, the three-ion ^{4}He-(^{3}He)-H ICRF heating scheme is particularly suited for the destabilization of AEs in the plasma scenarios before the DT operation phase and initial studies of the impact of AEs on the dynamics and confinement in ITER plasmas. The high efficiency of this ICRF heating scheme for AE studies in non-active H-^{4}He plasmas was experimentally confirmed at JET [139]. In line with modeling results [140], AEs were destabilized in H-^{4}He plasmas for a wide range of ^{4}He concentrations, varying from $\sim 5\%$ to $\sim 15\%$. The efficiency of fast-ion generation in these JET experiments was enhanced by utilizing the asymmetric ICRF antenna phasing, predominantly launching waves in the co-current direction.

3.4. Bulk-ion ICRF heating in DT plasmas of ITER and future fusion reactors

High ion temperatures $T_{\text{i}} \approx 15$-20 keV are essential for economical energy production in magnetic confinement fusion devices. Under these conditions, fusion-born alphas provide the dominant source of plasma heating and maintain the high rate of fusion reactions. However, reaching such ion temperatures during the ramp-up phase and ultimately the high-Q operational point cannot be done without auxiliary heating systems.

In future fusion devices, ICRF heating can provide a significant fraction of bulk-ion heating. In ITER, radiofrequency heating of a few percent of ^{3}He ions (~ 3-5%) is currently considered as the main option for increasing T_{i} with ICRF heating during the ramp-up [86, 141]. This technique was experimentally demonstrated in DT experiments on TFTR and JET [96, 98, 99], including recent JET DT experiments [43, 100]. This scenario can provide ~ 50-60% of bulk-ion heating in approximately 50/50 DT plasmas in ITER [82].

The efficiency of bulk-ion ICRF heating can be increased further by channeling RF power to a small amount of selected impurities with $1/3 < (Z/A)_{\text{imp}} < 1/2$ [142]. As a result of their higher atomic mass, these impurity ions provide an even larger fraction of bulk-ion heating, as compared to hydrogen and ^{3}He minority ions. The efficiency of the three-ion ICRF heating scenario for heating DT plasmas was demonstrated in recent experiments at JET, with intrinsic ^{9}Be impurities as resonant absorbers [139]. For ITER, a similar technique can be applied using neon, argon, or boron impurities. More recently, an extension of this technique with ^{7}Li impurities was proposed for bulk-ion heating in CFETR [143].

4. Diagnostics of EPs and instabilities

In this section, we will discuss the diagnostic of confined and lost energetic ions, runaway electrons,

and instabilities. It is essential to diagnose EPs and instabilities in ITER and other burning plasma machines in order to optimize plasma scenarios and fusion performance and possibly for plasma control. EP and instability diagnostic in ITER will allow us to test theory against experimental data, strengthening the predictive power of theory for devices beyond ITER and the first generation of burning plasma experiments. Measurements of alphas and alpha-driven instabilities are of particular interest, since alphas are the key ingredient of burning, predominantly self-heated and self-organized plasmas. We will focus on diagnostics that can survive the neutron and radiation fluxes emitted by burning plasmas. The design of the EP diagnostics in ITER is described in detail in chapter 8 of this volume [19]. Here we will focus on the EP physics and especially the alpha physics we can learn due to recent progress in the detector technology and integrated data analysis procedures.

4.1. Diagnostics of confined EPs

The great majority of alphas and EPs from auxiliary heating will be confined in the fusion plasma. The distribution functions of the EPs in the plasma are complex functions in a 6D phase space, which can be reduced to 3D assuming symmetries and near symmetries (see section 2). However, toroidal symmetry of the tokamak is not always a good assumption (see section 8). There is seldom enough measurement data to determine even the reduced 3D phase-space distribution functions fully, even though a promising first demonstration has been accomplished [144]. At ITER, integrated data analysis of all available experimental data is possible either by synthetic diagnostics or by tomographic inversion [3].

For measurements of confined alphas, ITER will be equipped with γ-ray spectroscopy (GRS) [145–147] and with collective Thomson scattering (CTS) [148–152]. Fast-ion charge-exchange recombination spectroscopy (CXRS) might detect low-energy alphas in the few 100 keV range. The high-energy neutral particle analyzer (NPA) [153] is quite insensitive to alphas and cannot distinguish them from deuterium. Note that a neutralization by charge-exchange reactions is far more likely for deuterium ($Z = 1$) than for an alpha ($Z = 2$). Neutron emission spectroscopy (NES) [154] is not directly sensitive to alphas, but it is sensitive to velocities of the fuel-ion populations. Alphas might produce a knock-on tail in the fuel-ion population, that has been detected by NES in the 1997 DT campaign at JET [155]. However, this specific measurement, besides being indirect, is possible only by using a magnetic proton recoil neutron spectrometer. Ion cyclotron emission (ICE) is hoped to give further diagnostic information.

For measurements of energetic hydrogen, deuterium and tritium, ITER will be equipped with a neutral particle analyzer (NPA) [153, 156] and an array of neutron diagnostics [154]. CTS and GRS are also sensitive to energetic deuterium and tritium. For measurement of lost alphas and other EPs, ITER will be equipped with a fast-ion loss detector (FILD). ICE might be another option to measure lost alphas and other EPs. While these diagnostics are described in detail in various sections of chapter 8 of this volume [19], we will summarize EP diagnostics briefly here in the following.

4.1.1. Gamma-ray spectroscopy.
GRS detects γ-ray emission from nuclear reactions in the plasma, either between an EP and an impurity or, in some cases, by the fusion reactions themselves [157, 158]. The impurity (especially carbon, beryllium or boron) is generally naturally present due to the composition of the machine first wall, but it can also be injected on purpose to enhance the signal. The instruments are placed in shielded areas at the end of collimated sightlines. Simultaneous measurements along distinct sightlines make it possible to infer spatial information on the emission and hence the EPs by tomographic inversion. Two GRS instruments are planned for ITER, both with a radial sightline: one is a spectrometer integrated in the ITER NPA [156]; the other is a set of GRS diagnostics integrated in the ITER radial neutron camera [147].

First GRS measurements have been made in the early '90s, and routine GRS measurements have been established at JET since then. A major advancement was the deployment of high-resolution detectors with MHz counting rate capabilities in 2010. This allowed expanding the range of experimental conditions where measurements are possible, for example towards high-performance deuterium [103, 159, 160] and DT plasmas [44]. It also allowed measuring the spectral shapes of individual peaks [161, 162]. The spectral shape is determined by the Doppler shift caused by the EPs, which hence gives experimental access to the EP velocities, either via velocity-space tomography [87], or by comparison between data and a synthetic signal starting from a model of the EP distribution function [163, 164]. Different detector options, notably lanthanum bromide (LaBr) [165] or high-purity germanium (HpGe) [161] are used, depending on whether the scope is to make measurements in scenarios with a significant residual neutron background or to enable measurements of the spectral shapes of the individual lines. When they are used in combination with silicon photo-multipliers for light readout [166], the detectors can be made very compact, allowing their installation on multiple

sightlines to obtain information on the spatial profile of the emission via tomographic inversion. An example of a high-resolution GRS measurement of the 2868 keV peak of the $^9\text{Be}(\text{D},n\gamma)^{10}\text{B}$ reaction from JET appears in figure 6.

Measurements of confined alphas by GRS in the recent JET DT experiments were demonstrated in [44, 47]. Figure 7 shows a gamma-ray spectrum from a JET DT plasma [44]. The gamma-ray spectrum shows three main features. First and foremost, the dominant 4.44 MeV peak from the $^9\text{Be}(\alpha,n\gamma)^{12}\text{C}^*$ reaction is clearly detected, along with its single escape peak at 3.93 MeV (an instrumental feature). Second, two high-energy, low-intensity peaks at $\mathcal{E}_\gamma = 8.53$ MeV and $\mathcal{E}_\gamma = 9.0$ MeV are detected, originating from the capture of thermalized neutrons on the impurity nickel. Third, a broad feature at low intensity extending up to about $\mathcal{E}_\gamma = 20$ MeV is detected which can give information about the fusion power in this discharge. The inset shows a synthetic GRS spectrum computed for ITER for a beryllium wall [147]. While GRS measurements on ITER will need a different reaction following the new 2024 ITER baseline, the overall similarity between JET DT measurements and the simulation nevertheless demonstrates that expected peaks in GRS spectra can be detected in the recent DT experiments at JET.
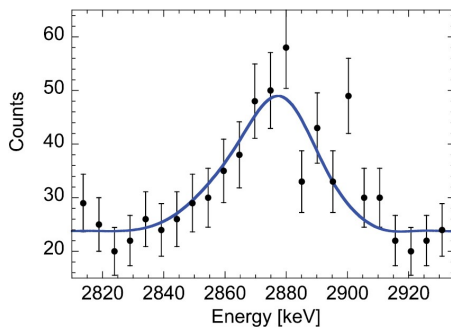

Figure 6. High-resolution GRS measurement at JET. The spectrum resolves the 2868 keV peak of the $^9\text{Be}(\text{D},n\gamma)^{10}\text{B}$ reaction. Reproduced from [163].

4.1.2. Collective Thomson scattering. ITER will be equipped with a CTS diagnostic, which detects alphas and other EPs spatially resolved in seven measurement volumes where a probe beam from a 60 GHz gyrotron overlaps receiver beams [148, 150]. A synthetic spectrum for ITER and the corresponding inferred 1D projected velocity alpha- and NBI distributions appear in figure 8. The radiation is scattered due to EPs in the measurement volume. Alphas and other EPs cause large Doppler shifts in this scattered radiation which, as for GRS, gives experimental access to the velocities of the EPs [167, 168]. The spectral resolution of CTS measurements has substantially increased in
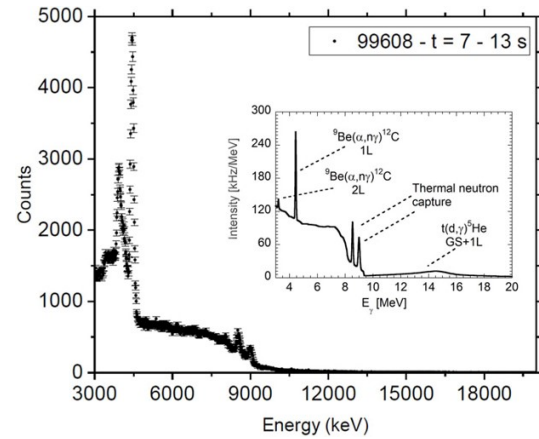

Figure 7. Gamma-ray spectrum measured by the vertical gamma-ray detector at JET in a typical DT discharge. The inset shows a calculation of the gamma-ray spectrum expected from a ITER DT plasma (from [147]). Reproduced from [44].

the last decades. The first-generation CTS receivers split the signal into tens of channels via bandpass filters [169–172]. Modern CTS receivers digitize the signal at high rate [173–176], and the spectrum is found by Fourier transformation, leading to a substantially higher spectral resolution and hence better diagnosis of the EP velocities. Unlike GRS, CTS cannot distinguish alphas and other EPs since the Doppler shift of any ion moving at the same velocity is the same [151, 152].

4.1.3. Neutron emission spectroscopy and cameras. The array of neutron diagnostics consists of neutron flux monitors, a neutron activation system, a neutron calibration, vertical and radial neutron cameras and neutron emission spectrometry (NES) [154]. The neutron diagnostics measure neutrons moving towards the detector along collimated sightlines, similar to GRS. The neutron cameras yield 2D profiles of the neutron emission in the poloidal plane by tomography. The NES diagnostics are based on three detection principles: a thin proton-recoil spectrometer, two time-of-flight spectrometers, one using forward scattered neutrons and the other backward scattered neutrons, and a single-crystal diamond detector. The thin proton-recoil and time-of-flight spectrometers are optimized for fuel-ion-ratio measurements but might also give information on fast ions. An advantage of diamond detectors is that they are much more compact than time-of-flight detectors. The NES diagnostics can provide information about the velocities of the fuels, i.e. energetic deuterium and energetic tritium [164]. Additionally, since equally many neutrons and alphas are generated in the DT reaction, the alpha birth rate can be inferred, too, and it may be possible to infer the alpha birth velocity distribution, which is expected to be slightly anisotropic [3]. High-resolution NES
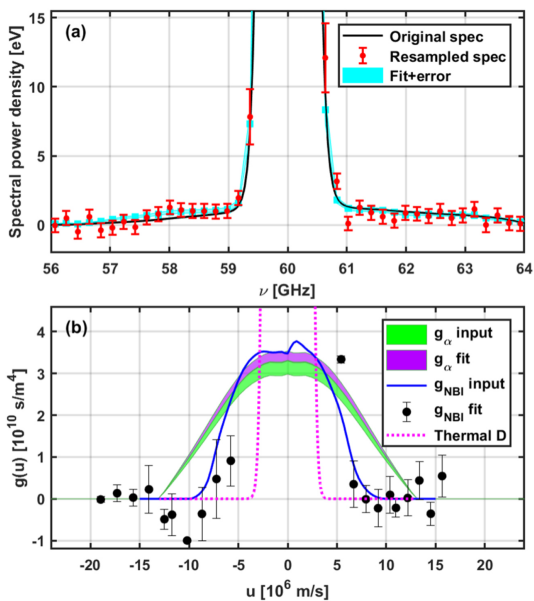
Figure 8. (a) Synthetic spectrum (black) and a corresponding randomized, resampled spectrum accounting for noise (red). The cyan curve shows the best-fit spectrum and associated uncertainties. (b) 1D projected distribution functions for alphas and fast deuterium NBI ions leading to the synthetic spectrum and the average fitted distributions with uncertainties. The bulk ion feature leads to large spectral power densities at small Doppler shifts, masking the fast-ion feature. Reproduced from [150].
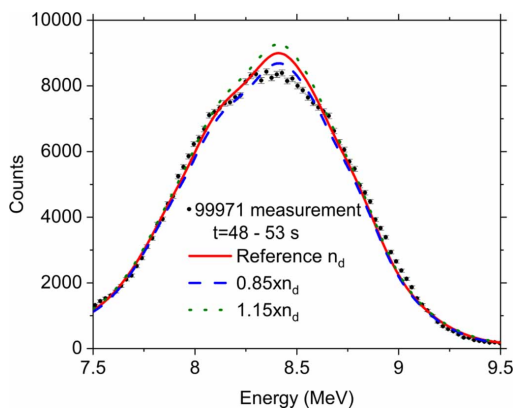

Figure 9. Spectrum of 14.1 MeV neutrons measured by the vertical line-of-sight diamond detector in the recent DT campaign in JET, compared with synthetic spectra for different D/T plasma compositions. The neutron energies are 5.702 MeV larger then deposited energies measured by the diamond detector, which are shown on the abscissa. Reproduced from [39].

measurements of DT neutrons with diamond detectors have recently been demonstrated at JET as shown in figure 9 [39, 44].

4.1.4. Neutral particle analyzers. Energetic hydrogen, deuterium and tritium can be detected by a neutral particle analyzer (NPA) [153]. The NPA will

measure energies of the neutral particles leaving the plasma, which have been generated from the corresponding ions in the plasma in charge-exchange reactions. NPAs hence provide measurements of the confined hydrogen, deuterium and tritium in the plasma. The detected neutrals can be born along the sightline but signals from the plasma edge typically dominate in passive NPAs since a large population of neutral particles must be in the sightline in order to have many charge-exchange reactions. The NPA measures a narrow pitch range of the detected species, since the charge-exchange reactions leaves the momentum of the detected species almost unchanged and the neutral must move along the sightline towards the detector. The energy, on the other hand, is well resolved over a broad energy range, so that energy spectra for a given pitch are obtained. NPAs are quite insensitive to alphas, since the neutralization of an alpha requires that two electrons are transferred in charge-exchange reactions to generate a neutral helium atom, which is more unlikely than for deuterium, which only requires the transfer of one electron. NPA measurements of tritons during high-performance JET DT discharges for various ICRF heating schemes are shown in figure 4 in section 3 [43].
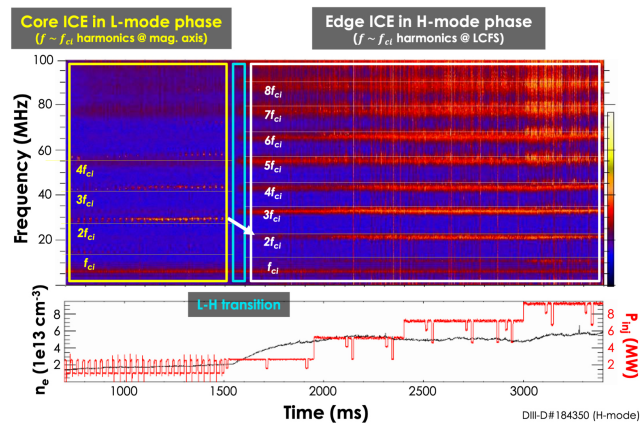
Figure 10. (a) An H-mode shot at DIII-D showing both core and edge-localized ICE, where horizontal lines indicate f_{ci} evaluated at the magnetic axis in L-mode (left, yellow) and the LCFS in H-mode (right, white). In L-mode, core ICE harmonics 1–4 f_{ci} are excited. In H-mode, edge ICE harmonics 1–9 f_{ci} are excited. (b) NBI power (red) and electron density (black). Reproduced from [177].

4.1.5. Ion cyclotron emission. Due to the crucial role played by alphas in sustaining the thermonuclear burn in burning plasmas, the alphas must be studied using any methods compatible with the challenging environment of reactor-grade plasmas. ICE is likely to provide one such method. We will review the possibility to use ICE as diagnostic when we discuss instabilities in section 6. ICE radiation is

frequently observed in current tokamaks [177–190] and stellarators [191–193] and is associated with EP-driven instabilities. ICE signals can be related to either the core or the edge plasma by the frequency separation of peaks in measured spectra as illustrated in figure 10. Edge ICE may be related to lost ions. However, it remains a challenge to interpret ICE signals quantitatively, since it requires understanding of the drive, damping and saturation levels of the instability. The ICE linear theory outlined in section 6 indicates that the EP distribution function is related to the ICE signal, but it is not yet clear how that information can be extracted from the ICE signals. Further efforts in theory and in experiments on various conventional tokamaks, spherical tokamaks and stellarators are still needed. At ITER, ICE could be measured with the ICRF antennas foreseen if the ICRF transmission line was equipped with a spectrometer. The fast-wave reflectometer could also be used. Lastly, ICE is also worth detailed studies because it may offer the possibility of phase-space engineering of the EP distribution function.
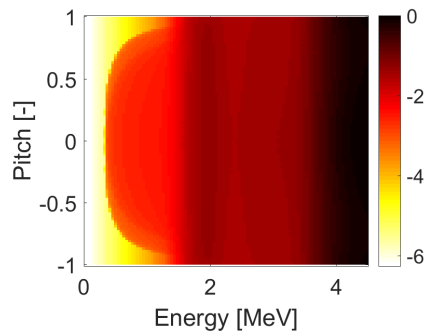

Figure 11. Total alpha velocity-space sensitivity of all CTS and GRS measurements at ITER combined, i.e. the weight function is computed for the entire spectral range of all CTS and GRS measurements. The color scale shows the base ten logarithm such that the sensitivity is highest in black regions and lowest in white regions. Reproduced from [3].

4.1.6. Phase-space sensitivity of EP diagnostics. The development of diagnostics with high spectral resolution allowed better experimental access to the EP velocity space or even phase-space which has triggered new methods exploiting this frequency resolution in recent years. The velocity-space sensitivity of several EP measurements has now been understood and can be visualised using so-called weight functions [194]. Velocity-space weight functions show the signal generated per EP in velocity space for each small bin in a measured spectrum and thus reveal the velocity-space sensitivities of a given measurement. Such weight functions have been computed for the several fast-ion diagnostics, and their velocity-space space sensitivity

has been understood: FIDA [194, 195], NPAs [194], CTS [168], NES [196, 197], GRS [198, 199] and FILD [200, 201], 3 MeV proton diagnostics [202], ICE spectroscopy [203, 204], and imaging neutral particle analyzers (INPAs) [205]. Recently, the phase-space sensitivity of FIDA, CTS, NES and GRS diagnostics to the possible orbits in a tokamak have been numerically computed, too, [49, 61, 144, 206–208]. as well as using a semi-analytically tractable model in COM space [209].

An overall summary of the velocity-space sensitivity of alpha measurements at ITER appears in figure 11 [3]. Typical weight functions for the individual measurements can be found in [3]. Alphas with energies higher than about 1.7 MeV are diagnosed most accurately in ITER due to detection by CTS and GRS. This study was done assuming a reaction between beryllium and alphas, but other GRS reactions will typically lead to a similar overall pattern. For reactions between alphas and beryllium, the GRS diagnostic has the peak sensitivity near the nuclear resonances at 2 MeV and 4 MeV [210, 211]. Alphas with energies between 300 keV and 1.7 MeV are diagnosed by CTS only. The yellow region below 300 keV and extending up to 1.7 MeV for pitches $p \sim \pm 1$ is not observable by either CTS or GRS installed at ITER. This is a consequence of the nearly perpendicular viewing geometry of CTS. A second consequence of the perpendicular viewing geometry is that the sign of the pitch cannot be measured, i.e. co- and counter-going particles cannot be told apart.

4.1.7. Measurements of velocity-space and phase-space distribution functions. The new high-resolution measurements and the understanding of their velocity-space sensitivity have allowed the formulation of tomography problems in velocity space [212, 213] and phase space [144], which can be solved by standard methods of tomography [214]. It has been shown that velocity-space and phase-space tomography allow integrated data analysis of the different diagnostics [215], e.g. FIDA and CTS [216], GRS and NES [87] or FIDA and NES [217]. The formalism is described in detail in section 10 in Chapter 8 of this volume [19].

An example of a measured 2D fast-ion velocity distribution function by velocity-space tomography and a corresponding numerical simulation appears in figure 12 [214]. This inversion is based on five simultaneously acquired FIDA spectra with lines-of-sight crossing the NBI path in the plasma center. The overall shape of the NBI velocity distribution function is captured well by the tomographic inversion. The NBI distribution is biased towards positive pitch due to the co-current NBI injection. The NBI injection energy is 60 keV, and the half-energy is 30 keV leading to local bumps-on-tail in the distribution which are
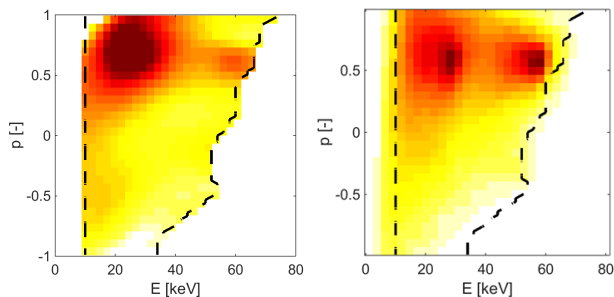
24

Figure 12. Measurement (left) and TRANSP/NUBEAM simulation (right) of an EP velocity distribution function [a.u.] in the center of a plasma at AUG heated by NBI. The measurement is a tomographic inversion of five simultaneously acquired FIDA spectra. Reproduced from [214].

found in the TRANSP/NUBEAM simulation and in the tomographic inversion of FIDA measurements. An inversion of GRS and NES measurements at JET was illustrated in figure 3 in section 3.

Until now velocity-space tomography has been applied at AUG [213, 214, 216, 218–221], JET [87, 222], MAST [223], DIII-D [224], EAST [217, 225] and TCV [226]. Two to five simultaneous detectors have been used at these tokamaks, measuring velocity distribution functions in plasma with NBI or ICRF heating. Based on the orbit sensitivities, first inversions of a 3D phase-space distribution describing the possible orbits have been computed [144, 227] (see also section 5).

At ITER, velocity-space tomography of the alpha distribution function based on GRS and CTS has been shown to be feasible for energies from about 1.7 MeV upwards [3]. However, since all currently foreseen diagnostics observe in a perpendicular direction with respect to the magnetic field, the sign of the pitch p of the alphas cannot be determined. But the absolute value $|p|$ can be determined, so that the velocity distribution function $f(E, |p|)$ can be measured. If an oblique γ-ray detector were to be installed, the sign of the pitch could be found, too [3]. Since below 1.7 MeV CTS is the only diagnostic for confined alpha-particles, a 2D inference seems difficult if not impossible, unless cogent prior information can be supplied. Energy spectra can be determined by 1D inversion of CTS spectra, for example by assuming isotropy. Reviews of velocity-space tomography are available in references [35, 228] as well as in chapter 8 of this volume [19].

Looking into the future, we need to deal with the heavily underdetermined nature of the velocity-space and phase-space tomography problems based on sparse measurement data. Promising approaches incorporate physics-based prior information, such as nonnegativity [214], the unlikely phase-space based on null-measurements [214, 223], the geometry of heating NBIs [214], numerical simulations [214], near-isotropy

[3, 229], monotonicity [224], the physics of collisions and slowing down of EPs [217, 230] or the physics of wave-particle interactions [231]. Recently, neural networks have been used to infer phase-space distribution functions from FILD and INPA measurements as well as from synthetic ICE measurements [203, 232]. This new approach to tomographic phase-space inversion problem should certainly be developed further, which might allow very rapid tomographic inversion.

4.2. Diagnostic of lost EPs

Despite the good confinement in ITER, some alphas and other EP are inevitably lost from the plasma and hit the first wall. EP losses are to be minimized in fusion devices since EPs can generate hot spots leading to localized melting of plasma-facing components. To understand the transport and loss of alphas and other EPs, both the confined and the lost EPs must be diagnosed.

ITER is planned to be equipped with one FILD detector [233]. In FILDs, the EPs enter the FILD through an entrance slit, are dispersed in the magnetic field, and hit a scintillator plate emitting light due to the impact. The time resolution of FILD measurements has greatly improved in recent years. The spectral content of the light can reveal what mode has ejected the ions (figure 13) [234, 235].
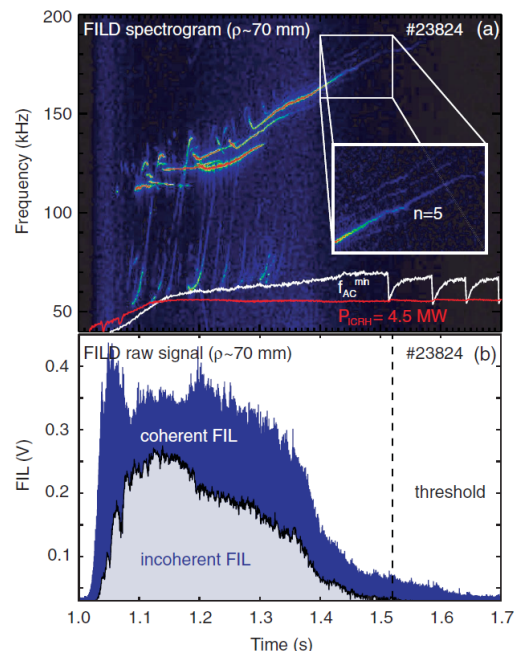

Figure 13. FILD spectrogram measured at AUG showing the spectral content of the fluctuation that has ejected the ions. Reproduced from [235].

The light can also be imaged to study the velocity-space distribution (figure 14) [234]. Such a
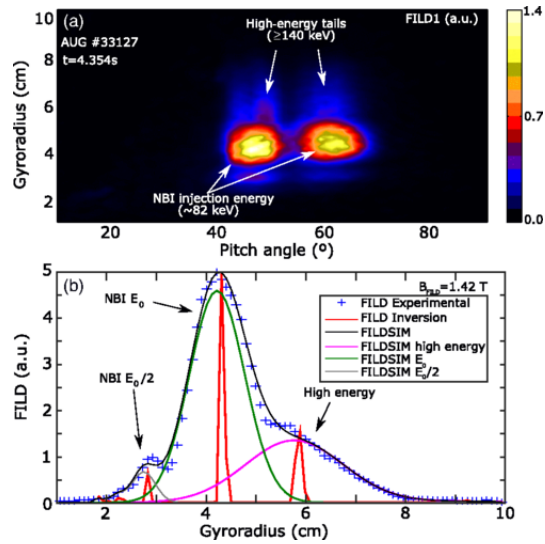
Figure 14. FILD measurement from AUG showing the formation of a high-energy tail above the NBI injection energy. Tomographic inversion shows that the most likely velocity distribution at the entrance slit of the FILD detector is localized in velocity space. Reproduced from [236].

Figure 15. Measurements of lost alphas during JET DT shot #99500 from the scintillator probe showing counts resolved in pitch angles and Larmor radii (cm) during the time interval 6.5–7.5 s. The major radius coordinates the alphas most likely originated from are indicated. Reproduced from [41].

measurement appears in figure 14 which shows the formation of a tail above the injection energy of the ions during ELMs. The fast-ion distribution in the entrance slit can be found from the image on the scintillator plate by tomographic inversion [200]. Here the most likely solution is that an ion population entering the slit with a distinct Larmor radius leads to the formation of the a tail due to instrumental broadening. This points to resonant interaction between the ELM and the mode accelerating the ions to a distinct energy [236]. A slice through the tomographic inversion is shown in figure 14b.

Measurements of lost alphas from the recent JET DT experiments using a FILD have been demonstrated in [41, 46, 47], as figure 15 illustrates. The detected Larmor radii are consistent with alphas at the magnetic field of the scintillator plate. At the time of the measurement, modes in the TAE frequency range were observed [41].

4.3. Runaway electron diagnostic

Runaway electron (RE) diagnostics at ITER should measure the maximum energy of the runaway electrons up to 100 MeV with a time resolution of 10 ms, and the RE current after the thermal quench and for failed breakdown from 1–15 MA with a time resolution of 10 ms. This measurement capability has been demonstrated in current tokamaks using both GRS|| [158, 237, 238] and synchrotron emission in the infrared

|| As customary, we will use the term GRS to indicate measurements of hard x-ray (HXR) emission in the MeV energy range, even though the origin of this radiation is not a nuclear

band [239]. A measured spectrum of HXR emission at DIII-D and the corresponding inferred RE energy spectrum appear in figure 16.
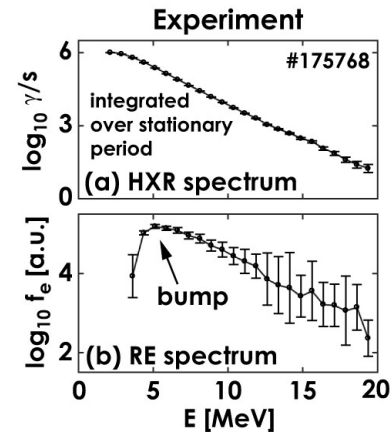
Figure 16. (a) Measured hard x-ray (HXR) emission at DIII-D and (b) inversion to runaway electron energy spectra. Reproduced from [240].

RE diagnosis by GRS is based on measuring the spectrum of the bremsstrahlung hard x-ray emission produced when (predominately MeV) runaways collide with ions. The detectors must be able to cope with signals at MHz counting rates to have sufficient statistics in the measured spectrum (say, at least 10^4 counts) within the required time resolution (10 ms or less). Measurements under these conditions have been possible only in the past few years, mostly thanks

decay.

to the rapid development of fast digitizers [165], and have been established in a number of major tokamaks, such as JET [241], DIII-D [240], AUG [242] and EAST [243]. The maximum energy of the REs is obtained by the inversion of the measured gamma-ray spectrum, starting from the known response function of the detector and the cross sections of hard x-ray emission [244]. This gives the one-dimensional runaway electron distribution function that is most compatible with the measurements and from which the maximum runaway energy can be determined. The runaway electron current is calculated from the integral of the runaway electron distribution function obtained by inversion.

RE diagnostics by measurements of their synchrotron emission in the infrared band have been established at TEXTOR [239, 245], and applied at other major tokamaks [246–248]. Modeling tools to relate the properties of the infrared emission to the runaway electron distribution function have also been developed [249, 250] and applied to interpret the emission in present experiments, instead of the former analytic models based on several additional approximations. Interpretation of data from the infrared cameras provides the location and size of the runaway electron beam, while the analysis of its wavelength spectrum gives information on the RE energies.

At ITER, both gamma-ray and infrared diagnostics will be used to measure REs. Two gamma-ray systems are currently planned: a hard x-ray monitor [251] and the radial gamma-ray spectrometers [147]. The hard x-ray monitor is installed right behind the machine first wall and, being sensitive to runaway current as low as few kA, will provide a first signal as runaway electrons develop in the plasma. However, due to the harsh measurement conditions behind the first wall, the hard x-ray monitor may not be able to provide reliable information on the RE energies.

The REs are detected with the already described radial gamma-ray spectrometers which will also provide clean measurements of the gamma-ray spectrum from RE bremsstrahlung and are expected to be the main instrument providing information on the RE energies and their evolution in ITER.

As far as infrared diagnostics are concerned, no dedicated synchrotron camera for runaway electrons is currently planned for ITER, but standard infrared (as well as visible) cameras will be used. As a consequence, infrared cameras will remain the main tool to determine the spatial extent of the runaway electron beam but, unlike present experiments, they will not be able to provide information on the runaway electron energies, which will be measured by the radial GRS only.

4.4. Diagnostics of instabilities in fusion plasmas

Key to interpreting the EP measurements discussed in the previous section and fully leveraging ITER's unique access to alpha physics will be measurements of any instabilities driven by or transporting EPs. Ensuring appropriate measurements of AEs in ITER will allow the validation of predictions of alpha-driven instabilities in plasmas dominated by self-heating. Alpha-driven TAEs have recently been detected in a DT discharge at JET with magnetics, soft-xray, interferometry and reflectometry diagnostics [40]. Ensuring appropriate measurements will further provide the control capability for optimizing performance, reducing the alpha losses, and minimizing potential first wall damage. In addition, such measurements may provide key information on the bulk plasma through Alfvén spectroscopy [252]. The discussion here will focus on recent advances in measurements of AEs with a particular emphasis on those techniques and systems that will be possible on ITER; this need is called out in ITER measurement specifications as "TAE mode-induced perturbations in B, T, n with a bandwidth of 30-300 kHz" [253]. None of the ITER diagnostics we will describe will be capable of resolving toroidal mode number or core EP-driven instabilities. This is a significant deficit and will impact the ability to rigorously validate models for EP transport by instabilities in ITER.
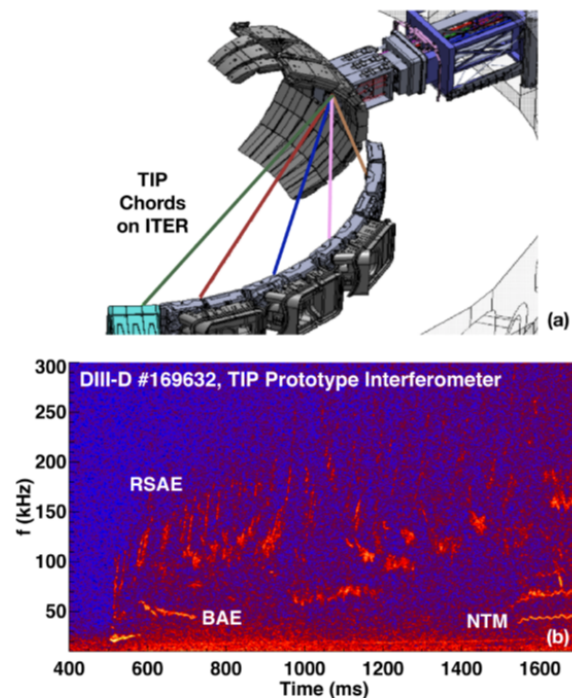

Figure 17. (a) TIP chord layout on ITER, (b) TIP prototype interferometer spectrogram from DIII-D discharge 169632. Reproduced from [254]

27

4.4.1. Toroidal interferometer polarimeter. One of the primary diagnostics expected to contribute to the detection of EP-driven instabilities on ITER is the toroidal interferometer and polarimeter (TIP) [254–257]. A detailed description of key design elements appears in chapter 8 of this volume [19]. TIP is essentially a two-color CO_2 laser based mid-infrared (4.6 and 10.59 μm) interferometer system [258–263], probing line-integrated electron density with a combined polarimetry measurement to probe line-integrated Faraday rotation (product of $n_e B_\parallel$). As shown in figure 17a, TIP will feature five independent tangentially viewing chords spaced across the device midplane. Two-color interferometers like these are extremely valuable for the detection of core instabilities and are capable of producing high quality fluctuation data for both coherent and incoherent fluctuations with wavenumbers $k < 2/a_o$, where a_o is the Gaussian beam-waist, and with frequencies up to several MHz [264]. They can operate in almost all tokamak plasma conditions, rarely suffer from refraction, are based on well developed CO_2 laser and detector technology and are able to take advantage of modern digital phase demodulation techniques for very low noise phase measurement. The TIP interferometric measurement provides the mode induced line-integrated density fluctuation along each sightline while the polarimetry Faraday effect measurement, in principle, will provide a combination of density and magnetic fluctuations, although the minimum resolvable fluctuation levels are significantly higher due to the relatively small effect being exploited [256, 264–266]. An example interferometric density fluctuation spectrum from the ITER TIP prototype tested on DIII-D is shown in figure 17b, where different types of beam-driven AEs as well as other coherent fluctuations are present [254]. In the figure, BAEs, RSAEs and NTMs are labeled. These modes will be discussed in detail in the following sections. Resolvable fluctuation levels in the AE frequency range are predicted to be on the order of $\delta n_e/n_e \approx 10^{-5}$ [256]. Additionally, because of its role in plasma control, ITER TIP data will be available in "real-time," allowing its use as a monitor of core AEs and other fluctuations for instability control purposes.

4.4.2. ECE radiometer. Another diagnostic technique that will be available on ITER and has proven to be extremely valuable for EP physics studies is electron cyclotron emission (ECE) radiometer measurements of electron temperature fluctuations [267–270]. Figure 18a is an example radial profile of ECE power spectra from a reversed magnetic shear DIII-D discharge in which various RSAEs and TAEs are clearly observed with ECE [267, 271]. Each type of mode is labeled along with the detailed radial structure of an
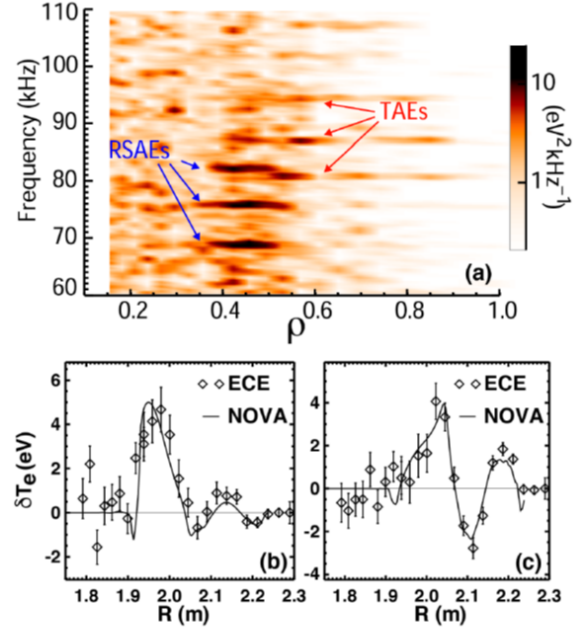
Figure 18. ECE radiometer data from a DIII-D beam-heated discharge with AEs. (a) Radial profile of ECE power spectra vs. normalized minor radius. (b) Radial profile of ECE radiometer measured temperature perturbation vs. major radius for an $n = 3$ RSAE and for (c) an $n = 3$ TAE. Reproduced from [267].

individual RSAE and TAE in figure 18b and figure 18c respectively [267]. The RSAEs are localized near the minimum in the safety factor profile and the TAEs are seen for radii outside of q_{min} extending to the plasma edge. As an example of the type of validation enabled by ECE measurements, figures 18b and 18c show a comparison of measurements and calculations of the ideal MHD eigenmode electron temperature perturbation from the NOVA code. The ECE radiometer in ITER will span approximately 70% of the device midplane from inside the magnetic axis to the last closed flux surface on the low-field side ($R \approx 5.2 - 8.2\,\mathrm{m}$) with about 64-128 channels giving a rough spacing of ΔR=2.3-4.6 cm [271]. The poloidal and toroidal resolution is determined by the beam spot size, which is expected to be $< 10\,\mathrm{cm}$ in ITER [271]. To avoid averaging effects, the poloidal wavelength should be less than the beam size which, at mid-radius, would correspond to poloidal mode numbers of $m < 60$. The radial resolution is determined by the instrumental RF frequency channel widths and relativistic broadening, which depends on electron temperature and is expected to dominate in ITER high temperature plasmas. For 1st harmonic O-mode measurements in ITER scenario 2 plasmas, the expected radial resolution is $< 10\,\mathrm{cm}$ across the device midplane and significantly better at

lower temperatures [271]. The resolvable mode amplitudes will depend on several factors including electron temperature, analysis approach (Fourier interval, spatial averaging, correlation measurements, etc.) and detailed hardware choices. The modes shown in figure 18 have amplitudes $\delta T_e/T_e \approx 0.5 \times 10^{-3}$.

Figure 19. AUG discharge #25528. (a) ECEI spectrogram, (b) Reflectometer spectrogram, (c) model for RSAE frequencies. Calculated RSAE minimum frequency overlaid as solid white line. Yellow labels and dashed vertical lines show q_{min} values used as input to RSAE model. Reproduced from [272]
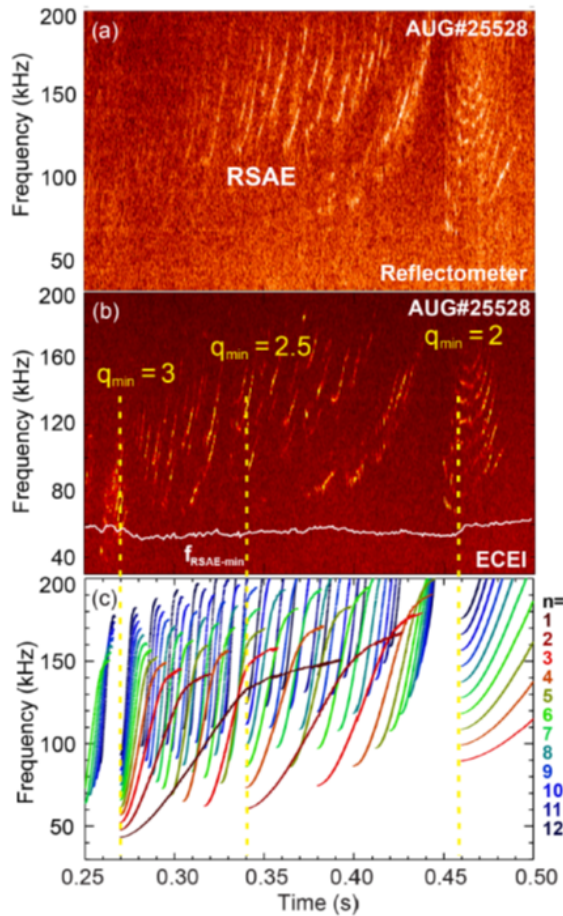
4.4.3.   Microwave reflectometry. ITER will also be equipped with multiple microwave reflectometry systems that will likely be capable of resolving density fluctuations due to coherent EP-driven instabilities. Reflectometry is an established approach with a long history of research in its use for measurement of both coherent and incoherent core fluctuations [273–278]. Density fluctuations along the path of the beam can modulate the phase or amplitude of the reflectometer signals or both.   Under certain conditions, phase modulation of the probe beam is localized at the cutoff [279–281] (the point of reflection of the microwaves), so

that localized measurements of density fluctuations are possible. A more sophisticated analysis approach using multiple channels has also been developed that takes the nonlocal response of reflectometers into account, and estimates of both the density and magnetic perturbations can be derived [277].

The two main reflectometer systems on ITER, each with planned capabilities for measuring EP-driven instabilities, are the low-field side reflectometer (LFSR) [282, 283] and the high-field side reflectometer (HFSR). Each will supply simultaneously measurements of the n_e-profile and n_e fluctuations. The broad measurement capability of LFSR is enabled by an array of six monostatic antennas which inject from an equatorial port on the outboard side of the ITER vessel. A low-loss transmission line transmits the $30 - 165$ GHz, O- and X-mode signals to and from the ITER plasma. The design of LFSR has been optimized to probe the edge region ($r/a > 0.85$) for a broad range of ITER conditions. However, penetration into the core with X-mode is possible with either reduced toroidal field or full field and n_e not exceeding $\approx 7 \times 10^{19} \mathrm{m}^{-3}$. Broadband transmission signals are realized by full-band microwave transceivers combined with quasi-optical multiplexing. Both frequency-modulated continuous wave (FMCW) and fixed-frequency continuous wave (FFCW) operations are incorporated. LFSR is equipped with conventional and Doppler reflectometry systems, enabling detection of low-to-intermediate wavenumber fluctuations. Full-band FMCW operations with repetition rate of $1\,\mathrm{MHz}$ are planned for LFSR, providing a means to measure n_e fluctuation profiles with high time resolution. Ignoring the effects of the profile gradient and turbulence, the radial resolution depends explicitly on the signal-to-noise ratio and the RF bandwidth. LFSR is expected to achieve better than 26 dB signal-to-noise ratio over most of its operating space, and with a RF bandwidth of $250\,\mathrm{MHz}$, a radial resolution of 5 mm is achievable. Flat profile gradients and turbulence tend to broaden the radial resolution, and the cumulative effect is strongly dependent on the plasma conditions. Full-wave reflectometry simulations indicate that LFSR can access and should be sensitive to core-localized weak density fluctuations ($\delta n_e/n_e \approx 10^{-6} - 10^{-4}$) similar to TAEs. The ability to make this measurement unambiguous can be complicated by strong fluctuations ($\delta n_e/n_e > 10^{-3}$) in the path of the beam that can also modulate the signal, scrambling the phase.   However, reflectometer measurements combined with synthetic diagnostic modeling provide a powerful tool for interpreting the signals and resolving possible ambiguities. An example reflectometry measurement of RSAEs in a reversed magnetic shear AUG plasma is shown in figure 19a where a broad spectrum of RSAEs is clearly visible [272,284].

These measurements are to be compared to ECE imaging measurements shown in figure 19b, where it can be seen that the different localizations result in a slightly different spectrum of observed modes [285].

4.4.4. Magnetic probes. Like the majority of present machines, ITER will be equipped with a large array of magnetic sensors with varying sensitivities (bandwidth, polarization, amplitude, etc.) Several "High-frequency" coils have been designated to meet the measurement requirement 062 for the measurement of TAEs. These probes are a standard inductive pickup coil design and will have a minimum bandwidth of $0.5\,\text{MHz}$ and sensitivities in the range $1 \times 10^{-6} - 3.5 \times 10^{-4}$ T over 30 kHz to 0.5 MHz [286]. The system will consist of an array of coils spaced toroidally and poloidally for resolution of toroidal mode number and poloidal structure. While edge modes will likely be clearly resolved by these sensors, it is questionable whether core modes that do not reach the edge can be measured.

4.4.5. Other potential diagnostics of EP-driven instabilities at ITER. Several other diagnostics on ITER have the potential to measure EP-driven instabilities. However, due to hardware or approach choices or other issues, they may not have the required bandwidth or sensitivity. These diagnostics include: poloidal polarimeter (PoPola), Mirnov/magnetic pickup loops, dispersion interferometer polarimeter (DIP) and soft x-ray (SXR) spectroscopy. The PoPola is a fan of 119 μm poloidal polarimeter channels with potential to measure core density and magnetic fluctuations. As discussed in chapter 8 of this volume [19], this diagnostic will have 100 Hz bandwidth but a modified approach could extend its bandwidth and utility to the measurement of instabilities. The ITER DIP, similar to TIP, is a multi-channel CO_2 laser based interferometer system that will use a photoelastic modulator approach limiting its fluctuation measurement bandwidth to $\approx$10 kHz [287]. Soft x-ray systems, like those planned for ITER, have been used successfully to measure AEs in the past [288]. Unfortunately, the specified bandwidth of the ITER system appears to be 100 kHz which is marginal for measurements of AEs in ITER [289]. Recently, a promising diagnostic technique has been demonstrated using launched fast Alfvén waves in an interferometer configuration - the fast wave interferometer (FWI) [290, 291]. Because the fast wave velocity depends on ion mass density and magnetic field, the diagnostic is capable of probing line-integrated mass density along with probing core density and magnetic field fluctuations. Recent experiments clearly show the diagnostic ability to resolve core fluctuations for the first time. The FWI is not currently an assigned ITER diagnostic but its use is under investigation.

4.4.6. AE spectroscopy. Beyond measurements of the modes themselves, work since the last ITER physics basis has clearly demonstrated the potential of EP-driven instability measurements for providing information about the equilibrium plasma, so-called "AE spectroscopy" [252]. A particularly compelling application of this technique is the determination of the minimum safety factor $q_{\min}$ through measurements of RSAEs. As mentioned, figure 19a and figure 19b show measurements of RSAEs in AUG reversed shear plasmas during the current ramp phase. During this time period, $q_{\min}$ and the mode spectrum are evolving rapidly. The RSAE spectral evolution is well described using a simple ad hoc model [257, 264, 292], the results of which are shown in figure 19c; the dominant feature of the RSAE frequency sweep is the $q_{\min}$ dependence which roughly scales as $(m - n q_{\min})/q_{\min}$ [252, 293, 294]. In figure19b and 19c, the overlaid $q_{\min}$ evolution has been determined by adjusting the values until the predicted RSAE timing matches that measured experimentally. Discharges on DIII-D with motional Stark effect (MSE) polarimetry have confirmed the validity of this approach and show the precision with which $q_{\min}$ can be determined [264]. Further, when RSAE localization information is present through measurements of the AE mode structure with ECE or even coarsely with interferometry, this information can be used to place constraints on not only the value of $q_{\min}$, but its location. Also, the RSAE minimum frequency depends on T_e and T_i and also provide a check on those values [294].

5. Interaction of EPs with thermal-plasma-driven instabilities

In this section, we review the interaction between EPs and thermal-plasma-driven instabilities, which are instabilities also appearing in the absence of EPs. The EP-driven Alfvénic modes are discussed in the following sections. Important thermal-plasma-driven instabilities interacting significantly with EPs are neoclassical tearing modes (NTMs), kink modes, sawteeth, kinetic ballooning modes (KBMs), resistive wall modes (RWMs), and edge-localized modes (ELMs), which we will review in the following. The recent JET DT experiments highlight the importance of the interaction between alphas and thermal-plasma-driven instabilities. Alpha losses due to NTMs, sawteeth, and ELMs were observed in these experiments [46, 47].

5.1. Neoclassical tearing modes

NTMs are a type of helical MHD instability in tokamak plasmas where magnetic islands with low poloidal and toroidal mode numbers (m/n) form on rational q-surfaces. Inside the island, the pressure profile is flat, which leads to a low bootstrap current. NTMs are discussed comprehensively in chapter 4 of this volume [16]. EP transport and losses can be strongly affected by NTMs, and in turn EPs can play an important role in the stability and growth of NTMs [295]. This has been documented in numerous experimental and theoretical studies of the stability of NTMs and their effect on EP confinement [189, 296–320]. Analytic and numerical modeling predicts that the EP distribution function and equilibrium parameters influence the NTM stability in complex ways, e.g. using the M3D-K [321], NIMROD [302, 322] and GTC [313] codes.

In turn, the influence of NTMs on EP losses has been studied analytically as well as numerically with orbit following codes. Recently the reduced "kick" model in TRANSP has been extended to include EP transport by NTMs [323]. The "kick" model simulations suggest that (N)TMs, as well as fishbones (see section 7), can interact through modification of the EP distribution in phase space, which influences the drive.

Analytic and numerical modeling [305, 307, 308, 321] indicates that EPs can have a stabilizing or a destabilizing effect on tearing modes, depending on the relative balance of trapped EPs compared to co- and counter-passing EPs, on the presence of direct resonances between EP drift orbit frequencies and the tearing mode rotation frequency, and on the equilibrium parameters, notably the EP orbit size and the magnetic shear. Analytic models find that the island frequency in the local plasma frame, an important but not well understood or measured parameter, can have an impact on the stability (leading to stabilizing or destabilizing EP terms in the extended Rutherford equation) [309]. Additionally, the interaction between EPs and NTMs is qualitatively different if orbital frequencies resonate with the NTM frequency. We will deal with both non-resonant and resonant interaction in the following.

5.1.1. Non-resonant EP-drive of NTMs.

Analytic modeling of the interaction of EPs with tearing modes, done in the context of the extended Rutherford equation [310], can provide useful physical insight into the interaction mechanisms. The stability of resistive instabilities such as tearing modes is described by a 4th-order differential equation [324] which is difficult to deal with analytically. Rutherford had the insight that this 4th-order differential equation could be reduced to a 2nd-order differential equation in the region outside the island, except for in a narrow boundary (tearing) layer. Furthermore, the tearing mode stability and growth rate can be determined by matching the solutions of the 2nd-order equation outside the island across the tearing layer, with no need to solve the 4th-order equation.

The original Rutherford equation not modified to include EP effects is of the form

$$\frac{\tau_s}{r_s}\frac{dW}{dt} = \Delta_c, \qquad (39)$$

where W is the island width, $\tau_s = \frac{\mu_0 r_s^2}{1.22\eta}$ is the resistive time, r_s is the radius of the rational surface, η is the resistivity, μ_0 is the vacuum permeability, and $\Delta_c = r_s\Delta'$ is the classical stability parameter. Δ' is calculated from the equilibrium q-profile and current-profile in the regions outside the tearing layer [325]. It is proportional to the perturbed sheet current at the rational surface required to match the external solutions across the tearing layer. The perturbation decays in time for a negative sheet current, whereas it grows for a positive sheet current. The Rutherford equation can be extended by adding other sources of current perturbations. For example, a magnetic island flattens the pressure profile in the vicinity of the island, resulting in a positive perturbation current (in normal shear plasmas), which leads to the "bootstrap drive" term that gave neoclassical tearing modes their name [326].

The extended Rutherford equation including non-resonant EP drive terms for NTMs Δ_{EP} is of the form

$$\frac{\tau_s}{r_s}\frac{dW}{dt} = \Delta_c + \Delta_{GGJ} + \Delta_{bs} + \Delta_{pol} + \Delta_{EP}. \qquad (40)$$

The classical stability parameter Δ_c from the original Rutherford equation may be affected by EPs through the EP-driven currents changing the equilibrium current profile. The additional terms are the Glasser-Greene-Johnson curvature term Δ_{GGJ} [327], the bootstrap current drive term Δ_{bs} [326, 328], the thermal-plasma polarization current term Δ_{pol} [329, 330] arising from island motion through the equilibrium plasma, and the EP term Δ_{EP}, which results from the perturbed currents on the rational surface arising from the effect of the island magnetic perturbations on the EP population. It consists of several contributions due to various sub-populations of the EPs, such as co-passing, counter-passing and trapped populations, usually derived for magnetic island widths either much larger or much smaller than the EP orbit width. To determine if the plasma is linearly stable or unstable to NTM formation, one determines if an initially small island grows, so the island width is generally assumed to be much smaller than the EP orbit width. For currently operating tokamaks and especially spherical tokamaks, which are

smaller than ITER and have lower magnetic fields, even most saturated islands are smaller than the EP orbit width. However, the extended Rutherford equation typically predicts islands to be metastable with a threshold island size. An ideal linearly unstable "classical" tearing mode grows from small a amplitude. Additionally, many linearly stable tearing modes can also become unstable when an MHD event (like an ELM or sawtooth) creates an initial perturbation that is greater than the threshold island size.

Influence of EPs in the outer region The first term on the right-hand-side of the extended Rutherford equation captures the effect of the current drive from EPs on the current profile shape in the region outside the island. In practice, the effects of the EPs on the current profile are independently calculated with codes such as TRANSP. However, it is useful to have a qualitative understanding of how EP current drive affects the tearing mode stability through this term. Co-passing EPs tend to decrease the value of Δ' and have a stabilizing effect. Conversely, counter-passing EPs tend to increase the value of Δ', a destabilizing effect decreasing the onset threshold of the NTMs [304, 321]. The effect of trapped EPs on the instability criterion is primarily through the asymmetric pressure of trapped EPs because the parallel current they produce is small [304]. Analytic studies have found that trapped EPs can be destabilizing in weak magnetic shear, but stabilizing in strong magnetic shear [305, 308].

Many experiments have investigated the effect of EPs on NTM stability. Counter-NBIs have been found to have different effects for various plasma scenarios. In DIII-D experiments [296] it was found that increased co-NBI power stabilized NTMs, but there was no corresponding decrease in stability for increasing counter-NBI power. In beam-heated DIII-D hybrid plasmas, the most unstable mode switched from AEs to chirping NTMs when the perpendicular beam pressure decreased [331]. In AUG experiments [297], both increasing co-NBI power and increasing counter-NBI power stabilized NTMs. The analytic and simulation results discussed above do not explain these experimental discrepancies for the counter-NBI. A possible reason is that the toroidal rotation could not be controlled in these experiments and may have been partly responsible for the observed changes in stability [311, 332–335]. However, the effects of toroidal rotation should be independent of the rotation direction. Unfortunately, appropriate codes have not yet been developed to model both the changes in the EP populations and the changes in equilibrium parameters. It is also important to remember that experiments, by their nature, will include all types of

EP effects on NTM stability, including potential effects of EP resonances and EP-driven polarization currents discussed below.

Influence of EPs in the island region In addition to the neoclassical perturbed polarization current generated by the thermal plasma, EPs can also generate a perturbed cross-field $\boldsymbol{E} \times \boldsymbol{B}$ current which induces a parallel electron current to satisfy charge neutrality [309]. The contribution of this polarization current can be expressed as

$$\Delta'_{\mathrm{u}} = -G_3 \frac{r_s^2}{s^2 L_{n_{\mathrm{i}}}^2} \frac{\beta_{\mathrm{i}}}{W} \frac{\omega}{\omega_{*\mathrm{i}}} \frac{L_{n_{\mathrm{i}}}}{L_{n_{\mathrm{f}}}} \frac{n_{\mathrm{f}}}{n_{\mathrm{i}}}, \qquad (41)$$

where $G_3 \simeq 1.58$ is a numerical coefficient, s is the magnetic shear, and $L_{n_{\mathrm{i}}}$ and $L_{n_{\mathrm{f}}}$ are the lengthscales of the thermal-ion and EP densities, β_{i} is the ion beta, and ω is the island frequency relative to the background plasma. Δ'_{u} depends on the magnetic shear, island propagation frequency, and EP density gradient at the rational surface. $\Delta'_{\mathrm{u}} > 0$ if $\omega < 0$ and the density gradients of thermal ions and EP on the resonance surface have the same sign, i.e., the onset threshold of NTMs is increased. In weak shear plasmas with large EP fractions, the EP polarization term can become comparable to the bootstrap term, and $|\Delta'_{\mathrm{u}}/\Delta'_{\mathrm{bs}}|$ increases as $n_{\mathrm{f}}/n_{\mathrm{i}}$ or s decreases. Thus, this term can affect the island growth when the EP orbit size is greater than the island width.

Some operational regimes in ITER steady-state and hybrid scenarios are expected to have weak magnetic shear [20], which hence deserve particular attention. In a low-shear, high-performance regime on JT-60U, no NTMs were observed in several discharges during NBI with high bootstrap fraction [336]. In these experiments, the effects of EPs may be important. The relative importance of the EP polarization current term has also been investigated for tearing modes in the spherical tokamak NSTX [310, 337]. For these experiments, it was found that the destabilizing EP polarization term overcame the stabilizing effect of the thermal polarization term, allowing growth of the island to widths where the other terms in the extended Rutherford equation dominate the island dynamics.

5.1.2. Numerical simulations of EP effects on NTM stability. Simulations find that EPs interact with tearing modes mainly in the outer region and the growth rate of the tearing modes is reduced dramatically by EPs [302]. Furthermore, the net effect of co-passing EPs is weakly stabilizing whereas the net effect of counter-passing EPs is destabilizing [304]. The simulation results are in qualitative agreement with the analytic results for the passing particles discussed above.

32

Simulations using similar parameters to the DIII-D experiment [300] were performed using the global gyrokinetic toroidal code GTC. The perturbed parallel current induced by EPs was added to Ampère's law [313], resulting in a small stabilizing effect on the excitation of NTMs.

Simulations of DIII-D equilibria with the NIM-ROD code have also found that EPs were generally stabilizing, although this effect was from EPs in the plasma bulk rather than a tearing layer effect. However, NIMROD simulations also found that a precession drift resonance with the core mode destabilizes the 2/1 mode [322]. The M3D-K code [338] has been used to study the effect of EPs on tearing modes [304]. The results agreed in large parts with previous analytic results for the effects of passing EPs. It was also found that trapped EPs are much more destabilizing than counter-passing EPs at the same beta. In M3D-K simulations of HL-2A equilibria, co-passing EPs were responsible for destabilizing the bursting/chirping 2/1 modes [317, 319]. Additionally, it was found that $q(0) = 1.5$ was most unstable for a scan of the safety factor $1.2 \leq q(0) \leq 1.9$.

Tearing modes with different mode numbers can appear simultaneously. For such double tearing modes, simulations find that passing EPs are destabilizing, although this result is limited by the assumption of a "top-hat" model for the double tearing mode [339]. The effects of EPs on double tearing modes were studied by M3D-K [340], where co-passing EPs are destabilizing but trapped EPs are stabilizing. Double tearing modes can undergo a transition to a fishbone-like mode if the EP beta β_f is larger than a threshold.

We note that self-consistent codes for describing NTMs that include the physics of the EPs and the effects of toroidal rotation are still lacking, but would be essential to explain the experimental results and to explore methods for controlling NTMs.

5.1.3. Resonant interaction between EPs and NTMs. At first sight, resonances of NTMs with EPs were thought to be unlikely because the typical EP bounce, transit and precessional frequencies are much larger than typical NTM frequencies. However, indications of resonant interaction between EPs and NTMs have been found in several tokamaks [189,314–317] when the NTM frequency chirps up and down (figure 20 [189]). The NTM frequency suddenly increases strongly and quickly and then chirps back down to the NTM frequency within a few milliseconds. During each chirp the neutron rate is reduced by about 1%, as was also observed at TFTR. This implies that there is a redistribution or loss of EPs during each chirp. Experiments at AUG suggest that this is caused by a resonance between EPs and NTMs [315]. However,

it is not clear from presently available experimental data whether the resonances of passing or trapped EPs cause chirping NTMs.

In [318], it was shown using a particle model that an additional toroidal torque is generated by the resonance of NTMs and trapped EPs which increases the propagation frequency of NTMs. However, the calculated duration of the frequency chirping up and down is approximately a factor 100 longer than in the experiments. A model based on drift kinetic theory reduces the predicted chirping times to a few milliseconds for the DIII-D experimental parameters [303]. An alternative interpretation is that the frequency chirping may be caused by a fishbone-like mode resonance with an EP precession frequency, which is supported by analytic and simulation studies [319, 320]. Analytic results predict that the fishbone-like mode is driven by trapped EPs above an EP beta threshold [320] but simulations have also found that a fishbone-like mode can be driven by co-passing EPs [319].

Related phenomena have been found in HL-2A where a fishbone-like mode rather than a chirping tearing mode or NTM were observed. Similarly, it is believed that the fishbone-like mode is excited by resonance of the tearing mode with trapped EPs [319, 320]. In simulations for a reversed q-profile, a fishbone-like mode and a double tearing mode were found to co-exist [340, 341]. This fishbone-like mode is excited by resonance between the tearing mode and co-passing EPs. These disparate results suggest that the physical mechanism of frequency chirping during NTMs still remains unresolved. They have also not yet revealed whether trapped or co-passing EPs are most important in this process. The physical mechanism is still under debate and will likely require further experiments and investigations.

5.1.4. EP transport by tearing modes. Since magnetic islands break the tokamak axisymmetry in a way similar to the toroidal field ripple, enhanced particle diffusion can be expected due to NTMs. However, the mechanisms affecting the EP confinement have proven a lot richer. In DIII-D, large coherent MHD modes were observed to reduce the neutral beam current drive efficiency [342] and 2.5 MeV neutron emission [343] by as much as 80% and 65%, respectively. Guiding-center simulations with the ORBIT code suggest that the intrinsic orbit stochasticity leads to transport of co-passing EPs, similarly to the finding of earlier work for low-n magnetic perturbations [344, 345]. In AUG experiments, time-resolved pitch and energy measurements of the EP losses found that the losses were modulated at the frequency of a (2,1) NTM [346, 347]. Even trapped EPs experience increased
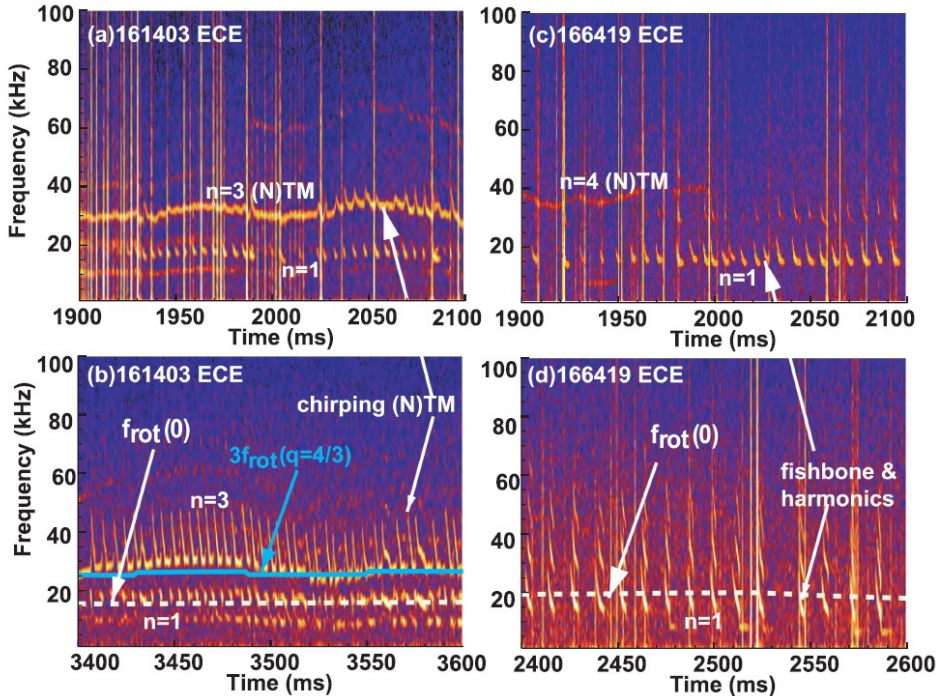
Figure 20. Cross-power spectrograms of electron temperature fluctuations measured by the ECE diagnostic for two hybrid NBI- and ECRF-heated discharges in DIII-D. It is often observed that steady NTMs and chirping $n = 1$ fishbones coexist for more than 100 ms [see (a)] and then trigger chirping NTMs [see (c)]. It is occasionally observed that NTMs can be fully stabilized and that fishbones and harmonics become dominant [see (d)]. The central toroidal rotation frequency is plotted in (b) and (d) as the dashed white lines. The rotation frequency at the $q = 4/3$ rational surface is shown by the blue line in (b). Reproduced from [189].

transport when the NTM resonates with the bounce and toroidal precession frequencies [348], as confirmed by recent drift-kinetic calculations [349]. Also within a drift kinetic framework, the passing EPs were found to experience resonances with the rotating islands, providing an explanation to the observed phase locking between the enhanced transport and the NTM perturbation [339]. More recently, the resonances for trapped, co- and counter-passing MeV alpha particles with a (2,1) tearing mode were found using the GPU-accelerated TAPAS code, showing the impact of the rotation frequency of the magnetic island on the losses of EPs [350].

NTM-induced EP losses can be caused by stochastization of drift orbits. Simulations of an AUG discharge with a (2,1) NTM revealed that the NTM-induced losses of passing beam ions were caused by the formation of a (4,1) NTM [351]. In a purely RF-heated discharge in AUG, resonant interaction between the EPs in the high-energy tail of the ICRF distribution and a (5,4) NTM was found to lead to enhanced EP losses [200]. In DIII-D experiments, beam modulation was applied to study the interaction between EPs and a (2,1) NTM in different parts of the phase space [300]. The mode was observed to affect the confinement of both the counter-passing and trapped beam ions. The

kick model in TRANSP, extended to NTMs [323], allowed analyzing the effect of NTMs on EPs in a variety of DIII-D plasmas [352]. Above a threshold width for the island, EP losses were found to increase, leading to reduction in beam-driven current and torque across the entire plasma. Kick modeling in conjunction with velocity-space tomography show that NTMs alter the positive-pitch distribution [224].

Note that the experimental studies described above have used plasmas with very large island sizes to help identify the loss mechanisms. Such plasmas cannot be tolerated in reactor-level plasmas. For ITER, studies on the effect of MHD modes on EP confinement have mainly been done for the foreseen main operating phases with fusion alphas using the ASCOT code following full gyro-orbits, which can be important when the magnetic field has strong toroidal inhomogeneities [353,354]. Both (2,1) and (3,2) NTMs were simulated, together with realistic toroidal-field (TF) ripples, using a theory-based model for the NTM island built into the magnetic background. The simulations indicate that the total power density on the wall strongly depends on the NTM perturbation amplitude. However, even for an excessive amplitude, the wall power densities remain below the ITER design limits. Furthermore, the NTMs were not found to

cause additional hot spots on the wall, but only increase the wall power density in the places also found for simulated MHD-quiescent plasmas.

EP transport by NTMs was observed in the recent JET DT experiment [52]. Discharge #99886 was an MHD-active DT discharge with an NTM, fishbones, RSAEs, and TAEs as detected with the Mirnov coil measurements shown in figure 21. Despite this MHD activity, the energy confinement in this discharge was very good. FILD measurements sensitive to lost alphas detected the NTMs and the fishbones which suggests transport and loss of alphas due to the NTMs and fishbones as shown in figure 22.
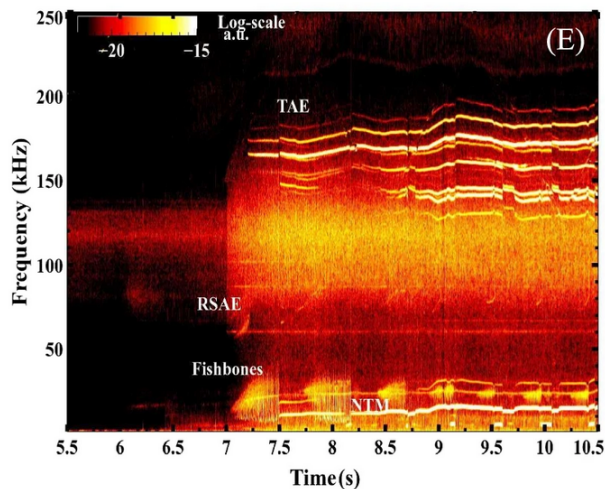

Figure 21. Mirnov coil spectrogram during JET DT discharge #99886 showing an NTM, fishbones, RSAEs, and TAEs. Alpha losses at the fishbone and NTM frequencies were detected with the FILD (figure 22). Reproduced from [52].
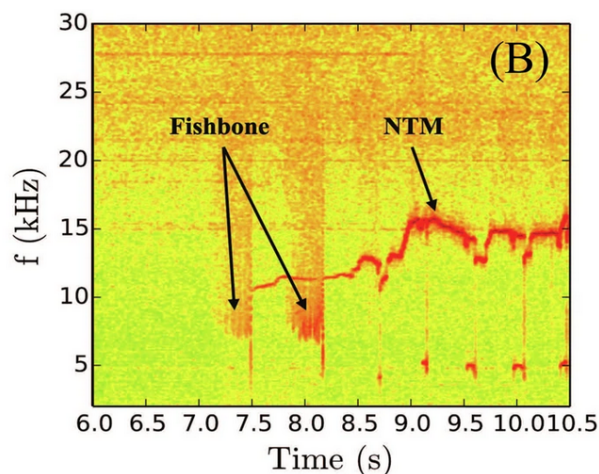

Figure 22. FILD measurements showing alpha losses during NTMs and fishbones in JET DT discharge #99886. Mirnov coil measurements detected the fishbones and NTM at the same frequency (figure 21). Reproduced from [52].

5.2. Sawteeth and kink modes

The redistribution of EPs by sawteeth and kink modes and the effect of trapped and passing EPs on sawtooth stability have long been studied theoretically and experimentally. The sawtooth instability causes a periodic cycle of the core plasma, where the core density and temperature slowly increase and then suddenly drop, an event referred to as the sawtooth crash, giving their timetraces the form of sawteeth. A kink mode has often been observed to become unstable right before the sawtooth crash. The sawtooth instability is triggered at an on-axis safety factor of $q(0) < 1$. During the sawtooth crash, the on-axis safety factor jumps up to $q(0) \approx 1$ and the plasma profiles T_e and n_e change abruptly. This is thought to result from reconnection of the poloidal magnetic field, leading to rapid redistribution of particles from within the $q = 1$ surface to outside. Figure 23 shows this redistribution for the EP population at AUG [144]. The EP density before and after the crash has been inferred by orbit tomography based on 27 simultaneously acquired FIDA spectra (see section 4). After the sawtooth crash, the current density profile peaks and $q(0)$ decreases below unity on the resistive timescale of the plasma. This pattern repeats with the characteristic time called the sawtooth period. Sawteeth are discussed comprehensively in chapter 4 of this volume [16].
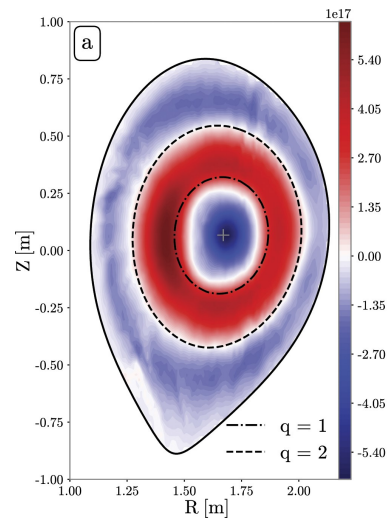
Figure 23. Ejection of EPs from the inside to outside the $q = 1$ surface during a sawtooth crash at AUG, as shown by the difference in EP densities before and after the crash. The image has been computed by orbit tomography based on FIDA measurements. Reproduced from [144].

It is known that EPs within the $q = 1$ surface can stabilize the internal $n = 1$ kink mode and increase the sawtooth period significantly [108, 355]. However, long sawtooth periods lead to "monster" sawtooth crashes

with particularly strong pressure drops [356], which can trigger NTMs leading to significant reduction of plasma confinement [357]. Both trapped and passing EPs can stabilize sawteeth. Experiments on JET [110, 358], MAST [359], TEXTOR [360] and DIII-D [361] have shown that off-axis passing EPs stabilize sawteeth if they move in opposite direction to the plasma current, whereas on-axis EPs stabilize sawteeth if they move in the same direction as the plasma current.

Sawteeth are a concern for burning plasmas since the alphas and EPs from auxiliary heating will stabilize sawteeth [362], so we might expect monster sawteeth in burning plasmas, and the deleterious effects that go with that. Modeling has predicted that the fusion alpha population will increase the sawtooth period on ITER [363]. It would be advantageous to develop methods to pace sawteeth, resulting in a short sawtooth period with weaker sawteeth. Sawteeth also have positive applications since they eject impurities, and so sawteeth could be used to remove helium ash from the plasma core in burning plasmas.

5.2.1. EP redistribution by sawteeth and kink modes. The redistribution of EPs by sawteeth is relatively well understood theoretically. EPs with moderate energies are thought to remain attached to reconnecting field lines and behave like thermal particles. They suffer appreciable transport, since the finite $\boldsymbol{E} \times \boldsymbol{B}$ drift tends to attach the particles to the evolving flux surface [364]. However, for high-energy EPs, their large orbits can decouple them from the evolving flux surfaces. Three timescales are important [365]: the crash duration τ_{cr}, the bounce-averaged toroidal precession time τ_ϕ and, for passing particles, the timescale of longitudinal motion (period around a perturbed flux surface) τ_ψ. Particles experience significant transport when their energy $\mathcal{E}$ is smaller than a critical energy $\mathcal{E}_{\mathrm{crit,st}}$; however, because τ_ϕ, τ_ψ, and the orbit size differ for passing and trapped particles, $\mathcal{E}_{\mathrm{crit,st}}$ has different values for different orbit types. For trapped particles, $\mathcal{E}_{\mathrm{crit,st}}$ is sufficiently low that trapped EPs usually decouple from the flux surfaces and suffer little transport. In contrast, for passing particles, $\mathcal{E}_{\mathrm{crit,st}}$ is higher, so passing EPs with $\mathcal{E} \lesssim \mathcal{E}_{\mathrm{crit,st}}$ often experience significant radial transport. This selective transport pattern is corroborated in figure 24 which shows a comparison of fast-ion densities calculated using TRANSP/NUBEAM with a sawtooth model and calculated from velocity distribution functions inferred by velocity-space tomography based on FIDA measurements at AUG [214]. Whereas the sawtooth model in TRANSP/NUBEAM ejects EPs at all pitches, the measurements show that the EPs with pitches close to zero are not affected by the sawtooth,
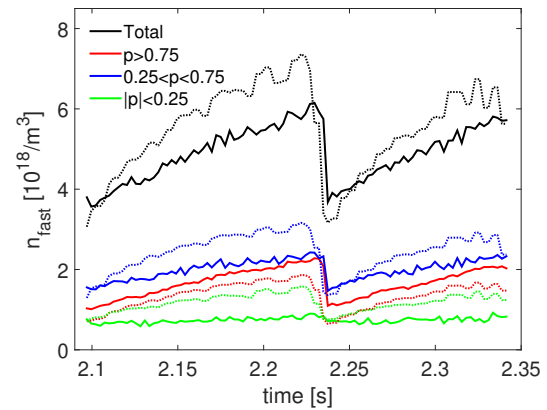
as predicted by theory.

Figure 24. Comparison of simulated and measured EP densities in the plasma center for various pitch ranges in a sawtoothing plasma at AUG. The full lines are measured EP densities found by velocity-space tomography based on FIDA measurements. EPs with pitches $p > 0.25$ are ejected by the sawtooth, whereas EPs with pitches $|p| < 0.25$ are not. The dotted lines are simulations with TRANSP/NUBEAM with a sawtooth model ejecting particles at all pitches. Reproduced from [214].

In addition to these mechanisms associated with reconnection at the sawtooth crash, resonances with the internal kink that triggers the sawtooth are also possible. However, the roles of trapped and passing particles are reversed: the passing-particle precession frequency is too high to resonate with the internal kink but the trapped-particle precession frequency may resonate, so only trapped particles experience significant transport by this mechanism.

In DT plasmas in TFTR, the core density of alphas with energies between 0.15 and 0.6 MeV significantly decreased during the sawtooth crash [24, 366]. A similar redistribution of energetic ions was also observed on JET [367]. Additionally, neutron spectroscopy showed that the EPs in the 100 keV range generated by ICRF heating in JET were redistributed by sawteeth [368], whereas 1 MeV tritons only experienced minor redistribution at sawtooth crashes [98].

Recent experimental work has focused largely on validating the detailed predictions of our theoretical understanding regarding redistribution of EPs in different regions of EP phase-space as in the AUG example discussed above. The theoretical model has been found to be consistent with the recent measurements of EP redistribution on TEXTOR, DIII-D and AUG [144, 214, 216, 221, 365, 369–372].

The study of EP interactions with sawteeth has also been extended to the low field, tight aspect ratio tokamak regime on NSTX (including NSTX-U) and MAST, testing the models in this new regime. NSTX comparisons between tangentially and radially viewing FIDA and NPA diagnostics show

that passing particles experience greater transport [373], as theoretically expected. Modeling of sawtooth crashes on NSTX found that it was necessary to introduce energy selectivity to improve the agreement between experimentally measured and simulated neutron rates and the EP profiles measured with FIDA. At lower energy, trapped EPs showed the strongest redistribution [374, 375]. The redistribution is consistent with theoretical models which predict that redistribution will be stronger for those trapped and barely trapped ions whose precession periods are shorter than the sawtooth crash time [364]. For the NSTX crash time of 40-50 μs, the estimated critical energy was ≈ 65 keV for nearly co-parallel EPs and down to 25-30 keV for trapped EPs. In contrast to the NSTX results, trapped and passing EPs are found to be equally affected by sawteeth on MAST, based on neutron camera data [376] [377] and FIDA data [378]. These results might be reconciled with theory predictions as the beam injection energy is lower in MAST, so that the EP distribution is at lower energy [323]. Thus, the experimental data support the predictions of redistribution dependence on energy, pitch and sawtooth crash time [364,379]. Models of EP redistribution have been used to predict strong alpha redistribution by sawteeth in ITER [380]. Sawteeth do not usually occur in stellarators, but they can be induced by NBCD and ECCD. Sawteeth induced this way at the stellarator LHD showed no measurable effect on the EPs [381].

Kink modes are often observed just before sawtooth crashes. It has long been known that kink modes or other low frequency magnetic perturbations can cause losses of EPs. The losses have been explained with a model of random "kicks" to the EP orbits making EP orbits stochastic at magnetic perturbation levels lower than those needed to make the magnetic fields stochastic [344, 345]. There has been substantial work on modeling of the redistribution of EPs during the sub-millisecond reconnection period of the sawtooth crash where the (1/1) kink-tearing mode is growing rapidly. However, many sawteeth are preceded for a long period by a saturated (1/1) internal kink instability. Recent work has focused on modeling EP redistribution by ideal kink modes. A reduced "kick" model for EP transport has been developed [382] and used to study the EP redistribution associated with sawteeth [383, 384] in JET plasmas. In a comparison of the EP redistribution from both a saturated internal kink mode and a sawtooth in a JET discharge, the losses from the saturated internal kink mode were found to be larger or comparable to the losses from the sawteeth [385].

5.2.2. Pacing of sawtooth instabilities with EPs. Sawteeth could affect fusion performance on ITER by redistributing the fusion alphas, helping control impurities in the plasma core, and they are implicated in the triggering of tearing modes which can lead to performance degradation or disruptions. For these reasons, it is desirable to have a method to control sawteeth in ITER to minimize their impact on plasma performance. ICRF heating has been proposed and used for active feedback sawtooth control on JET [386–389], see section 3. Sawtooth pacing is expected to be an important capability needed for ITER to avoid potential giant sawteeth.

The EP population created by minority heating schemes can either suppress sawteeth (core heating), or trigger sawteeth by heating near the $q = 1$ surface. Both on-axis ICRF heating with notches and modulated ICRF heating outside the $q = 1$ surface have been used on JET for sawtooth control. As already mentioned, long-term suppression of sawteeth lead to large, typically more deleterious, sawteeth. Sawtooth pacing, keeping the sawtooth period short with smaller sawteeth can minimize the deleterious effects of sawteeth. Such pacing has recently been demonstrated on JET [389]. With on-axis ICRF heating, the sawtooth period is lengthened, but notches in the ICRF power, which reduce the core stabilizing EP population, can trigger sawteeth, reducing the sawtooth period to close to its natural period. This may not be sufficient for ITER where the fast-alpha population may result in an excessively long sawtooth period. Conversely, heating near the $q = 1$ radius can trigger sawteeth, but requires dynamic steering of the ICRF heating deposition radius.

5.3. Ballooning instabilities

The effects of EP populations on core plasma ballooning instabilities were initially analyzed in the mid 1980s to early 1990s time period prior to the discovery of EP destabilized Alfvén gap instabilities. High-n ballooning instability analysis was a convenient paradigm for the study of EP effects at that time since the ballooning transformation reduced the usual 3D MHD mode equations to a 1D ordinary differential equation, which was well within the computational capabilities of that period. The earliest models either examined FLR effects [390], EP diamagnetic drifts [391], or assumed that the EP drifts were large compared to the frequency of the ballooning mode [392–394]. The general conclusion of these studies was that the EP population had a stabilizing effect on ballooning instabilities; the presence of EPs could increase the beta threshold and open up access between first and second stability regimes. The reactor profile model assumed at that time was that

both plasma and alpha pressure profiles would be peaked near the magnetic axis with the expectation that this region would be the most susceptible to ballooning instabilities. The next step in model development was removal of the assumption that EP drifts and transit frequencies were large relative to the ballooning mode frequency [395–402] and inclusion of thermal ion diamagnetic drifts (resulting in a real frequency $\simeq \omega_{*i}/2$ for the ballooning mode). The trapped alpha particle precessional drift frequency could be comparable to the ballooning mode real frequency, resulting in the introduction of wave-particle resonances. These generally had a destabilizing effect and could degrade ballooning mode stability boundaries.
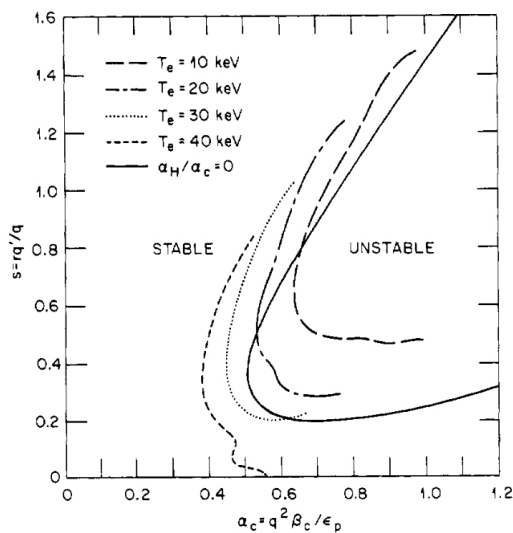

Figure 25. Marginal stability boundaries for $\alpha_{\mathrm{H}}/\alpha_{\mathrm{c}} = 0.3, T_{\mathrm{e}} = 10 - 40\,\mathrm{keV}, \lambda_{\mathrm{p}} = 0.25, b_{\mathrm{i}} = 0.04, q = 1.7$. A case with no hot component is also shown ($\alpha_{\mathrm{H}}/\alpha_{\mathrm{c}} = 0$, solid line) Reproduced from [396].

Figure 25 shows an example of this in the form of an s-α plot (normalized shear vs. normalized pressure gradient, $s = rq'/q$, $\alpha = -8\pi q^2 B^{-2} R_0 dp/dr$) for the case of a slowing-down distribution of deeply trapped alpha particles. As the electron temperature is increased, the mean energy of the alpha distribution increases, resulting in stronger coupling/destabilization and a blocking off access between first and second stability regimes. While alpha-destabilized ballooning instabilities were of concern during this period, interest rapidly shifted in the early 1990's to the Alfvén gap modes and fishbone instabilities since the gap modes were more global and could exist independently of plasma-driven instabilities; also there were early observations of the fishbone instabilities and their ability to eject fast ions. Furthermore, since ballooning instabilities required higher $\beta's$ than experiments were achieving at those

times, they evaded direct observation. The ballooning analysis technique was also applied toward the study of high-n Alfvén instabilities [403, 404].

Currently the role of thermal plasma-driven ballooning instabilities in tokamak operation is seen from a somewhat different perspective than at the time EP effects on ballooning modes were studied. Access to interesting high performance advanced tokamak regimes relies on a delicate balance between pressure and current gradient driven instability boundaries [405]. The most likely region for encountering ballooning limits is at the pedestal region near the plasma edge. While this would seem well-removed from the core region where the alpha pressure is dominant, there will be a transport flux of energetic alphas from the core through the edge pedestal region, likely enhanced over classical levels by EP instabilities. Since trapped alpha precessional drifts may resonate with and destabilize ballooning modes in this region, potentially degrading the pedestal region β limit, this area of EP physics deserves reexamination taking into account the newer scenario/profile modeling.

5.4. Resistive wall modes

In burning plasmas operated above the no-wall β-limit, e.g. in the ITER steady-state scenario, resistive wall modes (RWMs) are prone to become unstable [406]. The q-profile in this scenario is reversed, and there are no internal transport barriers. Without a surrounding wall, the plasma would be stable against kink modes until $\beta > \beta^\infty$ where β^∞ is the no-wall β-limit. If the plasma was surrounded by an ideally conducting wall, it would remain stable up to a higher critical value β^{b} throughout the so-called wall-stabilised region. However, real vessel walls have finite resistivity, which leads to loss of wall-stabilisation. Resistive wall modes are discussed comprehensively in chapter 4 of this volume [16].

Several tokamaks have operated in the wall-stabilized region where interaction between EPs and RWM must be understood to make predictions for ITER and burning plasmas [407–411]. Numerical simulations have shown that damping resulting from resonance with the precession frequencies of thermal ions or EPs could play a role, in addition to sound-wave damping and ion Landau damping [31, 412–416]. Thermal kinetic effects on RWM stability in generalized toroidal geometry were assessed, both with perturbative and self-consistent treatments of the interaction EPs and the RWM displacement. Both thermal particle transport [417] and alphas [31] stabilize the RWM above the ideal no-wall limit. Finite orbit width effects of the EPs have been shown to stabilize the RWM, too [418, 419]. Trapped EPs are stabilizing for the RWM [420] but, as discussed in

section 7.1, the off-axis fishbone, a type of EPM related to the RWM can be driven unstable when the EP pressure is sufficiently large.

NSTX experiments investigated the effect of rotation on RWM stability. For increasing rotation, RWM stability first improves, then degrades when the mode is in resonance with the precession frequency of the bulk ions, then improves again at higher rotation [421]. Experiments at DIII-D varying the EP distribution have shown a change in the damping of the RWM as measured by the resonant field amplification [422]. The RWMs were observed to become more stable at lower rotation. The stabilisation due to rotation counteracted the resonance between EP precession frequency and the Doppler-shifted mode frequency.

5.5. Edge-localized modes

H-modes in tokamaks have steep edge pressure gradients that typically drive ELMs unstable, as described comprehensively in chapters 3 and 5 of this volume [15, 17]. Recent experiments at several tokamaks have shown that ELMs eject the edge EP population to the wall which can form on localized hot spots on the wall [423]. Velocity-space resolved FILD measurements indicate that the EPs are significantly accelerated by the ELM perturbation that cause their losses (figure 14), highlighting the strong interplay between the EP population at the plasma edge and the electromagnetic perturbation developed during an ELM crash [236, 424, 425]. However, it should be noted that a recent work questions the role of ELMs in producing the observed fast-ion acceleration. Analysis of the measured lost ions using neural networks for tomographic reconstructions of the ion velocity-space suggests that the fast-ion acceleration might be observed over a wide range of events and not only correlated with ELMs [232].

Nonlinear 3D kinetic-MHD simulations with the MEGA code indicate that EPs may play a key role in the non-linear spatio-temporal structure of ELMs [426]. The interaction between the EP drift orbits at the edge and the electromagnetic perturbations of ELMs results in wave-particle energy and momentum exchange, influencing the overall structure of ELMs. Although ELMs are initially triggered by steep thermal plasma pressure gradients at the edge, the effects of EP kinetics significantly alter various characteristics of ELMs, such as the growth rate, crash timing, amplitude, frequency spectrum, and ballooning structure. In the presence of EP effects, a broad radial structure leads to a considerable redistribution of the EPs. MEGA simulations replicate key ELM observations seen in low-collisionality plasmas with high levels of EPs in AUG. The simulations show abrupt and sizable type-I

ELM crashes with frequencies up to 250 kHz. Notably, filamentary EP losses observed during ELM crashes exhibit a comparable frequency pattern with dominant frequencies spanning a wide range up to 250 kHz, gradually reducing in amplitude and frequency in the post-ELM crash phase. Preliminary estimates predict a strong interaction between alphas and other EPs with ELMs in ITER (if they are allowed to grow unabated).

6. Linear stability of EP-driven modes and energetic particle modes

In all tokamaks with significant EP populations, electromagnetic fluctuations in a wide frequency regime can be observed, from acoustic up to Alfvénic and ion cyclotron frequencies. In some cases they can be excited by externally applied electromagnetic waves, but typically they are destabilised by resonant interaction with the EP population. Two types of fluctuations can be distinguished: firstly, the Alfvénic eigenmodes (AEs), which are the normal modes of the MHD equations in toroidal geometry, and their kinetically modified branches (which are here called EP-driven AEs), and secondly the energetic particle modes (EPMs) whose properties are mainly determined by the characteristics of the EPs. Often, these two types are connected to each other, i.e. the fluctuations start as AEs and then evolve non-linearly into EPMs.

A comprehensive and predictive description of a burning fusion plasma needs global, nonlinear kinetic models and codes, which we will discuss in section 7. Here, we will focus on linear stability and on the underlying stable or unstable linear mode spectrum which is of crucial importance for the analysis of AE modes for several reasons. First, weakly damped modes are a prerequisite for the excitation by EPs in many experimental situations. Second, measured mode structures of AEs close to marginal stability often agree remarkably well with linear predictions and thus can be used for Alfvén spectroscopy. Third, reduced EP transport models rely on linear mode information, in particular on the damping rate that balances the drive in the saturated state. Here, we review basic concepts of linear theory and summarize recent efforts applying linear theory to various plasma scenarios of interest. For further discussion, please refer to the recent review papers [27–30, 32, 34] and references therein.

6.1. Drive and damping of AEs

The excitation of AEs requires a positive effective growth rate, so the drive must exceed the damping,

$$\gamma_{\text{eff}} = \gamma_{\text{drive}} - \gamma_{\text{damp}}. \tag{42}$$

The drive can be large when the mode frequency resonates with the gyro-, transit-, bounce- or precession frequencies of EPs (equations 11 and 14), which leads to an efficient energy exchange between the EPs and the mode. Thermal ions in fusion plasma are usually not fast enough to resonate with Alfvén waves, but the birth speed of alphas exceeds the Alfvén speed, and hence wave-particle interaction between the alphas and AEs is possible. Free energy to drive the mode via inverse Landau damping is available when the phase-space distribution has spatial gradients or deviates significantly from a Maxwellian distribution in velocity space, for example by inverted velocity gradients or anisotropy.

The drive of a distribution via inverse Landau damping depends on the EP beta β_{f} and the gradients in the EP distribution function. To asses this drive, we take the energy derivative of the distribution. Since μ and $\mathcal{E}' = \mathcal{E} - \omega P_\phi / n$ of a resonating particle are constant during the wave-particle interaction for modes in Alfvén frequency range and below (section 2), we take the energy derivative of the distribution at fixed μ and $\mathcal{E}'$ [34]:

$$\gamma_{\mathrm{drive}} \propto \beta_{\mathrm{f}} \omega \frac{\partial f}{\partial \mathcal{E}}\Big|_{\mu,\mathcal{E}'} \tag{43}$$

This gives $\frac{\partial f}{\partial \mathcal{E}}\big|_{\mu,\mathcal{E}'} = \frac{\partial f}{\partial \mathcal{E}}\big|_{\mu,P_\phi} + \frac{\partial P_\phi}{\partial \mathcal{E}} \frac{\partial f}{\partial P_\phi}\big|_{\mu,\mathcal{E}}$, so with $\frac{\partial P_\phi}{\partial \mathcal{E}} = \frac{n}{\omega}$, we get the drive

$$\gamma_{\mathrm{drive}} \propto \beta_{\mathrm{f}} \left(\omega \frac{\partial f}{\partial \mathcal{E}}\Big|_{\mu,P_\phi} + n \frac{\partial f}{\partial P_\phi}\Big|_{\mu,\mathcal{E}} \right). \tag{44}$$

At high frequencies on the order of the cyclotron frequency, μ is no longer constant but varies with energy, so that $\frac{\partial \mu}{\partial \mathcal{E}} = \frac{N \omega_{\mathrm{c}}}{B_0 \omega}$ (see section 2). If the distribution is anisotropic in velocity space, we express this anisotropy as a dependence on the normalized magnetic moment $\Lambda = \mu B_0 / \mathcal{E}$ [34]. Then the energy derivative at fixed P_ϕ (but no longer fixed μ) becomes $\frac{\partial f}{\partial \mathcal{E}}\big|_{P_\phi} = \frac{\partial f}{\partial \mathcal{E}}\big|_{\Lambda,P_\phi} + \frac{\partial \Lambda}{\partial \mathcal{E}} \frac{\partial f}{\partial \Lambda}\big|_{\mathcal{E},P_\phi}$ with $\frac{\partial \Lambda}{\partial \mathcal{E}} = -\Lambda/\mathcal{E}$. After insertion into equation (44), we find three derivatives of the distribution function that can potentially drive a mode:

$$\gamma_{\mathrm{drive}} \propto \beta_{\mathrm{f}} \left(\omega \frac{\partial f}{\partial \mathcal{E}}\Big|_{\Lambda,P_\phi} + n \frac{\partial f}{\partial P_\phi}\Big|_{\Lambda,\mathcal{E}} - \omega \frac{\Lambda}{\mathcal{E}} \frac{\partial f}{\partial \Lambda}\Big|_{\mathcal{E},P_\phi} \right). \tag{45}$$

The first term shows that drive is obtained from a positive gradient in energy, which appears for velocity distribution function with a bump-on-tail, as was recently studied in JET DT plasmas [41]. Since the drive is proportional to the mode frequency, velocity-space gradients can significantly contribute to driving high-frequency modes. The second term approximately reflects drive from spatial gradients,

which is often the dominant drive for intermediate-to low-frequency AEs in present experiments. If we approximate $P_\phi \approx Ze\psi \approx \pm ZerR_0 B_\theta$, the second term becomes [34]

$$n \frac{\partial f}{\partial P_\phi}\Big|_{\Lambda,\mathcal{E}} \approx \pm \frac{n}{ZeR_0 B_\theta} \frac{\partial f}{\partial r}\Big|_{\Lambda,\mathcal{E}}, \tag{46}$$

giving an approximation to the drive due to spatial gradients. The third term reflects drive due to anisotropy of the distribution. In ITER, about 10% more co-going alphas then counter-going alphas are expected, an only slightly anisotropic distribution [3]. On the contrary, EP populations from ICRF and NBI heating are highly anisotropic. This last term is, as the first term, proportional to the mode frequency and therefore its contribution to the excitation of high-frequency modes could be significant. Note also that the first and third term do not depend on the toroidal mode number and are hence the only terms that can excite low-frequency axisymmetric ($n = 0$) modes, such as the EP-driven geodesic acoustic mode (EGAM) [427] discussed in sections 6.6.3 and 9.2.

Several damping mechanisms need to be considered. The so-called continuum damping originates from the non-uniform ion densities and magnetic field, leading to a non-uniform Alfvén speed. In the cylindrical limit, radial variations lead typically to a 'closed' shear Alfvén wave continuum (SAWC): For any shear Alfvén wave (SAW) propagating at a certain frequency, there is at least one intersection with the continuum, where the wave resonates. This causes phase mixing of a wave packet with finite $\Delta\omega$ at the resonant layer, leading to dispersion and thus strong continuum damping of the mode, of order

$$\gamma_{\mathrm{cont}} \propto \frac{\partial}{\partial \mathrm{r}} (k_\parallel(r) v_{\mathrm{A}}(r)). \tag{47}$$

However, local extrema or coupling of two poloidal harmonics (breaking various symmetries), lead to radially local or global gaps of the Alfvén continuum where the gradient in equation (47) vanishes and continuum damping is absent. AEs can easily be excited in these gaps, which we will discuss in the next subsection. Other damping mechanisms are thermal ion and thermal electron Landau damping, electron collisional damping and radiative damping. These damping mechanisms require a kinetic description beyond the MHD model since they rely on the resonant interaction of the thermal ions and electrons with the mode. Whereas for ion Landau damping only thermal ions in the Maxwellian tail contribute to the damping, electron Landau damping has contributions from passing and trapped electrons, depending on the parallel mode structure of the perturbation [428]. Radiative damping, which is often found to be one of the dominant damping mechanisms in the core of a

tokamak, requires a global description, since the mode-converted kinetic Alfvén wave [429] carries wave energy away from the gap location via radial propagation and subsequent electron Landau damping (see also section 6.4.1).

Depending on the effective linear growth rate on the collisionality and on various nonlinear saturation mechanisms to be discussed in the following, the waves can reach amplitudes up to $\delta B/B \sim 10^{-3}$ in present day experiments. The related radial transport, here represented by the change of the canonical toroidal angular momentum ΔP_ϕ can be understood by using the Hamilton formalism [430] of the wave-particle system leading to $\Delta P_\phi = \frac{n}{\omega}\Delta\mathcal{E}$ (see section 2). Note that toroidally symmetric modes with $n = 0$ that tap energy only from velocity-space gradients cannot cause radial transport larger than a poloidal gyroradius [431] unless a topological boundary (e.g. passing-trapped) is crossed. (Even for $\Delta P_\phi = 0$, a change in $v_\parallel$ implies a change in Ψ.)

6.2. Overview of AEs

We will start with a brief overview of the zoology of AEs and their basic characteristics, ordering them by their characteristic frequency bands. A typical Alfvén continuum for an ITER scenario and mode number $n = 12$ is illustrated in figure 26. At intermediate frequencies on the order of the Alfvén frequency much less than the ion cyclotron frequency, $\omega \sim \omega_A = v_A/R \ll \omega_{ci}$, the toroidicity-induced, ellipticity-induced and non-circular triangularity induced AEs (TAEs, EAEs, and NAEs) are found in gaps of the shear Alfvén continuum. RSAEs have similar frequencies but sit close to a local maximum of the continuum. A typical ECE spectrogram with TAEs and RSAEs is shown in figure 18 in section 4. At high frequencies close to the ion cyclotron frequency ω_{ci}, the global AEs (GAEs) and the compressional AEs (CAEs) are found, which we refer to as high-frequency AE modes. At frequencies much lower than the Alfvén frequency, the β-induced AEs (BAEs) and the β-induced Alfvén acoustic eigenmodes (BAAEs) are found, which we refer to as low-frequency AE modes. Theese modes depend on pressure effects. A spectrogram from the TIP prototype installed at DIII-D showing BAEs and RSAEs appears in figure 17 in section 4. Finally, the low-frequency Alfvén modes (LFAMs) have frequencies down to the diamagnetic frequencies (not illustrated in figure 26.).

Next, we will estimate the location and frequencies of the TAEs, EAEs and NAEs. For low frequencies compared with the ion cyclotron frequency and neglecting kinetic effects, the dispersion relation of shear Alfvén waves in a uniform magnetic field is

$$\omega = k_\parallel v_A, \tag{48}$$

where $v_A = B/\sqrt{\mu_0 \rho_m}$ is the Alfvén velocity. In a toroidal plasma with a safety factor profile q, discrete modes with a toroidal mode number n and a poloidal mode number m form. Periodicity demands that the parallel wave number be given by

$$k_\parallel = (n - m/q)/R. \tag{49}$$

Gaps in the shear Alfvén continuum arise when two counter-propagating waves with the same toroidal mode number and close-by poloidal mode numbers couple. The mode surface locations, frequencies and resonance conditions with EPs can then be found by solving

$$k_{\parallel,m} + k_{\parallel,m+\Delta_m} = 0 \tag{50}$$

where $\Delta_m = \{1, 2, 3, ..\}$ and using equations (48) and (49). The first three values of $\Delta_m = \{1, 2, 3, ..\}$ correspond to the TAEs, EAEs, and NAEs. For example, for TAEs we set $\Delta_m = 1$ giving $(n - m/q_{TAE})/R + (n - (m+1)/q_{TAE})/R = 0$ and hence

$$q_{TAE} = (m + 1/2)/n, \tag{51}$$
$$k_{\parallel,TAE} = 1/(2q_{TAE}R), \tag{52}$$
$$\omega_{TAE} = 1/(2q_{TAE}R)v_A. \tag{53}$$

In terms of the Alfvén frequency $\omega_A = v_A/R$, we get $\omega_{TAE} = \omega_A/(2q_{TAE})$. Inserting $\omega = \omega_{TAE}$ and the drift orbital frequencies ω_ϕ and ω_θ (section 2) for the mode surface location q_{TAE} into the resonance condition,

$$n\omega_\phi + (m + l)\omega_\theta - \omega = 0, \tag{54}$$

with arbitrary poloidal harmonic integers l yields the resonances $v_\parallel = v_A/(2(m + l) + 1)$. So EPs and TAEs can resonate for $v_\parallel = v_A, v_A/3, v_A/5$ and so on. The mode locations, parallel wavenumbers, frequencies and resonances of EAEs and NAEs can be found in the same way for $\Delta m = 2$ and $\Delta m = 3$. The mode locations and frequencies of TAEs, EAEs and NAEs as well as other AEs discussed in the following are summarized in table 4. The mode width in the minor radius coordinate can be estimated as $\Delta_{AE} = r_{AE}/m$ where r_{AE} is the minor radius coordinate where $q(r_{AE}) = q_{AE}$. If the mode width is comparable to the drift orbit width of a resonant EP, $\Delta_{AE} \simeq \delta$, the power transfer between EPs and AEs is typically largest. Alphas in ITER can fulfill the resonance condition $v_\parallel = v_A$. In recent JET DT experiments, TAEs were found to be driven by alphas [40], as anticipated in DD afterglow experiments [432].

Reversed shear AEs (RSAEs) are located at the shear reversal point for q-profiles with a local minimum, q_{min}, appearing due to non-monotonic current profiles. This leads to a local maximum in the SAWC where the radial derivatives and hence the continuum damping vanish, $\gamma_{cont} \sim 0$ (equation 47). The parallel wave number of the RSAE is $k_\parallel = |n - m/q_{min}|/R$, giving the frequency $\omega_{RSAE} = |n -$
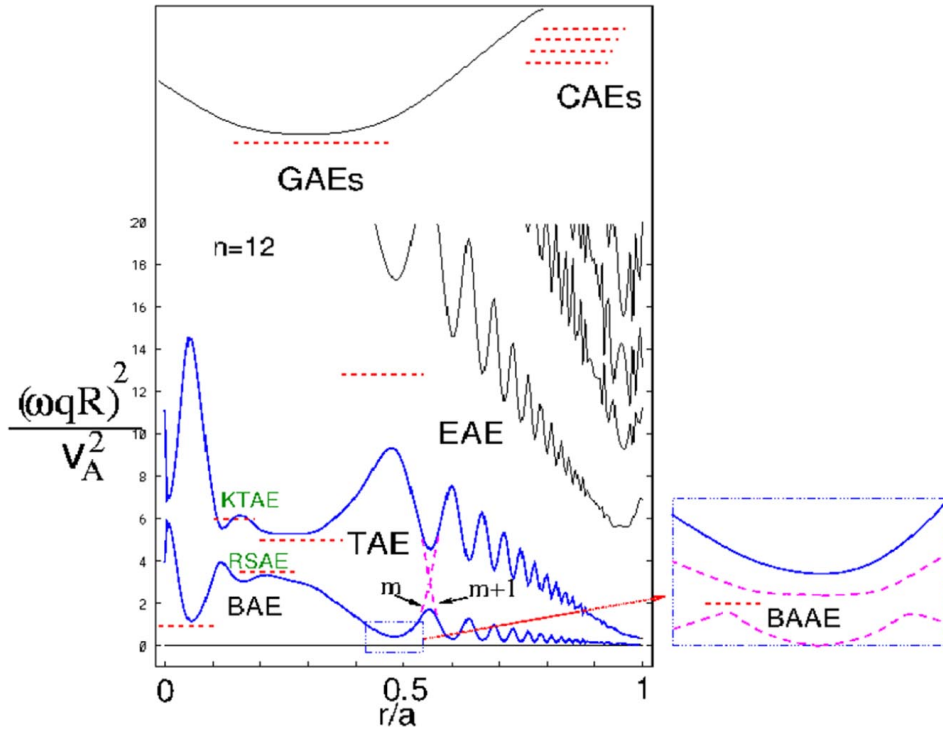
Figure 26. Alfvén continuum for $n = 12$ in ITER obtained by the ideal MHD code NOVA. The gaps in the continuum correspond to the BAE, TAE, EAE and BAAE modes. The low frequency BAE gap is due to Alfvén continuum upshift by the coupling of the Alfvénic and acoustic waves. This coupling also leads to the formation of a new gap near the rational magnetic surface called the BAAE gap shown in the insert. Dashed curves in the insert show the coupling of the Alfvénic and acoustic waves. Dashed horizontal lines correspond to the global eigenmode solutions. Reproduced from [30].

$m/q_{min}|\omega_A$. Alfvén spectroscopy exploits this relation between q_{min} and the RSAE frequency to infer the evolution of the q-profile from the measured mode frequencies. Often q_{min} decreases during plasma discharges, leading to an increasing RSAE frequency. When several RSAEs appear at rational q_{min}, they are also called "Alfvén cascades" (ACs) [433].

Global AEs (GAEs) and compressional AEs (CAEs) are high-frequency AEs. GAEs are related to extrema, typically minima, of the global SAWC for the minimum Alfvén frequency $\omega \sim \min(\omega_A)$. They are located at $q = m/n$. The GAE frequency is often higher than the TAE frequency, but it can also be in the same frequency range. Formally this branch arises from the combined effects of finite ω/ω_{ci} and the equilibrium current density gradient, but the ion cyclotron effects may be dropped in typical fusion plasma regimes [434].

The compressional AEs (CAEs) have frequencies in the range of the ion cyclotron frequency, often higher. Whereas the AEs discussed so far are typically excited by spatial gradients, the CAEs are typically excited by velocity-space gradients, as ω in the drive term is large. CAEs are thought to be connected with ion cyclotron emission (ICE) and are hence of strong interest for diagnostic purposes in burning plasmas.

Beta-induced AEs (BAEs), which are Alfvénic modes in the continuum gap at $q = m/n$ caused by finite plasma β, are related to the geodesic curvature [435–439]. The BAE frequency is $\omega_{BAE} = \sqrt{\beta_i(7/4 + T_e/T_i)}\omega_A$. The electrostatic geodesic acoustic mode (GAM) [440] has the same frequency and β dependence. The beta-induced Alfvén-acoustic eigenmode (BAAE) gaps [441–443] are induced by the coupling of the SAW and the $m + 1$ sound wave branches. This coupling is reflected by the intrinsically mixed polarisation of BAAEs, neither purely Alfvénic nor purely compressional, which has important consequences for the damping of the modes [444–446]. Higher-order geodesic Alfvén-acoustic couplings and gaps can be found when taking plasma shaping into account, in particular elongation [447]. The low frequency BAAE gap can be computed analytically [442] which was later reproduced in Ref. [448]. The BAAE gap structure was recently reexamined [449, 450] where the coupling with the neighboring acoustic harmonics was ignored [451].

All branches are modified in the kinetic description compared to the MHD limit described so far, and new, purely kinetic branches arise. In particular, the low-frequency part can be strongly influenced by diamagnetic effects and kinetic effects of the thermal ion

42

transit or bounce drift motion with characteristic frequencies ω_{*i} and $\omega_{ti,\theta}$. Here,

$$\omega_{*i} = \omega_{*ni} + \omega_{*Ti} = \left(\frac{T_i \boldsymbol{b}}{ZeB} \times \left(\frac{\nabla n_i}{n_i} + \frac{\nabla T_i}{T_i} \right) \right) \cdot \boldsymbol{k}$$

$$\approx \frac{T_i}{ZeB} \frac{1}{n_i} \frac{\partial n_i}{\partial r} (1 + \eta_i) k_{m,\theta} \qquad (55)$$

where $k_{m,\theta} \approx -m/r$ is the poloidal wave number and $\eta_i = \frac{\partial}{\partial r} \log T_i / \frac{\partial}{\partial r} \log n_i$.

General dispersion relations including finite orbit width effects have been derived [438, 446, 452–454] and implemented in various codes [29, 455, 456]. The general fishbone-like dispersion relation (see also section 7.2), relying on the separation of scales between the singular and regular layers, includes additional expressions for the EP contribution to the EP-drive and the thresholds to EPM branches that exist for all the modes discussed above [32, 400]. The EPM branches often emerge from the least damped part of the spectrum where the drive can overcome continuum damping.

As already mentioned, an overview over some of the properties of AEs are given in table 4. It should be noted, however, that these expressions describe the gap locations, whereas the equilibrium non-uniformities have to be considered for calculating the global mode frequencies, since they remove the degeneracy with the continua. Thus, in many cases of practical interest global analyses are required for quantitative comparisons. Useful approximate formulas including finite beta effects, ellipticity and triangularity for many AEs are given in [457] and in the Appendix of [458]. For BAAEs and the low-frequency Alfvén modes (LFAMs) with frequencies $\omega \sim \omega_{ti,\theta} \sim \omega_{*i}$, the kinetic dispersion relation has to be solved, including ellipticity [459] and trapped particle contributions [445, 446, 448, 453, 460, 461].

6.3. AE eigenfunction

The AE eigenfunction is important because its structure determines both the resonance condition (Eq. 11) and the amount of energy the particle exchanges with the wave. By definition, a resonant particle is one that encounters the same wave phase on multiple orbits [37]. Consequently, the net linear energy transferred per orbit $\Delta\mathcal{E}$ is the integral of the instantaneous power transfer (given in Eq. 12) averaged over a complete orbit,

$$\Delta\mathcal{E} = Ze \oint \delta\boldsymbol{E} \cdot \mathrm{d}\boldsymbol{l}. \qquad (56)$$

Equation (56) implies that the eigenfunction must be known accurately to calculate the drive term γ_{drive} correctly so, in order to determine the stability

Mode	Δ_m	q	ω/ω_A
TAE	1	$(m+1/2)/n$	$1/2q$
EAE	2	$(m+1)/n$	$1/q$
NAE	3	$(m+3/2)/n$	$3/2q$
RSAE$^\diamond$	0	$q_{\min}$	$m/q_{\min}(t) - n$
GAE	0	m/n	$\min[\omega_A(r)]/\omega_A$
BAE	0	m/n	$\sqrt{\beta_i(7/4 + T_e/T_i)}$
BAAE†	1	$\sim m/n$	$(n - m/q)/\sqrt{1 + 2q^2}$
LFAM‡	0	m/n	$\sim 0.5\omega_{*i}/\omega_A$

Table 4. Summary of basic properties of various AE branches. TAE: Toroidal AE, EAE: Ellipticity-induced AE, NAE: Non-circularity-induced AE, RSAE: Reversed-shear AE, GAE: Global AE, BAE: Beta-induced AE, BAAE: Beta-induced acoustic AE. LFAM: Low-frequency Alfvén modes. $^\diamond$ RSAEs only exist at frequencies larger than the BAE frequency. † For the BAAEs in the MHD limit, we quote a simplified expansion around the rational surface according to [442, 449, 450]. ‡ For LFAM please refer to further details in the text.

threshold correctly, both the eigenfunction and the resonant orbits need to be known accurately.

Fortunately, the linear mode structures of all AEs are well understood. There are three directions to consider: the toroidal mode number n, the poloidal structure that is (in general) a combination of different mode numbers m, and the radial structure. The most unstable toroidal mode number occurs when the eigenfunction and EP orbit are comparable in size. In the simplest theory of AEs driven by the spatial gradient, the EP drive is proportional to the EP diamagnetic drift frequency ω_{*f}

$$\omega_{*f} = \left(\frac{T_{f,\mathrm{eff}} \boldsymbol{b}}{ZeB} \times \left(\frac{\nabla f_f}{f_f} \right) \right) \cdot \boldsymbol{k} \qquad (57)$$

with $T_{f,\mathrm{eff}} = \int v^2 f_f \mathrm{d}v$. If f is separable as $f(E, \mu, P_\phi) = n(r)f(E, \mu)$, a simplified expression is

$$\omega_{*f} = \omega_{*nf} + \omega_{*Tf} = \left(\frac{T_{f,\mathrm{eff}} \boldsymbol{b}}{Z_f eB} \times \left(\frac{\nabla n_f}{n_f} + \frac{\nabla T_{f,\mathrm{eff}}}{T_{f,\mathrm{eff}}} \right) \right) \cdot \boldsymbol{k}$$

$$\approx \frac{T_{f,\mathrm{eff}}}{ZeB} \frac{1}{n_f} \frac{\partial n_f}{\partial r} (1 + \eta_f) k_{m,\theta} \qquad (58)$$

where $k_{m,\theta} \approx -m/r$ is the poloidal wave number and $\eta_f = \frac{\partial}{\partial r} \log T_{f,\mathrm{eff}} / \frac{\partial}{\partial r} \log n_f$. The EP diamagnetic drift frequency is linearly proportional to the poloidal mode number $m \simeq n \cdot q$ [462]. However, the radial extent of the eigenfunction tends to decrease with increasing toroidal mode number n so, when the EP orbit size significantly exceeds the spatial extent of the mode, the energy exchanged with the wave $\Delta\mathcal{E}$ decreases, reducing the EP drive [463]. The most unstable toroidal mode number occurs when the spatial extent and orbit size are comparable, an expectation that is roughly consistent with experiment [464]. Because of the large size and magnetic field of ITER, this scaling predicts that the most unstable toroidal mode numbers

n in ITER will be many times larger than in most contemporary experiments; an ITPA benchmark study (see section 6.4.4) predicts that mode numbers between $n \simeq 20$ and $n \simeq 30$ will be most unstable.

Available measurements of the poloidal structure agree with the expectations summarized in Table 4. For example, soft x-ray measurements of the poloidal structure of a GAE are consistent with a single m; in contrast, nearly equal values of m and $m+1$ describe a TAE [465]. Similarly, electron cyclotron emission images of an RSAE at the start of the frequency sweep are consistent with a single m [466, 467], as expected.

The predicted radial structure has also been compared with experiment. In the example shown in figure 18 in section 4, the radial amplitude profile measured along the midplane agrees well with ideal MHD theory for both an RSAE (figure 18(b)) and a TAE (figure 18(c)) [264]. Another example of excellent agreement between the TAE radial amplitude profile and ideal MHD theory appears in [468]. RSAEs with the same toroidal mode number can appear with different radial mode numbers; the lowest radial mode is approximately Gaussian in shape but higher radial mode numbers contain nodes [467, 468].

Many authors have noted that the AE radial phase profile depends upon the radial location of EP drive and wave damping. For example, a thorough theoretical overview of the connection between localized sources and sinks of energy, energy and momentum transport, and mode structure appears in [469]. Experimental observations of radial phase variation are commonplace for both TAEs and RSAEs [466, 468, 470, 471]. A recent paper [472] conducted a comprehensive survey of thousands of RSAE and TAE mode structure measurements from DIII-D beam-heated discharges. Amidst extremely large variability in the radial phase profile, the phase profile for a typical RSAE is approximately flat, while a typical TAE often has a phase ramp at large major radius. The authors speculate that the typical TAE radial phase profile reflects power flow from smaller minor radius (where the EP gradient and hence power flow from the EPs is large) to edge regions (where wave damping predominates).

During the current ramp phase of the discharge, RSAEs often first appear when $q_{\min}$ is a rational number, then the mode sweeps upward in frequency as the q-profile evolves [252]. Observations of RSAEs that sweep downward in frequency to a minimum at the time of the rational $q_{\min}$ crossing are relatively rare; for example, $< 1\%$ of JET cases surveyed were downward sweeping [473]. Proposed theoretical explanations for the enhanced stability of downward-sweeping RSAEs are summarized in [474]. Experimentally, the radial eigenfunctions of downward-sweeping and upward-sweeping RSAEs are very similar [474].

Despite its importance for correct mode identification and stability calculations, measurements of mode polarization are rare. Recently, however, a method to infer the electrostatic potential $\delta\phi_\parallel$ and the parallel component of the vector potential $\delta A_\parallel$ from measurements of electron temperature and density δT_e and δn_e was developed [475]. Application of the method to instabilities in DIII-D shows that RSAEs and TAEs have small values of $\delta\phi_\parallel$ (as expected for shear Alfvén wave polarization) but lower frequency modes often have appreciable electrostatic potentials.

It should be noted that the measured AE mode structure is already in the nonlinear phase. Nonlinear simulations with the gyrokinetic code GTC found that the AE eigenfunction shifts radially in time as the EP gradient evolves, as observed experimentally [476]. A computationally expensive nonlinear simulation with the MEGA code achieved good agreement with experimental eigenfunction measurements for both mode amplitude and radial amplitude and phase profiles [477]. (This MEGA simulation modelled the EPs kinetically and the bulk plasma with resistive MHD.)

6.4. Alfvén frequency range: TAEs, EAEs, and RSAEs

Here we consider AEs in the intermediate frequency range on the order of the Alfvén frequency (TAEs and EAEs) and RSAEs or ACs with frequencies typically below the TAE frequency. Neutral beam, ICRF-accelerated, and energetic electron populations have driven these AEs unstable in virtually all toroidal magnetic confinement configurations [478]. TAEs and EAEs driven by electrons during lower-hybrid heating have been observed on EAST [479]. Alpha-driven TAEs were observed on TFTR [278] and in the recent DT campaign at JET using magnetics, soft-xray, interferometry and reflectometry diagnostics [40]. At JET, it was clear that alphas drove the TAEs since they were observed in an afterglow experiment 50 ms after NBIs had been turned off and fusion alphas were still being produced, as illustrated in figure 27. The observed mode was found on the outboard midplane and was driven by both trapped and passing alphas originating from the plasma core.

6.4.1. Perturbative and non-perturbative simulations.
EP-driven instabilities are often described by a perturbative approach, i.e. the waves are linear eigenmodes of the bulk plasma and their frequencies and spatial structures are determined by the bulk plasma only. However, to model AEs with shear Alfvén polarization accurately, the descriptions of the interaction of EPs require the more sophisticated
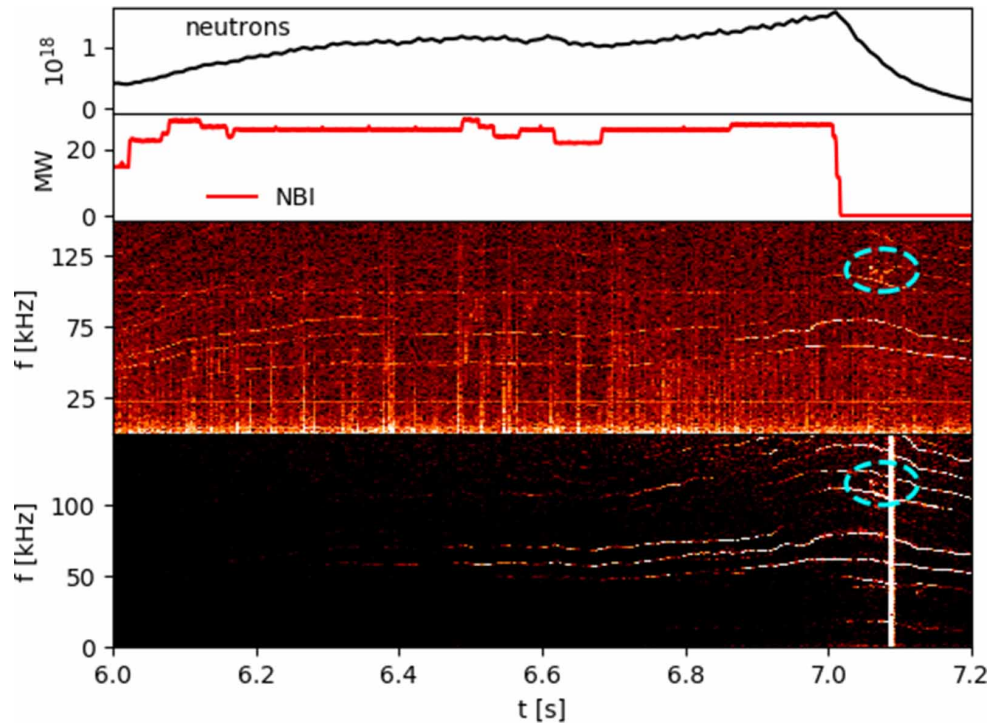
Figure 27. Mode observations during the afterglow in JET DT shot #99946. From top to bottom: Fusion neutron rate, NBI power, Fourier spectra from interferometry, and SXR emission. The TAE appears in both spectra at 7.05 s with frequency 115 kHz (circled). Reproduced from [40].

global, non-perturbative approach [480]. The term non-perturbative means that the simpler perturbative approach cannot be applied since the interaction between the EPs and the modes is too strong, and so the mode properties are not only determined by the bulk plasma, but also by the EPs. Non-perturbative eigenmode features also arise when the coupling to kinetic Alfvén waves is considered.

For the assessment of the damping, usually the gap structure is analysed first in order to find regions without continuum damping. It is important to realize that some of these modes are in between rational surfaces $q = m/n$, e.g. the TAE $q_{\text{TAE}} = (m + 1/2)/n$, whereas others reside at rational surfaces with very small $k_{\parallel}$. Both electron and ion Landau damping depend very sensitively on $k_{\parallel}$, since the ratio of $\omega/k_{\parallel} v_{\text{th,i,e}}$ enters the damping rate exponentially [481]. Close to $k_{\parallel} = 0$, ion Landau damping can only occur through sidebands, and electron Landau damping can be dominated by trapped electrons. For TAEs, the high-energy tail of the thermal Maxwellian ions can contribute to the damping of the two main harmonics, whereas electron Landau damping depends critically on the background non-uniformities, i.e., the distance to the next rational surface [428]. Often trapped electrons dominate the damping, and thus also trapped-electron collisional damping has to be considered [482, 483].

The coupling of global modes to the kinetic Alfvén wave (KAW) introduces short wavelength-scales on the order of the ion Larmor radius ρ_{Li} into the system, constituting the microscale. Formally, this coupling arises due to the ion polarisation term and finite Larmor radius contributions in the coupled system of quasi-neutrality and the gyrokinetic momentum equation causing finite $E_{\parallel}$ [484] that is dissipated by electron Landau damping. Since the damping scales with $\sim (k_{\perp} \rho_{\text{Li}})^2$, the mode structure needs to be calculated non-perturbatively. A non-ideal parameter [429, 485] can be derived for a local estimate of the KAW coupling, but, for global modes with various (radial) contributions to the radiative damping, this can lead to difficulties when interpreting experimental measurements. This issue was pointed out in [486, 487], but the strongly coupled TAE-KAW wavefield found in this work could not be reproduced with modern gyrokinetic codes, except when electron Landau damping is artificially reduced or omitted [488, 489].

This multi-scale, non-perturbative nature of the problem and the requirements for low-frequency modes (section 6.2) motivated various studies using global, fully self-consistent, gyrokinetic simulations that can simultaneously resolve micro- and mesoscales to map out the linear stability boundaries quantitatively and to accurately predict the nonlinear saturation

amplitude and transport level for contemporary and future fusion devices. We will deal with non-perturbative approaches in section 7.

6.4.2. AE antenna measurements and benchmarks. A powerful way to probe the linear stability of AEs is to launch waves with an external antenna [490]. By sweeping the antenna frequency across the resonance and detecting the response with fast magnetic coils, the resonant frequency ω, net damping rate γ/ω, and toroidal mode number n of the mode can be inferred. These are then compared with theory and numerical simulations, improving extrapolations to future burning plasma operations such as in ITER and DEMO. Measurements of γ/ω are particularly valuable, as the mode drive must exceed mode damping for linear instability. Since the method is most sensitive to modes with radial eigenfunctions that are appreciable near the antenna, TAEs, EAEs, or globally extended GAEs are usually studied [491]; for similar reasons, low-n modes are more readily detected than high-n modes.

The Alfvén antenna technique was introduced at JET [492]. After around 15 years and more than 100,000 individual damping rate γ/ω measurements, the original saddle coil system used for the active excitation of low-frequency AEs in JET was replaced with a set of eight, small and localized in-vessel antennas capable of driving AEs with higher toroidal mode numbers. Recall that these higher mode numbers are relevant for ITER and future burning plasma experiments. Details on the design of these new antennas and on the first results obtained with this system can be found in [493–499]. The system can drive, detect and track individual AEs for a given range of toroidal mode numbers [500, 501].

These first sets of measurements were then followed by a full campaign, totaling more than 30000 γ/ω measurements for individual toroidal mode numbers, now ranging from the low-n previously probed with the saddle coil system (still a majority, covering about 50% of the measurements) to modes up to $|n| = 10 - 12$. Details of these measurements, which covered the analysis of the dependence of γ/ω for higher n modes on the edge plasma shape and on the plasma isotopic composition can be found in [502–504]. One important result is that the damping rate tends to increase with increasing plasma isotope mass (figure 28). The first detailed comparisons with theory for these higher-n modes can be found in [505–508], and the first use of these higher-n modes for MHD spectroscopy of the plasma isotopic composition can be found in [509].

A dedicated ITPA EP group effort aimed to understand the damping rates as measured by the
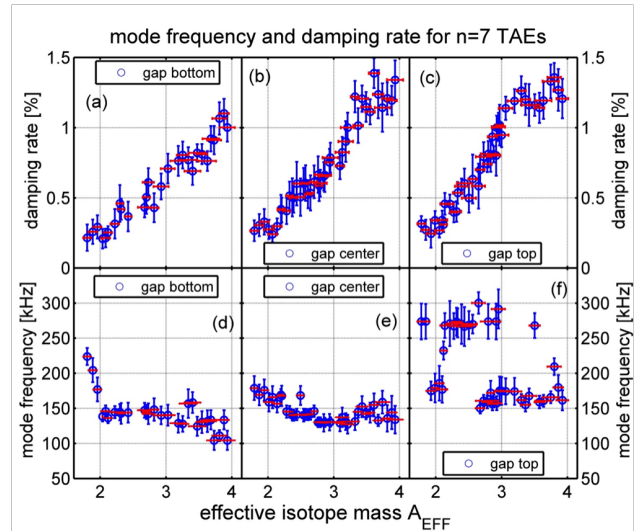

Figure 28. JET antenna measurements of the damping rate and the mode frequency for $n = 7$ TAEs as a function of the effective isotope mass for modes with frequencies near the bottom (left), center (middle), and top (right) of the TAE gap. The damping rate increases strongly with increasing mass in all cases. Reproduced from [504].

JET TAE antenna. Perturbative, fluid codes and non-perturbative, kinetic codes were benchmarked against each other and validated against experimental antenna results from JET for an elongation scan (figure 29 [510]). In this study, all codes captured the experimental trend, showing that radiative damping is the dominant contribution (see also [511]) for an open TAE gap (no continuum damping). However, figure 30 demonstrates that the damping in general cannot be estimated by one set of local parameters, since the global mode structure can cause both core and edge KAW coupling.
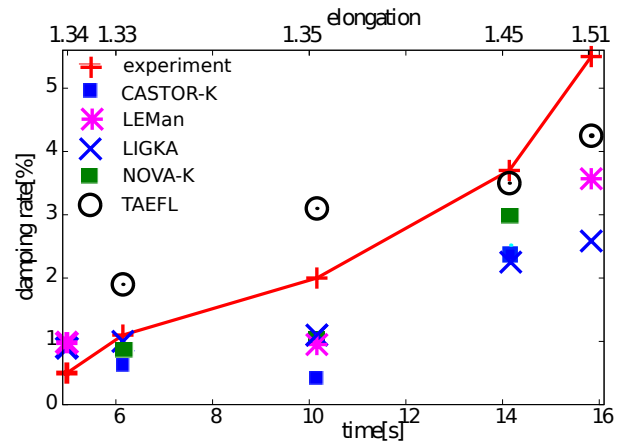

Figure 29. ITPA benchmark and validation study: JET elongation scan comparing the damping rates of the TAE antenna with various code results; see also subsection 6.4.2. All involved codes captured the experimental trend of an increasing damping rate for increasing elongation. Reproduced from [510].
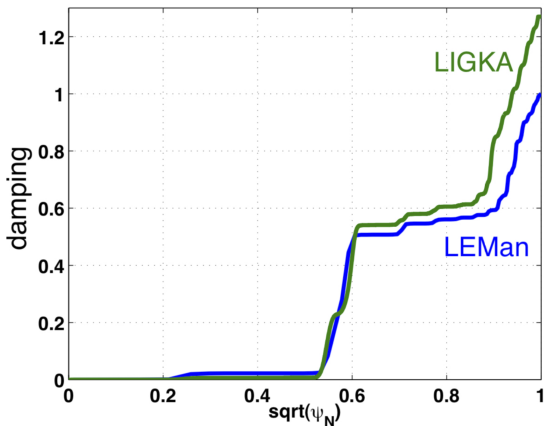
46

Figure 30. ITPA benchmark and validation study: the radial absorption profile for a global $n = 3$ TAE based on JET discharge #77788, $10.157s$ as calculated by LEMAN [512,513] and LIGKA [514], normalised to the LEMAN result $\gamma/\omega = 0.95\%$ [510]; see also section 6.4.2. The damping in general cannot be estimated by one set of local parameters. Reproduced from [510].

Figure 31. Normalized damping rate as a function of the non-ideal parameter λ that is associated with radiative damping for a large database of JET antenna measurements. The correlation with λ is the strongest dependence in the database. Reproduced from [527].

Over the past few years, an upgraded JET antenna diagnostic [515–520] has been operated on nearly a thousand JET plasma discharges, measuring thousands of stable AE resonances. Analyses of data collected during the 2019-2020 JET campaign of mainly deuterium plasmas has been reported, including comparisons with gyrokinetic codes [521–525]. Statistical analysis of these data shows that, as expected, the damping rate is correlated with parameters that are related to continuum damping and radiative damping. Since the edge safety factor determines if the TAE gap is open or closed at the edge, the importance of continuum damping is reflected in a statistically significant dependence on q_{95} [526]. (q_{95} is the safety factor at the the surface the contains 95% of the poloidal flux.) The measured damping rate also correlates strongly with the non-ideal parameter associated with the finite Larmor radius effects that cause radiative damping (figure 31) [526].

In recent work, a marginally stable AE was tracked by the JET antenna diagnostic in real-time in a discharge with 25 MW of external heating [527]. Interestingly, the AE was deduced to be an edge-localized EAE with a lab-frame frequency aligned with the core TAE gap. AEs were also monitored from destabilization through stabilization in a JET EP experiment [122].

AE antenna studies have also been conducted on MAST and C-Mod [528]. In C-Mod, damping-rate measurements for inner wall limited and diverted cases over a range of toroidal mode numbers $4 \le |n| \le 9$ were compared with NOVA-K calculations that included continuum and radiative damping [529]. Good agreement between the measurements and theoretical calculations were obtained but the results depended sensitively on the assumed q-profile.
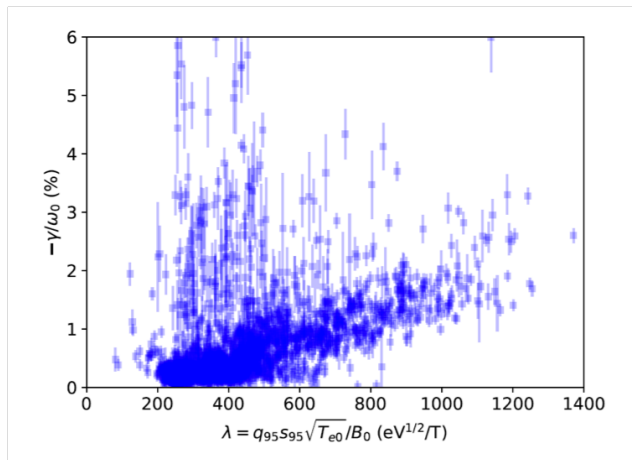
6.4.3. Code benchmarks. The ITPA EP group has performed several code benchmark studies on various machines. A detailed study of damping mechanisms for AEs, that successfully compares eigenvalue and initial value gyrokinetic codes for an AUG case, can be found in [530]. It should be noted that a straightforward comparison of numerical results with the general nonlinear theory 7.2 can be carried out by adopting the mode structure decomposition approach [531] and the ballooning formalism [455, 532].

For benchmarking the linear drive, also in the non-perturbative regime, a synthetic test case with aspect ratio 10 has been set up within the ITPA EP group [533]. 11 codes with a broad variation in the physical and numerical models participated. The eigenfunctions as well as mode frequencies match in a satisfactory way. The growth rates were within around 20%. However, they are found to depend strongly on the complexity of the model (see figure 32). Further code verification is necessary to improve the match of the results by including further physical effects. Furthermore, it was found that the mode frequency and mode structure of TAEs can change in the presence of a considerable EP population, as also documented for a DIII-D case [534]. This work also found symmetry breaking effects of TAEs due to the EPs. Such effects were analysed in more detail for BAEs and RSAEs [535–538]: an asymmetry in the EP gradient with respect to the rational surface of the modes leads to finite k_r and tear-drop shaped 2D mode structures in excellent agreement with measurements [334,466,467,534,539–541], which can lead to enhanced
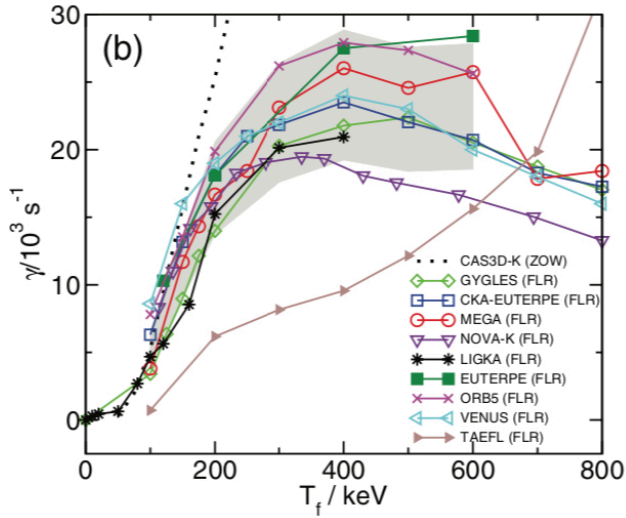
EP transport [542].

Figure 32. Comparison of growth rates computed with various codes including FLR effects for an $n = -6$ TAE. The dashed line from CAS3D-K is valid in the limit of zero orbit width (small energies) and is shown for comparison. The shaded grey area marks the $\pm 20\%$ margin around the mean value. Reproduced from [533].

Extensive studies of RSAEs have been carried out on DIII-D [478]. RSAEs on spherical tokamaks have been found to be largely suppressed due to their relatively higher β [543]. A linear RSAE benchmark and a comparison between simulations and experiments based on a DIII-D discharge (figure 33) [539, 544] was done with modern gyrokinetic and gyrokinetic-MHD codes. RSAE frequencies and mode structures for $n = 4, 5, 6$ of eight participating codes agree very well with the experiment as measured by ECEI. The RSAE frequencies differ by less than 5% whereas the growth rates differ by about 20%. It is found that pressure gradients of the thermal plasma make a significant contribution to the growth rates. The differences become larger when the RSAE-TAE transition is approached by varying q. Due to the open SAWC gap, various TAEs closely spaced in the frequency domain but with different radial structures can co-exist. Moreover, using a calculated EP profile that takes diffusion by multiple unstable modes into account, a TAE with $n = 6$ is found to be unstable at the outer edge, which is consistent with the experimental observations. Finally, electron temperature fluctuations and radial phase shifts from simulations show no significant differences with the experimental data for the strong $n = 4$ RSAE, but significant differences for the weak $n = 6$ TAEs. Other DIII-D stability studies have found: (1) that flattening the EP spatial gradient with off-axis beams stabilizes RSAEs, consistent with TAEFL stability calculations

[545], (2) that creation of a bump-on-tail feature in the beam-ion velocity distribution has little impact on TAE and RSAE stability, consistent with MEGA calculations [546], and (3) that, owing to their longer slowing-down time, deuterium beams drive RSAEs more strongly than hydrogen beams, as predicted by MEGA [547].

Gyrokinetic simulations can incorporate realistic toroidal geometry and comprehensive physics such as effects of equilibrium currents [548] and compressible magnetic perturbations [549, 550]. As discussed above, these simulations find that accurate damping and growth rate calculations require non-perturbative, fully self-consistent simulations to calculate the true mode structure. The radial position of the AEs can move with the location of the strongest EP pressure gradients as confirmed by experimental data [534]. Further validation of gyrokinetic simulations of TAEs have been carried out on many tokamaks including KSTAR [551], HL-2A [552], AUG [530, 553, 554] and JET [524, 555].
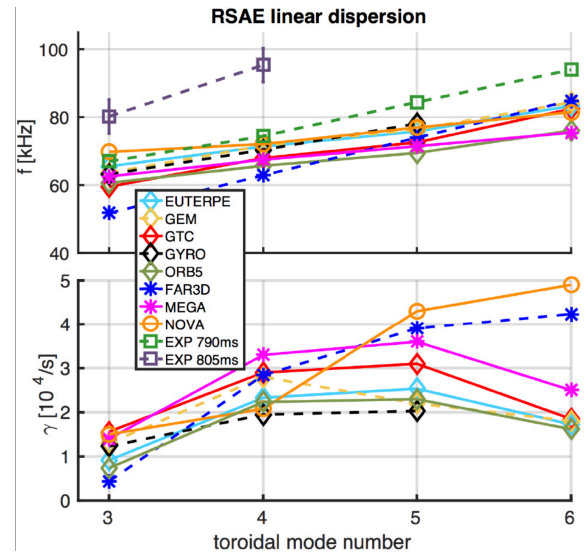
Figure 33. Comparison of the linear dispersion relation calculated with various codes for an RSAE in DIII-D shot 158243 at 805 ms. Top: real frequencies. Bottom: growth rates. The plot markers are diamond, star, and circle for the gyrokinetic, kinetic-MHD, and perturbative eigenvalue codes, respectively. Reproduced from [544].

6.4.4. ITER predictions. Based on scenario simulations using the ASTRA code [556] (very similar to simulations stored under #131018, 50 in the ITER IMAS database), the ITPA EP group motivated a study concerning TAE stability and related EP transport for the standard ITER $Q = 10$, 15 MA scenario. Various groups contributed to this study [31, 557–565], extending previous studies [566, 567]. It is encouraging to observe, that all studies using nearly identical

profiles predict only weakly unstable TAEs with small or negligible EP transport. As mentioned above, the range of the most unstable mode numbers lies between $n = 20 - 30$. However, it has to be noted that the n-number spectrum of the most unstable linear modes varies significantly, depending on the model and the details of the safety factor profile. This leads to different results when carrying out sensitivity scans in order to determine the thresholds for benign AE transport. For example, density peaking effects not included in the ASTRA simulations may lead to steeper alpha gradients. It has been shown in [565] that global gyrokinetic models [568] and gyrokinetic-MHD models [514, 569] agree reasonably well on linear and nonlinear features, emphasizing the importance of the linearly stable spectrum in the nonlinear phases. It should be noted that for this comparison neither collisions nor zonal flows were included for benchmark reasons. Relaxing these simplifications is an ongoing effort (see subsection 7.3) needed for an increasingly realistic description and prediction of a burning fusion plasma. Recent developments try to mitigate the problem of exponential sensitivity of the mode stability with respect to the background profiles by setting up integrated automatic workflows that combine equilibrium evolution and linear stability, in order to correctly capture parametric dependencies (e.g during ramp-up or during heating power scans) [561, 570].

Apart from the $15\,\mathrm{MA}$ scenario, also various studies of the $9\,\mathrm{MA}$ steady-state ITER scenario have been carried out [557, 571, 572]. Similar mode number ranges are found to be unstable (again with a strong dependence on the background profile details), but in this case RSAEs, RSAE/TAE hybrids, and BAEs are expected to be the most unstable modes, rather then TAEs. Significant EP transport was predicted for nominal parameters [571], hinting to the necessity to include this EP transport in the scenario modeling in order to obtain consistent background and EP profiles that may deviate considerably from neoclassical values. Further, the drive due to off-axis neutral beam heating is expected to be more significant than in the $15\,\mathrm{MA}$ scenario [572].

6.5. High-frequency modes: CAEs and GAEs

Significant progress has been achieved in understanding and modeling of modes with frequencies in the ion cyclotron frequency range (higher than ω_A) since the publication of the Progress in the ITER Physics Basis [20]. This frequency band includes the compressional and the global Alfvén eigenmodes (CAEs and GAEs). These modes do not cause strong transport of EPs in radius but they do cause transport in energy. They are primarily connected with the ion cyclotron emission (ICE) phenomena. The physics of CAEs in particular and its relationship with ICE is discussed in two review papers [573, 574]. Here we present a brief introduction to GAEs and CAEs. These modes have been found in low aspect ratio tokamaks [575–578] and in the conventional aspect ratio tokamaks DIII-D [579] and AUG [183, 580]. Experiments have studied the parametric stability boundaries for a wide variety of EP-driven modes in NSTX [581].

6.5.1. *CAEs.* CAE linear stability theory has potentially attractive prospects for understanding ICE as a potential EP diagnostics (see section 6.5.3). The main elements of CAE linear stability theory have been developed [582].

CAE theory can be presented heuristically on the basis of the fast Alfvén wave dispersion relation, $\omega_\mathrm{CAE} = k_\perp v_\mathrm{A}$ for $k_\parallel \ll k_\perp$, as expected for these modes in tokamaks [583]. The CAE dispersion relation can be used to obtain an eigenvalue equation for the dominant magnetic perturbation $\delta B_\parallel$, i.e. $\hat{k}_\perp^2 \delta B_\parallel = \left(\omega_\mathrm{CAE}^2/v_\mathrm{A}^2\right) \delta B_\parallel$ where $\hat{k}_\perp^2$ is treated as a differential operator [584]. To leading order in inverse aspect ratio $\epsilon = r/R$, this equation becomes

$$
\frac{1}{r}\frac{\partial}{\partial r} r \frac{\partial}{\partial r} \delta B_\parallel + \frac{1}{r^2}\frac{\partial^2}{\partial \theta^2} \delta B_\parallel
$$
$$
= \frac{\omega_\mathrm{CAE}^2}{v_\mathrm{A}^2(0)} \frac{n(r)}{n_0} \left(1 + \epsilon \cos\theta\right)^2 \delta B_\parallel, \tag{59}
$$

where r is the minor radius coordinate, θ is the poloidal angle, $n(r)/n_0$ is the plasma density normalized to its value on the magnetic axis, and $v_\mathrm{A}(0)$ is the Alfvén speed on axis. The coefficient of $\delta B_\parallel$ on the right hand side plays the role of an effective potential and has a minimum absolute value in the low field side midplane. Within the heuristic approach we follow here, CAEs are located in the vicinity of this minimum.

Radially localized CAE solutions can be found for potential wells which are narrow and deep in the radial direction and shallow and long in the poloidal direction. The CAE poloidal wavelength is then shorter than the radial wavelength. This justifies the choice of the eikonal for the following poloidal mode structure [583]:

$$
\delta B_\parallel(r, \theta) = b(r, \theta) \exp\left[-i\omega t + im\left(\theta + \epsilon_0 \sin\theta\right) - in\phi\right], \tag{60}
$$

where ϕ is the toroidal angle, (m, n) are the poloidal and toroidal mode numbers, and the subscript 0 denotes the value taken at the minimum of the local effective potential well, $r = r_0$. Because the potential well is typically poloidally elongated in tokamaks, the wave number components of CAEs have the ordering

$$
k_\theta \gg k_\phi \gg k_r \tag{61}
$$

as also found in CAE stability theory.

49

Because of the complexity of the above eikonal, the realistic CAE dispersion relation is difficult to analyze and compare with experiments. For example, the theoretical methods employed in [585, 586] are based on the assumption for the eikonal and so are approximate. Instead, a heuristic dispersion relation of CAEs [587] leads to the identification of characteristic lengthscales and corresponding "quantum" numbers in each of three relevant directions: the toroidal mode number, n, associated with the major radius R; radial mode number, S, associated with the radial width of the effective potential in the radial direction, and the poloidal mode number, M, associated with the plasma minor radius. The CAE mode frequency is then

$$\omega_{\text{CAE}}^2 \simeq v_{\text{A}}^2 \left(\frac{M^2}{r^2} + \frac{S^2}{L_r^2} + \frac{n^2}{R^2} \right), \tag{62}$$

which is consistent with the tokamak ordering (61).

CAE solutions obtained numerically [587] using the ideal MHD code NOVA agree with the dispersion relation (62) which is consistent with the eikonal (60). It was also found to be consistent with numerical frequency splitting for low $n = (0, 1)$ but not for higher n due to the strong coupling of the dominant compressional Alfvénic polarization of CAEs and the shear Alfvénic polarization of KAW structures. This may mask the observed frequency splitting because, in experiments, the most unstable modes are excited first [588], and they likely have high toroidal mode numbers, $n \gg 1$ [589–591]. Numerical simulations show the complicated CAE dispersion relation which only qualitatively agrees with equation (62). This is due to finite $k_\parallel$ and ω/ω_c effects as was pointed out recently [592].

One new finding in CAE theory is that the shift of the eigenmode frequencies depends on the sign of CAE poloidal mode number m. For a plasma cross section with ellipticity κ, the CAE eigenfrequencies were found to be asymmetric with respect to the sign of the poloidal mode number [593]:

$$\omega_{\text{CAE}} = \frac{m}{r} \sqrt{\frac{1 + \kappa^{-2}}{2}} v_{\text{A}*}$$

$$\times \left[\frac{\sigma_m v_{\text{A}} \left(\ln \rho_{\text{m}} \right)'}{2\omega_{\text{ci}}(\kappa)} + \sqrt{1 + \left(\frac{v_{\text{A}} \rho_{\text{m}}'}{2\omega_{\text{ci}}(\kappa) \rho_{\text{m}}} \right)^2} \right]_{r_*}, \tag{63}$$

where $*$ represents location of the eigenmode, $'$ the radial derivative, and $\sigma_m = m/|m|$. The location of the eigenmode is given by

$$2 + r \left(\ln \rho_{\text{m}} \right)'$$

$$-\sigma_m \frac{v_{\text{A}}}{\omega_{\text{ci}}(\kappa)} \left(r \left(\ln \rho_{\text{m}} \right)' \right)' \sqrt{1 - \frac{2 + r \left(\ln \rho_{\text{m}} \right)'}{\left(r \left(\ln \rho_{\text{m}} \right)' \right)'}} = 0, \tag{64}$$

where ρ_{m} is the plasma density, ω_{ci} is the thermal ion cyclotron frequency.

The expression for CAE growth rate was obtained in the tokamak approximation, which neglects $k_\parallel$ and assumes high frequencies, $\omega/\omega_{\text{ci}} \gg 1$ [574, 594]:

$$\frac{\gamma}{\omega_{\text{ci}}} \simeq \frac{\omega^3}{\omega_{\text{p}}^2 \omega_{\text{ci}}^2} \frac{\sqrt{2} ecB}{\sqrt{\pi} \Delta r_0 R_0}$$

$$\times \sum_{l,\sigma} \int \mathrm{d}P_\phi \mathrm{d}\mathcal{E} \mathrm{d}\mu I^2 \frac{E_1^2}{E_0^2} \frac{\mu l J_l^2}{z^2} \left[\frac{\partial}{\partial \mathcal{E}} + \frac{l\omega_{\text{ci}}}{\omega B} \frac{\partial}{\partial \mu} \right] \tilde{f}, \tag{65}$$

where ω_{p} is the plasma frequency, $E_1 = E_0 f(r, \theta)$ is the CAE structure in the poloidal cross section required for proper averaging of the local growth rate expression, Δ is its radial mode width, $I^2 = 8\pi / \left| \frac{\mathrm{d}}{\mathrm{d}t} (l\omega_{\text{ci}} + \omega_{\text{D}}) \right|$ is the resonant factor accounting for phase variation of wave particle interaction near the resonance, J_l is the Bessel function of order l with the argument $k_\perp \rho_{\text{Lf}}$, and ρ_{Lf} is the Larmor radius of the EPs. The resonance condition is then $\omega - l\omega_{\text{ci}}(r, \theta) - \omega_{\text{D}}(r, \theta) = 0$ which is to be evaluated along the EP drift orbit.

6.5.2. GAEs. GAE modes were found theoretically, with $q = m/n$ and the frequencies just below the minimum of the ideal MHD shear Alfvén continuum [595], and experimentally in tokamaks when plasma was heated by ICRF at frequencies lower than the cyclotron frequency [596]. These modes, called global Alfvén eigenmodes (GAEs), are localized in radial direction near the continuum minimum point outside the plasma centre [597]. These modes are also called the conventional GAEs, when their frequency is just below the Alfvén continuum minimum point where the GAE mode structure is localized. The so-called non-conventional GAEs (NGAEs) are found in stellarators [598] and in helical plasmas. They were studied theoretically in an attempt to explain sudden drops of the plasma beta during the low-frequency instabilities in the W7-AS shearless stellarator due to subsequent electron heating of the plasma periphery. According to [598], NGAEs have frequencies above the maximum of the Alfvén continuum.

The GAE dispersion relation, $\omega_{\text{A}} = k_\parallel v_{\text{A}}$, offers an efficient way to identify the modes, such as at NSTX [590], especially if the GAE frequency signal peaks overlap with each other, and their poloidal and toroidal numbers are known. Indeed, GAE modes with different (m, n) mode number pairs not only have different frequencies but they also have distinguishable temporal frequency patterns which was confirmed by direct comparison with the Alfvén wave dispersion relation [599].

Estimates of the GAE growth rate were made from the time-dependence of the frequency chirps and

compared with more traditional estimates based on the growth and decay rates of mode bursts [577, 600]. These estimates were found to agree well with numerical estimates by the HYM code. The frequency and mode number dependence of GAEs on the toroidal field and the EP distribution function has been documented in NSTX and NSTX-U [600].

In DIII-D, sub-cyclotron modes were originally identified as CAEs [579] but more recent analysis persuasively argues they were actually GAEs [601]. Recent experiments compared GAE theory and experiment at the stability threshold [591] and confirmed that the toroidal mode number of the unstable GAEs is $n \simeq 20$ [177].

A more accurate analytic evaluation of CAE and GAE growth rate drive in the sub-cyclotron frequency range was done recently with applications to spherical tokamak devices [602]. One important observation is that the addition of a small number of tangential NBI ions ($\sim 7\%$) stabilizes the counter-propagating GAE instability in NSTX-U [603], as observed experimentally [600, 604].

These modes observed in NSTX can exhibit EPM features [605], as was found numerically, a new and surprising result in GAE stability theory. EPMs will be treated in sections 6.7 and 7. The frequency of the most unstable GAEs changes significantly with beam parameters such as injection energy and injection geometry. It was demonstrated that such changes depend on the Alfvén velocity and are in qualitative agreement with the Doppler-shifted cyclotron resonances driving the modes. This unexpected result holds for counter-propagating GAEs, which are routinely excited in NSTX, and for high frequency co-propagating GAEs, which had not been previously studied. Large changes in frequency without clear corresponding changes in the mode structure are signatures of an EPM, referred to as EPM GAEs [605].

6.5.3. ICE-based diagnostics for burning plasma devices. As discussed in [573], EP-driven ICE has been detected in many fusion devices and is commonly identified with CAEs: compressional Alfvén waves can be excited by non-Maxwellian populations of energetic ions through cyclotron resonances [606]. New observations of ICE have been reported from JT-60U [179, 180], LHD [191, 192, 607], AUG [181–184], KSTAR [185, 186], NSTX and NSTX-U [187], DIII-D [177, 188], and EAST [189, 190]. EP-driven ICE in tokamak plasmas has been studied using either ICRF antennas [608] or dedicated RF probes [609]. Nevertheless, ICE detection is in principle possible using any technique for measuring electric, magnetic or density fluctuations with a sampling rate in the ion cyclotron range.

Density fluctuations can be observed using microwave reflectometry, which is planned for ITER [610] and has been used in NSTX to determine the structure of eigenmodes with frequencies up to several hundred kHz [470] and at DIII-D with frequencies up to ~ 40 MHz [611].

High time-resolution measurements of the ICE bursts on MAST [575], NSTX and NSTX-U have revealed that frequency-chirping can occur during the short bursts of ICE. The growth rate determined from the frequency chirping was in good agreement with the direct measurement of the edge magnetic fluctuation amplitude growth [612].

Simulations are crucial to gain understanding of the ICE phenomenon. Fully nonlinear simulations of ICE in the ion cyclotron range and in the presence of energetic ion populations approximating those in tokamaks and stellarators have been carried out using the fully kinetic particle-in-cell (PIC) code EPOCH [613] and also using the kinetic-MHD code PROMETHEUS++ in which bulk and energetic ions are kinetic whereas electrons are treated as a charge-neutralising fluid [614]. A limitation of the latter approach is that the waves cannot exchange energy with the electrons. However, PIC simulations typically show that in the nonlinearly saturated state only a small fraction of the energy lost from the energetic ion population is transferred to electrons [615] while a substantial fraction is transferred to bulk ions [613, 615]. For this reason the excitation of ICE is one of several possible means of channeling the energy of fusion alphas directly into bulk ions rather than via electrons, thereby providing the possibility of sustaining the hot ion condition required for the thermonuclear fusion burn more effectively [616]. This idea for direct ion heating is sometimes called "alpha channeling", which we will discuss in section 10.

A key result from the kinetic-MHD simulations of ICE reported in [614] is that the nonlinearly-saturated ICE intensity (as measured by the square of the perturbed magnetic field component parallel to the equilibrium field $\delta B_\parallel$) was found to be proportional to the energetic ion concentration. This scaling reproduces a linear dependence of ICE intensity on neutron flux over six orders of magnitude observed in JET [608], which indicates that ICE in future burning plasma devices could be used to obtain diagnostic information on the fusion alpha distribution.

Another conclusion of the PIC and kinetic-MHD studies of ICE is that nonlinear wave-wave interaction plays an essential role in the excitation of emission at lower ion cyclotron harmonics which are often found to be linearly stable. The three-wave interactions underlying these nonlinear excitation processes in the simulations can be studied using bicoherence analysis,

51

as discussed for example in [613].

Most likely, ICE will be observed in ITER through the detection of magnetic fluctuations, as in the majority of contemporary experiments. Furthermore, ITER will have an ICRF heating system [135], and it has been demonstrated on JET that ICRF systems can be used to detect ICE either passively (during periods in which ICRF heating is not used [608]) or actively (during ICRF heating). In the latter case, detection was made possible in JET through the use of a sub-harmonic arc detection system [615]. The RF signals were sampled in the ICRF antenna transmission lines, which acted as resonators. The frequency response of these resonators depended on the antenna configuration and the length of the transmission line matching elements. As a result, the measured ICE spectra were strongly filtered, limiting the information that could be obtained. More complete spectra have been obtained using ICRF antennas in receiver mode (i.e. passively) [608] and it would be worth considering this option in the DT operation phase of ITER.

6.6. Low frequency modes: BAEs, BAAEs, LFAMs, EGAMs

6.6.1. BAEs. In recent years, much attention was given to low-frequency modes in the BAE and BAAE regime. BAEs have been widely observed in present tokamaks. The excitation of BAEs is affected by both the energetic and thermal ion populations as well as coupling between the Alfvénic and ballooning mode branches [438, 617]. The BAEs can be divided into the three groups i-BAEs, e-BAEs and m-BAEs, depending on different energy sources. The letters 'i', 'e' and 'm' refer to mode instability drive by energetic ions, by energetic electrons and by magnetic islands, respectively.

The i-BAEs were first confirmed on DIII-D operated near the beta limit [437] and proved to be deleterious, causing large losses of EPs at levels similar to TAEs. The mode frequencies are approximately half the TAE frequency and display long-living or quickly-chirping behavior, depending on the plasma scenario. The i-BAEs are always localized in the core region. The mode structures have been measured by ECEI diagnostic at AUG, as shown in figure 34. The 2D imaging suggests that the mode numbers are either $m/n = 4/2$ or $2/1$. The modes move radially outward, following the outward moving $q = 2$ surface. Such a localized mode structure can also be observed by the microwave reflectometer on HL-2A [618]. Linear excitation threshold analysis of BAEs based on observations at Tore Supra indicates that ion Landau damping is important for the mode in the acoustic frequency range. The BAEs will be driven unstable only when EP-drive exceeds ion

Landau damping [619]. A major study of BAE stability in DIII-D found that the observed mode frequencies are usually close to analytic estimates of the BAE accumulation point, that the modes occur in bursts with rapid frequency chirping, and that BAEs are most likely to be unstable when the poloidal beta exceeds 0.5 [620]. A DIII-D study of isotope dependence found that, with deuterium NBIs, BAEs are at least as unstable in mixed hydrogen-deuterium plasmas as in deuterium plasmas; however, with hydrogen NBIs, BAEs are stable [621]. In HL-2A, modes were more readily excited in low-density plasmas [618] but the density dependence is relatively weak in DIII-D.

The e-BAEs were first observed on HL-2A [622]. They can be excited in both Ohmic and ECRF-heated plasmas with low densities (figure 35). Since these modes appear in plasmas with low ion temperatures, the mode frequencies are always lower than for i-BAEs and range from 10 to 30 kHz. The e-BAEs are driven unstable by barely circulating or deeply trapped particles. The mode characteristics are affected not only by the population of the energetic electrons, but also by their energies and pitch angles. Theoretical analysis further indicates that the frequency and growth rate are sensitive to the energetic electron temperature, and there exists a maximum growth rate [623]. Moreover, the growth rates, the mode width and its radial asymmetry can be affected by the energetic electron density [456].

The BAEs occuring in the presence of magnetic islands (m-BAE) were first reported on FTU [624] and subsequently found on HL-2A [625] and EAST [626]. The m-BAE is a mode formed when counter-propagating Alfvén waves form a standing-wave structure within a magnetic island [627]. The m-BAEs can be driven only when the magnetic islands width exceeds a threshold, and then they appear in pairs. Two m-BAEs usually propagate in different diamagnetic drift directions, and their mode numbers are $m/n = 2/1$ and -2/-1 for modes propagating in ion or electron diamagnetic drift directions.

The BAE dispersion relation and the related global modes as obtained by kinetic models [26, 435, 438, 453, 541, 629–633] could be clearly linked to experimental observations [453, 460, 467, 620, 633–636]. Alternative interpretations as Alfvén-acoustic modes [450] seem less likely, given that a clear relation to rational surfaces is observed experimentally [467, 620, 636], and that all branches with predominantly acoustic or mixed Alfvén-acoustic polarisation are generally very strongly ion Landau-damped, as demonstrated in direct MHD-gyrokinetic comparisons [637].
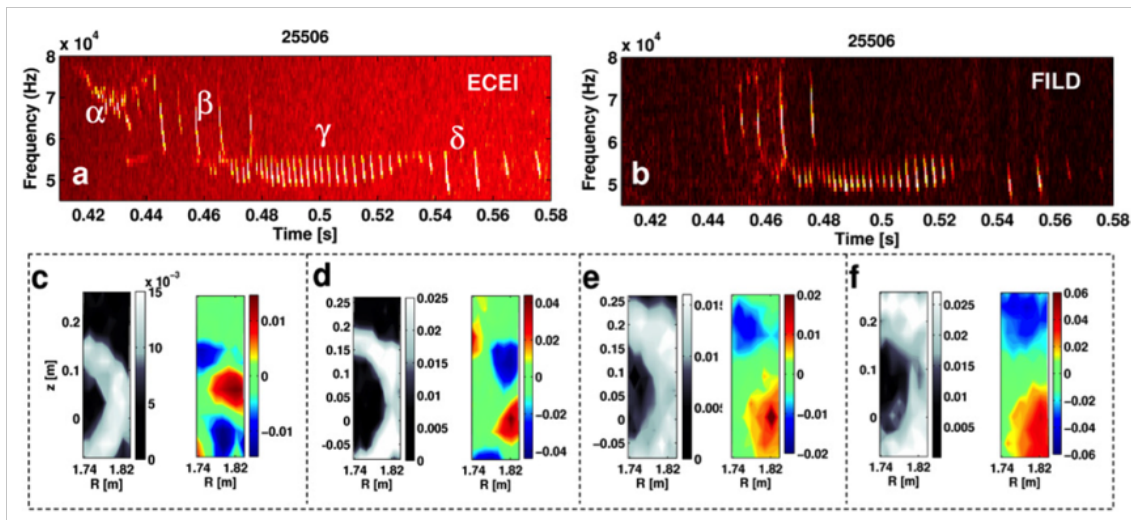
52

Figure 34. ECEI spectrogram showing the bursting BAE modes associated with the $q = 2$ surface on AUG. (b) These modes are also observed by the FILD. Figures (c)-(f) show the 2D mode structures of the selected modes α–δ, respectively (in pairs of left the amplitude A and right $A\cos(\Phi)$). Modes α and β are 4/2 modes, modes γ and δ are 2/1 modes. The modes are observed to move radially outward with time. Reproduced from [467].
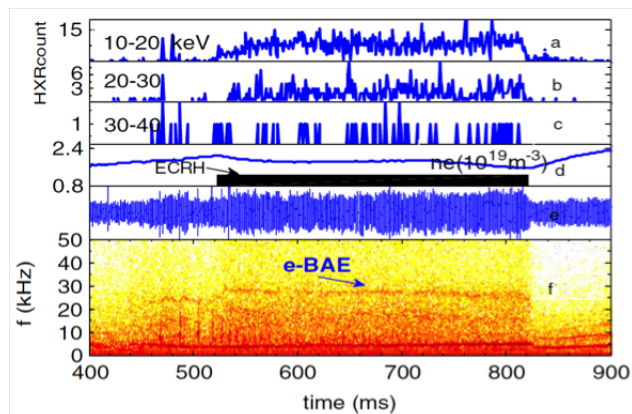

Figure 35. An e-BAE observed on HL-2A. (a)–(c) Counts of HXR photons in different energy ranges, (d) central line-averaged density, (e) magnetic probe signal, (f) spectrogram of magnetic probe signal. Reproduced from [622].

6.6.2. BAAEs and LFAMs. As for the BAE frequency range, it has been recognised [29, 638] that kinetic theory is needed to describe modes in the BAAE frequency regime, because the mode frequencies become comparable to diamagnetic frequencies, and ion Landau damping is very effective. Modes with frequencies below the BAE frequency are observed on DIII-D and NSTX [628, 638] and have been initially dubbed BAAEs. However, experiments at ASDEX-Upgrade [453, 460, 467, 635] and DIII-D [628] show a clear connection of the observed instabilities to the evolution of rational surfaces, which contradicts the interpretation as Alfvén-acoustic gap modes. Accordingly, these modes were dubbed low-frequency

Alfvén modes (LFAMs). Figure 36 shows a typical example of LFAMs on DIII-D [628]. LFAMs appear in ascending patterns in plasmas with EPs and high electron temperature but modest beta. The mode frequencies are in the diamagnetic frequency range, and the toroidal mode numbers are in the range $n = 3 - 12$. The mode occurrence is correlated with rational values of the safety factor q. The gyrokinetic dispersion relation [438, 453, 456, 639] was successfully applied to interpret the experimental frequency and mode number patterns of LFAMs and their connection to the kinetic ballooning branch [29, 448, 460, 639]. Extensions including the trapped particle response [446] are needed for accurate quantitative analyses. The excitation mechanisms were further investigated [448, 461, 639–641], demonstrating that EPs are not necessary to destabilise LFAMs (as reported in DIII-D experiments [628]), i.e. the drive can be provided by the thermal background pressure gradients ($\sim \omega_{*i}$). The modes exhibit a predominantly Alfvénic polarisation, are favoured by high T_e and can have a reactive character. LFAMs are often observed at low β [628], which can be understood from the coupling of Alfvénic, diamagnetic and acoustic branches [29, 446, 448]. The same type of analysis also demonstrates that for increasing β the BAE branch is favoured over the LFAM branch which leads to the conclusion that no strong EP transport is expected from LFAMs under reactor-relevant conditions. Modes with similar properties, but at higher thermal ion beta and ω_{*i} than in DIII-D, have been recently reported at JET [555]. Additionally, modes between the BAE and TAE frequencies at JET have been interpreted as global
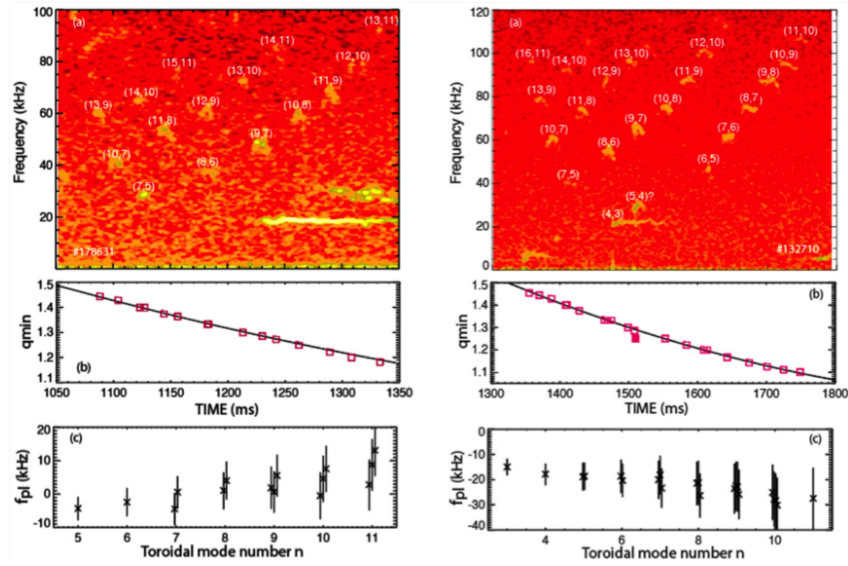
Figure 36. LFAMs during discharges #178631 (left) and #132710 (right): (*a*) ECE spectrum from channels near $q_{\min}$ on the reference discharge, each mode is labeled by the (m, n) value (*b*) $q_{\min}$ from the equilibrium reconstructions (line) and fitted rational q values m/n (symbols) vs time. (*c*) Inferred frequency in the plasma frame $f_{\text{lab}} - nf_{\text{rot}}$ vs fitted toroidal mode number. Reproduced from [628].

perturbations within higher-order geodesic Alfvén-acoustic gaps [447].

Due to different interpretations as BAAEs or LFAMs in the literature, simulated mode properties need to be carefully analysed when comparing to the experiment. However, for most typical experimental conditions, the BAAE branch is always more stable than the LFAM/KBM branch [639]. Recent global gyrokinetic simulations [641] find that the LFAM mode structure and many of its parametric dependencies are consistent with the theoretical analyses and the experimental observations: the linear growth rate increases rapidly with increasing electron temperature; the LFAM can be excited without EPs and has a frequency in the BAAE gap; an antenna scan confirms that it is not the conventional BAAE. Instead, the LFAM is an interchange-like electromagnetic mode excited by non-resonant drive of pressure gradients. Trapped electrons and equilibrium current have modest effects on the LFAM [641]. Recent polarisation measurements on DIII-D show that LFAMs exhibit a fast changing mixed Alfvén-acoustic polarisation during their lifetime, indicating that LFAMs indeed consist of a mainly Alfvénic component and electrostatic sidebands. While the location of the rational surface evolves, the measurements pick up a rapidly varying mix of electrostatic and electromagnetic components [475].

In the BAE/BAAE frequency range, there are two other instabilities, i.e. kinetic ballooning modes (KBM - typically at high n) due to finite diamagnetic drifts [642] and Alfvénic ion temperature gradient (AITG)

modes due to kinetic thermal ion compressibility and wave-particle resonance [643, 644]. The AITG mode, a new branch connecting KBM and BAE modes, was first experimentally identified in Ohmic plasmas on HL-2A [32], see figure 37. These modes appear in plasmas with peaked density profiles and weak magnetic shear, which indicates that corresponding instabilities are excited by pressure gradients. The time trace of the fluctuation spectrogram is either a frequency staircase with different modes excited at different times, or multiple modes may simultaneously coexist. AITG-like modes that trigger disruptions are also observed in high ion temperature (> 10 keV) plasmas [645].
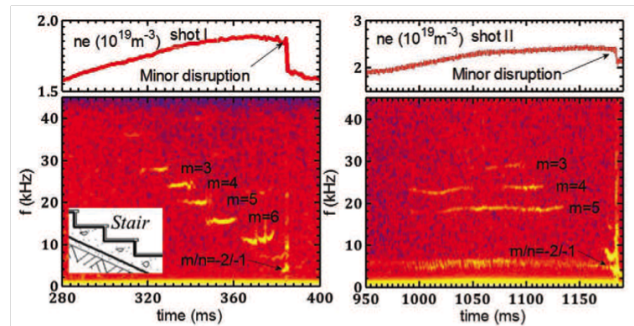

Figure 37. AITG modes with different mode numbers in an Ohmic plasma at HL-2A. The 2D patterns are spectrograms of ECEI (left) and SXR (right) signals. Left: with the frequency staircase. Right: with the multi-mode coexistence. Reproduced from [32].

6.6.3. EGAMs. EGAMs are similar to the standard GAMs [440], and as for standard GAMs, their existence is based on the geodesic curvature of the magnetic field lines. The main difference with respect to the standard GAMs is that they are driven by the EP population and therefore the EGAM frequency and radial structure depend on the EP distribution. EGAMs have been described analytically [427, 646–657] and have been observed on DIII-D [658–660], LHD [661–663], HL-2A [664, 665] and AUG [666, 667]. Similar modes were also observed on JET as global geodesic acoustic modes (GGAMs) [668, 669]. EGAMs have also been studied in a series of numerical gyrokinetic simulations using GYSELA [649, 670–672], ORB5 [650, 673, 674] GENE [675] and GTC [676], as well as in kinetic-MHD simulations using MEGA [334, 534].

EGAMs are axisymmetric oscillations ($n = 0$) of the electrostatic potential, density, pressure and magnetic perturbations. The latter have been measured, for example, at LHD [663], HL-2A [664], DIII-D [660] and AUG [666]. Their location, mode structure and non-linear mode structure evolution has been measured by SXR e.g. in HL-2A [664] and AUG [666]. The electrostatic potential is dominated by a zonal structure ($m = 0$), the density and pressure exhibit a poloidally up-down asymmetric structure (with $m = 1$), as illustrated in figure 38, and the magnetic perturbation is characterized by $m = 2$ structure. The expected $m = 1$ structure of the density was imaged in [677], the potential in [663], and the radially broad E_r structure was measured in [660].

confinement [670, 671]. Theoretical analysis reveals that EGAMs can be regarded as a potential energy channel to transfer the fusion-born alpha energy to the thermonuclear plasma, referred to as GAM channeling [648]. Such effects will be discussed in section 9. EGAMs are in some cases accompanied by strong bursting and frequency chirping. Also, significant density perturbations and large drops in neutron emission can be observed in the presence of EGAMs [658, 659], which suggests EP losses, as corroborated by modeling [659, 672].
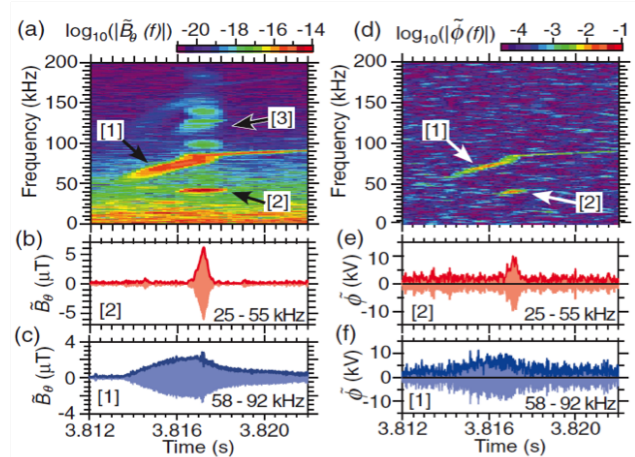
Figure 39. EGAM observed on LHD: spectrograms of (a) magnetic field fluctuations and (b) electric potential fluctuations; waveforms extracted by bandpass filters with a passband of $25 - 55$ kHz [(b), (e)] and $58 - 92$ kHz [(c), (f)], respectively. The bold curves show the envelopes. Reproduced from [648].

Since EGAMs are axisymmetric, they are linearly driven by positive gradients in velocity space. The EGAM linear dispersion relation $\mathcal{D}(\Omega) = 0$ has been derived in several works making various assumptions for the equilibrium distribution function of EPs. For instance, in a kinetic-MHD approach the thermal plasma is modelled as a fluid, and the response of EPs is computed using the perturbed distribution function obtained from the drift kinetic equation [427, 647].

A kinetic approach for both the thermal plasma and the EPs [649–651] can explain the existence of two types of EGAMs, as illustrated in figure 40, where the zeros of the dispersion relation are represented in the complex plane. Solving the kinetic dispersion relation of the standard GAM (without EPs) results in a branch of highly Landau damped modes ($\mathrm{Im}(\omega) < 0$) and in a mode marginally stable ($\mathrm{Im}(\omega) \approx 0$), which is the so-called GAM. When EPs are introduced, the distribution of zeros in the complex plane is modified. Depending on the conditions of the plasma (safety factor, energy and mass of EPs) the driven mode can originate either from the standard GAM (top panel of figure 40) or from the Landau branch (bottom panel
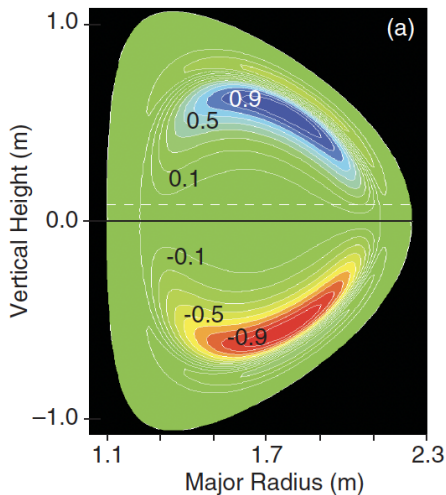

Figure 38. Calculated $m = 1$ poloidal structure of a DIII-D EGAM. Reproduced from [658].

EGAMs on LHD have been found to contribute to nonlinear destabilization of a subcritical mode (figure 39). Moreover, the EGAMs may couple with turbulence and significantly degrade the plasma

of figure 40). In the figure, the thick black solid lines with arrows represent the evolution of the excited mode when the density of EPs is increased. The dashed lines represent the evolution of a secondary mode getting closer to marginal stability. These two types of EGAM were found in gyrokinetic simulations using the ORB5 [650] and the GYSELA [672] codes, which were in very good quantitative agreement. Moreover, using a kinetic approach, other branches can be found depending on the resonance between characteristic EP frequencies and the mode, e.g. due to the resonance between EPs and the magnetic drift frequency [653]

$$\omega_{\mathrm{d}} = k_{\mathrm{GAM}} \left(R \omega_{\mathrm{ci}} \right)^{-1} \left(v_\parallel^2 + v_\perp^2/2 \right) \sin\theta, \qquad (66)$$

with k_{GAM} the GAM radial wavenumber, R the major radius, ω_{ci} the ion cyclotron frequency and θ the poloidal angle.

Finally, in a fluid approach [652], the EPs are modelled by a distribution with a narrow width in energy, leading to the excitation of a reactive branch. Since the frequency is determined by EP kinetic effects, the EGAM is qualitatively different from the pure MHD mode GGAM observed in JET [646, 669]. The radial structure is determined by the EP drift orbit width [427, 647]. The effect of the elongation of the plasma on the linear excitation of EGAMs has been studied in a joint investigation with GENE and ORB5 [675].
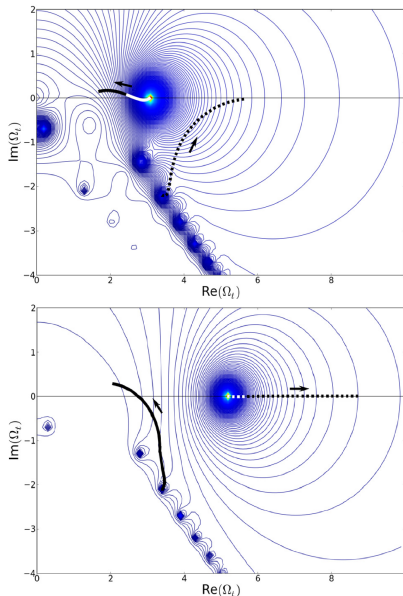

Figure 40. Evolution of the zeros of the dispersion relation (represented by thick black solid lines) in the complex plane for an increasing EP density. The top panel corresponds to the case where the EGAM is excited from the standard GAM and the bottom panel corresponds to the case where the EGAM is excited from the Landau branch. Reproduced from [651].

The linear excitation of EGAMs has been extensively studied in numerical simulations in different frameworks. Depending on the framework, different strategies can be employed to model EPs. In full-F global gyrokinetic simulations like GYSELA [678] or ORB5 [679], an initial value problem can be solved. In that case, EPs are initialized using a distribution function which depends on the motion invariants [649, 650, 672, 673]. Alternatively, an external source can be used to force the distribution function to be as close as possible to a distribution required to excite EGAMs [670, 671], which is useful to excite EGAMs in the presence of turbulence. On the other hand, one can use δF codes such as GENE [680], where an equilibrium distribution function is imposed and does not evolve.

6.7. Linear stability of EPMs

The frequencies and eigenfunctions of the EP-driven AEs discussed so far are determined by the bulk plasma, almost unaffected by the presence of EPs, but the EPs usually provide the drive through gradients in the distribution function. These EP-driven AEs are usually described by a perturbative approach. New types of modes, the energetic particles modes (EPMs) appear when the EP pressure is similar to the bulk plasma pressure, such that the EPs significantly influence the dielectric response of the plasma. The EPs then affect the very existence of the mode and not just the mode growth rate. To describe EPMs, for example fishbones, we need the more sophisticated non-perturbative approach [480]. Due to the larger EP pressure, the EP drive is often strong enough to overcome continuum damping, and so EPMs can exist at frequencies in the Alfvén continuum, and their frequencies and drive depends strongly on EP distribution. The frequencies of EPMs are those maximizing the power transfer of the interaction between the EPs and the wave and are often given by the characteristic EP drift orbit frequencies discussed in section 2.

One of the technical difficulties, associated with the EPMs requiring a non-perturbative approach, is that their spatial structure and frequency can change significantly and rapidly in the nonlinear phase of the instability. Rapidly changing mode frequency on short timescales relative to the timescales for changes to equilibrium parameters, often on the order of milliseconds, is referred to as chirping.

Chirping events are routinely observed [681, 682], and their salient features have been reproduced qualitatively using theoretical models [683–687]. EPMs can be driven by runaway electrons [688] as well as fast ions. A quantitative understanding of experiments requires detailed numerical modeling which is challeng-

ing but should be a feasible task to be discussed in section 7.

Experimental studies of the stability of EPMs range from parametric studies of the presence of chirping modes (e.g., [681]), direct measurements of mode growth rates based on growth and decay rates of bursting modes (e.g., [612]), and indirect measures of mode growth rates (e.g., [578]) based on theoretical frequency-chirping rates [683,684]. Finally, theoretical predictions of methods to reduce the size of mode bursts and frequency chirps by scattering resonant particles have been tested experimentally [689–692].

Estimates of growth rates based on the frequency chirping of EP-driven instabilities and their related EPM branches have been made for TAEs [693–695], GAEs [578], and ICE [612]. The correlation of mode amplitude and chirping rate has been studied on START, MAST and NSTX [687, 693, 696]. The parameter dependence of chirping TAEs has been characterized on NSTX [693]. The TAE instability is excited by the free energy in the EP distribution present in gradients in radius or energy. Flattening the EP distribution, e.g., by off-axis NBI, is often considered a method to suppress TAEs. However, experiments have found that far off-axis co-current NBI, that is when creating a hollow EP profile, can destabilize counter-propagating TAEs [697,698].

Similarly, on AUG, off-axis NBI heating without any central NBI heating leads to a hollow EP profile with large ratios of $\beta_{\mathrm{NBI}}/\beta_{\mathrm{th}} \sim 1$ and $\mathcal{E}_{\mathrm{NBI}}/T_{\mathrm{i,e}} \sim 100$. In this regime, nonlinear coupling signatures between co- and counter-propagating AEs and their corresponding EPM branches have been observed in the ramp-up and flat-top phases, as well as the coupling of zonal modes (EGAMs) and AEs/EPMs [666, 667, 699, 700]. Linear and nonlinear modeling and code validation efforts are ongoing [554, 674, 701, 702].

6.8. Impact of anisotropy and toroidal flows

The introduction of auxiliary heating in tokamak plasmas can introduce toroidal and poloidal flows and pressure anisotropy as well as change the magnetic configuration. In this subsection, we discuss how these effects can change the linear MHD stability of the plasma. Since NBI and ICRF heating generate highly anisotropic EP distribution function with a kinetic EP pressure comparable to the bulk plasma pressure, the total plasma pressure can become anisotropic. NBI heating in MAST can cause anisotropy up to $p_\perp/p_\parallel = 1.7$ [704], and ICRF heating in JET can cause anisotropy up to $p_\perp/p_\parallel = 2.5$ [705], where $p_\parallel$ and $p_\perp$ are the parallel and perpendicular pressures. At AUG, the anisotropy was inferred to be $p_\perp/p_\parallel = 1.2$ in an NBI heated plasma based on velocity-space

tomography [706]. However, most MHD equilibrium codes do not account for anisotropy and solve the usual static isotropic Grad-Shafranov equation. MHD equilibria with anisotropy and flows are described by the generalised Grad-Shafranov equation, written as (e.g. [707] and references therein)

$$\nabla \cdot \frac{(1-\Delta)\nabla\psi}{R^2} = -\frac{F(\psi)F'(\psi)}{(1-\Delta)R^2} - \mu_0\rho$$

$$\times \left[k_B T'_\parallel(\psi) + H'(\psi) + R^2\Omega(\psi)\Omega'(\psi) - \left(\frac{\partial W}{\partial \psi}\right)_{\rho,B} \right]$$

(67)

where five constraints are used: $F(\psi)$, $\Omega(\psi)$, $H(\psi)$, $T_\parallel(\psi)$, and $\Theta(\psi)$. Here, the anisotropy is reflected in the flux function $\Theta(\psi) = B(1/T_\parallel - 1/T_\perp)$, where $T_\parallel$ and $T_\perp$ the parallel and perpendicular temperatures of a plasma with a bi-Maxwellian velocity distribution function [708].

Several studies have examined the impact of anisotropy and flows on the plasma equilibrium (for an analytic approach, see [709]). For MAST equilibria, the $J_\parallel$ contribution can reach 20% of the total current for $p_\parallel/p_\perp = 1.5$ [703]. This is significant as it results in a 10% change in the current profile and consequently the q-profile, which influences the plasma stability. Figure 41 shows the differences in the equilibrium reconstruction using the EFIT TENSOR code for MAST.

EFIT TENSOR [710] solves the generalised Grad-Shafranov equation, equation (67) using magnetic and kinetic constraints. The unique solution to the generalized Grad-Shafranov equation is determined by the plasma boundary contour $C_A(R, Z)$ and the profiles of the flux functions $\{F(\psi), \Omega(\psi), H(\psi), T_\parallel(\psi), \Theta(\psi)\}$. A recent study examined the impact of toroidal flow and anisotropy for the same magnetic configuration (q-profile) and plasma stored energy [707] using the fixed boundary solver HELENA+ATF [703]. As the anisotropy is varied for a constant q-profile, the most striking observation of the equilibrium profiles are that contours of constant $p_\perp, p_\parallel$ and ρ shift outboard of the magnetic axis for $T_\perp > T_\parallel$ and inboard of the magnetic axis for $T_\perp < T_\parallel$. Figure 42 shows this shift as a function of $\Theta = 1 - T_\parallel/T_\perp$.

A recent study [711] extends pressure anisotropy and toroidal flow equilibrium models to include the EP orbit width. An equilibrium model with q-solver constraint enabled a wider systematic study of the parametric dependencies for the same q-profile. The addition of finite orbit width effects reduces the shift in magnetic axis, reducing the change in the TAE gap frequency from the centre of the gap, reducing continuum damping and thereby destabilising the TAE.

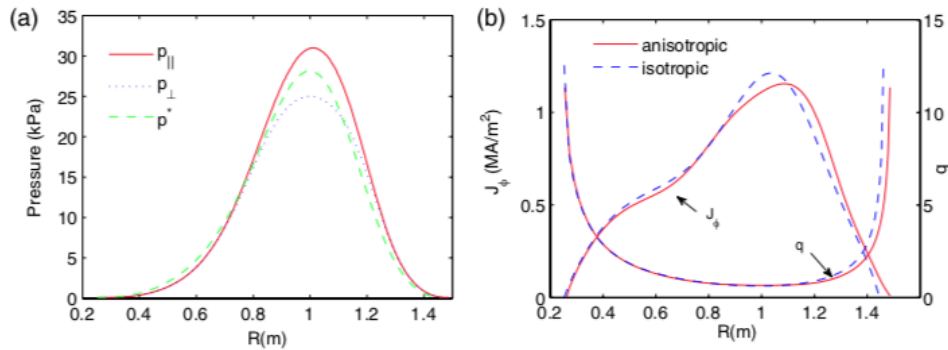The impact of pressure anisotropy can be

Figure 41. (a) Pressures on the mid-plane in the anisotropic reconstruction (two pressures, shown with the solid and dashed–dotted lines) and in the isotropic reconstruction ($p*$, shown with the dotted line) for MAST discharge #18696 at 290ms. (b) The reconstructed J_ϕ profile and q-profile on the mid-plane. Reproduced from [703].
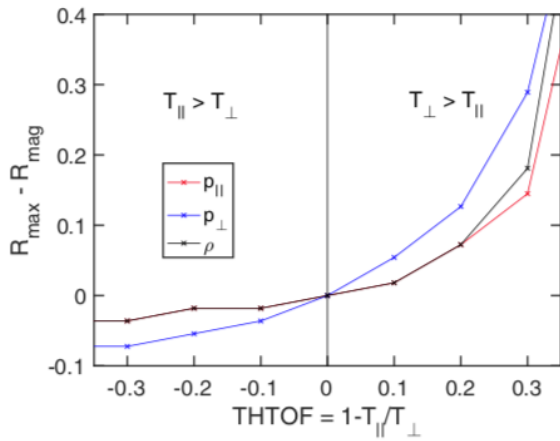

Figure 42. Calculation of the displacement of peaks in density ρ, parallel pressure $p_\parallel$ and perpendicular pressure $p_\perp$ in MAST from the magnetic axis as a function of $\Theta = 1 - T_\parallel/T_\perp$. Reproduced from [707].

investigated using kinetic energy principles [712] [713]. Chew, Goldberger and Low (CGL) [714] introduced the now widespread form of the pressure tensor and derived the double-adiabatic CGL closure. The corresponding energy principle was later derived and studied [712, 715, 716]. CGL ignores the heat flow when the mode frequency is comparable to or smaller than the particle streaming frequency, especially in the vicinity of marginal stability boundary [717]. Alternative fluid closures without this drawback are, e.g., the double polytropic closure, a higher-order-momentum closure, and, recently, the single adiabatic closure [710] which produces the same result as MHD for an isotropic equilibrium.

MHD linear stability was computed [707] using MISHKA-AD [713], which uses the CGL closure and the single adiabatic closure [710]. As the q-profile remains unchanged, the shear Alfvén continuum, the gap modes and the gap frequencies remain largely

unchanged. However, the compressional continuum changes significantly. Figure 43 illustrates this change by plotting the continuum for $T_\parallel/T_\perp = 0.8, 1.2$.

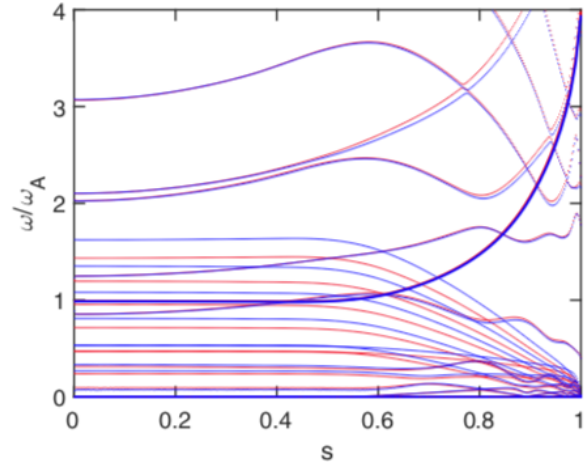**Figure 43.** Compressional Alfvéen continuum for $n = 1$ with $T_\parallel/T_\perp = 0.8$ (blue) and $T_\parallel/T_\perp = 1.2$ (red). Reproduced from [707].

The equilibrium and stability of $n = 1$ TAE modes in MAST were computed using EFIT-TENSOR and MISHKA-AD [718], and here substantial changes in the equilibrium compared to the isotropic EFIT were found, and consequently the stability was significantly affected. The anisotropic solution had a q-profile with reversed shear, the $n = 1$ shear Alfvén continuum gap opening near the core, and the core safety factor lowering, resulting in a broader TAE mode. Mode drive was computed the wave-particle interaction code HAGIS [569]. The resonant regions of phase space were significantly modified between the isotropic and anisotropic cases. The anisotropic $l = 1$ bounce resonance shifted radially inward for given particle energy relative to the isotropic case. The linear growth rate in the anisotropic case was 35% larger than in

the isotropic case (see figure 44), and the saturation amplitude in the anisotropic case was 18% smaller than in the isotropic case. The linear growth rate was larger in the anisotropic case because the radial gradient of the distribution function at resonance was larger. The saturation amplitude in the anisotropic case was slightly smaller, despite the larger linear growth rate. This may be caused by the differences in the safety factor and magnetic shear affecting the nonlinear bounce frequency.
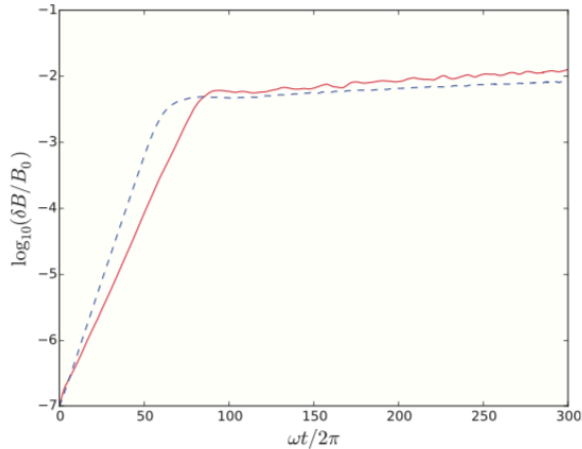

Figure 44. Wave amplitude $\delta B/B_0$ for the isotropic (red solid line) and anisotropic (blue dashed line) cases. Reproduced from [718].

Recently, the impact of anisotropy on the stability of infernal modes, driven when $q \approx 1$ over a wide region, was studied [719]. Infernal instabilities are instabilities in plasmas with weak shear, such that bands of unstable n-values can form, even when standard ballooning theory predicts stability. The guiding centre plasma motion was described by fluid equations, whereas the motion parallel to the magnetic field was described by a collisionless kinematic equation. In this model, the plasma anisotropy enters through a modification to the magnetic well, yielding better stability for tangential injection. A stability criterion for the linear stability of plasma equilibria with incompressible flow parallel to the magnetic field, constant mass density and constant $\sigma_d = \mu_0(P_\parallel - P_\perp)/B^2$ can be found in [720].

In all cases studied, the change in equilibrium affects the change in plasma stability. In ITER, strong flows or anisotropy are not anticipated to have a significant effect on the equilibrium reconstruction, and uncertainty in the experimental inputs to the equilibrium reconstruction will likely predominate. Nevertheless, such effects may play a role in other burning plasma devices.

7. Nonlinear mode evolution, theory and simulation

This section describes progress made in the field of nonlinear EP physics since the topical review in the Progress of the ITER Physics Basis [20]. The build-up of the EP population in fusion plasmas is typically slow compared to the growth times of EP-driven instabilities. This scale separation suggests that we need nonlinear studies of unstable waves in the near-threshold regimes. We need to characterize the long-time behavior of the waves and resonant particles in the presence of particle sources and sinks. In some observations of EP-driven instabilities and EPMs, the unstable modes grow to a level at which they enhance transport and cause anomalous losses of the EPs. In other observations, the losses are small, but the modes exhibit an complex nonlinear behavior, such as the generation of sidebands, quasi-periodic bursts, or changing mode frequencies. The fishbone instability exhibits such features, which we will describe in the following subsection 7.1. This section presents a first-principles physics basis for modeling these phenomena as well as reduced models.

As explained in section 2, the resonance condition for interaction of EPs with AEs in a tokamak is

$$\omega - n\omega_\phi(\mathcal{E}, \mu, P_\phi) - l\omega_\theta(\mathcal{E}, \mu, P_\phi) = 0. \tag{68}$$

Here we state the arguments of the toroidal and poloidal frequencies $\omega_\phi(\mathcal{E}, \mu, P_\phi)$ and $\omega_\theta(\mathcal{E}, \mu, P_\phi)$ of the unperturbed ion motion explicitly to highlight that equation (68) selects a surface in the 3D phase space $(\mathcal{E}, \mu, P_\phi)$. A single resonance in $(\mathcal{E}, \mu, P_\phi)$ thus covers a relatively thin region of phase space, and it causes transport only across this thin surface, which can flatten the distribution function only locally. But when the phase space is covered by overlapping resonances, there can be a significant transport of particles via stochastic diffusion [721].

The nonlinear simulation of EP-driven modes remains a significant challenge for future devices. In these systems it is expected that a dominant component of alpha particle transport will be driven by interactions with various instabilities rather than classical orbit losses. There are several issues that make modeling the fusion reactor regime difficult. These include the large timescale separation between the instabilities (on the order of microseconds) and the alpha slowing-down times (on the order of a second). Next, disparate spatial scales are involved ranging from the ion gyroradius, (on the order of 0.01 meter) to the device size, (on the order of several meters). Finally, there are no existing experiments that operate in the reactor parameter regime, so there is no possibility for model validation until DT operations in ITER or elsewhere.

59

These challenges have resulted in a variety of approaches, ranging from global full-f gyrokinetic, fluid-kinetic, gyrofluid, quasilinear, as well as various semi-analytic approaches. Some of the physics issues that must be addressed include: mode-coupling (wave-wave) nonlinearities vs. wave-particle nonlinearities, global vs. local (flux tube), interaction of alpha particles with both Alfvén instabilities and core microturbulence, inclusion of multiple fast ion species (beams, ICRF, alphas), roles of zonal flows and currents, perturbative quasilinear vs. non-perturbative nonlinear, collisionless vs. collisional, absence vs. presence of external sources and sinks, and linear critical gradient profiles vs. nonlinearly flattened profiles. Currently, there is no single approach that includes all known relevant effects and is sufficiently computationally efficient and robust to run for even a small fraction of an alpha slowing down time. All of them involve some degree of simplification, but each tries to address at least some of the above challenges in ways that should be complementary to the others.

In this section some of the nonlinear simulation models currently in use will be reviewed. We will start with a description of fishbones, which is a prominent example of an instability requiring a nonlinear description. We will then progress from gyrokinetic theory and simulations, which is the most fundamental description, to reduced descriptions requiring an increasing amount of modeling. We will review nonlinear gyrokinetic theory of wave-particle and wave-wave interaction, discuss progress in nonlinear gyrokinetic simulation, nonlinear kinetic-MHD simulations, gyrofluid model simulations, and nonlinear simulations with reduced models. Development is continuing, and it is expected that increasingly comprehensive and sophisticated simulations will be available by the time of ITER DT.

7.1. Fishbones

Historically, the so-called fishbone was the first EPM observed experimentally. It was discovered in experiments with NBI heating on the PDX tokamak [722] and then found in most tokamaks with EP populations (either ions or electrons). Figure 45 shows how this perturbation appears on a Mirnov coil measurement; the similarity to a fish skeleton for multiple bursts resulted in the name "fishbones". Such bursts can enhance EP losses [22, 722, 723], as also observed for fusion alphas in the recent DT experiments and JET [47], and deteriorate the confinement of the thermal plasma via triggering kink modes and neoclassical tearing modes (see section 5) [576, 724–728].

Fishbones are an EPM that has the mode structure of an $(m/n) = (1/1)$ internal kink. They are
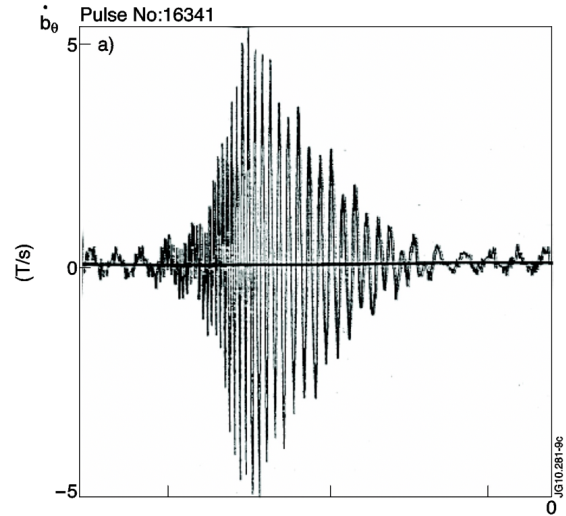

Figure 45. Oscillations of the perturbed magnetic field time derivative during a fishbone burst (JET discharge #16341). The gradual lengthening of the period associated with frequency chirping is visible to the eye. Reproduced from [28].

usually observed in a repetitive bursting cycle when the central safety factor $q(0)$ has fallen below unity when, in the absence of EPs, the MHD internal kink growth rate γ_{MHD} drives instability. As discussed in section 5.2 and [355], because the EP precession frequency is large compared to the MHD mode frequency, EPs on trapped-particle orbits stabilize the internal kink that triggers the sawtooth crash. However, when the EP population becomes too large, the EPs destabilize a new branch of the internal kink, the fishbone (figure 46a). In present-day tokamaks with so-called "hybrid" scenarios of improved performance [730], fishbones often appear when $q(0) \gtrsim 1$.

The fishbone bursts involve oscillations with a time-dependent frequency, as seen in figure 45. There are two kinds of internal-kink fishbone instability. The first are the so-called "precessional" fishbones [731] appearing when the mode frequency ω resonates with the bounce-averaged precession frequency of the trapped EPs, $\omega_{\phi,\text{tr}}$, and it is much greater than the thermal ion diamagnetic frequency, $\omega_{*\text{i}}$. The precessing EPs then destabilize the $(1/1)$ mode in the Alfvén continuum. At the onset of the fishbone pulse, the drive from the EPs is almost balanced by the continuum damping coming from two Alfvén resonances near the $q = 1$ surface: $\omega = \pm k_{\parallel}(r_A)v_A(r_A)$ (see section 6). To overcome strong continuum damping, the precessional fishbones require relatively high values of the EP pressure. The fluid nonlinearity at the Alfvén resonances tends to reduce the continuum damping. This is the dominant nonlinear effect at the onset of the fishbone pulse. It leads to an explosive
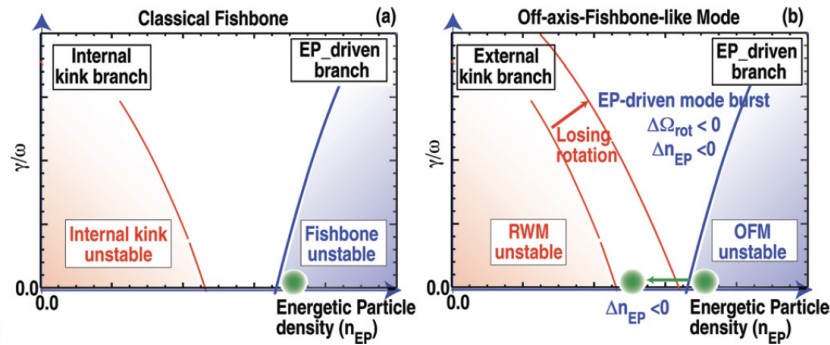
60

Figure 46. Schematic stability diagram for (a) classic fishbones and (b) off-axis fishbones. The abscissa is the EP density n_{EP} and the ordinate represents the MHD drive γ_{MHD} of the (a) internal kink or (b) resistive wall mode. Moderate EP density stabilizes the MHD-driven instability but, when n_{EP} grows too large, the fishbone EPM is destabilized. Reproduced from [729].

growth of the pulse so that the precessional fishbones follow a hard excitation scenario [732].

The second kind of fishbones are those with $\omega \approx \omega_{*\mathrm{i}}$ [733, 734]. This mode lies in a low-frequency gap in the shear Alfvén continuum and consequently is not damped by continuum damping. These fishbones are one of the two oscillatory kink modes stabilized by FLR effects. These modes are unstable within the framework of ideal MHD [735].

The explosive growth of the fishbone oscillations and the significant change of the oscillation frequency call for a systematic nonlinear description of fishbones with a self-consistent treatment of kinetic and MHD nonlinearities [732]. This is a challenging technical issue for numerical modeling. One of the difficulties here comes from the need to incorporate an accurate description of the narrow phase-space resonances into global MHD simulations. For linear problems, this difficulty is only a moderate obstacle since the resonant response of the system is insensitive to the width of the resonance and can be treated in terms of Landau damping. In contrast, nonlinear problems typically need much better resolution to calculate the resonant response appropriately, which is very demanding for the existing global codes. Several attempts have been made to address this issue. The full-geometry M3D and MEGA codes have both nonlinear MHD and nonlinear EPs [338, 736], but they still face the challenge of overcoming the resolution issue at the fluid resonance because of the unphysical numerical viscosity. This need is particularly evident for precessional fishbones. Nevertheless, simulations that reproduce many experimental features for internal-kink fishbones have been reported [737, 738]. Recently, gyrokinetic GTC simulation of a DIII-D plasma found that nonlinear saturation of the fishbone instability is dominated by self-generated zonal flows, which could induce the formation of an internal transport barriers in this experiment [739]. An additional open issue

for fishbones is quantitative modeling of recurrent pulses in the presence of EP sources and sinks. This problem is more demanding computationally than the description of a single fishbone pulse because of the multiple timescales that are involved. We expect future theoretical studies of fishbones to provide a more complete picture of the near-threshold regime for fishbones with an interplay between the kinetic and fluid nonlinearities.

A second type of EPM, known as "EP-driven wall mode (EWM)" or "off-axis fishbones", has many similarities to the "classic" internal-kink fishbone described above (figure 46b). In this case, the mode structure is an $(m/n) = (2/1)$ internal kink. The low-frequency mode that is stabilized by trapped EPs is the resistive wall mode (RWM) that was discussed in section 5.4. However, as with the classic fishbone, when the EP population becomes too large, a new higher-frequency branch appears at the trapped EP precession frequency, the off-axis fishbone [740, 741].

Off-axis fishbones occur in wall-stabilized plasmas with large normalized beta β_{N} (figure 47) in a regime associated with "advanced tokamak" operation in future devices. In ITER, they may be observed in a high β_{N} steady-state scenario that has a large trapped alpha population near the $q = 2$ surface.

Off-axis fishbones have been thoroughly characterized [743]. Like classic fishbones, they occur in repetitive bursts and chirp downward in frequency but, while the classic fishbone waveform retains approximately sinusoidal shape throughout the burst (figure 45), the waveform of the off-axis fishbone becomes highly distorted (figure 48). Both types of fishbones are driven by trapped EPs. Both classic fishbones [744] and off-axis fishbones [743] convectively expel trapped EPs in a concentrated "beacon" when the $\boldsymbol{E} \times \boldsymbol{B}$ phase of the oscillation pushes EPs radially outward. As expected for convective transport, EP losses scale linearly with mode amplitude for both [743, 745]. The non-
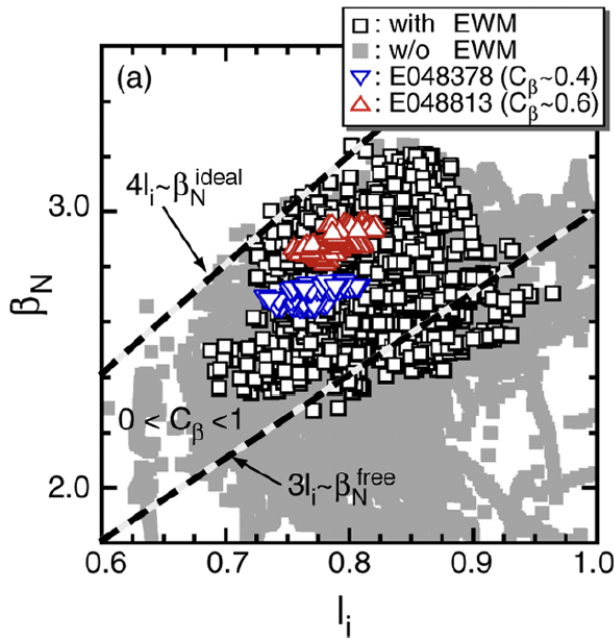
61

Figure 47. EWM stability domain vs. normalized beta and plasma inductance in JT-60U. The modes occur in the parameter space associated with resistive wall modes. Reproduced from [742].
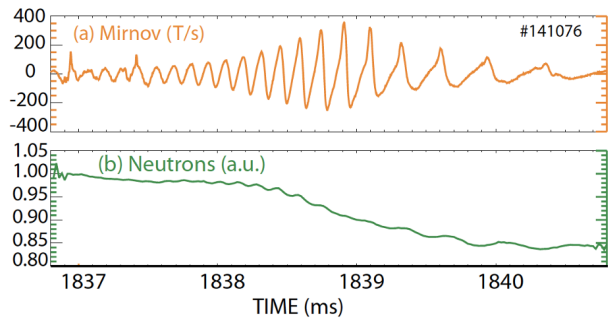

Figure 48. (a) Magnetic probe and (b) neutron signals during an off-axis fishbone in DIII-D. As with the classic fishbone of figure 45, the gradual lengthening of the period associated with frequency chirping is evident to the eye but, unlike the classic fishbone, the magnetic waveform becomes increasingly distorted by higher frequency harmonics as the burst evolves. The coincident drop in neutron rate is caused by ejection of trapped EPs. Reproduced from [743].

ambipolar EP loss causes a coincident, rapid change in radial electric field [743].

MEGA simulations that treat the EPs kinetically and the bulk plasma with resistive MHD have successfully reproduced an off-axis fishbone burst [746] and the nonlinear distortion of the waveform caused by coupling to higher harmonics [747]. In both theory [748] and experiment [749, 750], transport of EPs by off-axis fishbones can trigger ELMs.

7.2. Nonlinear gyrokinetic theory

Nonlinear gyrokinetics [751–753] provides the most comprehensive framework for addressing EP physics in reactor relevant fusion plasmas. It accounts for the resonant excitations of instabilities, the ensuing transport processes as well as the broad range of spatio-temporal scales associated with their nonlinear dynamics. Employing gyrokinetic theory is not only necessary for the correct assessment of wave-particle resonant interactions, which provide crucial driving and damping mechanisms, but is also mandatory for dealing with the short scales that are spontaneously produced by the spatial phase mixing of the SAW continuous spectrum [754]. KAWs [484, 755], excited by mode conversion at resonances with the SAW continuum, enhance nonlinear wave-wave couplings and modify the spectral features of the fluctuation spectrum qualitatively and quantitatively [756–758].

Nonlinear gyrokinetics is the foundation of the unified and self-contained theoretical framework describing these physics, as discussed in a recent review [32]. The self-consistent theory treats the fluctuation spectrum evolution and EP transport on the same footing. The first aspect is dealt with by the so-called general fishbone-like dispersion relation [617, 759], which consists of the weak formulation of nonlinear gyrokinetic quasi-neutrality and vorticity equations. This can be seen as a gyrokinetic energy principle, valid in a wide frequency interval, ranging from the low-frequency MHD up to the Alfvén wave frequencies. It has been systematically verified numerically and validated experimentally [32, 617, 759]. In the high-n (toroidal mode number) limit, the general fishbone-like dispersion relation has the form

$$i\Lambda(\omega, r) = \delta\bar{W}_f(\omega, r, k_r) + \delta\bar{W}_k(\omega, r, k_r) , \qquad (69)$$

where $\Lambda(\omega, r)$ is the generalized inertia, depending on the mode frequency and the radial coordinate. $\delta\bar{W}_f(\omega, r, k_r)$ and $\delta\bar{W}_k(\omega, r, k_r)$ are the fluid and kinetic potential energies, which also depend on the radial wave vector. Equation (69) can be cast as a nonlinear Schrödinger-like equation, describing the amplitude evolution of short wavelength Alfvénic fluctuations [760]. The EP transport description is based on the derivation of the renormalized EP response, i.e., the EP distribution function in the presence of a finite fluctuation level [761–763]. The evolution equation for the renormalized EP response self-consistently accounts for EP transport in phase space and is cast in the form of a Dyson-like equation [761]. Summarizing, a key point is that there are two "routes" to nonlinear dynamics of EP-driven Alfvénic fluctuations in magnetized fusion plasmas [32]; i.e., nonlinear wave-wave and wave-particle interactions [757]. Each of these routes is discussed in the following two sub-sections.

7.2.1. Nonlinear wave-wave interactions. Nonlinear wave-wave interactions have been first addressed by Alfvén [764], who demonstrated that, in uniform, incompressible ideal MHD plasmas, SAWs can exist in the pure "Alfvénic state", independently of their amplitude, due to the cancellation of the Reynolds and Maxwell stresses [765, 766]. The pure "Alfvénic state" is closely linked, in realistic nonuniform plasmas, with the existence of the SAW continuum spectrum (section 6). As a consequence, the equilibrium magnetic field geometry and the plasma nonuniformity play crucial roles in the nonlinear dynamic evolution of the system [32] along with previously mentioned short-scale kinetic effects, plasma compressibility as well as deviation of the Alfvén eigenmode frequency from the local continuum [757, 767, 768]. Therefore, the nonlinear gyrokinetic approach is crucial to qualitatively and quantitatively assess the nonlinear wave-wave coupling process. In fact, it may also be applied to the polarization nonlinearity at long wavelengths as well as to Reynolds and Maxwell stresses in the short wavelength kinetic regime [756, 757]. Among the various nonlinear wave-wave interactions, excitation of zonal field structures (ZFs) [760, 769] and frequency cascading via ion induced scattering [770, 771] are two channels expected to significantly influence the SAW instability nonlinear dynamics in fusion plasmas. These physics have been analyzed taking TAEs [772] as an example. That general approach, developed for TAEs, can be applied to other SAW instabilities based on their corresponding linear properties [773–775].

ZFs are toroidally and predominantly poloidally symmetric variations of scalar and parallel vector potentials and are connected with the radial corrugations of the equilibrium profiles such as zonal flows and fields/currents (ZF & ZC) [776, 777]; in other words, zonal flow and fields/currents are low-frequency $n=0$ and predominantly $m=0$ structures characterized by appreciable radial wavenumber k_r. ZFs may regulate fluctuations by radial mode structure shearing and scattering the fluctuations into the short-wavelength stable domain, as typically occurs for drift wave turbulence [777]. In reactor relevant fusion plasmas, EPs dominate the local power balance and, thus, play a unique role as mediators of cross-scale couplings [778] as they may linearly and nonlinearly excite ZFs, acting, thereby, as generators of nonlinear equilibria, or zonal states (ZS), that generally evolve on the same timescale as the underlying fluctuations [761–763, 778].

Nonlinear excitation of zero frequency ZFs by TAEs was investigated in [769], which found that both electrostatic zonal flows and electromagnetic zonal current can be excited. The former results from non-cancellation of Reynolds and Maxwell stresses due

to toroidicity, while the latter is related to dynamo effects. The condition for the spontaneous excitation of zonal field structures is more easily satisfied when the neoclassical polarizability enhancement by trapped particles is properly accounted for [779], causing the zonal current to be preferentially excited with a much smaller threshold on the TAE amplitude being $|\delta B_r/B_0| \sim \mathcal{O}(10^{-4})$, compatible with the fluctuation amplitude in tokamak experiments [780].

Due to the typically weak ballooning feature of SAW instabilities, zonal field structures excited by TAEs have a fine radial scale structure [773, 781], in addition to the usual well-known mesoscale structures. This additional fine radial structure may lead to enhanced nonlinear coupling and a corresponding much lower TAE saturation level. It was further demonstrated that the nonlinear contribution of resonant EPs to plasma compressibility may dominate the thermal plasma contribution to the Reynolds and Maxwell stresses. In that case, zonal flows may be forced driven [773, 782] rather than spontaneously excited by finite amplitude TAEs, with the zonal flow growth rate being twice of the instantaneous TAE growth rate [782], as observed in kinetic-MHD [783] as well a PIC simulations [784]. A thorough discussion of zonal field structures generation by TAEs is given in [781], with emphasis on the various underlying physics, e.g., zonal flow vs. zonal current generation, the roles of fine- vs. mesoscale structures, as well as spontaneous decay vs. forced driven processes. Further important applications of the same theoretical framework to, e.g., zonal flow generation by BAEs [681, 773, 785] as well as finite frequency GAM [440] generation by TAEs [786–788] have also been investigated. Simulations find that zonal flows and currents play an important role in the saturation of AEs are discussed further in section 7.3.1.

Another important channel of wave-wave coupling is TAE frequency cascading via thermal-ion induced scattering, also called nonlinear ion Landau damping [789]. In reactor-relevant realistic geometry, there exists $\mathcal{O}(n^2 q)$ TAEs, with $n \gtrsim \mathcal{O}(10)$ [790] (section 6). Thus, many TAEs with overlapping radial structures and slightly different frequencies co-exist. The TAE spectral cascading was first investigated using a drift kinetic theory [770], and then generalized using a nonlinear gyrokinetic approach [771]. In a single process, a test TAE couples with a counter-propagating fluctuation of the TAE spectrum with slightly lower frequency and generates a low frequency ion-sound-wave quasi-mode, with ion Compton scattering and shielded-ion scattering contributing to the process on the same footing. The nonlinear evolution of the TAE spectrum can then be cast as wave-kinetic equation by summing all the strongly interacting background

TAEs in the continuum limit. This describes the downward spectral energy transfer and TAE saturation due to enhanced continuum damping. The nonlinearly saturated TAE spectrum can be derived from the wave-kinetic equation, which yields the estimated TAE saturation amplitude as $|\delta B_r/B_0| \lesssim \mathcal{O}(10^{-4})$; i.e., typically one order of magnitude smaller than that in the MHD limit [770] due to enhanced nonlinear coupling in the kinetic regime [757]. The resulting transport of circulating EPs can be derived from quasi-linear transport theory [791], and be estimated in the range of $\sim 1 - 10\,\mathrm{m}^2/\mathrm{s}$ for typical reactor parameters [771]. The resulting bulk ion heating rate can also be derived [792]. Specific applications to ITER to quantitatively assess the impact of wave-wave interactions on AE saturation and ensuing EP transport will require dedicated numerical simulations accounting for all the various nonlinear processes mentioned above, since they all compete on the same footing and estimating their effect independently would produce an incorrect prediction.

7.2.2. Nonlinear wave-particle interactions. Nonlinear wave-particle interactions between Alfvénic fluctuations and EPs are an essential element for the assessment of EP transport in fusion plasmas. The theoretical framework discussed in [32] suggests that burning plasmas in ITER will require lifting the transport description to phase space in order to capture the complex nonlinear behaviors due to the many interacting degrees of freedom [761, 778]. A new approach has been recently proposed within this framework [762,763] to effectively compute the self-consistent evolution of plasma equilibria and fluctuation spectra on the energy confinement time scale. This approach is consistent with the general nonlinear gyrokinetic description and is verified and validated in a number of proof-of-principle cases. First results are briefly discussed in the following, showing that they provide a practical tool to make feasible predictions in realistic ITER plasma conditions [793,794](see also section 6 for recent results on ITER simulations). A hierarchy of reduced models with verifiable fidelity can be constructed which should lead to applications of increasingly higher sophistication and reliability before ITER operations, using numerical simulation tools that are integrated within the IMAS framework.

Wave-particle interactions must be described in phase space, where resonant processes dominate due to the relatively small fluctuation levels ($|\delta B_r/B| \lesssim 10^{-4}$). For the proper definition of nonlinear EP equilibrium evolving on the spatio-temporal mesoscales, the concept of phase-space zonal structures (PSZS) has been introduced [32, 761, 763, 778], that is, the part of the distribution function remaining undamped

by collisionless processes on the characteristic nonlinear timescale. The PSZS, accounting for the "renormalized" (nonlinear/evolving) equilibrium distribution function, depend only on the invariants of motion, $\bar{F}_z0(\mathcal{E}, \mu, P_\phi; t)$ ¶ Introducing the magnetic-drift/banana center pull-back operator e^{-iQ_z}, with $Q_z = g(\psi)(v_\|/\Omega)k_z/(d\psi/dr)$ and $k_z \equiv -i\partial_r$ the zonal field structures radial wave-number, the evolution equation for the phase-space zonal structures is given by [760, 762, 763]

$$\partial_t \overline{e^{iQ_z}\bar{F}_0} = -\overline{e^{iQ_z}\frac{F(\psi)}{B_0}\partial_t \langle \delta A_{\|\mathrm{g}}\rangle_z \frac{\partial}{\partial\bar{\psi}}\bar{F}_0}$$
$$+ \overline{e^{iQ_z}[C_g + \mathcal{S}]} - \frac{1}{\tau_\mathrm{b}}\frac{\partial}{\partial\psi}\left[\tau_\mathrm{b}\overline{e^{iQ_z}\delta\dot{\psi}\delta F}\right]$$
$$- \frac{1}{\tau_\mathrm{b}}\frac{\partial}{\partial\mathcal{E}}\left[\tau_\mathrm{b}\overline{e^{iQ_z}\delta\dot{\mathcal{E}}\delta F}\right] . \qquad (70)$$

Here, τ_b denotes bounce/transit time[+], $\overline{[\ldots]}$ denotes bounce/transit averaging and, thus, $\overline{e^{iQ_z}[\ldots]}$ denotes orbit averaging [760]. The first term on the right hand side represents the nonlinear equilibrium change associated with the zonal field structures due to the gyro-averaged parallel vector potential, $\langle\delta A_{\|\mathrm{g}}\rangle_z$. δ-quantities stand for fluctuations, while C_g and $\mathcal{S}$ on the right hand side represent gyro-center collision and source terms [795–798]. Equation (70) can generate all spatio-temporal scales, from micro- via meso- to macroscales. For the sake of convenience and numerical implementation, it is often useful to separate slow meso- and macroscale variations, which define the mean equilibrium evolution, from the fast scales that describe the zonal state deviations about it, as discussed above in section 7.2.1 [760, 762, 763]. In addition, it serves as fundamental equation defining EP transport in the phase space. It provides the basis for any reduced approach that seeks to describe EP dynamics over transport timescales (for a practical implementation see e.g. [793, 794]). In these works, various simplifying assumptions can be adopted in the quantitative evaluation of the phase space fluxes on the RHS. The crucial element is that all these models can be readily verified/falsified within a unified theoretical framework [32, 763] by means of nonlinear GK codes that incorporate specialized diagnostics, as demonstrated by the work of [799]. Meanwhile, verification/falsification is based on comparisons of fluctuation spectra as well as the corresponding phase space fluxes, which provide a credible assessment of

¶ The COMs are here defined per unit mass, i.e. $\mathcal{E} = v^2/2$, $\mu \simeq v_\perp^2/2B_0$ the leading order expression of the magnetic moment and $P_\phi \simeq (e/c)\left(g(\psi)(v_\|/\Omega) - \psi\right) \equiv -(e/c)\bar{\psi}$ the leading order toroidal canonical angular momentum, where $g(\psi) = RB_t$ is the covariant component of the toroidal magnetic field and $\Omega = eB/(mc)$ is the cyclotron frequency.
[+] The bounce/transit time τ_b is the same as τ_θ defined in section 2; we name it τ_b here to comply with the cited references.

64

the predictive capability of self-consistent evolution of fluctuation spectra and equilibrium profiles.

The approach based on equation (70) and the self-consistent solution of the Alfvénic fluctuation spectrum allow describing the non-perturbative dynamics of EP nonlinear equilibria that generally evolve on the same timescale τ_{NL} of the underlying fluctuations; i.e., $\gamma\tau_{\mathrm{NL}} \sim \omega_B\tau_{\mathrm{NL}} \sim \mathcal{O}(1)$, with γ the instantaneous (nonlinear) growth rate and ω_B the wave-particle trapping frequency. By construction, thus, this approach can handle both weak and strong drive regimes and naturally recovers the approaches that assume $\omega_B\tau_{\mathrm{NL}} \gg 1$ near marginal stability, as shown in [32, 761, 800].

Equation (70) reduces to the quasilinear diffusion equation for a broad spectrum of overlapping resonances [801, 802]. More generally, for a narrow spectrum of quasi-coherent fluctuations, it describes a broader class of transport processes [803, 804] and can be cast into the form of a Dyson-like equation, which accounts for convective transport and avalanches in the EP phase space [32, 761]. A particular application of practical interest of the Dyson-like equation, coupled with the nonlinear Schrödinger-like equation for the self-consistent description of the fluctuation amplitude (section 7.2), is the nonlinear dynamics of the EPMs [403], (section 6) which is shown to yield convective amplification of the EPM wave packet as a soliton leading to an EP avalanche. This case was discussed earlier in [20], while the EPM chirping rate, $\dot{\omega} \sim \omega_B^2$, and the radial structure of the EPM wave packet are analyzed in [32, 761]. Extensive verifications of the the linear scaling of chirping rate with the mode frequency have been recently reported in [805, 806]. In particular, it can be shown that the self-similar shape of the EPM envelope, $A(r,t) = U(\xi)e^{\int^t \gamma(\tau)d\tau}$, with $\xi = k_{\mathrm{NL}}(r - r_0 - \int^t v_g d\tau)$, k_{NL} the EPM nonlinear wave number, r_0 the location of the linear instability, and v_g the EPM group velocity, obeys the nonlinear equation [32]

$$\partial_\xi^2 U = \lambda U - 2iU|U|^2 \ , \tag{71}$$

with $\lambda = -\sqrt{2}/3 + i(4/3)$, which is a particular case of the complex Ginzburg-Landau equation [32]. In this case, the linear scaling of the theoretical prediction of frequency chirping [32, 761], which can be cast as

$$\dot{\omega} \ \simeq \ \pm \frac{1}{2}\omega_{\mathrm{B}}^2 \tag{72}$$

$$\omega_{\mathrm{B}}^2 = \left| en\frac{\partial\omega_{\mathrm{res}}}{\partial P_\phi} + e\omega\frac{\partial\omega_{\mathrm{res}}}{\partial E} \right| \left| \overline{\frac{\mathbf{v}_{\mathrm{d}} \cdot \nabla\delta\phi}{\omega}} \right| \tag{73}$$

Here, ω_{res} is the wave particle resonance frequency and $\delta\phi$ is the EPM scalar potential fluctuation, while $\overline{(...)}$ indicates equilibrium orbit averaging as defined above [763]. The $\pm$ sign shows that both up- and downward chirping are possible, although the downward chirping

is the most typical case due to equilibrium non uniformity [32]. Another successful application of the Dyson-like equation is the fishbone burst cycle [32], which is consistent with recent nonlinear kinetic-MHD simulation results [807, 808] and proves the secular loss mechanism conjectured by [809], reducing, in the proper limit, to the model equations originally introduced by Chen-White-Rosenbluth [731]. This fundamental understanding of the secular loss of EP to be expected in ITER and reactor relevant fusion plasmas imposes the necessity of identifying operation regimes where these phenomena are mitigated in suitably designed operation scenarios and/or, possibly, even controlled by means of the interplay of ZFs and PSZS [739]. In this case, the fishbone downward frequency chirping can be obtained by the same expression given above, with a proper extension to take the effect of zonal flow decorrelation properly into account [810].

7.3. Nonlinear gyrokinetic simulations of EP-driven instabilities and EPMs

Effects of collective EP instabilities (AE/EPM) on the EP confinement depend ultimately on the self-consistent nonlinear evolution of the fluctuation spectrum. More precisely, this self-consistent evolution will be reflected by the properties of the zonal state (ZS), introduced above, which consists of the ZFs and corresponding PSZS, which depend critically on the nonlinear phase-space dynamics of EPs as well as on the nonlinear mode-mode couplings among the multiple EP-driven modes, which are mesoscale (defined as fast ion gyroradius ρ_{Lf}) with intermediate toroidal mode numbers, typically $n \sim (10, 40)$ in ITER plasmas [31, 559]. Both nonlinear effects, in turn, depend on the global features of wave-particle resonances and mode structures whose description requires to accurately account for kinetic effects of thermal particles; e.g., the existence of kinetic Alfvén waves. Furthermore, wave-wave interaction and resonance overlap in EP phase space will induce cross-scale coupling between AE/EPM and macroscopic MHD modes such as the $n = 1$ fishbone instability. Finally also, the coupling between EP-driven turbulence and the ubiquitous drift-Alfvén wave turbulence driven by thermal particles, which are micro-scale (defined as thermal ion gyroradius ρ_{Li}) with high toroidal mode numbers, typically $n \sim (100, 200)$ in ITER [565] needs to be retained. A unified simulation model treating consistently macro-, meso- and microturbulence is needed to explore new physics frontiers associated with the complex dynamics of cross-scale couplings (see section 7.2) [32].

For fully self-consistent simulations, we highlight that they therefore must incorporate three physics

elements: kinetic effects of thermal particles, nonlinear interactions of many mesoscale modes, and cross-scale couplings of macro-meso-microturbulence. The large dynamical ranges of spatial-temporal processes further require global simulation codes that are efficient in utilizing massively parallel computers at the exascale. Global gyrokinetic simulation [753, 811] is a suitable approach. Since the publication of the EP chapter in the Progress in the ITER Physics Basis [20], several gyrokinetic codes with comprehensive physics and realistic geometry have been developed, verified, and partially validated [539, 544, 568, 680, 812–815]. In particular, for PIC codes these advances were facilitated by the development and implementation of advanced noise control [816] and 'pull-back' schemes [812,817–819]. These nonlinear gyrokinetic simulations are providing more complete physics insights on nonlinear dynamics of EP instabilities regarding their saturation by ZF, regulation of EP-driven turbulence by microturbulence, and fast frequency chirping. Improved understanding from gyrokinetic simulations provides physics foundation for reduced EP transport models. For example, effects of zonal flows have been incorporated in the critical gradient model (CGM) and resonance broadening quasilinear (RBQ) models [558] and effects of microturbulence have been implemented in the RBQ model [820].

7.3.1. Saturation of EP instabilities by wave-particle and wave-wave nonlinearities. Since EP nonlinear dynamics depends linearly on the wave amplitude while nonlinear wave-wave coupling depends on the wave intensity, it is generally believed that wave-particle nonlinearity dominates over wave-wave nonlinearity near marginality where the wave amplitude is low. Consequently, the saturation mechanism for the EP instability near marginality has been attributed to the nonlinear wave-particle trapping [821], a 1D model [683] that has been successfully utilized to explain many simulation results and experimental observations near marginality. In this classic view, an EP instability saturates when the nonlinear trapping frequency equals the linear growth rate. In the presence of multiple resonances, overlap of phase space islands leads to EP diffusion and associated flattening of the EP distribution function at resonance, which diminishes the instability drive. Another mechanism of wave damping is the resonance broadening which arises from EP scattering by an ensemble of non-interacting waves.

Far away from marginality, wave-wave coupling could become the dominant nonlinear process. The transition from wave-particle to wave-wave nonlinearity needs to be quantitatively determined by gyrokinetic simulations. Gyrokinetic simulations with the GEM code [823] show that when the RSAE growth rate $\gamma > 0.03\omega_r$ (here ω_r is real frequency), wave-wave nonlinearity becomes important. In the wave-dominated weak turbulence, unstable modes can saturate through energy transfer to damped modes in a three-wave coupling process. A nonlinearly-generated ZF often plays an important role in the saturation of the instability in the toroidal geometry. The ZF is associated with the perturbed distribution function (called zonal structure) [761] averaged over the flux-surface, i.e., the $n = m = 0$ component of the perturbed density and flows that generate ZF such as zonal flows and zonal currents. Zonal flows have been found to often dominate the nonlinear saturation of the toroidal drift wave instability [824, 825]. On the other hand, nonlinear toroidal coupling is sub-dominant, but can lead to an inverse cascade to the lower toroidal mode number n at a longer timescale [826].

ZFs and PSZS have been shown to be generated by, and in turn, suppress AEs in global simulations using gyrokinetic codes GTC [541, 822, 827], GEM [823], ORB5 [633], and kinetic-MHD codes TAEFL [828], FAR3D [829], and MEGA [783]. Effects of zonal flows are typically stronger than that of the zonal currents, but zonal structures have also been reported to dominate the AE saturation [823]. Local gyrokinetic GYRO simulations [830] found that strong zonal flows generated by microturbulence are needed to saturate RSAE. Global gyrokinetic GTC simulations using realistic plasma profiles and geometry of DIII-D experiments [640] found that zonal flows dominate the nonlinear RSAE saturation even in the presence of multiple unstable modes ($n = 3 - 9$) [831]. These results suggest that effects of ZFs and PSZS on EP instabilities are universal and could play an important role in EP transport.

7.3.2. Regulation of mode saturation by microturbulence. An outstanding issue in global simulations of mesoscale EP instabilities is the absence of a steady state EP-driven turbulence and related transport. The nonlinear dynamic of a huge initial burst followed by a quickly diminished AE amplitude and EP transport is a common phenomenon in global gyrokinetic [784,823] and kinetic-MHD [783,828,832] simulations, where quasi-steady state EP transport can only be sustained by artificially large dissipation due to, e.g., resistivity or scattering by Coulomb collisions. However, collisions are found to have negligible effects on EP turbulence when using realistic experimental parameters. This issue has recently been addressed in global gyrokinetic simulations coupling mesoscale AE turbulence and microturbulence, where microturbulence is found to regulate EP-driven modes, resulting in a quasi-steady state EP transport [822,827]. In this work, larger EP transport has been found for stronger
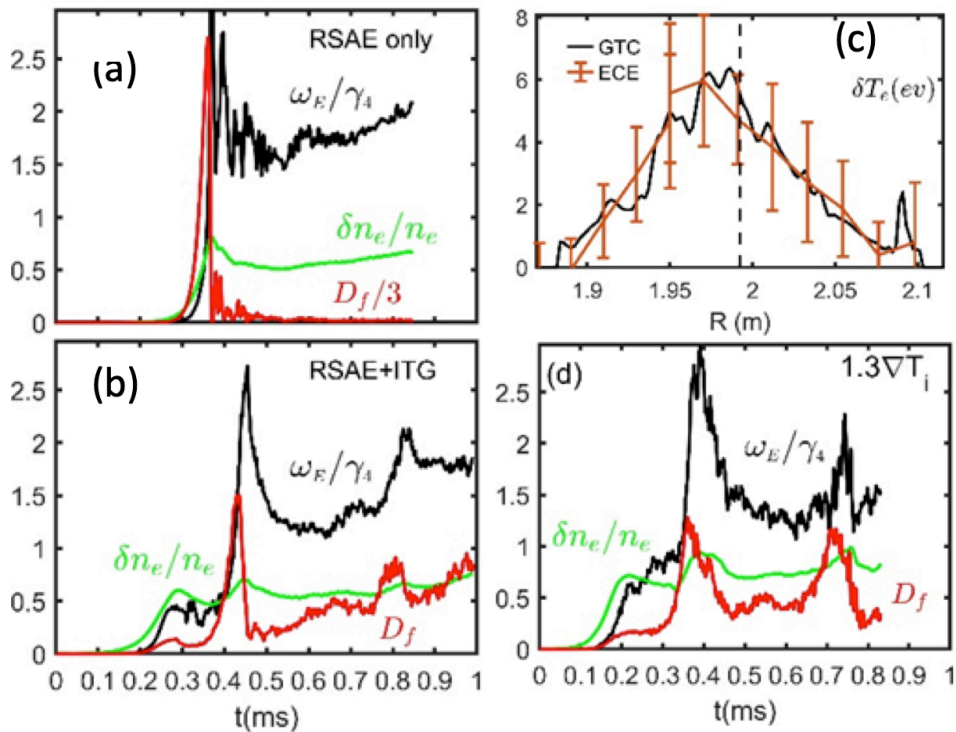
Figure 49. Time history of the zonal flow shearing rate ω_E/γ_4, electron density perturbation $\delta n_e/n_e$[%], and effective EP diffusivity D_f [m^2/s] from the simulation of an RSAE only (panel a) and from the simulation of an ITG-RSAE (panel b). Panel c shows radial profiles of the electron temperature perturbation δT_e from GTC simulations and ECE measurements in DIII-D. In panel d, the thermal ion temperature gradient is increased by 30%. Reproduced from [822].

microturbulence even though the microturbulence directly drives little EP transport due to gyro-averaging effects, as expected by conventional wisdom [833–835]. When background microturbulence is artificially suppressed in the simulation, the RSAE amplitude and EP transport are much higher than experimental levels at nonlinear saturation, but quickly diminish to very low levels after the saturation (figure 49a). In contrast, in simulations coupling micro-mesoscales, the RSAE amplitude and EP transport decrease drastically at the initial saturation but later increase to the experimental levels in the quasi-steady state with bursty dynamics due to regulation by thermal ion temperature gradient (ITG) microturbulence (figure 49b). The RSAE amplitude in the quasi-steady state mediated by ITG-RSAE turbulence agree well with experimental measurements (figure 49c). When the thermal ion temperature gradient is increased, owing to the stronger microturbulence, the quasi-steady state EP transport is larger (figure 49d).

Pressure gradients of thermal particles excite various drift-wave instabilities, leading to ubiquitous microturbulence responsible for turbulent transport of thermal plasmas. Despite the separation in the spatial and temporal scales, there can be strong cross-scale coupling between AEs and microturbulence. Zonal flows can be nonlinearly generated by AEs, and in turn, suppress both AEs and microturbulence. Microturbulence can dampen the zonal flows and zonal structures generated by the AEs. EP scattering by the microturbulence [836] can affect the phase space dynamics in nonlinear AE-EP interactions [837]. Drift waves and AEs can also nonlinearly interact through wave-wave coupling. Furthermore, mesoscale EP turbulence can also drive significant thermal transport as shown in recent gyrokinetic ORB5 simulations that find large electron heat fluxes driven by BAEs excited by EPs [784].

7.3.3. *Fast frequency chirping in gyrokinetic simulations.* Increased EP transport by AEs has been correlated with a fast frequency oscillation (chirping) with a sub-millisecond period that has been observed in many experiments. An analytic model for the chirping based on the one-dimensional (1D) nonlinear wave-particle interaction near marginal stability has been constructed, and single [838] and repetitive [839] bursts of chirping have been observed in kinetic MHD simulations with sources and sinks. Global gyrokinetic GTC simulations [840] of BAEs found fast and repetitive fre-

67

quency chirping without sources and sinks. The wave frequency exhibits a fast, repetitive and mostly downward chirping with a sub-millisecond period and a 90° phase shift from the amplitude oscillation (figure 50). The frequency chirping is induced by the evolution of coherent structures in the EP phase space. The dynamics of the coherent structures is controlled by the competition between the phase-space island formation due to the nonlinear particle trapping and the island destruction due to the free streaming process, an intrinsically 2D dynamics in toroidal and radial directions [840, 841].
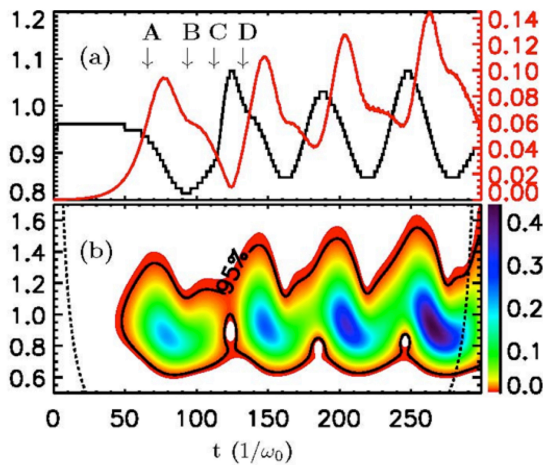

Figure 50. Time evolution of (a) BAE amplitude $|e\delta\phi/T_i|$ (red) and dominant frequency ω (black), and (b) frequency power spectrum. The y-axis on the left is ω/ω_0. The unit of the power intensity in panel (b) is arbitrary. Reproduced from [840].

7.4. Nonlinear kinetic-MHD simulations of EP-driven modes

Kinetic-MHD simulations for EPs interacting with an MHD fluid have now become irreplaceable for understanding and predicting EP behavior [338, 808, 842–851]. In kinetic-MHD models, the bulk plasma is described as an MHD fluid, and a particle simulation method is applied to EPs. The MHD fluid and the EPs are coupled through EP pressure or EP current in the MHD momentum balance equation. Both the MHD nonlinearity and the nonlinear EP dynamics are included in the simulations. Nonlinear dynamics of EPs interacting with MHD waves is also studied in reduced simulations [569, 819, 852] and in gyrokinetic simulations [633, 834, 853, 854]. Gyro-Landau closure models such as FAR3d [829] and TGLF-EP [855] constitute a further type of kinetic-MHD hybrid model and are described in the next section. The reduced simulations are computationally more efficient, but they can be sensitive to simplifying assumptions and are less detailed in predictions. The gyrokinetic codes,

on the other hand, offer more complete description of the bulk plasma but they are computationally more demanding than the kinetic-MHD simulations. One of the most capable kinetic-MHD codes is the MEGA code. It uses a multi-phase simulation method of the classical collisional processes and EP interactions with an MHD fluid. This approach makes it possible to simulate a population of EPs taking into account the injection of a neutral beam, collisional drag, pitch-angle scattering and energy diffusion, beam losses and transport processes due to MHD waves with the effects of MHD nonlinearity and EP finite Larmor radius [736]. We present some examples of the MEGA modeling. In DIII-D experiments with neutral beam injection, there was a significant flattening of the EP profile during AE activity as shown in figure 51 [780].
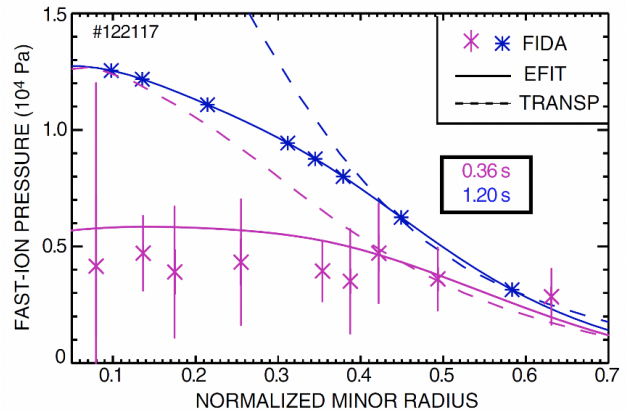

Figure 51. EP pressure profiles and FIDA density profiles versus normalized minor radius at two different times in DIII-D. The dashed lines are the classical pressure profile predicted by TRANSP. Reproduced from [780]

In these experiments, there was a rich spectrum of TAEs and RSAEs during the current ramp-up phase with reversed magnetic shear [466, 468, 780, 856, 857]. The ORBIT code calculations of the EP for the measured mode amplitudes [858, 859] have shown that the profiles of NBI-produced EPs flatten, consistent with the measurements. These calculations also reveal that resonance overlap of multiple AEs is essential for EP transport. The multi-phase MEGA simulation of DIII-D discharge #142111 with a self-consistent calculation of the mode amplitudes has demonstrated that the simulated flattened EP pressure profile matches with the experimental profile within the error bars (see figure 52) [477].

The simulated temperature fluctuation profiles were quantitatively compared with the ECE measurements, and they, as well as phase profiles, showed good agreement with the measurements. Additionally, the saturated AE amplitudes were $\delta B/B \sim 10^{-4}$, which is within a factor of 2 of those measured. [858, 859].
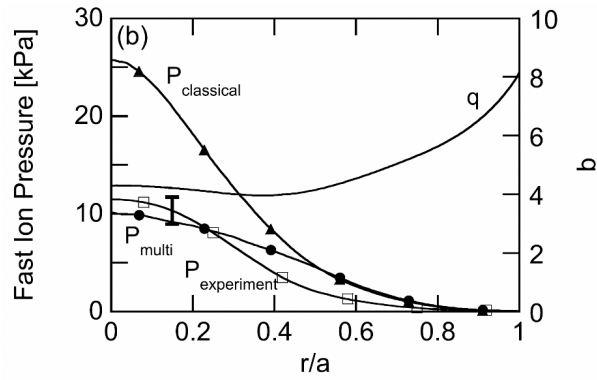
Figure 52. Comparison of an EP pressure profile for DIII-D discharge #142111: a multi-phase MEGA simulation (circles), a classical simulation (triangles), and experiment (squares), also showing an error bar. Reproduced from [477]

Experiments in DIII-D also show that EP transport suddenly becomes "stiff" above a critical threshold in the presence of many overlapping small-amplitude AEs (see figure 53) [860–862].
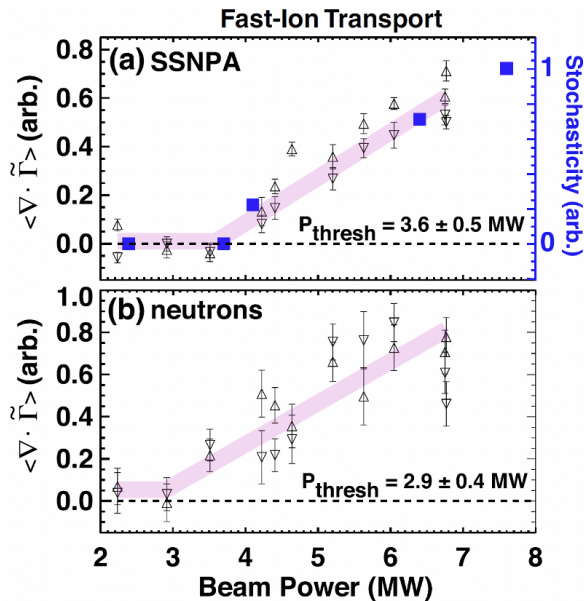

Figure 53. Time-averaged divergence of modulated flux, i.e., transport, inferred from (a) solid-state neutral particle analyzer (SSNPA) signal and (b) neutron emission for the first half (triangles pointing up) and second half (triangles pointing down) of the modulation period at DIII-D. Error bars are the standard error of the time average over the half period. The onset of transport corresponds to the theoretical level of stochasticity [solid squares in (a)]. Reproduced from [860]

.

The EP profile is regarded as "stiff" when the increase of the EP profile gradient above a critical value is lower than the proportional increase to the beam power. The threshold is phase-space dependent

and occurs when particle orbits become stochastic due to resonances with AEs. The multi-phase MEGA simulations predict the EP pressure profile and the EP transport flux for different beam power levels [863]. They show stiffness and a monotonic degradation of EP confinement with increasing beam power. The confinement degradation and profile stiffness are due to the presence of multiple AEs when the EP pressure gradients exceeds a critical value. The critical pressure gradient and the corresponding beam power depend on radial location. The EP pressure gradient stays moderately above the critical value, and the profiles of the EP pressure and EP transport flux spread radially outward from the inner region, where the beam is injected. The resonance regions in the EP phase space have been analyzed for the eigenmodes observed in the MEGA simulations. Figure 54 shows the particle trajectories in the phase space of normalized major radius and energy with the AEs present in the simulations for DIII-D experiments for different beam deposition power levels [863]. With increasing beam power, the resonance regions broaden due to the larger amplitude of eigenmodes leading to the overlapping.

This analysis verifies that the overlap of multiple resonances is the underlying reason for the sudden increase in EP transport with increasing beam power. The multi-phase MEGA simulations [864] of the TAE bursts and EP losses in TFTR have reproduced the observed synchronized bursts of multiple TAEs and the corresponding variations of the stored beam energy with regular time intervals close to the experimental value, as shown in figure 55.

The mode saturation amplitude is now lower than in the earlier reduced simulations with a linearized description of the bulk plasma [865]. The inclusion of nonlinear MHD effects [767, 783, 828] in MEGA prevents the AE amplitude from excessive growth.

In experiments with super-Alfvénic beam ions, repetitive bursting events consisting of multiple AEs or EPMs are observed. In JT-60U, negative-ion beams drove a series of repetitive bursts dubbed "fast frequency sweeping modes" that culminated in an "abrupt large event" (ALE) [866]. Similarly, in NSTX, a sequence of bursting AEs often culminated in a larger burst with multiple harmonic content dubbed an "avalanche" [867, 868]. The avalanche events caused substantial drops in neutron [867, 869] and FIDA signals [868, 870]. Many features of the JT-60U ALE [839, 871, 872] and NSTX avalanche [873] are reproduced by simulations, including the entire repetitive burst cycle in simulations with MEGA [839].

The EP-driven AEs and EP transport in ITER plasmas have been studied numerically in [31, 557, 562, 564, 855, 874]. It was found that the EP drive of AEs can overcome the thermal ion Landau damping
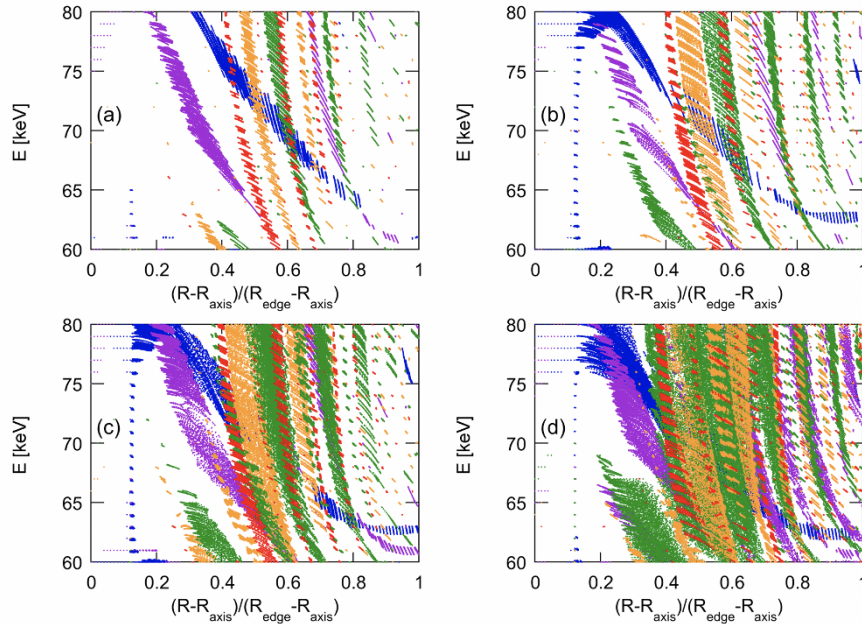
Figure 54. Particle trajectories in the phase space of normalized major radius $\hat{R} = (R - R_{\mathrm{axis}})/(R_{\mathrm{edge}} - R_{\mathrm{axis}})$ and energy $\mathcal{E}$ (keV) for beam deposition power (a) 1.56 MW, (b) 3.13 MW, (c) 6.25 MW, and (d) 15.6 MW. Particle orbits are followed with the electromagnetic perturbations of a single TAE with fixed amplitude and frequency, and $\hat{R}$ and $\mathcal{E}$ are recorded when the particle passes the mid-plane from bottom to top. Only the particles trapped by the TAE are plotted in the figure. The eigenmodes are represented by colors: n = 1 (blue), n = 2 (purple), n = 3 (green), n = 4 (orange), and n = 5 (red) . Reproduced from [863].
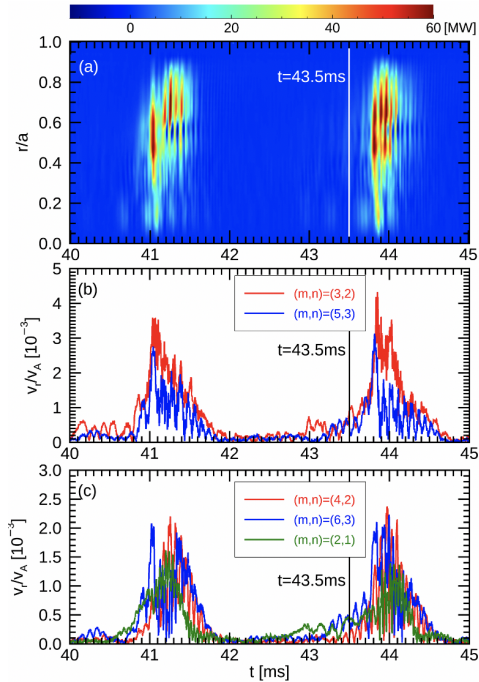

Figure 55. (a) Radial profile evolution of EP energy transport flux in the radially outward direction, and amplitude evolution of radial MHD velocity fluctuation for (b) the dominant n = 2 (red) and n = 3 (blue) AEs and (c) the other AEs with n = 1–3. The unit of color bar is MW and the beam injection power is 10 MW. Reproduced from [34]

only in the outer half of the plasma, and AE-induced redistribution is not expected to affect the fusion burn in the ITER 15 MA baseline scenario [31]. For the steady-state scenario with 9 MA plasma current, BAEs with low toroidal mode number were found to dominate in the nonlinear phase although many TAEs with $n \sim 15$ are more unstable in the linear MEGA simulations [557].

7.5. Nonlinear kinetic-MHD simulations of dynamics and frequency chirping of single-n Alfvén modes

The nonlinear dynamics of a single toroidal Alfvén mode and, in particular, the saturation mechanisms have been investigated by particle-in-cell simulations performed with the gyrokinetic-MHD code XH-MGC [845, 875, 876] and the so-called Hamiltonian-mapping technique [877], both for constant and chirping frequencies. This technique samples the regions of phase space that provide the most important contribution to the growth or damping of modes by means of a population of test particles evolving in the electromagnetic fields obtained from self-consistent particle simulations. Wave-trapped particles form an island structure, around the resonance radius, in the 2D space (Θ, r), with Θ being the wave phase seen by the particle and r its radial coordinate (figure 56). This yields a density flattening delimited by a suffi-
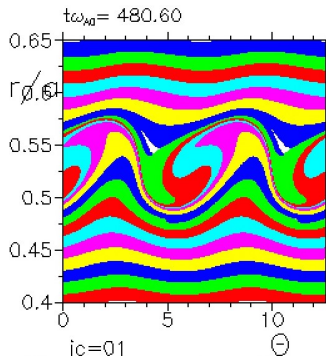
70

Figure 56. Hamiltonian mapping of test-particle markers in the (Θ, r) plane in the nonlinear stage. Each marker is coloured according to the birth r value of the particle. The formation of an island-like structure around the resonance radius, including the trajectories of particles trapped in the potential well of the wave, is clearly seen. Reproduced from [805].

Figure 57. Scaling of the saturation amplitude of the scalar potential (defined as the radial peak, in arbitrary units, of the dominant poloidal harmonic) versus the linear growth rate γ for XHMGC simulations. The reference quadratic and linear γ scalings associated with the resonance-detuning and radial-decoupling regimes are also shown. Reproduced from [849].

ciently steep negative density gradient. In general, mode saturation occurs as the flattening region extends over the whole radial region where the mode-particle power transfer can take place [849, 877]. A variety of phase space diagnostics can be used to characterize the trapping-detrapping process by multiple resonances, see e.g. [805, 806, 878, 879].

In the constant-frequency case, two regimes can be distinguished. In the first regime, the power-transfer region is mainly limited by the need to satisfy the resonance condition $|\omega - \omega_{\mathrm{res}}(r)| \lesssim \gamma$, where $\omega_{\mathrm{res}}(r)$ is the resonance frequency at radius r, and γ is the linear growth rate of the mode. This is the case occurring for low values of the growth rate, sharp profiles of the resonance frequency or extended mode structure. The second regime, occurring in the opposite limits, sees the power-transfer region limited by the finite radial width of the mode structure. The two different regimes correspond to different scalings of the saturation mode amplitude with the linear growth rate: the former (*resonance detuning* regime) exhibits a quadratic scaling; the latter (*radial decoupling* regime), a linear scaling; this is shown in figure 57 [849].

In the case of chirping frequency, the dynamics, in a first nonlinear stage, is analogous to that analysed in the constant-frequency case. If the frequency is allowed to change, however, the resonance region may move such that the coverage of the power-transfer region by the density-flattening region is delayed and the mode can extract more power from the resonant particles. In turn, the island and, then, the density-flattening region reconstitute around the new resonance radius, counteracting this retarding effect. This process goes on until a further change in frequency becomes unable to produce a significant displacement of the resonance region. To further grow, the mode has to tap a different
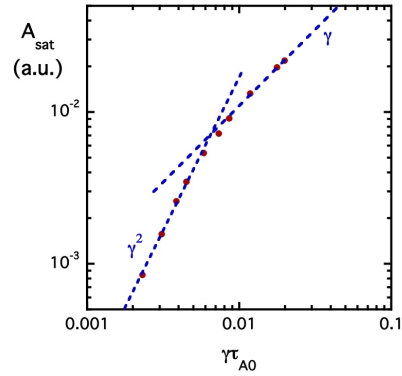
resonant structure, possibly making use of additional frequency variations. The phenomenology described above has been observed in simulations referring to a variety of physical situations, ranging from AE modes driven unstable by EPs (both fusion alphas [877] and EPs from auxiliary heating [805,849,880,881])as well as energetic electrons (as in the case of electron fishbones [807]).

7.6. Nonlinear gyrofluid simulations of EP-driven instabilities

Gyrofluid models are a further step in the evolution of the MHD-kinetic hybrid paradigm for EP instability analysis. This approach is motivated by the fact that all gyrokinetic models must communicate kinetic information to field equations through some form of moments integral (e.g., charge/current density, pressure, etc.). Since these low order moment integrals will inherently average away some of the fine structure of the kinetic distribution function, this motivated replacing the kinetic component with a hierarchy of moment equations. The advantages of this approach are: a significant dimensionality reduction from 5D/6D to 3D, leading to fewer degrees of freedom and high computational efficiency; no discrete particle noise; no issues with time-evolving uneven particle phase space densities (cavitation); and a mathematical structure that is compatible with direct eigenmode solvers. While moments hierarchy or MHD models have been developed and applied for many years in plasma physics, they were not capable addressing the phase-mixing and instability feedback effects associated with wave-particle resonant phenomena, such as Landau damping/growth until the development of gyro-Landau closure methods. These
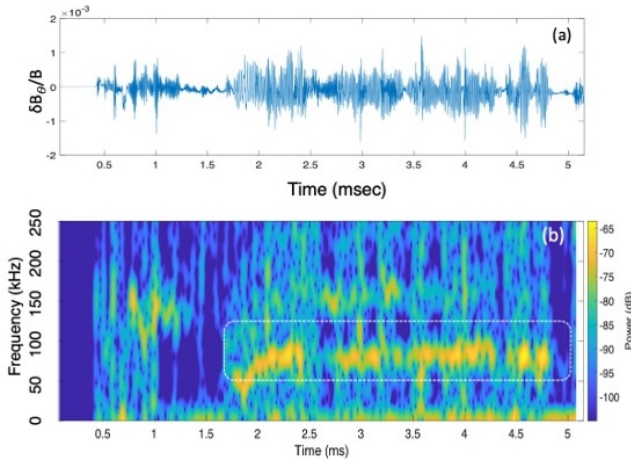
Figure 58. (a) Time evolution of poloidal magnetic field component at $\rho/\rho_{\text{edge}} = 0.2$, $\theta = 0$, $\zeta = 0$, (b) spectrogram of magnetic field signal in (a), with the dominant mode indicated at $\simeq 100$ kHz. Reproduced from [829].

new forms of moments closures, developed originally by Hammett and Perkins [882] demonstrated that Landau resonance phenomena could be included in fluid-like equations. This approach has been adapted to the analysis of EP instabilities through models such as TAEFL [844], FAR3d [883], MAS [884] and TGLF-EP [885, 886], which use closure relations optimized for Alfvénic instabilities. FLR stabilization effects are also included. FAR3d and TAEFL were based on coupling a set of EP gyrofluid equations to an existing global reduced MHD model. MAS [884] is also a global Landau closure model that has been tested in the linear regime for drift waves (ITG and KBM), internal kinks, and Alfvén instabilities (KAW, TAE and RSAE). TGLF-EP was developed starting from the flux-tube model TGLF [887] that incorporated gyro fluid closures for the modeling of drift waves.

The global EP gyrofluid model, FAR3d has been used to model a variety of EP instability observations in both tokamaks and stellarators [888]. It includes both linear and nonlinear options. The nonlinear saturated state is achieved through the inclusion of convective and $\boldsymbol{J} \times \boldsymbol{B}$ nonlinearities [829, 889, 890]. This model has been used for the long-time scale simulation of nonlinearly saturated AE modes observed in the DIII-D experiment, and has shown reasonable agreement. An example of the simulated poloidal magnetic field fluctuations and their associated spectrogram is shown in figure 58 [829]. In the EP density evolution equation the convective nonlinearity drives flattening of the fast ion profile in the region where the EP instability amplitude is strongest; EP transport fluxes can be derived from these profile changes. 2D zonal flow and current generation effects also are present and play a role in

regulating the nonlinear state. Mode coupling effects are well-resolved in this model and indicate that for the case of simulations with multiple toroidal modes, linear growth rates can be strongly altered by nonlinear mode coupling effects.

The TGLF-EP model [885, 886] provides a rapid method to evaluate local EP instability properties and has mostly been used for linear stability evaluations. TGLF-EP goes higher in the moments hierarchy than FAR3d and includes trapped particle and drift effects in the resonance conditions, in addition to the usual passing particle resonance. This model has been particularly useful in the development of critical gradient models for EP transport. Local variations in the EP density gradient drive are made until a local marginal stability state is achieved. By repeating this process over the full range of flux surfaces, a marginal stability EP density profile can be reconstructed and EP transport rates inferred from the profile flattening effects.

7.7. Nonlinear simulations of EP-driven modes with reduced models

Apart from the cutting-edge numerical models aimed at rigorous first principle coverage of all known essential physics effects, there has been significant progress in less rigorous but fast modeling that involves some phenomenological assumptions and free input parameters. Less accurate quantitative interpretation of wave-particle phenomena can be expected from such an approach with respect to first principle codes, especially for predictive simulations that are not constrained by experimental data. Nonetheless, these simplified models allow inexpensive scans across multiple discharges for a quick assessment of the relative role of instabilities in EP transport and losses. Such reduced models distill information from theory and first-principles codes and implement efficient numerical methods to cover EP transport in long-timescale integrated simulations [891–893].

The degree of model reduction determines which physics aspects are retained and to which degree of fidelity. The most common simplifications are assumptions about the instability spectrum and the transport mechanisms, a simplified representation of the EP population, and simple ad-hoc transport coefficients. When a Monte Carlo approach is used to simulate the EP evolution, such as in the NUBEAM module of TRANSP [894, 895], EP transport coefficients can be represented by matrices that describe the impact of modes on EP orbits as kicks in EP variables during the simulation. This EP kick model [896, 897] has been implemented in NUBEAM. The kick matrices are defined for the EP constants of motion (COM) $(\mathcal{E}, \mu, P_\phi)$ [898]), see section 2. For

each $(\mathcal{E}, \mu, P_\phi)$ region (or bin), a 2D matrix represents the conditional probability $p(\Delta\mathcal{E}, \Delta P_\phi | \mathcal{E}, \mu, P_\phi)$ of correlated kicks in $\mathcal{E}$ and P_ϕ resulting from EP interaction with instabilities. The kick matrix comes from particle following codes such as ORBIT [897, 898]. For Alfvénic modes, MHD codes such as NOVA [899] provide a radial mode structure to use in ORBIT. Analytic representations can also be used to represent kink modes, fishbones, and NTMs. Kick amplitudes in NUBEAM are time-dependent according to a user-supplied waveform. If the mode damping rate is known, the model can adjust the amplitude accordingly [897]. The kick model has been applied to several experiments to study EP transport by Alfvénic modes [224, 861, 897, 900], NTMs [224, 300, 352, 901] and internal kinks [375, 379, 382], including scenarios with multiple instabilities present simultaneously [323, 331]. By retaining full phase-space details and realistic EP distribution functions from NUBEAM, the model is suitable for detailed comparisons between simulation results and EP diagnostics [224, 300, 352, 375, 379] via synthetic diagnostic codes such as FIDASIM [902, 903]. Application of the kick model to ITER requires more work to meet the remaining challenges. Work is in progress to extend and validate the model to multi-species plasmas (D, T, or fusion products) [46, 904, 905], leveraging new data from the recent JET D-T campaign [50, 51]. Also, depending on the granularity of $(\mathcal{E}, \mu, P_\phi)$ bins, matrices can be memory-consuming, and the model requires amendments to cover multiple modes.

For multiple Alfvénic modes, in scenarios with either isolated or overlapping resonances, a resonance-broadened quasi-linear theory, originally proposed in [906], provides a way to reduce the dimensionality of the problem while still capturing the essential dynamics in the EP diffusive regime [907]. The Resonance Broadening Quasi-linear model RBQ [820, 908] computes the diffusion coefficients to relax the distribution function of EPs while simultaneously evolving the amplitudes of multiple modes. The model, originally developed to account for diffusion along P_ϕ only [820, 908], has recently been upgraded to resolve the $(\mathcal{E}, P_\phi)$ correlation (equation 13) for resonant interactions, $\Delta P_\phi/\Delta\mathcal{E} = n/\omega$ [909]. RBQ has motivated recent basic analytic work on the formulation of quasilinear theory in a broad sense. For instance, sufficiently close to marginal stability, collisions regulate the wave evolution, phase memory is poorly retained and the EP dynamics becomes time-local [910, 911]. This understanding led to the formulation of a self-consistent quasi-linear theory [912, 913] that recovers the exact saturation level of the more complex nonlinear theory [914], while being considerably less computationally demanding.

An essential ingredient of the theory, the shape of the resonance (window) function, previously employed with an arbitrary ad-hoc shape, emerges spontaneously in the self-consistent derivation [912, 913]. This self-consistent window function is used in RBQ [837], yielding better agreement when compared with the nonlinear Vlasov code BOT [915]. Verification of the width of the wave-particle interaction has been performed using the guiding center following code ORBIT [916]. The model can be used to find the relaxed EP profile with self-consistent mode amplitudes, based on AE structure and spectrum from MHD codes such as NOVA [899] or LIGKA [514], and the EP drive calculated for an analytic slowing down distribution. RBQ has been used to assess NBI ion transport by AEs on DIII-D [917]. At present, RBQ communicates with TRANSP/NUBEAM via the same 5D transport matrix formalism as the kick model. The RBQ diffusion coefficients provides Gaussian probabilities for $(\Delta\mathcal{E}, \Delta P_\phi)$. Work is in progress to provide a direct interface and reduce the memory usage with respect to the kick model. Further heuristic elements lead to critical gradient models such as TGLF-EP [855, 885, 918] and CGM [919], which seek a solution for the EP radial flux such that the EP drive balances the mode damping at each radial location. The radial diffusion coefficient computed from the EP flux can be used as an input for TRANSP.

As mentioned above in subsection 7.4, the TGLF-EP reduced model [885, 886] provides an additional method for evaluating nonlinear Alfvén instability driven EP transport using an approach known as a critical gradient model. TGLF-EP uses the TGLF [887] local flux tube gyro-Landau closure model to evaluate AE instability growth rates on each flux surface in the ballooning limit and find the marginal stability point (or point where the growth rate is below some minimum level) by varying the EP gradient drive. Under the assumption of stiff transport (i.e., rapidly increasing transport as AE modes destabilize), a steady-state solution of the EP continuity equation (including beam/fusion source, slowing-down sink, and diffusive AE flux) gives the marginally stable EP density profile. The underlying stiff-transport assumption has been checked [830, 886] against simulations using the gyrokinetic code GYRO [920]. The calculated effective diffusivity can be coupled into integrated simulations. This model has been confirmed with EP profiles measured on DIII-D from FIDA measurements and neutron deficit data [547, 860, 921]. It has also been applied to cases from ITER [855].

Finally, reduced modeling can also lead to simulations of the EP distribution function fast enough to allow real-time control of discharges.

The RABBIT code is such a model allowing very fast computations of the NBI distribution functions neutral-beam populations based [922–924].

7.8. Application of nonlinear simulation models to ITER

The parameters of ITER introduce new regimes for nonlinear Alfvén turbulence with unstable modes extending to higher toroidal mode numbers (i.e., smaller ρ_{Lf}/a allows instability at higher wavenumbers before FLR stabilization becomes active). This results in many interacting modes and closely spaced Alfvén gap locations. As described above, there are a variety of models now under development to address the nonlinear physics of ITER burning plasma scenarios. A recent collaboration of nonlinear EP models focused on simulating these effects as part of an ITPA joint simulation activity [571]. Both an ITER pre-fusion baseline scenario case (#101006) and a steady-state case (#131041) with a reversed shear q-profile [925] were considered. The pre-fusion baseline case indicated that a weak fishbone instability was present, but that Alfvén modes were stable; only weak neutral beam ion redistribution was predicted. The steady-state case (in the DT phase) contained both anisotropic neutral beam ions and isotropic alpha particles. Due to the stronger drive and reversed q-profile, it showed stronger Alfvénic growth rates than for cases with monotonic q-profiles. The global nonlinear models applied to this case included GTC, MEGA, FAR3d, M3D-C1 [926], [571]. Also, the reduced RBQ and TGLF-EP models [927] were applied in this study. The most unstable modes were BAEs and RSAEs and were located near the $q_{\min}$ surface. All models [571] indicated high levels of transport (50 to 70 m^2/s) both for the beams and alphas. The simulations were limited to relatively short time intervals (~ 0.25 ms). In contrast, NBI-driven cases from DIII-D with similar q-profiles only resulted in a few unstable AEs. If this level of transport extrapolates to longer timescales, it would be difficult to sustain a steady-state burning plasma. In particular, the maintenance of reversed shear q-profiles will be important to achieve non-inductive (bootstrap current aligned) steady-state operation. Future directions for this type of modeling should include longer timescale integrated simulations that include cross-scale coupling between MHD, AEs, microturbulence and the self-consistent effects of alpha and beam source functions.

7.9. Soft and hard nonlinearities of near-threshold instabilities

The advent of burning plasmas might suggest an increase focus on alpha-driven instabilities in burning plasmas. However, a large part of the underlying physics is generic and understandable at a very basic level within properly idealized models of wave-particle interaction. Even though the EP pressure can be comparable to the bulk plasma pressure, the EP density is usually much smaller than the bulk particle density. EPs hence interact mainly with the bulk plasma rather than among each other. EPs have, by definition, a non-Maxwellian distribution which has free energy available to excite waves via wave-particle resonances. Depending on the problem of interest, the free energy can come either from inverted velocity-space gradients, anisotropy, or from spatial gradients of the EP distribution function (section 6).

EP instabilities have typically much shorter intrinsic timescales than the particle or energy confinement time. Consequently, linear stability analysis of a given initial configuration does not cover how the instability saturates in the presence of particle sources and the slow collisional relaxation processes. To address saturation in general, the theory must be nonlinear, which is still a challenge. However, given the difference in timescales and given that the system is weakly driven, the instability should occur in a near-threshold regime, and then the nonlinear stage is often tractable analytically.

There are two basic sources of nonlinearity: the nonlinearity of the EP motion in the field of the excited waves and the nonlinearity of the bulk plasma. In each of these two cases, it is critical to determine whether the near-threshold instability exhibits a soft or a hard nonlinear regime, i.e., whether it can be stabilized by weak nonlinearity or not. First, the soft or hard regime require different theoretical and numerical tools to describe the system, and second, there are immediate experimental implications. In particular, the fishbone instability [722] generally requires treatment of wave-particle resonances and bulk plasma nonlinearities. For AEs, the nonlinear interaction of EPs with linear waves dominates the problem. In what follows, we first present a theory of single resonance phenomena, and then discuss particle transport in the presence of multiple modes.

7.10. Weakly nonlinear near-threshold dynamics

The interplay of the key ingredients in the problem of wave-particle interaction can be understood within a simple electrostatic bump-on-tail model that exhibits the characteristic nonlinear scenarios. Within this model, the bulk plasma is represented by cold electrons, and we assume that there are sources and sinks that create an unstable energetic electron tail. The tail provides an instability drive γ_{drive} due to a positive gradient of the velocity distribution function F (see figure 59).
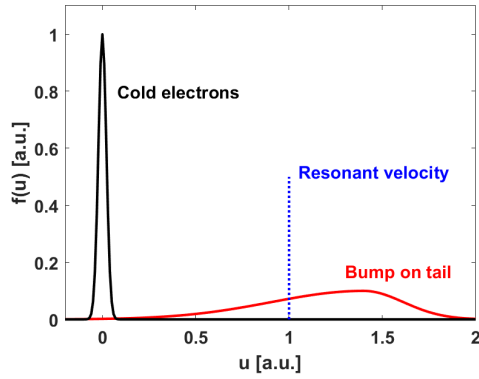
The unstable mode in this case is a plasma wave,

74

Figure 59. Unstable bump-on-tail distribution function with a positive gradient at the resonant velocity.

and its eigenfrequency, ω_{pe}, is the cold-electron plasma frequency. The cold-electron collision frequency ν_{cold} provides a linear damping rate $\gamma_{\mathrm{damp}} = \nu_{\mathrm{cold}}/2$ of the mode that determines the the minimum slope of $F_0(u)$ needed to excite a mode, i.e. the instability threshold. The spectrum of EP-driven modes in a tokamak is generally discrete due to periodicity in the toroidal and poloidal directions and the radial boundary conditions (section 6). To take that into account in the bump-on-tail model, we consider a single electrostatic mode with a given wavelength λ and wavenumber $k = 2\pi/\lambda$. The electric field of the mode can then be written as

$$E = \frac{1}{2}\left[\delta E(t)\exp(ikx - i\omega_{\mathrm{pe}}t) + \mathrm{c.c.}\right], \tag{74}$$

where $\delta E(t)$ is a slowly varying complex amplitude and c.c. denotes the complex conjugate. The basic equations for the bump-on-tail problem are the kinetic equation for the energetic electrons and the wave evolution equation

$$\frac{\partial F}{\partial t} + u\frac{\partial F}{\partial x} + \frac{e}{2m}\left[\delta E(t)\exp(ikx - i\omega_{\mathrm{pe}}t) + \mathrm{c.c.}\right]\frac{\partial F}{\partial u}$$

$$= \left[\frac{\nu^3}{k^2}\frac{\partial^2}{\partial u^2} + \frac{\alpha^2}{k}\frac{\partial}{\partial u} - \beta\right](F - F_0) \tag{75}$$

$$\frac{\partial \delta E}{\partial t} = -4\frac{\omega}{k}\pi e \int \langle F\exp(-ikx + i\omega_{\mathrm{pe}}t)\rangle\,\mathrm{d}u - \gamma_{\mathrm{damp}}\delta E, \tag{76}$$

where $\langle ... \rangle$ denotes averaging over wavelength. The right-hand side of the kinetic equation describes three different collision models for the resonant tail electrons: velocity-space diffusion, drag, and Krook-type collisions [928]. The characteristic rates for these collisions are characterized by the quantities ν (velocity-space diffusion), α (collisional drag), and β (Krook model collisions), respectively (note that these

specific meanings for ν, α, β are specific for this subsection and do not apply in other parts of this paper). The collision operator also includes the source and sink terms written as $\left(\frac{\nu^3}{k^2}\frac{\partial^2}{\partial u^2} + \frac{\alpha^2}{k}\frac{\partial}{\partial u} - \beta\right)F_0$, which sets up an equilibrium distribution function F_0 in the absence of the wave field. The appropriate collision operator for the problem is determined by what collisional process is dominant at the wave-particle resonance in phase space. For EPs in a tokamak, Coulomb collisions can be described as a combination of pitch angle scattering and electron drag (section 2) [76, 929]. The former can be represented by a diffusive operator, while the latter introduces a slowing-down operator to the kinetic equation. The near-threshold regime of wave excitation makes it possible to expand the perturbed distribution function F in powers of the wave amplitude δE and solve the kinetic equation iteratively. The actual expansion parameter is $\omega_{\mathrm{B}}t$, where

$$\omega_{\mathrm{B}} \equiv (k|\delta E|e/m)^{1/2} \tag{77}$$

is the bounce frequency of the resonant particles trapped in the wave, and t is the time interval of interest. The first term in the power series for F gives the linear instability drive $\gamma_{\mathrm{drive}}\delta E$ in the wave equation (76). The difference between γ_{drive} and γ_{damp} is small in the near-threshold limit, which allows the lowest order nonlinear correction to compete with this difference. It follows from the expansion procedure that the nonlinear correction to the wave growth rate scales as $\gamma_{\mathrm{drive}}(\omega_{\mathrm{B}}t)^4$ whereas the linear growth rate itself is $\gamma_{\mathrm{drive}} - \gamma_{\mathrm{damp}} \ll \gamma_{\mathrm{drive}}$. Consequently, the lowest order nonlinearity becomes important when $(\omega_{\mathrm{B}}t)^4 \approx (\gamma_{\mathrm{drive}} - \gamma_{\mathrm{damp}})/\gamma_{\mathrm{drive}} \ll 1$. At this level, the next-order nonlinear term, $\gamma_{\mathrm{drive}}(\omega_{\mathrm{B}}t)^8$, is still negligible. Thus, the inequality $(\gamma_{\mathrm{drive}} - \gamma_{\mathrm{damp}})/\gamma_{\mathrm{drive}} \leqslant (\omega_{\mathrm{B}}t)^4 \ll 1$ defines a window in which the dynamics are already nonlinear, but the nonlinearity can still be treated perturbatively. The ensuing relation between the perturbed distribution function and the wave field involves a sequence of time integrations. Once this relation is used in equation (76), we obtain a cubic integro-differential equation for the wave amplitude, which can be written in the following dimensionless form:

$$\frac{\mathrm{d}A}{\mathrm{d}\tau} = A(\tau) - \frac{1}{2}\int_0^{\tau/2}\mathrm{d}z z^2 A(\tau - z) \times$$

$$\int_0^{\tau - 2z}\mathrm{d}x\exp\left[-\hat{\nu}^3 z^2(2z/3 + x) - \hat{\beta}(2z + x) - i\hat{\alpha}^2 z(z + x)\right]$$

$$\times A(\tau - z - x)A^*(\tau - 2z - x). \tag{78}$$

75

The dimensionless amplitude A in this equation is defined as

$$A = (k\delta Ee/m)\left(\frac{\gamma_{\text{drive}}}{\gamma_{\text{damp}}} - 1\right)^{-1/2}(\gamma_{\text{drive}} - \gamma_{\text{damp}})^{-2}, (79)$$

the dimensionless time is $\tau = (\gamma_{\text{drive}} - \gamma_{\text{damp}})t$ and the normalized relaxation rates are defined as $\hat{\nu} \equiv \nu/(\gamma_{\text{drive}} - \gamma_{\text{damp}})$, $\hat{\alpha} \equiv \alpha/(\gamma_{\text{drive}} - \gamma_{\text{damp}})$, and $\hat{\beta} \equiv \beta/(\gamma_{\text{drive}} - \gamma_{\text{damp}})$. The cubic nonlinear equation (78) was originally derived in [914, 930] for the diffusive and Krook-type collisions, and it has been generalized in [931] to include the effect of drag. According to equation (78), the initial linear instability can develop into a soft or hard nonlinear regime. In the soft case, the amplitude A saturates at a finite level. In the hard case, the solution for the amplitude A rapidly grows in a finite time. Without drag ($\hat{\alpha} = 0$), a saturated solution of equation (78) is

$$|A|^2 = 2\left[\int_0^\infty \frac{z^2\mathrm{d}z}{\hat{\beta} + \hat{\nu}^3 z^2}\exp\left(-2\hat{\nu}^3 z^3/3 - 2\hat{\beta}z\right)\right]^{-1} (80)$$

for $\tau \to \infty$. If the annihilation rate $\hat{\beta}$ and/or diffusion rate $\hat{\nu}$ are above some threshold, the amplitude approaches that solution. However, if $\hat{\beta}$ and $\hat{\nu}$ are below this threshold, the steady saturated solution is unstable. The solution then has a characteristic "pitchfork splitting", a periodic limit-cycle behaviour. An experimental example of pitchfork splitting driven by ICRF-accelerated tail ions appears in figure 60 [932].

A further reduction in relaxation rates leads to period doubling bifurcations, resulting in a chaotic mode amplitude evolution and explosive growth of the mode [932–934]. The cubic nonlinear term in equation (78) destabilizes the mode for pure drag (where $\hat{\beta} = \hat{\nu} = 0$), so the mode is then explosive. Then there are no saturated solutions for equation (78), and the mode amplitude grows beyond the applicability range of equation (78). When both drag and diffusion are present, steady saturated solutions are only prohibited when the integral in equation (78) has a negative real part for $\tau \to \infty$. This occurs when $\hat{\nu}/\hat{\alpha} < 1.043$ (dashed line in figure 61). However, some of the formal steady solutions for $\hat{\nu}/\hat{\alpha} > 1.043$ have been shown to be unstable [931]. The solid line in figure 61 represents the stability boundary between stable and unstable steady solutions. Recent work shows that, in contrast to diffusion, drag fundamentally shifts the resonance condition in the quasilinear regime, producing shifts and splitting of the resonance lines that alter the saturated amplitude [913].

The explosive growth described by equation (78) allows the growing wave to reach the level of resonant particle trapping by the wave. One might, therefore, expect that particle trapping will flatten the
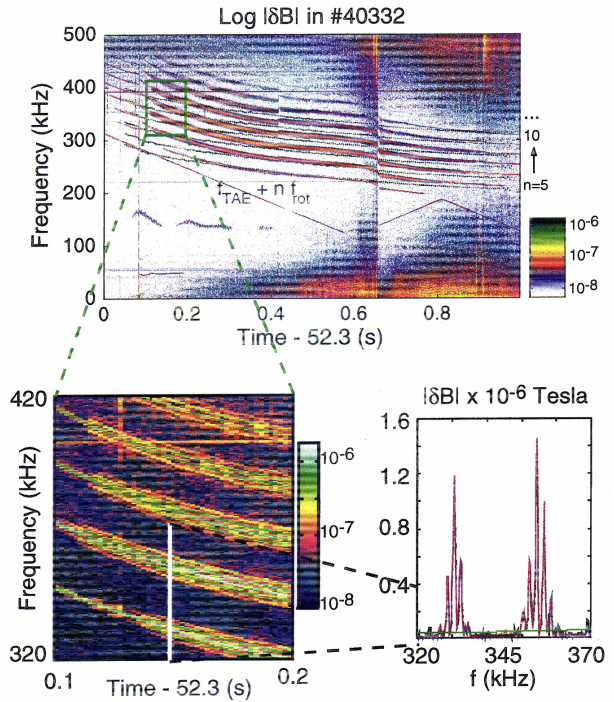

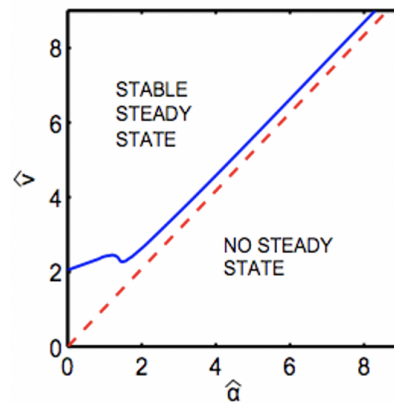**Figure 60.** Nonlinear splitting of AEs in JET [932, 933]. Reproduced from [932].

Figure 61. The boundaries in parameter space that give stable, unstable and no steady state solutions to equation (78). The unstable solution lies in between the solid and dashed lines. Reproduced from [931].

distribution function near the resonance and eliminate the instability drive, after which the wave will decay quickly because of the background damping. However, the solution of equations (75) and (76) reveals a remarkably different behaviour. It exhibits formation of long-living coherent structures with time-dependent frequencies, as discussed next.

7.11. Spontaneous frequency sweeping, phase-space holes and clumps

The tendency for the mode frequency to change in the strongly nonlinear regime is already seen in the explosive solution of the reduced cubic equation (78). The explosive solution is in fact oscillatory, and the period of oscillations in the wave amplitude A shortens as the solution approaches the singularity. These oscillations indicate that the wave tends to split into the upshifted and downshifted sidebands. The fully nonlinear set of equations (75) and (76) prevents the mode from growing indefinitely. However, the trend for frequency sweeping continues, as found numerically in [683, 684] and shown in figure 62.
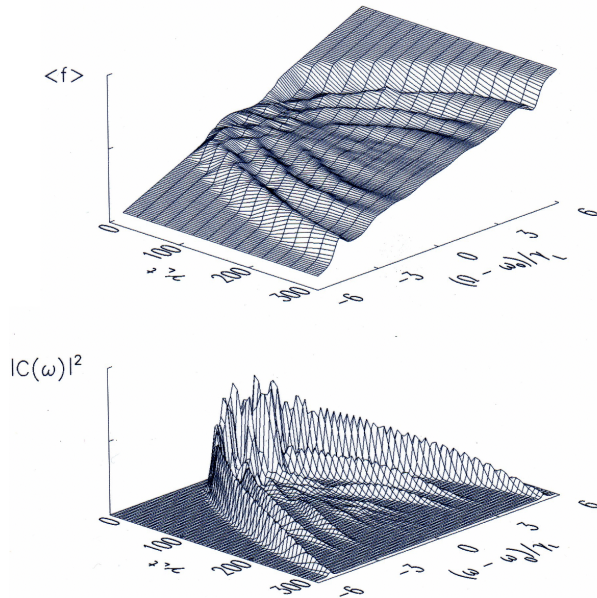

Figure 62. Evolution of the particle distribution function and wave spectrum after explosive formation of holes and clumps in the hard nonlinear regime of near-threshold instability. Reproduced from [684].

The time-dependent wave spectrum (lower plot in figure 62) correlates perfectly with the evolution of the spatially averaged particle distribution function (upper plot). The latter exhibits an upward moving depletion (hole) and a downward moving protrusion (clump). The hole and clump contain particles trapped

in the upshifted and downshifted waves, respectively. Unlike the fast explosive onset of holes and clumps, the evolution shown in figure 62 takes place over many bounce periods of the particles that are trapped in the wave, so that these particles respond to the wave field adiabatically. Conservation of the adiabatic invariant preserves the values of the particle distribution function within the trapped particle areas of phase space. The reasons for frequency sweeping shown in figure 62 are the presence of dissipation in the bulk plasma and the availability of free energy in the EP distribution.
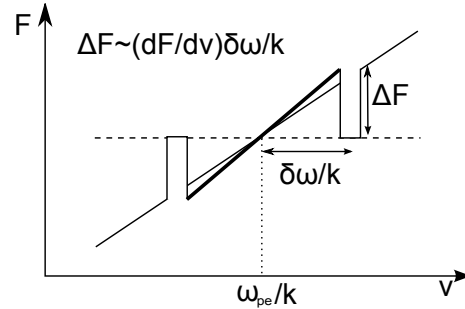

Figure 63. Adiabatic motion of hole and clump releases kinetic energy of the EPs. The increased slope of the distribution function in the wake (thick line) facilitates formation of subsequent holes and clumps. Reproduced from [915].

A schematic snapshot of the distribution function in figure 63 shows that the particle kinetic energy decreases when the hole and clump move away from the original resonance with the constant values of the distribution function at the bottom of the hole and the top of the clump. This energy release balances the dissipation in the background plasma to allow the wave to last over hundreds of linear damping times. As shown in [683], each hole and clump represent a nonlinearly saturated wave with

$$\omega_{\rm B} = \left(16/3\pi^2\right)\gamma_{\rm drive}. \tag{81}$$

Calculation of the power release via frequency sweeping relies on the knowledge that the distribution function of passing particles is smooth around holes and clumps. This calculation gives the following square root time-dependence for the frequency shift in the absence of EP collisions [683]:

$$\delta\omega = \left(16/3\pi^2\right)\gamma_{\rm drive}\sqrt{2\gamma_{\rm damp}t/3}. \tag{82}$$

The results shown in figure 62 are consistent with this relation. More recent simulations with improved computational accuracy [915] reveal that holes and clumps are produced continuously in the collisionless case. This can be understood by noting that the slope of the distribution function at the original resonance steepens somewhat after the hole and clump move away

from it. There is, therefore, a tendency for a recurrent instability. The presence of drag and velocity space diffusion adds interesting new features to the behavior of holes and clumps [915]. The drag alone breaks the symmetry of the sweeping pattern, as demonstrated in figure 64.
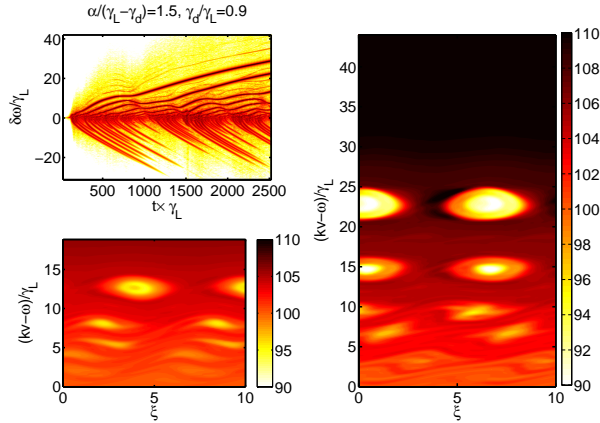

Figure 64. Effect of drag on holes and clumps. The plots show an asymmetric frequency spectrum and two snapshots of the particle distribution in phase space. Reproduced from [915].

The source term in the drag collision operator acts to enhance a phase space hole and weaken, or even suppress, a phase space clump. Also, the combined effect of drag and velocity space diffusion can produce the repetitive pattern of hook-shaped frequency chirping events shown in figure 65.
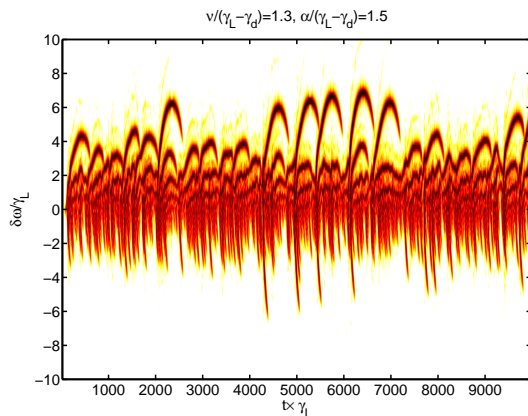

Figure 65. Hooked frequency spectrum of holes and clumps represents interplay of drag and diffusive collisions. Reproduced from [915].

7.12. Long-range sweeping

The initial theory for phase space holes and clumps was limited to the case of small frequency deviations from the bulk plasma eigenfrequency [683, 684]. However, there are multiple experimental observations of frequency sweeping events in which the change in frequency is comparable to the frequency itself [578, 690, 696]. A non-perturbative theoretical formalism [935] is needed to interpret such a long-range frequency sweeping event.

Since the EPs typically have a much lower density than the bulk plasma, at first sight it seems unlikely that they can change the Alfvén eigenmode frequency significantly. However, a small but coherent group of EPs can generate a detectable signal at a different frequency than the bulk plasma eigenfrequency. Consider, for example, a modulated beam in a plasma. The initial modulation occurs spontaneously because of instability at the plasma eigenmode frequency.

However, as the coherent structure evolves due to dissipation, the trapped EPs gradually decelerate while maintaining their coherency. Consequently, the resulting frequency undergoes a significant shift from the initial frequency. This can be described as a nonlinear Bernstein-Greene-Kruskal (BGK) mode [936]. A solution of this type was obtained for a one-dimensional bump-on-tail model with immobile ions. The perturbed electrostatic potential ϕ takes the form

$$\phi \equiv -\frac{1}{|e|} U\left(x - s(t), t\right). \tag{83}$$

The electron potential energy U is a periodic function of its first argument $(x - s(t))$ and a slowly varying function of the second argument t. Additionally, the wave phase velocity $\dot{s} \equiv \mathrm{d}s(t)/\mathrm{d}t$ is a slowly varying function of time, characterized by a sweeping rate $\ddot{s}$.

For small deviations of $\dot{s}$ from $\dot{s}_0$ (early phase of frequency sweeping), a sinusoidal mode with constant amplitude occurs at the beginning of frequency sweeping [683, 935]. For large deviations of $\dot{s}$ from $\dot{s}_0$, the amplitude and the mode structure change significantly. Figure 66 illustrates the separatrix between the passing and trapped particles which changes its shape.

While the separatrix shrinks, some of the originally trapped EPs now become passing particles. The EPs that remain trapped decelerate to lower velocities and supply their energy to the wave. The power extracted from the EP population balances the power dissipated in the bulk plasma, and thus determines the rate of sweeping needed to compensate for collisional dissipation of the BGK-mode. This power balance condition reproduces the square root scaling of frequency sweeping during the initial phase of the sweep [683]. Later on, the mode phase velocity $\dot{s}$ deviates gradually from this square root scaling. This process is interpreted as a transformation of the initial plasma wave into a nonlinear EPM. EPMs might be generated by Alfvén wave instabilities in an analogous way [403, 480, 937]. Such a nonlinear modification of
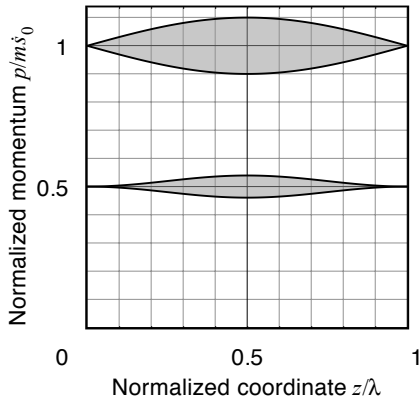
Figure 66. Evolution of the phase-space bucket during sweeping event. The plot shows the initial separatrix (upper shaded area) and the shrunken separatrix at half of the initial mode phase velocity (lower shaded area). Reproduced from [28].

the mode structure appears to be essential to generate EPMs from AEs.

The analysis of the 1D electrostatic bump-on-tail problem leads to an analogous approach for understanding frequency-sweeping phenomena in tokamaks. In experiments, these events can be linked to the resonant excitation of TAEs. For a linear mode, the resonance condition is

$$\omega - n\omega_\phi(P_\phi, P_\theta, P_\psi) - l\omega_\theta(P_\phi, P_\theta, P_\psi) = 0, \qquad (84)$$

where ω is the mode frequency, $\omega_\phi(P_\phi, P_\theta, P_\psi)$ and $\omega_\theta(P_\phi, P_\theta, P_\psi)$ are the toroidal and poloidal transit frequencies, and n and l are integers. The canonical action-angle variable pairs (P_ϕ, ϕ), (P_θ, θ), and (P_ψ, ψ) describe the integrable unperturbed motion. However, (P_ψ, ψ) describes the Larmor radius gyration which is much faster than the wave period, so that gyration does not resonate with shear Alfvénic perturbations. For an isolated linear resonance, the perturbed particle Hamiltonian is a sinusoidal function of $\omega t - n\phi - l\theta$. The transition to the nonlinear case now generalizes the Hamiltonian to

$$H = H_0 + U\left(\int_0^t \omega\,(\tau)\,\mathrm{d}\tau - n\phi - l\theta, t\right), \qquad (85)$$

where the function U to be determined numerically is a not necessarily sinusoidal but still periodic function of its first argument. Note that P_ψ and $P = lP_\phi - nP_\theta$ are constants of motion and that since the function U evolves slowly, it should preserve an adiabatic invariant for trapped particles. These three conservation laws suggest a relationship between the trapped particle distributions at any two locations of the resonance as illustrated in figure 67.
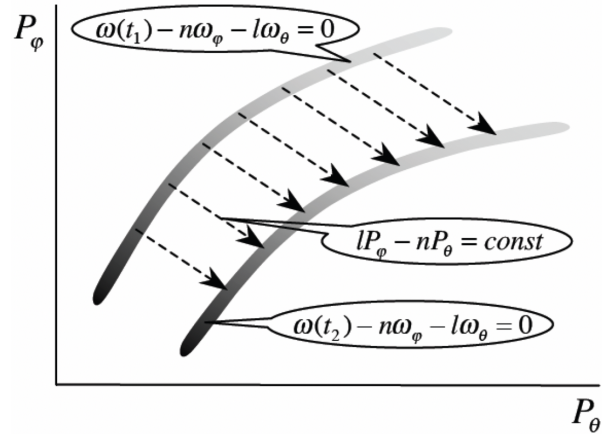

Figure 67. Transport of resonant particles during frequency sweeping. The shaded areas are snapshots of the moving resonant region in the momentum space. The shades of grey mark different values of the particle distribution function. The trapped resonant particles form a locally flat distribution across the resonance and preserve the value of their distribution function when the resonance carries them along the dotted lines. Reproduced from [28].

The macroscopic quantities, like the perturbed EP pressure, now become known functions of the potential energy profile U and the unperturbed distribution. To determine the wave profile U, we can now solve a set of linear MHD equations for the bulk plasma response with an analytic nonlinear source from the EPs. The frequency sweeping rate can then be obtained from the power balance condition.

7.13. Multiple modes and global transport of EPs

A single unstable Alfvén mode tends to be benign in terms of global losses of EPs. The fundamental reason for this is that the resonances associated with a single mode occupy only a small fraction of the particle phase space. Many modes are usually needed to achieve resonance overlap in a large part of phase space and thereby produce global diffusion. When more than one unstable mode is present in the system, these modes are basically independent if their wave-particle resonances do not overlap. Then the waves should flatten the particle distribution function locally near each resonance. However, when the resonances overlap, the particle motion becomes stochastic, which allows individual particles to diffuse in phase space over many resonances and flatten the distribution function over a larger phase space area. This stochastic motion gives rise to both the velocity space transport and real space transport. The relative importance of the two is different for different instabilities but the mathematical description of the resulting transport is essentially the same from the technical standpoint. Particle diffusion

over a set of overlapping resonances can be described by quasilinear theory. The constants of motion $(\mathcal{E}, P_\phi, \mu)$ of unperturbed particle orbits are no longer guaranteed to be constant if there are overlapping resonances. However, the particle magnetic moment μ remains almost constant for wave-particle interaction with AEs since the wave frequency is much smaller than the cyclotron frequency. In addition, the particle energy remains almost constant if the wave frequency is much smaller than the other two terms in the resonance condition

$$\omega - n\omega_\phi(\mathcal{E}, P_\phi, \mu) - l\omega_\theta(\mathcal{E}, P_\phi, \mu) = 0, \qquad (86)$$

which consequently almost balance each other. The waves then affect mostly the toroidal canonical angular momentum P_ϕ and hence the radial position of the particle orbit described by the flux surface in the poloidal cross-section of the tokamak. The width of the resonance (86) in δP_ϕ can roughly be estimated from

$$\delta P_\phi \frac{\partial}{\partial P_\phi}\left(\omega - n\omega_\phi(\mathcal{E}, P_\phi, \mu) - l\omega_\theta(\mathcal{E}, P_\phi, \mu)\right) = \omega_{\mathrm{b}}. (87)$$

Here, ω_{b} is the nonlinear bounce frequency for a resonant particle in the wave field. Whereas ω_{B} in subsection 7.10 represents an electrostatic mode, ω_{b} represents the perturbed magnetic field of an electromagnetic mode. Both ω_{B} and ω_{b} are proportional to the square root of the mode amplitude.

The 1D quasilinear diffusion equation in P_ϕ is

$$\frac{\partial f}{\partial t} - \frac{\partial}{\partial P_\phi} D \frac{\partial f}{\partial P_\phi} = -\nu\left(f - f_0\right). \qquad (88)$$

D is the diffusion coefficient, which is proportional to the wave intensity and and is given by

$$\frac{\partial D}{\partial t} = 2\left(a\frac{\partial f}{\partial P_\phi} - \gamma_{\mathrm{damp}}\right)D. \qquad (89)$$

The damping rate γ_{damp} sets an instability threshold and is assumed to be smaller than γ_0. f_0 is a classical equilibrium distribution function, and the Krook-type relaxation $-\nu\left(f - f_0\right)$ drives the distribution towards this equilibrium distribution. The gradient of this equilibrium distribution in P_ϕ can drive the waves unstable with a linear growth rate $\gamma_0 = a\frac{\partial f}{\partial P_\phi}$. The factor a depends on the modes that resonate with the particles for a given value of P_ϕ.

If there are no waves, the distribution function f will converge to $f = f_0 \sim \frac{\gamma_0}{a}P_\phi$. But if waves are present, the steady-state solution of (88) and (89) gives $f = \frac{\gamma_{\mathrm{damp}}}{a}P_\phi < f_0$, i.e. smaller than f_0. The diffusion coefficient can then be estimated as

$$D \approx \frac{a}{\gamma_{\mathrm{damp}}}\nu f_0 P_\phi \approx \nu\frac{\gamma_0}{\gamma_{\mathrm{damp}}}P_\phi^2. \qquad (90)$$

To obtain the resonance overlap constraint on the steady regime, we consider a set of barely overlapping resonances for which the correlation time is the inverse of the bounce frequency $1/\omega_{\mathrm{b}}$, and the diffusion coefficient is

$$D \approx \omega_{\mathrm{b}}(\delta P_\phi)^2$$
$$\approx \frac{\omega_{\mathrm{b}}^3}{\left\{\frac{\partial}{\partial P_\phi}\left[\omega - n\omega_\phi(\mathcal{E}, P_\phi, \mu) - l\omega_\theta(\mathcal{E}, P_\phi, \mu)\right]\right\}^2}, \qquad (91)$$

which can be written as

$$D \approx (\delta P_\phi)^3 \frac{\partial}{\partial P_\phi}\left[\omega - n\omega_\phi(\mathcal{E}, P_\phi, \mu) - l\omega_\theta(\mathcal{E}, P_\phi, \mu)\right]. \qquad (92)$$

If there are N resonant modes in the full range of P_ϕ, then the overlap condition becomes

$$D > \left(\frac{P_\phi}{N}\right)^3 \frac{\partial}{\partial P_\phi}\left[\omega - n\omega_\phi(\mathcal{E}, P_\phi, \mu) - l\omega_\theta(\mathcal{E}, P_\phi, \mu)\right]. \qquad (93)$$

Equations (90) and (93) suggest that the resonance overlap condition requires a source strength at least given by

$$\nu\frac{\gamma_0}{\gamma_{\mathrm{damp}}} > \frac{1}{N^3}P_\phi\frac{\partial}{\partial P_\phi}\left[\omega - n\omega_\phi(\mathcal{E}, P_\phi, \mu) - l\omega_\theta(\mathcal{E}, P_\phi, \mu)\right]. \qquad (94)$$

If the source strength is weaker than that, the global transport completely terminates, or it becomes intermittent if the individual modes can reach the overlap condition somewhere during their nonlinear evolution.

If there is no resonance overlap, the EPs are not transported from one resonance to the next, i.e., they do not move across the Kolmogorov-Arnold-Moser (KAM) surfaces between the resonances. If such transport barriers can be created on purpose, especially at the plasma edge, they may lead to good global confinement of EPs even if there is a local instability in the core.

We may also obtain an overlap condition for individually saturated modes, which follows immediately from equation (87) and the estimate for the nonlinear bounce frequency obtained in [938],

$$\omega_b \approx \gamma_0\left(1 + \frac{\nu}{\gamma_{\mathrm{damp}}}\right). \qquad (95)$$

This overlap condition for individually saturated modes is

$$\gamma_0\left(1 + \frac{\nu}{\gamma_{\mathrm{damp}}}\right)$$
$$> \frac{1}{N}P_\phi\frac{\partial}{\partial P_\phi}\left[\omega - n\omega_\phi(\mathcal{E}, P_\phi, \mu) - l\omega_\theta(\mathcal{E}, P_\phi, \mu)\right], \qquad (96)$$

which is much more restrictive than equation (94). The substantial difference between equations (94) and (96) for large N arises from the enhanced energy release per mode for overlapping resonances compared to isolated modes. Consequently, even if neighboring modes are linearly stable, an overlap of two closely spaced resonances could couple the neighbouring modes and trigger an avalanche-type relaxation event.
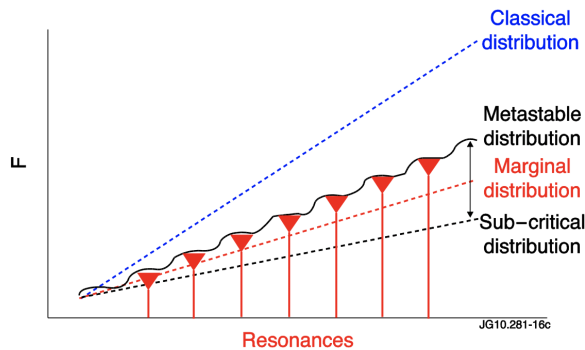

Figure 68. Cartoon illustrating intermittent quasilinear relaxation due to resonance overlap in the multi-mode regime. The resonances broaden and eventually overlap as the modes grow above the instability threshold. The EP population drops to subcritical values and then is replenished by the source to a metastable level that exceeds the linear threshold level due to separation of neighboring linear resonances. Reproduced from [28].

During such an event, rapid quasilinear diffusion can decrease the EP density to a subcritical value below the linear instability threshold. This process is illustrated in figure 68. Subsequently, the waves will decay within a linear damping time, and the system will be quiescent until a particle source makes the EP population unstable again, triggering the next avalanche.

In intermittent diffusion, the bursts of different modes are synchronized due to the triggering effect. Due to these bursts, the EP population is close to the marginally stable level, in the steady as well as the intermittent quasilinear regimes. The primary difference lies in the time behavior of the turbulence level. The profile stiffness resulting from this marginal stability condition causes the turbulence level to self-adjust, maintaining a similar profile regardless of the strength of the particle source. The time-averaged transport coefficients are given by the injection rate and gradients of the marginally stable profile. However, the turbulence responsible for enhanced transport is caused by the small deviations away from marginal stability. Predicting the turbulence level based on a few macroscopic parameters such as the EP pressure or density gradient becomes challenging but might turn out to be unnecessary. Instead, a better route for theory-experiment comparison might be to

examine marginal stability constraints and resonance overlap criteria. This requires numerical tools for linear stability assessments for realistic magnetic configurations and plasma parameters.

8. 3D effects on EP confinement and losses

3D effects are unavoidably present in all toroidal magnetic fusion devices due to a variety of sources: the discreteness of toroidal field (TF) coils, 3D ferritic inserts, externally applied 3D fields for plasma control, internal MHD perturbation developed by the plasma itself or, in ITER, test blanket modules (TBMs). In an idealized, perfectly axisymmetric tokamak, the EPs move along their drift orbits which from closed loops in the poloidal plane and guarantee optimal confinement (section 2). In actual tokamaks, internal and external perturbations break the perfect axisymmetry and deteriorate the confinement. Energetic ions are particularly vulnerable to enhanced cross-field transport from symmetry breaking due to their large velocities and, consequently, wide orbits and low collisionalities. The 3D effects on energetic ion confinement have to be understood and mitigated to ensure good performance. Transport in 3D fields is further discussed in chapter 2 of the volume [14].

8.1. Introduction to 3D perturbations

ITER has 18 toroidal field (TF) coils which leads to a non-axisymmetric geometry. The resulting TF ripple in the magnetic field is larger than 1% in the plasma periphery in standard full-field scenarios. Such a magnetic ripple causes stochastic diffusion since the drift orbits no longer close upon themselves in the poloidal plane. For deeply trapped ions, it even leads to direct losses due to ∇B-drift, leading to localized power loads on plasma-facing components that need to avoided. Ferritic steel inserts placed between the TF coils and the plasma reduce the peak TF field at the plasma edge near the TF coil. The optimised ferritic inserts were developed and demonstrated to reduce the TF ripple by a factor of 4 at JT-60U [939].

However, experiments at JFT-2M have shown that ferritic inserts must be carefully designed to avoid enhanced transport from higher harmonics of the ripple [939, 942]. Additional geometrical constraints, such as the toroidal distribution of ports, may hamper the ferritic insert design and optimisation, possibly leading to localised enhanced losses.

Since the unmitigated TF ripple in ITER is unacceptably strong, ITER is equipped with ferritic inserts at each coil as illustrated in figure 69. In the 15 MA baseline scenario, the optimized ferritic inserts reduce the TF ripple substantially, see figure 70: the TF ripple at the outboard midplane separatrix is
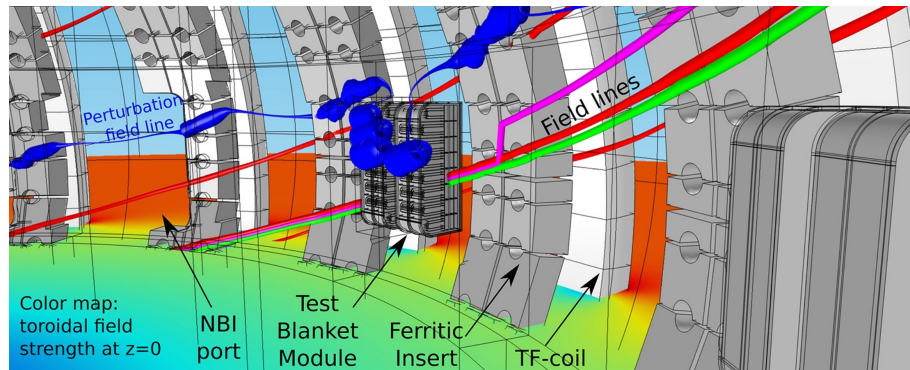
Figure 69. Illustration of spatial location of symmetry-breaking elements in ITER: finite TF coils (white), ferritic inserts (light grey), NBI ports (no color) and test blanket modules (light grey). Reproduced from [940].
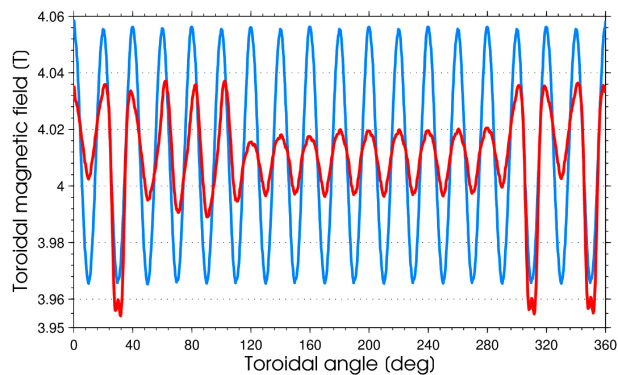

Figure 70. The toroidal field strength at the outer midplane, near separatrix, as a function of toroidal angle showing the cases without (blue) and with (red) ferritic inserts. The ferritic inserts are found to be very effective in mitigating the TF ripple down to 0.3%, but around the neutral beam ports, $\phi \approx 60° - 80°$, the mitigation is incomplete at around 0.6%. At about $\phi \approx 30°, 310°$ and 350°, the influence of the three pairs of TBMs is visible. Reproduced from [941]. Later, the number of pairs of TBMs has been reduced to two.

mitigated to 0.3% except for near the NBI ports where it is mitigated to 0.6%.

ITER will be the first tokamak to study tritium breeding, a critical technology for the production of tritium fuel to sustain operation of a fusion power plant. It is planned to test a range of design concepts for test blanket modules (TBMs) in the equatorial port plugs. The TBMs will be fabricated using ferritic steels and will consequently affect the edge magnetic field. Two pairs of TBMs, at different toroidal locations, are available in ITER for testing tritium breeding, producing localised perturbations of the magnetic field. Like the TF ripple, these symmetry-breaking fields could deteriorate the confinement of energetic ions. It is also expected that structural components of future reactor systems will predominantly utilize martensitic stainless steels, which are ferritic and may induce symmetry-breaking effects.

Since ITER is foreseen to operate in H-mode,

ELMs are expected and must be mitigated. External coils are widely used in present devices to suppress ELMs by means of externally applied resonant magnetic perturbations (RMPs). In most present tokamaks, RMPs are generated by two or three toroidal rows of window-frame coils. The current flowing through the coils is modulated toroidally, and the relative toroidal phase between the waveforms can be adjusted to vary its effect on the plasma. The relative toroidal phase between toroidal rows is thus used to modify the poloidal mode spectrum of the perturbation; this has been observed to affect the plasma stability in several experiments such as MAST [943], AUG [944] and DIII-D [945]. Further information on the interaction of ELMs and RMPs are found in chapters 3 and 5 of this volume [15, 17].

Furthermore, an efficient coupling between internal MHD fluctuations and externally applied 3D fields via particle transport, finite orbit width effects and mode couplings can lead to synergistic effects on EP transport with unexpected consequences. Recent advances in diagnostics and modeling techniques together with collaborative efforts between the tokamak and stellarator communities have led to significant progress in understanding the effects that symmetry breaking 3D effects have on tokamak plasma stability and related EP transport and losses [946]. In the following, the current state of experimental observations and modeling will be presented.

8.2. Experiments

8.2.1. Toroidal field coil ripple. Extensive experimental efforts carried out at JT-60U [947], JET [356, 948], TFTR [24, 949–951], JFT-2M [939, 952, 953] and Tore Supra [954, 955] have led to a solid understanding, allowing us to keep ripple losses at acceptable levels in present tokamaks as well as to make robust predictions for future devices. For a given device, ripple losses are numerically predictable but highly depen-

dent on the EP population and the q-profiles. The TF ripple can cause rapid losses of deeply trapped particles at the edge. These losses are usually lower for low-q, monotonic q-profiles than for high-q, reversed q-profiles, such as those used in "advanced tokamak" scenarios [24, 949–951, 956, 957]. Optimised ferritic inserts have successfully reduced the measured ripple losses at JT-60U [939] and EAST [958].
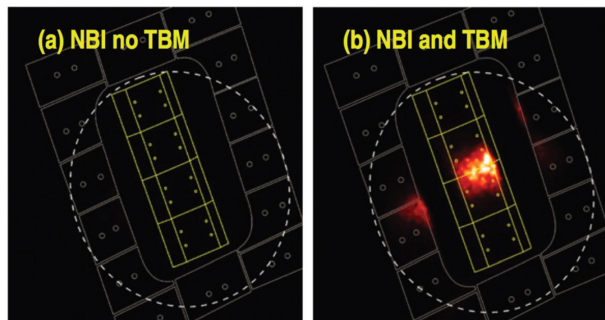

Figure 71. Infrared measurements of heat flux on DIII-D graphite tiles with TBM simulation coil turned off and on. Reproduced from [959]

8.2.2. Test blanket modules. The effect of TBM-like perturbations was studied using error fields produced by an external coil system at DIII-D [960]. The features of the ITER TBM perturbation were mimicked as closely as possible, but the magnitude of the perturbation was significantly larger. Heating was observed on the protective tiles of the TBM mock-up surface when NBIs and the TBM fields were engaged (figure 71). The EP core confinement was not significantly affected. Different orbit-following codes predicted the formation of a hot spot on the TBM mock-up surface arising from beam ions deposited near the edge of the plasma [959, 961]. The codes are in good agreement on the total power deposited at the hot spot, predicting an increase in power with decreasing separation between the plasma edge and the TBM surface.

Simulations carried out for the TBM parameters in ITER full-field, standard scenarios indicate that the TBM-induced losses can be be kept below 1% for alphas, below 2% for NBI ions, and below 3% for ICRF ions [941, 962]. However, in reduced magnetic field scenarios, alpha losses can be up to 10% and NBI losses can be up to 3%.

8.2.3. ELM mitigation coils. Application of the RMP coils has been observed to cause significant EP losses at AUG [963, 964], DIII-D [963] and KSTAR [374]. Figure 72 shows the measured losses at DIII-D with modulated perturbation amplitude for a counter-current and a co-current NBI. The measured power
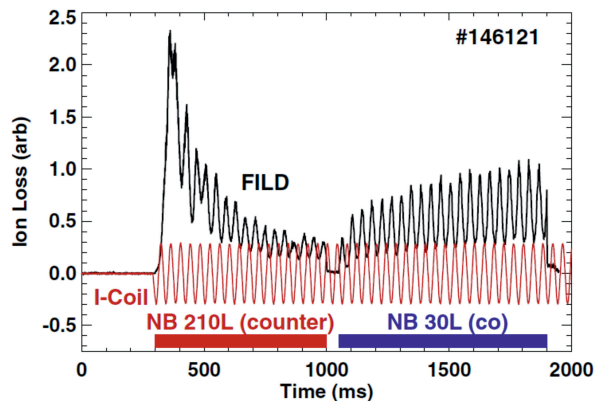

Figure 72. Midplane FILD signal showing modulation of EP loss correlated with rotating n = 2 field in DIII-D discharge #146121. Reproduced from [963].
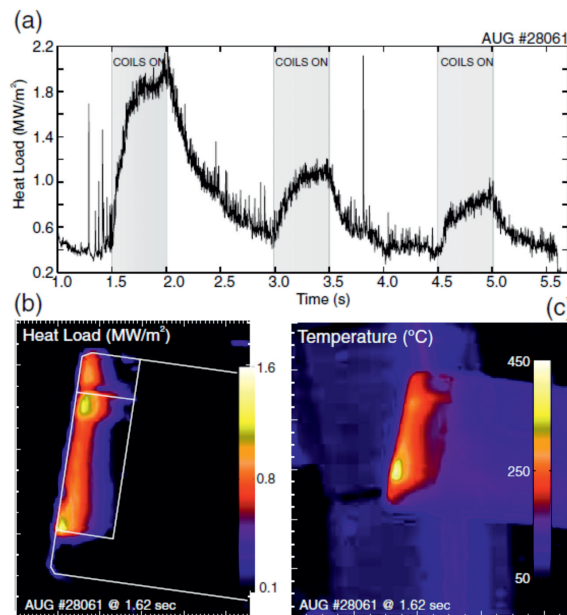

Figure 73. AUG discharge #28061. (a) Time trace of the heat load on the detector aperture. (b) 2D image of heat load due to ELM mitigation coils on FILD detector head. (c) 2D image of detector head temperature. Reproduced from [964]

load due to the EP losses on a FILD detector head reaches up to $2\,\mathrm{MW/m^2}$ as figure 73 shows [964]. However, the measured losses depend strongly on the existing EP distribution and on the poloidal and toroidal spectra of the applied perturbation. At AUG, striking differences in the velocity space of the EP losses have been measured by FILD systems for different NBI geometries (figure 74). Dedicated experiments and numerical simulations have revealed that the observed EP losses in the presence of externally applied RMPs are produced by an edge resonant transport layer with a high density of linear and nonlinear resonances between the EPs and the

externally applied static 3D fields [965]. In AUG [966] and DIII-D [967], the EP displacement during a single pass through the RMP-induced fields was measured using the "light-ion beam probe" [968, 969] technique. For comparison with theory, the plasma response was calculated by MARS-F and M3D-C1, respectively. In both studies, the EP displacement depends sensitively on the poloidal mode spectrum. In DIII-D, the displacement also depends sensitively on the normalized beta β_N, since this parameter impacts the plasma response to the perturbation.
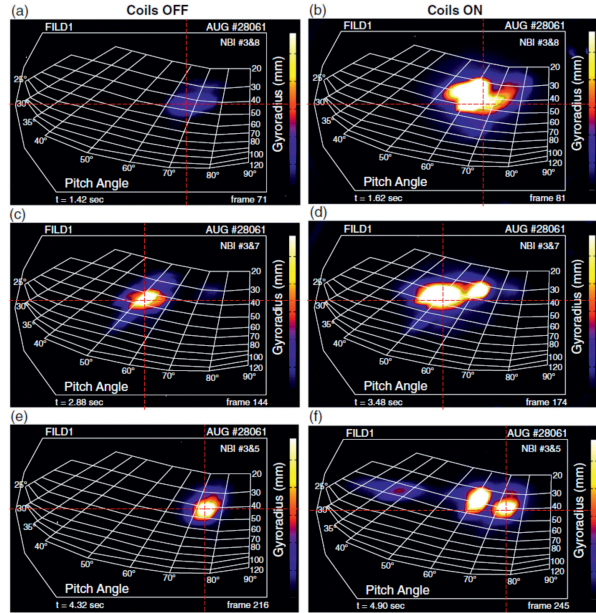

Figure 74. AUG discharge #28061. Velocity-space of escaping ions measured by FILD1 with RMP coils off, (a), (c) and (e) and with RMP coils on, (b), (d) and (f). Reproduced from [964]

8.2.4. Synergistic effects between internal MHD fluctuations and external 3D fields. Externally produced 3D perturbations predominately affect only the edge EP population. However, if an efficient coupling to the edge exists, internal MHD fluctuations that otherwise would cause only a minor particle redistribution, could now cause significant losses. DIII-D experiments explored the synergy between EP transport caused by the simulated test blanket model of figure 71 and NTMs, AEs, sawteeth, and RMP fields. A definitive synergistic effect was observed at sawtooth crashes where, in the presence of the TBM, the localized heat flux at a burst increased from 0.36 ± 0.27 MW-m^{-2} to 2.6 ± 0.5 MW-m^{-2} (figure 75). Similarly, AUG experiments show that, under certain conditions, the edge resonant transport layer produced by RMPs can couple to NTM-induced EP losses to channel particles from the core of the plasma to the wall. NTM induced EP losses were measured with FILD systems only when

the RMP was active (figure 76) [964]. This effect must be taken into account when applying external RMPs in future devices.

Experiments at NSTX have shown that RMPs can also be used to control AEs modifying the resonant EP distribution. RMPs were observed to reduce the amplitude and frequency chirp of global Alfvén eigenmodes and to increase the bursting frequency [970]. More recently, experiments at AUG have shown that RMPs can be used to not only mitigate TAEs but also to excite them by modifying the gradients in the EP distribution that drive the modes unstable [971] (figure 77).
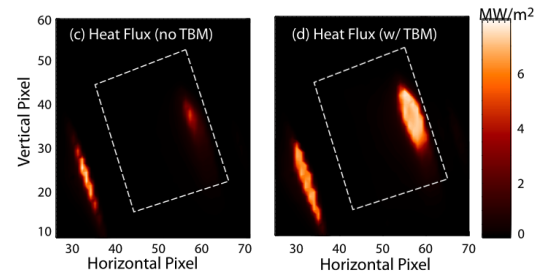

Figure 75. Measured heat flux near the TBM mockup coil (dashed rectangle) in a sawtoothing DIII-D discharge before (left) and after (right) application of the TBM field. Reproduced from [972].
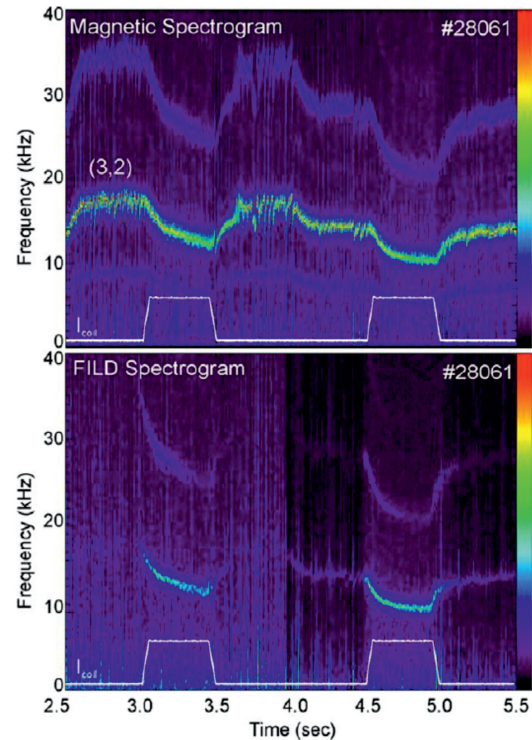

Figure 76. AUG discharge #28061. Spectrogram of (a) magnetic pick-up coil and (b) EP losses measured by FILD1. Reproduced from [423].
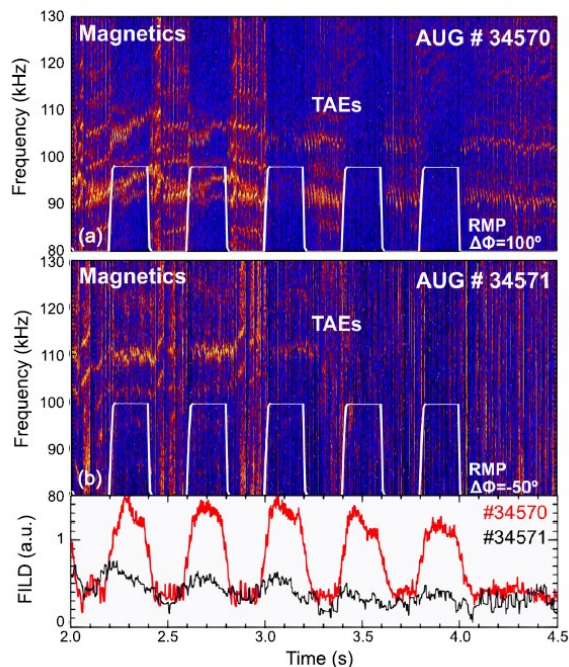
Figure 77. Magnetic spectrograms showing the TAE activity in two AUG discharges with RMP-induced TAE mitigation / suppression (a) and excitation (b). The RMP time traces are over-plotted in white. The bottom panel shows the temporal evolution of the EP losses measured with the FILD system. Reproduced from [971].

8.3. Modeling of 3D equilibria, stability and EP confinement

In the following, we will review the modeling tools available for 3D magnetic field effects on equilibrium, EP confinement, and stability. The efforts in modeling 3D effects have been increasing with the advent of large stellarator experiments. The same tools developed for stellarators can often be used to also model tokamak equilibria, EP confinement and stability, accounting for the 3D perturbation fields due e.g. TF coils, ferritic inserts, TBMs and ELM control coils.

8.3.1. Modeling of 3D equilibria. In non-axisymmetric devices, 3D equilibria with closed, nested flux surfaces are not guaranteed to exist. Magnetic islands can appear where the rotational transform, ι, is a rational number, which can deteriorate the confinement. The VMEC code [327, 973] solves the equilibrium problem in general geometry by minimizing the plasma energy, assuming closed, nested flux surfaces. VMEC has proven useful for the computation of 3D tokamak equilibria with applied RMPs [974–986] as well as 3D equilibria in ITER [987]. In plasmas with a large EP population, anisotropic 3D equilibria can be calculated using energy principles [988–990]. The 3D

equilibrium models HINT [991–994], PIES [995–997], and SIESTA [998–1000] do not need the assumption of closed, nested flux surfaces, allowing magnetic islands to form. 3D equilibrium effects can also be addressed using linear and nonlinear time-dependent MHD models, which are useful to study time-dependent effects such as time-varying RMP fields [971, 1001, 1002].

The simplest approach to generate the 3D magnetic fields in tokamaks for the purpose of studying EP confinement (see next subsection) is to calculate the 3D perturbations from vacuum solutions and superimpose these on a 2D Grad-Shafranov equilibrium [962]. At the next level, VMEC can provide a self-consistent, finite β plasma response to the external fields [987, 1003]. For time-dependent external 3D fields, such as from ELM coils, the plasma response becomes dynamic, which has been computed in [963, 1004].

8.3.2. EP confinement in tokamaks with 3D fields. Particle orbits in 3D fields, such as in realistic, non-axisymmetric tokamaks or stellarators, are more complicated than in idealized, axisymmetric tokamaks in several important ways. Trapped orbits may no longer remain centered on a fixed flux surface. As the magnetic field varies along the toroidal direction, the EPs may move radially. EPs with a large pitch may become trapped in the local ripple wells and drift out of the plasma. Passing orbits are not as directly affected by 3D perturbations as trapped orbits. However, over many toroidal turns, passing orbits can trace out drift surface islands, leading to enhanced radial transport [1005].

An important 3D effect compromising EP confinement is that of edge resonant transport layers (ERTLs), as found for AUG [965]. The plasma response to the 3D field perturbation was calculated with the MARS-F code, and the EP orbits were followed using AS-COT [1006]. The computed change of the canonical toroidal momentum $\langle \delta P_\phi \rangle$ of particles NBI was used to quantify their transport. The maxima of the computed change in $\langle \delta P_\phi \rangle$ are well aligned with resonances between drift and bounce motion of the particles [965] (see figure 78). Exploiting ERTLs may lead to scenarios where optimized RMP fields could be used to minimize the EP losses.

The 3D field effects on alpha and NBI ion confinement were assessed in the major ITER scenarios (15 MA baseline, 12.5 MA hybrid, 9 MA "advanced tokamak", and 7.5 MA half-field) [962, 1007], including ferritic inserts, TF coil ripple, TBMs and ELM control coils, using the OFMC code [1008, 1009] and ASCOT. The effect of the plasma responses to ferritic inserts and TBM perturbations was also assessed in [1010]. No significant deterioration of EP confinement due to
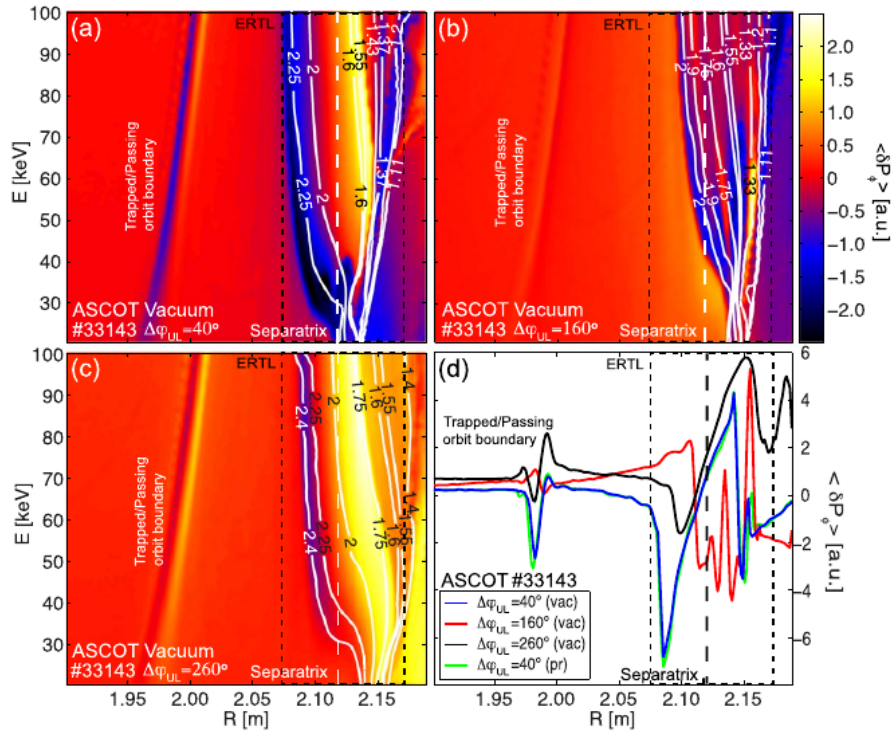
Figure 78. AUG#33143. $\langle \delta P_\phi \rangle$ as a function of particle major radius and energy for poloidal RMP phasing of: (a) $\delta\phi_{\mathrm{UL}} = 40°$, (b) $\delta\phi_{\mathrm{UL}} = 160°$, (c) $\delta\phi_{\mathrm{UL}} = 260°$, White contours indicate the particle frequency ratio ($\omega_{\mathrm{b}}/\bar{\omega}_{\mathrm{d}}$). (d) Radial profiles of $\langle \delta P_\phi \rangle$ for different $\delta\phi_{\mathrm{UL}}$ at energy of $\mathcal{E} = 50\,\mathrm{keV}$ and pitch $\lambda = -0.5$. Note that a negative sign of $\langle \delta P_\phi \rangle$ means an outward drift of the particle. Reproduced from [965].

the error fields from the TF coil ripple, ferritic inserts and TBMs were found in these studies. The key factors influencing the confinement were found to be the edge source rate, the plasma/first wall gap, and the plasma current [941], although for the 15 MA scenario part of load on the target plates in the divertor was found to be shifted to the divertor dome [1011].

However, the ELM control coil perturbation resulted in orders-of-magnitude increases in the power load on the wall up to the MW-range. This was attributed to the field line stochasticity penetrating deeper into the pedestal top, leading to an increase of losses. The mechanism for this large increase in EP transport was found to be a new loss channel for marginally trapped particles caused by a strong toroidal variation of the poloidal field near the X-point, leading to a displacement of banana tips and collisionless transport [1012].

The effect of the ERTLs on the confinement of NBI ions in ITER has been investigated as function of the applied RMP spectrum using ASCOT [1013]. The total EP losses depend on the poloidal spectra of the applied $n = 3$ RMP as well as on the absolute toroidal phase of the applied perturbation with respect to the NBI birth distribution. The absolute toroidal phase of the RMP perturbation does not affect the ELM control

capabilities, leading to an expectation that it could be used for NBI confinement optimization in ITER.

8.3.3.   Stability of 3D MHD equilibria. As in axisymmetric toroidal equilibria (see section 6), the gaps in the Alfvén continuum indicate the frequency ranges where weakly damped AEs reside. These modes are expected in the gaps or above or below flat branches of the continuum (e.g. in [597]). There are several numerical implementations for 3D equilibria available [1014–1016], including the coupled Alfvén and sound continuum [1017]. For weak 3D error fields, the Alfvén continuum structure changes only mildly. For example, small open gaps driven by toroidal field ripple couplings from discrete coils in the case of DIII-D have been identified [1003]. Also, structures known as continuum crossing gaps can be present in configurations with 3D perturbations [1018]; these were also identified in the DIII-D case with field ripple [1003]. For strong 3D error fields, new classes of Alfvén gaps appear. Helical variations in the magnetic field strength produce helicity-induced AEs (HAEs) and toroidal variations lead to mirror-induced AEs (MAEs).

Most of the existing nonlinear MHD implementations were initially developed for axisymmetric equi-

libria [846, 1019], but have now been extended to full 3D configurations [843, 1020–1023]. They can either consider equilibria with islands [994, 1020] or with nested flux surfaces from VMEC [1021, 1024]. Nonlinear 3D models using reduced MHD have been developed [985, 1025–1027].

The interaction of MHD eigenmodes with EP populations has an approximate analytic solution [1028] in 3D configurations, as for idealized tokamaks [462]. This solution is local on a flux surface and allows the determination of the resonance velocity of passing particles with fluctuations such as AEs in a 3D magnetic topology.

In 3D tokamaks and stellarators, there is not only a larger spectrum of eigenmodes, but also a larger number of wave-particle resonances. This is partly due to the more complicated particle orbit topologies [1029] as can be confirmed either analytically [1028] or numerically [1030, 1031] by coupling a drift kinetic equation perturbatively with a 3D ideal MHD stability model [1032, 1033]. The additional resonances may also lead to a destabilisation of AEs by interaction with the bulk plasma species [1031, 1034].

As for 2D fields, models ranging from full gyrokinetic), kinetic-MHD and reduced models have been used to evaluate the effect of 3D perturbations on AEs. These models originated from modeling either axisymmetric tokamaks or stellarators, but can now be used to describe 3D tokamaks.

8.3.4. Gyrokinetic and kinetic-MHD simulation with 3D fields and reduced models. The most complete description of wave-particle interaction is gyrokinetic simulations (section 7), in which all species can be handled on the same footing. A few codes provide the capabilities to perform global electromagnetic calculations in 3D geometries [1035–1038]. Most of the numerical approaches use PIC paradigms to solve the gyrokinetic equation in a δf-formulation. The electron dynamics is often solved iteratively starting with a fluid model [1039] or using a pullback scheme [812, 817, 818, 1040], a control variate scheme [1041, 1042], or a fluid electron model.

Recently, progress has been made using a grid-based method for the global electromagnetic calculation of ITG modes in W7-X [1038]. It showed that turbulence suppression by EPs stemming from ICRF heating, which has been observed for tokamaks [1043], can also be achieved in optimized stellarators [1044]. EP simulations have been performed for an LHD equilibrium with low mode numbers, and a successful benchmark with a kinetic-MHD model has been carried out [1045]. More recently, this approach has been extended to the full LHD radial and poloidal range [1046, 1047]. Fully gyrokinetic models have also

been used to calculate drift Alfvén waves in LHD [812].

3D kinetic-MHD models have been successfully applied to study EP effects on MHD modes in tokamaks [1048, 1049], and stellarators [1046, 1047]. Global gyrofluid models have also been developed for 3D systems. This approach is based on the Landau closure [882] which provides an efficient treatment of the effect of parallel resonances. In the FAR3d [883] and TAEFL [1050] models, moment equations of the EP density and parallel velocity have been coupled to a nonlinear reduced resistive MHD model for the bulk plasma. The closure for the fluid equations includes the linear wave-particle resonance effects required for Landau damping/growth. The speed advantage of this model has allowed rapid parameter scans as recently demonstrated for LHD [1051] and TJ-II [1052] plasmas.

For 3D plasma equilibria including magnetic islands, a fully nonlinear resistive MHD model [846] has been coupled to a gyro- or drift kinetic equation for the EPs in the MEGA model [1020, 1053]. Investigations for TAEs in LHD have been made in [1020]. Later, the experimentally observed EGAMs in LHD have been explained and the energy transfer between the bulk plasma and the EPs has been calculated [1054, 1055]. More recently, AE bursts in LHD have been investigated [1056]. Also, orbit-following codes for EPs have been added to a nonlinear resistive MHD model [1025] and successfully benchmarked [1057].

Finally, it has been shown that reduced MHD models are a reliable tool for modeling stable global Alfvén waves in 3D systems and can be used with wave-particle interaction models to assess EP stability [819, 1058, 1059], including FLR and finite $E_\parallel$ effects [1059]. The continuum damping of global modes in 3D has been quantified [1060, 1061].

Stability calculations for ITER including a realistic wall are found in [1062]. A resistive MHD stability model for tokamaks [1063] has been generalized to 3D and could also be applied to an AUG equilibrium with a helical core [1064].

9. Multiscale synergistic interactions between EPs, thermal-plasma- and EP-driven instabilities, and turbulence

This section describes the multiscale interplay between EPs and perturbations, both electrostatic and electromagnetic, ranging from large-scale to small-scale perturbations and including microturbulence. Firstly, we will deal with interactions between EPs, tornado modes, and sawteeth. Secondly, we will deal with the nonlinear wave-particle interactions between EPs and EGAMs (including the EGAM channeling and the EP transport induced by EGAMs) and wave-wave interaction between NTMs and EP-driven AEs and EGAMs;

an overview is given of synergistic effects in nonlinear simulations and experiments. Thirdly, the interplay between turbulence and EPs is reviewed. This includes the EP-turbulence interaction mediated by EGAMs and the mechanisms of microturbulence stabilization by EPs (dilution effect, linear stabilization and nonlinear electromagnetic stabilization). We then review the possible role of microturbulence on EP transport, including synergistic effects. An example is the impact of the pitch-angle scattering rate on the nonlinear evolution of AEs, mediated by ICRF heating and microturbulence. In particular, a 2D (toroidal momentum and energy) quasi-linear model implemented in the RBQ code computes the EP distribution function in the presence of AE-induced diffusion, Coulomb collisions and anomalous scattering due to microturbulence.

9.1. Interactions between EPs, tornado modes, and sawteeth

A synergistic effect observed in present-day tokamak experiments with significant populations of EPs is an interplay between EPs, sawtooth instability [355,1065], and high-frequency TAEs excited by the EPs inside the $q = 1$ magnetic flux surface, called *tornado* modes [356, 1066–1069]. The sawtooth and tornado instabilities are very different in their nature, but they are both affected by EPs and by temporal evolution of the safety factor $q(r)$, so they become coupled through these two essential elements they share.

As already discussed in section 5, the sawtooth [1065] is a global thermal-plasma instability driven by plasma current, and it is associated with the $q = 1$ magnetic flux surface. The high-frequency tornado modes are localized in the plasma core inside the $q = 1$ surface. They appear one-by-one with decreasing toroidal mode numbers when the on-axis safety factor $q(0)$ decreases through the relevant TAE safety factors of $q = (m + 1/2)/n$ after the sawtooth crash. The tornado modes are excited via resonant interaction with EPs inside the $q = 1$ surface. These modes were first observed at TFTR [1066] and then at JT-60U [1067], where they were nick-named tornado modes due to the temporal evolution of their frequencies.

Figure 79 shows typical magnetic spectrograms and main plasma parameters in JT-60U discharges with both the usual *global* TAEs localized outside the $q = 1$ radius (left panel) and with the core-localized tornado modes and sawteeth (right panel). Note that the frequencies of the tornado modes change on a rather short timescale compared to the Alfvén scaling $f \sim B/n^{1/2}$ of global TAEs. Note also from the right panel of figure 79 that the tornado modes (top panel) appear just before sawtooth crashes, which suggests a possible role of tornado modes as precursors to sawtooth crashes.

The role of TAE modes in redistributing EPs and causing sawtooth crashes was investigated first on DIII-D [1068]. However, the location of the TAEs could not be identified, leaving open questions. It was shown later for a TFTR discharge [1069] that when the amplitudes of tornado modes excited by EPs become sufficiently high, a significant radial redistribution of the EPs occurs from inside the $q = 1$ radius to outside. This depletion of EPs inside the $q = 1$ radius takes away the stabilizing effect of EPs on sawteeth, which leads to the sawtooth crash. In this way, a relatively minor local redistribution of EPs away from the plasma core can trigger a sawtooth crash, causing global transport with significant modification of the thermal plasma profiles.

Similar studies were performed later on JET confirming the synergistic character of the interaction between sawteeth and tornado modes coupled through the EP population [356, 1070, 1071]. Core TAEs inside the $q = 1$ surface were also implicated in DIII-D monster sawteeth [1072]. This synergy between sawteeth, tornado modes and EP-driven modes has yet to be simulated, so we are lacking a prediction for this phenomenon in ITER. Based on the possible occurrence of tornado modes and sawteeth in ITER, this synergy is likely to occur.

9.2. Interactions involving EPs and EGAMs

Linear stability of EGAMs was discussed in section 6.6.3. Here we deal with the nonlinear regime of EGAMs, the possibility to couple energy from EPs to EGAMs to eventually heat the thermal ions instead of the electrons (dubbed EGAM channeling), and on interactions between EPs, EGAMs and other modes.

9.2.1. Nonlinear regime of EGAMs and EGAM channeling. The nonlinear regime of EGAMs has been analyzed since the observation of the $n = 0$ chirping mode in JET [668, 669]. It has been shown that kinetic effects are essential for the generation of second harmonics in the density perturbation [1073]. In nonlinear simulations of non-chirping EGAMs using GYSELA [649], the distribution function was found to flatten during the mode saturation. Such a flattening of the distribution function was also observed in kinetic-MHD MEGA simulations [334], including the formation of holes and clumps [683, 684] at the start of the chirping [534], as anticipated in [668]. Further detailed analysis of the wave-particle nonlinearity effect on the saturation of EGAM including the nonlinear time evolution of the frequency was reported in [1074].

An important aspect of EGAMs is the possible transfer of energy from EPs to thermal ions mediated by the EGAM in collisionless regimes [649, 658]. Although energy transfer appears already in linear
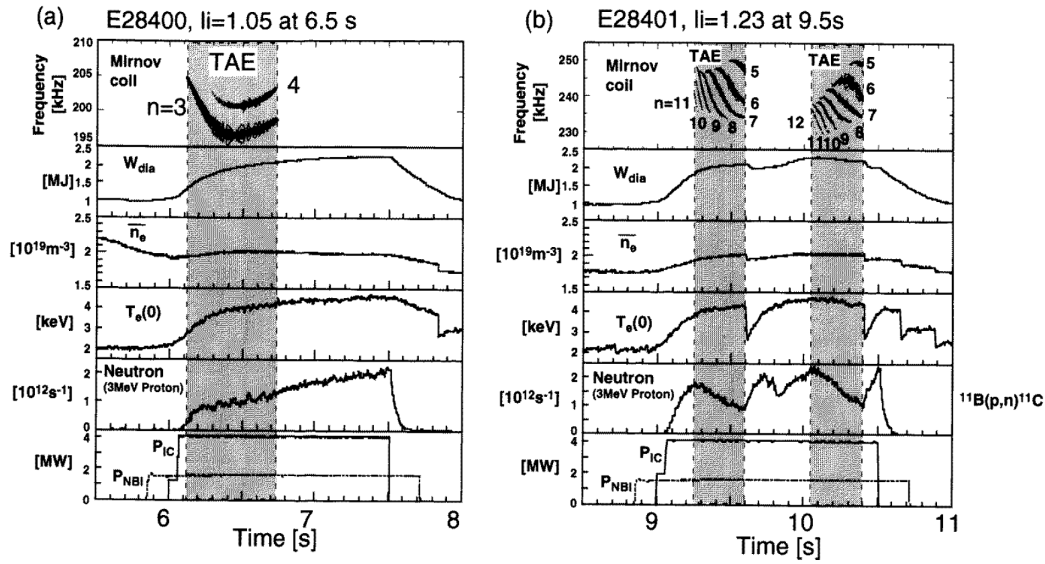
88

Figure 79. Comparison of two JT-60U discharges showing (left) low-n TAE modes outside the $q = 1$ surface and (right) high-n multiple TAE modes inside the $q = 1$ surface (tornado modes). Both discharges have almost the same plasma conditions except for the start time of ICRF and NBI heating. Reproduced from [1067].

regimes [650], the nonlinear transfer from high- to low-μ (magnetic moment) particles was confirmed from realistic simulations of LHD plasmas, which opened the possibility for *EGAM channeling* [1055]. Finally, the nonlinear generation of higher harmonics has been observed to play an important role in the EGAM channeling in GYSELA simulations [672] as well as in realistic kinetic-MHD MEGA simulation of LHD discharges [550, 1055]. Figure 80 shows an example of the energy exchange between EPs and thermal ions mediated by EGAMs. The solid lines in the top panel represent the time traces of the energy exchanged between EGAM and both ion species, measured as $\Delta\mathcal{E}_{s,\mathrm{trans}} = \int_0^t \mathrm{d}t' \int \boldsymbol{J}_s \cdot \boldsymbol{E}\mathrm{d}V$, with s the species (either EP or thermal ions), $\boldsymbol{J}_s$ the current density of species s, and $\boldsymbol{E}$ the electric field. The dashed line represents the curve for EPs scaled by a factor $k = 0.47$. Therefore, in this example, the efficiency of the energy exchange is $\Delta\mathcal{E}_{i,\mathrm{trans}}/\Delta\mathcal{E}_{f,\mathrm{trans}} \approx 0.47$, i.e. 47% of the energy transferred from EPs to EGAM is subsequently transferred to thermal ions. The bottom panel of figure 80 represents the time trace of the EGAM poloidal velocity, showing a good correlation between the onset of the nonlinear saturation and the exchange of energy between EPs and thermal ions. In that example, the power transferred to the thermal ions through the EGAM was estimated to be ~ 3.4 kWm^{-3} [1055]. The energy transfer efficiency depends on β_{f} [550]. In particular, it can reach values up to 60% for $\beta_{\mathrm{f}} = 0.08\%$. EGAM channeling could be an option for the idea of alpha channeling to optimize burning fusion plasmas (see section 10.4).
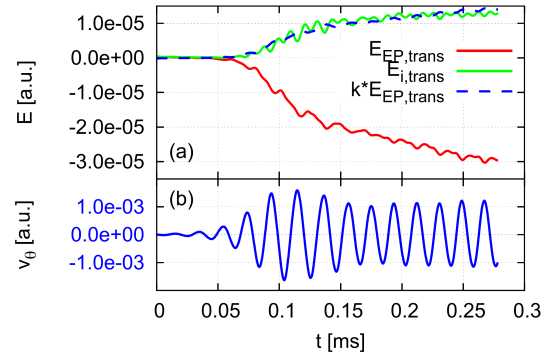

Figure 80. Top panel: The solid lines represent the time evolution of the energy exchange between EGAM and both EP ($\Delta\mathcal{E}_{f,\mathrm{trans}}$) and thermal ions ($\Delta\mathcal{E}_{i,\mathrm{trans}}$). The energy transfer efficiency from EPs to thermal ions mediated by EGAM is measured as $\Delta\mathcal{E}_{i,\mathrm{trans}}/\Delta\mathcal{E}_{f,\mathrm{trans}} \approx 0.47$. The curve for EPs (dashed line) is scaled to show that the energy transfer efficiency from EPs to thermal ions is constant. Bottom panel: Time trace of the poloidal velocity, representing the excitation and nonlinear saturation of the EGAM. Reproduced from [550].

9.2.2. EGAM-induced EP transport. Since an EGAM is an axisymmetric mode with $n = 0$, it does not change the toroidal canonical angular momentum P_ϕ of particles ($n\Delta\mathcal{E} = \omega\Delta P_\phi$) and therefore it has long been believed to have little effect on the transport of EPs. Yet, since P_ϕ depends on both the poloidal flux Ψ and the parallel velocity $v_\parallel$, wave-particle interactions can result in EP transport [431] and even losses when the orbits of counter-passing particles are changed into unconfined trapped particle orbits that intercept the wall [658]. Such a mechanism
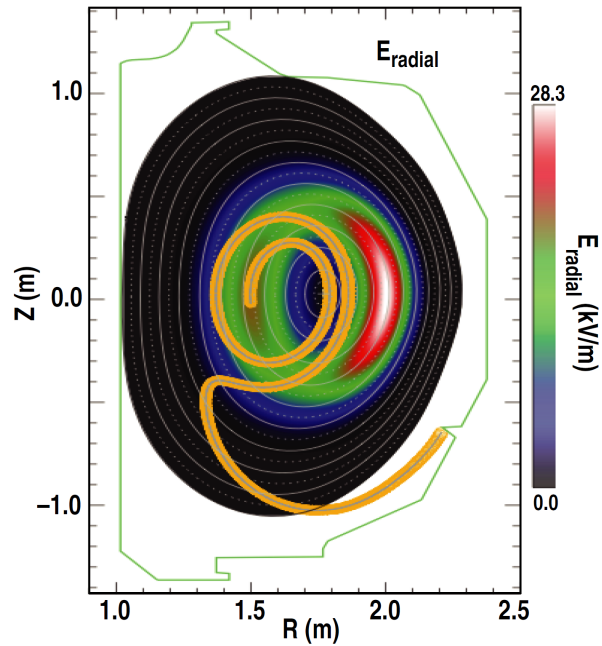
Figure 81. Trajectory of loss EP computed using the full particle-orbit code SPIRAL. The EGAM radial electric field is represented in the background. Reproduced from [659]

was corroborated in [659], where the orbits of lost EP detected by FILD were followed (in reverse) using the orbit-following SPIRAL code. Figure 81 illustrates a trajectory calculated using SPIRAL. The initially confined counter-passing particle interacts with the EGAM electric field, becomes trapped and is lost. Further analysis of the EGAM-induced EP transport was given in [1075], where it was shown that resonances of the form equation 86 can also occur when l is fractional. Such transport induced by fractional resonances is in principle only possible for a large amplitude of the perturbations. Later, nonlinear studies of EGAM-induced EP transport were performed in [672] using the EGAM potential self-consistently computed using the GYSELA code. Integer and fractional resonances were found, as well as a chaotic separatrix interacting with the trapped-passing boundary. The losses modulated at the EGAM frequency and the class of trajectories of lost particles (counter-passing) agreed with observations [659]. The existence of the chaotic separatrix motivated studies of the EGAM-induced EP transport in the radial direction, which was found to be non-diffusive. This non-diffusive radial transport was linked to a super-diffusive poloidal transport governed by rare events called Lévy flights [1076]. The original papers on Lévy processes are [1077,1078], but we recommend the more recent [1079] for an overview.

9.2.3. Interactions between EPs, EGAMs, NTMs and AEs.

Another topic of concern is the interaction between NTMs and other EP-driven modes [1080]. NTMs change the Alfvén continuum and transport EPs, which has immediate consequences for the AE stability. Several examples of such direct interactions in plasmas without EPs have been found. Pairs of BAEs are sometimes found in the presence of magnetic islands [317, 624, 1081, 1082]. Destabilization of BAEs has been attributed to the interaction between tearing modes and geodesic acoustic modes [1083]. A strong interaction between tearing modes and TAEs has also been found in simulations and experiments [618, 1084]. These interactions could enhance the transport and loss of EPs. Also TAE wave-wave coupling has been observed experimentally [1085].

Evidence indicates that nonlinear wave-wave interaction among tearing modes and m-BAEs leads to generation of geodesic acoustic modes induced by energetic electrons (eEGAMs) [493], as shown in figure 82. The m-BAE is a standing-wave structure formed by counter-propagating Alfvén waves within a magnetic island [627], when the island is above a certain threshold island width, see also section 6. The EGAMs are localized in the core plasma with a broad radial structure measured by several diagnostics, such as Mirnov probes, soft X-ray arrays and Doppler reflectometers. The $n = 0$ mode can only be observed in plasmas with line averaged densities $n_e < 0.5 \times 10^{19} \mathrm{m}^{-3}$ but the threshold can be increased by auxiliary heating. The squared bicoherence indicates that EGAMs are driven by three-wave resonance among m-BAEs and tearing modes. The radial structures of EGAMs and BAEs have been found to overlap. Therefore, AEs can propagate poloidally into the region of zonal flows (ZFs), then interact with GAMs/ZFs, and finally result in wave energy transfer between the GAMs and AEs.

9.3. Interactions between EPs and turbulence

On the route towards the steady-state production of energy in future fusion devices, understanding and controlling turbulent transport is of prime importance because turbulence limits the confinement of energy and particles. Indeed, experimentally measured diffusivities [1086] are largely above those predicted by neoclassical theory and in good agreement with the diffusivities computed in gyrofluid and gyrokinetic turbulent simulations [1087], i.e. $\chi_{\mathrm{sim}} \sim \chi_{\mathrm{exp}} \sim 1 \, \mathrm{m^2 s^{-1}}$. Since EPs are ubiquitous in current fusion devices and are a key ingredient to achieve good plasma performance, understanding and predicting the mutual interplay between microturbulence and EPs is an active research topic. It is especially important to assess whether the presence of EPs will have a significant
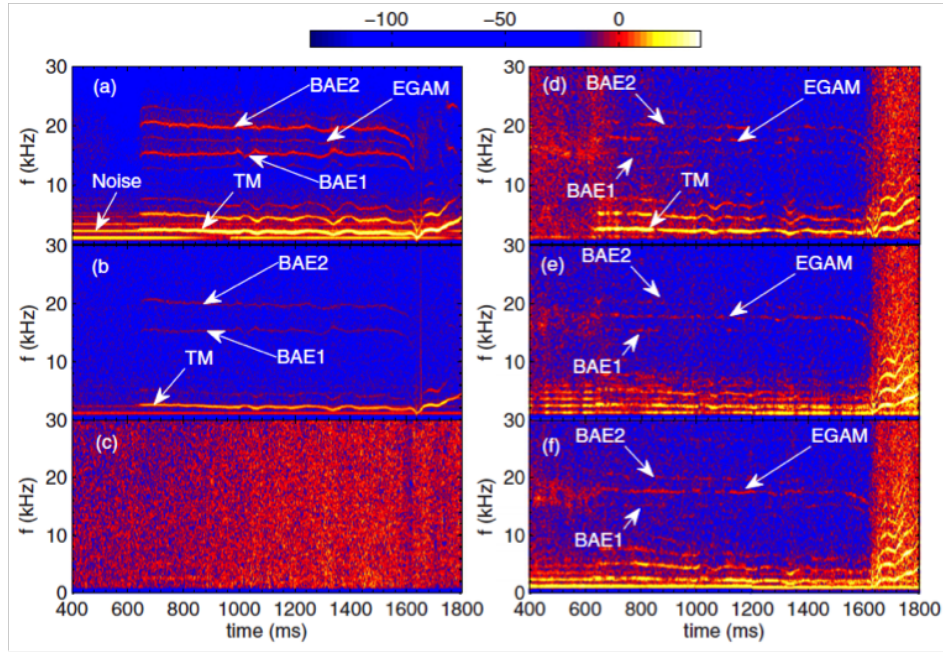
Figure 82. Spectrograms of fluctuations from EGAMs on (a) Mirnov signal, (b) SXR signal in the core. (c)–(f) Density fluctuations of Doppler reflectometers with different work frequencies: (c) X-mode, $f = 34$ GHz; (d) O-mode, $f = 17$ GHz; (d) O-mode, $f = 23$ GHz; and (f) X-mode, $f = 48$ GHz. Reproduced from [664].

impact on the dynamics of microturbulence or not. In typical conditions of present tokamaks, turbulent transport in the plasma core is dominated by ion-temperature gradient (ITG) driven instabilities for relatively flat plasma density profiles [1088]. Hence most studies have focused on the interaction between EPs and ITG turbulence.

9.3.1. Energy transfer from EPs to microturbulence mediated by EGAMs and AEs When GAMs were excited by EPs at JET for the first time, the possibility to use them as a knob to control turbulence became appealing [668, 669], especially because GAMs are interpreted as the oscillatory component of zonal flows, which are known to play a crucial role in the self-regulation of turbulence [777, 824]. In that context, gyrokinetic electrostatic simulations using GYSELA were performed to study the possibility of controlling turbulence by means of a source of EPs that can drive EGAMs unstable [670]. The EP source in this study accelerated thermal particles, reducing the available energy for the linear destabilization of ITG, and hence reducing turbulence. This is illustrated in the top panel of figure 83 by the solid black line, where the time evolution of the measured $\boldsymbol{E} \times \boldsymbol{B}$ heat flux is plotted. As comparison, a second source injecting the same energy, but without accelerating particles to supra-thermal energies was introduced. In that case, no reduction of turbulence was observed, as shown in figure 83 (dashed blue line). This suggests that EPs

were indeed the reason for the turbulence reduction.

However, the source of EPs resulted in the excitation of EGAMs, and a coupling between the EGAM structure and the ITG-avalanches was evident in the temperature gradient, as observed in the bottom panel of figure 83. This coupling leads to an energy channel from the inner to the outer region of the tokamak, increasing the turbulent transport to previous levels. An explanation based on a wave-kinetic equation was proposed in [656], suggesting that EGAMs can trap turbulence clumps and carry them across the transport barrier. Additionally, the transfer of energy from EPs to ITG turbulence via EGAMs was also found to be due to a local three-wave coupling mechanism [671]. The global and local mechanisms can be concomitant.

Studies were also conducted in the electromagnetic regime using the ORB5 code for the case of BAEs excited by EP [784]. It was shown that the heat fluxes are generally increased, especially for electrons, first at low toroidal mode numbers corresponding to large scales, where BAEs are dominant, and subsequently at high toroidal mode numbers corresponding to smaller scales, where ITG modes are dominant. However, it was also found that TAEs excited by EPs might have a beneficial impact on the stabilization of turbulence, which is discussed in the next subsection.

9.3.2. Turbulence stabilization by EPs. Among the first experimental indications that EPs might play
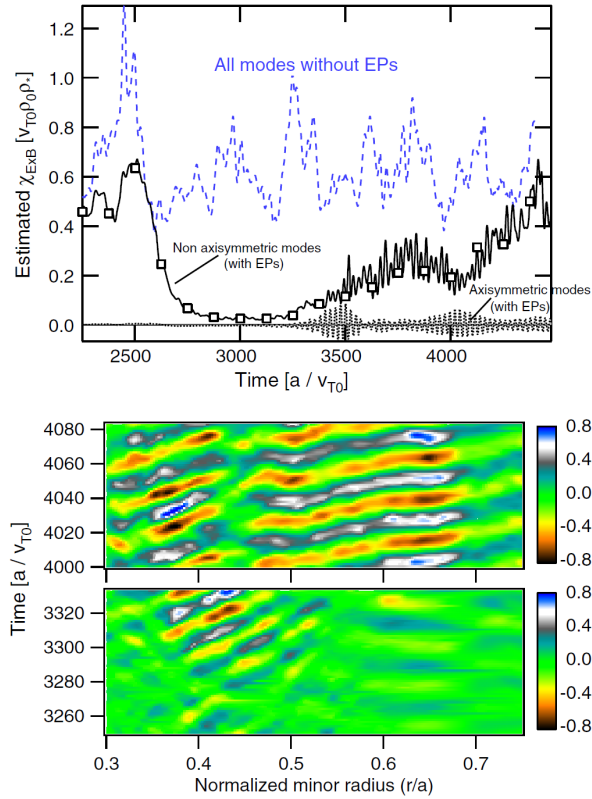
Figure 83. (Top panel) Time trace of the $\boldsymbol{E} \times \boldsymbol{B}$ heat flux in the absence of EPs (blue dashed line) and in the presence of EPs separated into the non axisymmetric and the axisymmetric modes. (Bottom panel) Oscillating part of the temperature gradient, showing the coupling between EGAM oscillations and ITG-avalanches. Reproduced from [670].

a role in the stabilization of turbulence was the observation that the ion stiffness was mitigated at high NBI and ICRF power in hybrid regimes [1089] with internal ion transport barriers (ITB) on JET [1090]. The ion stiffness refers to the degree of sensitivity of the ion heat flux to the mode drive, $\gamma_{\text{drive}} \propto R/L_{T_i} \equiv R\frac{\partial}{\partial r} \log T_i$ [1091]. Although this enhanced confinement was initially thought to be due to low magnetic shear and high rotational flow shear [1092], further experiments with only ICRF ^{3}He minority heating in deuterium plasmas have shown that similar ITG stabilization is also obtained in the absence of rotation [1093]. Efforts to explain the fundamental mechanisms underlying the observed stabilization were therefore required.

EPs can contribute already linearly to stabilize ITG modes and thereby reduce turbulent transport in different ways. The first stabilization mechanism is that they dilute the main species, and consequently the background free energy available to drive ITG modes is reduced [1094, 1095]. It was shown in [1095] that the formation and sustainment of an ion ITB

in AUG could not be explained by the $\boldsymbol{E} \times \boldsymbol{B}$ shear alone, but required the inclusion of EPs from NBI. Moreover, the existence of such EP-induced ITBs is limited to the thermalization timescale of EPs. The second stabilization mechanism is due to a modification of the resonance between the EP frequency and the wave. For example, the increase of $\alpha_{\text{S}} = -q^2 R\frac{\partial \beta}{\partial r}$ affects the mode stability by changing the wave-particle drift resonance in phase space, known as the Shafranov-shift effect [1096–1098]. Recent analytic calculations accompanied by gyrokinetic simulations with the GENE code [680] were reported in [815], demonstrating the possibility to stabilize ITG modes by means of the modification of the magnetic drift resonance. Moreover, since the linear resonant mechanism requires also that $\eta_{\text{f}} = \mathrm{d}\ln n_{\text{f}}/\mathrm{d}\ln T_{\text{f,eff}}$ is larger than one, mainly EPs generated by ICRF heating have the optimal profiles for this mechanism. Experimental observations of these effects have been made at JET [1093] and AUG [1099]. The third stabilization mechanism is due to electromagnetic fluctuations. Experimental studies of the reduction of ITG-driven turbulence were conducted at JET in the presence of ICRF-accelerated minority energetic hydrogen [1100]. This study found that the increased pressure due to EPs resulted in a transition from electrostatic ITG modes to nearly electrostatic tearing-parity modes and that the EPs locally modify α_{S} in such a way that the electrostatic ITGs are stable and the kinetic ballooning of Alfvénic modes stays quiescent [1100].
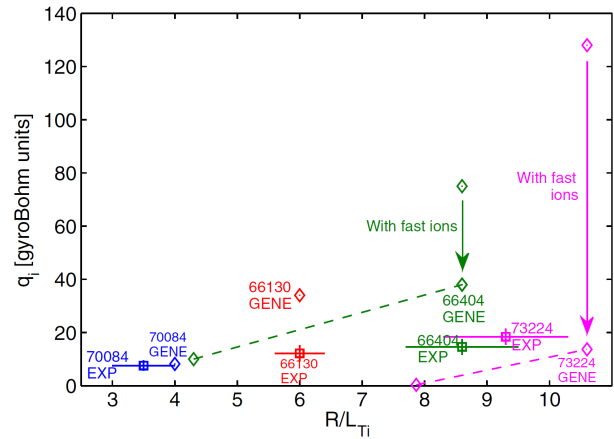
Figure 84. Comparison of nonlinear GENE simulations and experimental measurements of ion heat flux as a function of the normalized logarithmic gradient of the ion temperature. This shows that taking into account the EPs facilitates the agreement with experimentally observed reduction of ion stiffness. Reproduced from [1091].

EP-induced stabilization of turbulence has also been investigated extensively in the nonlinear regime. Experimental work on JET [1090, 1092] reported a

significant reduction of ion stiffness which might open the possibility of controlling the onset of turbulence by means of EPs. Linear effects alone are not enough to explain the enhanced confinement observed on JET [1091]. This motivated further gyrokinetic simulations with the GENE code [1091], where electromagnetic effects resulted in the nonlinear stabilization of turbulence by EP pressure, which helped explain the heat flux and ion stiffness reduction observed in [1090, 1092]. Figure 84 shows a comparison between nonlinear GENE simulations and the experiments. Nonlinear gyrokinetic simulations predicted the EP-induced stabilization of ITG-driven turbulence in JET [1101–1104] and AUG [1105] discharges. Comparisons of linear and nonlinear electromagnetic gyrokinetic simulations pointed out the key role of EPs generated by NBI and ICRF in enhancing the nonlinear electromagnetic stabilization of ITG modes [1091, 1101–1103, 1105]. The stabilizing effects of fast ions are further enhanced at low magnetic shear [1091], and the rotational flow shear is effective only at outer radii [1106], in agreement with experiments [1092].

First attempts to partially explain the elusive physics behind the enhancement of the nonlinear electromagnetic stabilization due to EPs suggested the possible role of EPs in the nonlinear transfer of energy from ITG modes to zonal flows through mode-mode coupling involving EP-driven marginally-stable modes as nonlinear mediators [1107, 1108]. The experiments at JET with deuterium plasmas with minority ^{3}He [1093] corroborated both the linear stabilization via a wave-particle interaction and the nonlinear electromagnetic stabilization. Furthermore, whereas most simulations showing a significant reduction of turbulence by EPs were performed using an equivalent Maxwellian, it was demonstrated that a more realistic modeling of EPs using a non-Maxwellian distribution function still stabilizes ITG turbulence, although in a less significant manner [1109]. Recent simulations using GENE were performed to extend the analysis of the stabilization of turbulence by EPs to other turbulent regimes such as turbulence driven by the trapped electron mode (TEM), concluding that EPs have little impact on TEM-induced turbulent transport [1110]. Turbulence is also thought to be implicated in a new possibility to control the density profile via anisotropy in the EP distribution [1111].

Recent gyrokinetic simulations of a DIII-D discharge with the GTC code illuminate the complicated relationship between EP-driven AEs, zonal flows, and ITG turbulence [822, 827] (see section 7.3.2). In the simulations, ITG turbulence can scatter the resonant EPs that are nonlinearly trapped by the RSAE, thereby damping the zonal flows generated by the

RSAE. Simulations without coupled interactions overestimate both EP and thermal-ion transport, but predicted transport levels are consistent with experiment when coupling between AEs, ZFs, and ITGs are included.

The EP-induced stabilization might be also significant in the presence of alphas in ITER DT plasmas [1112] or in the initial phase of ITER with He^3 minority ICRF heating in DT plasmas [1107]. Since most experiments in current devices do not produce fusion-born alpha particles, studying their physics including their impact on turbulence is a challenging task. In that respect, the three-ion ICRF scheme [107] with ^{3}He traces in mixed hydrogen-deuterium plasmas can generate highly energetic ($\sim$ MeV) helium ions, which can help in addressing some aspects of the physics of fusion-born alpha and thermal-ion turbulent-transport stabilization. This heating scheme was recently employed in JET with the observation of enhanced thermal-ion confinement even in the presence of linearly unstable EP-driven modes. Nonlinear gyrokinetic simulations corroborated the experimental evidence, explained by the formation of zonal structures due to the excitation of TAEs [133]. This promising result is further discussed in chapter 2 of this volume [14]. Recent analytic and numerical studies indicate that a phase synchronization between trapped electrons and passing energetic ions might also result in the total suppression of ITG-driven turbulence [1113]. Finally, it is to be noted that a new stable impurity-free D-T plasma regime has been recently found, exhibiting high thermal confinement as a result of the zonal flows generated by EP-driven instabilities [52].

9.3.3. Turbulence-induced EP transport. Here, we discuss the impact of microturbulence on the transport and confinement of EPs. Since EPs can have large Larmor radii, it has been generally believed that gyro-averaging might lead to negligible EP transport [1114]. Based on this idea, the diffusivity is expected to decrease down to $D_f \sim 0.01\,\mathrm{m^2 s^{-1}}$, which is much smaller than the diffusivity of thermal particles. Recent advances in flux-tube gyrokinetic modeling as well as in experimental measurement techniques made it possible to gain further insight into this important research topic.

First self-consistent flux-tube gyrokinetic simulations were performed to study the alpha particle transport induced by microturbulence with the GYRO code [920]. It was found that alphas might interact significantly with ITG turbulence in the core of a fusion reactor, despite their large Larmor radius. The simulations resulted in density modifications of the order of 15% in the presence of microturbulence [1115]. Later,

simulations with the GENE code [680] suggested that the effect observed in [1115] might occur if the Larmor radius of EPs does not exceed the turbulence correlation length and if the poloidal drift velocities are sufficiently small [1116]. The EP transport in the presence of ITG turbulence was also analyzed in [836] using the GTC code [824], showing that the probability density function of the radial excursion is close to Gaussian, suggesting diffusive transport. The diffusivity is found to decrease strongly with energy due to gyro-averaging, in agreement with conventional wisdom. At the same time, gyrokinetic simulations using the GENE code showed that the EP diffusivities are significant for EPs with energies up to 10 times the thermal energy. The particle diffusivity then decreases as $D_{\mathrm{f}} \sim 1/\mathcal{E}_{\mathrm{f}}$ [1117].

In addition, flux-tube gyrokinetic analyses of transport of EPs as passive tracers have been reported in several works [833, 835, 1118, 1119]. Multi-code gyrokinetic analyses were performed using the GKW [1120], GYRO and GS2 [1121, 1122] codes, which mainly focused on impurity transport, but also included transport of alphas [1119]. In these studies, only microturbulence induced by electrostatic fluctuations was included, such as ITG- or TEM-driven turbulence. Moreover, alphas were modelled as passive tracers using a slowing-down distribution function. The derivatives of the EP distribution function with respect to the energy and to the radial coordinate were introduced in the gyrokinetic equation in GS2 and GKW, but not in GYRO. The three codes agreed well on the transport of alphas in both the linear and the nonlinear phases. It was again found that the diffusivity of alphas decreases strongly with their energy, leading to 20 times smaller diffusivity compared to thermal helium ash diffusivity in the core of ITER. The gyrokinetic results for particle transport were included in ITER transport modeling, concluding that the electrostatic microturbulent transport of alphas occurs on a characteristic timescale at least one order of magnitude larger than the slowing-down time. According to this multi-code analysis, on the timescale of the slowing-down process of alphas, electrostatic microturbulence might not play a significant role in the modification of the radial profiles of alphas. Further numerical simulations with the GENE code computed the diffusivities of EPs as passive tracers moving in fields with both electrostatic and magnetic fluctuations [833]. Whereas the electrostatic part indeed decreases with the energy of EPs as $1/\mathcal{E}_{\mathrm{f}}$, the magnetic counterpart does not and was found to be independent of the energy. The explanation that the gyro-averaging operation might not be valid for EPs has subsequently been debated in the literature [1123, 1124]. Finally, flux-tube simulations with GENE using passive highly energetic deuterium in ITER scenarios

concluded that the EP transport can be significant for intermediate energies on the order of 100 keV, with the electrostatic fluctuations dominating over the magnetic fluctuations [835].

From the experimental viewpoint, measurements in an ITPA joint experiment [1125] have suggested the possibility of anomalous spatial EP transport induced by microturbulence. Multi-machine analyses with measurements of NBCD on four different tokamaks (AUG, DIII-D, JT-60U and MAST) were done. In particular, the measured NBCD profile with a neutral beam injected power of 7.2 MW in the DIII-D tokamak was compared to calculations assuming various EP diffusion coefficients. As shown in figure 88, discussed in the next section, the best fit to one measurement occurred for an assumed EP diffusion coefficient of $D_{\mathrm{f}} \simeq 0.3$ m^2/s. A similar comparison was reported in [1125] for AUG, but in that case the EP diffusion coefficient required to obtain a match between the measurements and calculations depended on the triangularity, suggesting that other unexplored parameters may play a role.

FIDA measurements on DIII-D found evidence for EP transport when the ratio of EP energy to temperature was $\mathcal{E}_{\mathrm{f}}/T < 10$ [1126], which seems consistent with the ordering given by flux-tube simulations [1117]. The inferred transport rates in [1126] were found to be of the same order of magnitude as those predicted by the NUBEAM module. However, a subsequent DIII-D study concluded that any EP transport is dwarfed by EP transport induced by coherent fluctuations [1127]. In the absence of MHD activity, the confinement of energetic ions was shown to be neoclassical in plasmas characterized over a wide range of the ratio $\mathcal{E}_{\mathrm{f}}/T_{\mathrm{i}}$. These conclusions are consistent with the theoretical predictions that no significant energetic ion transport by microturbulence is expected in ITER half-field scenarios for intermediate energies [835]. Basic physics studies on LAPD confirmed the expected dependence of EP transport on finite gyroradius [1128] and turbulence wavenumber [1129]. Studies of cross-field EP transport in turbulent magnetized plasmas in TORPEX [1130] concluded that transport can be super-diffusive due to the intermittent transport of EPs mediated by turbulent structures elongated in the parallel direction that propagate radially (the so-called *blobs*). Such non-diffusivity of EP due to rare events dominated by Lévy statistics [1077–1079] can be concomitant with the mechanism described in [1076].

In conclusion, the numerical and experimental studies performed so far suggest that alphas and other EPs with energies $\gtrsim$100 keV in ITER scenarios might not suffer transport due to microturbulence alone for most of the slowing-down process. However, further

modeling is required to include global and full-orbit effects in order to completely assess the impact of turbulence on EP transport.

9.3.4. Interaction between EPs, turbulence and AEs. Fusion experiments such as ITER are expected to have a multitude of marginally unstable modes in the TAE frequency range [560, 563]. It has recently been shown that when pitch angle scattering is enhanced above classical Coulomb scattering levels, it will likely lead to AE amplitudes larger than those expected in the absence of anomalous processes [837]. Therefore, any modification of the EP pitch angle scattering rate could have an impact on the EP transport by means of the modified AE amplitude. Here, we review two mechanisms that are known to modify the pitch angle scattering rate: ICRF heating and microturbulence.

The first possible mechanism has been explored in TFTR experiments with the ICRF heating as a mediator, where the enhanced scattering of minority energetic ions increased the AE amplitude by an order of magnitude [1131]. However, the effects of RF injection on the stability of AEs is still an active research topic, especially when additional heating and current drive by RF and NBI are used simultaneously. As discussed in section 3, ICRF can create super-Alfvénic EPs which can easily destabilize AEs. The use of external RF injection to alter AE mode activity has been experimentally studied on several devices. Results vary greatly, from very weak effects observed [691] to AE activity suppression [692]. Mixed results have been reported even from the same device and similar plasma conditions (see figure 17 of [693]). Encouraging results were obtained when RF fields were employed to successfully terminate wave chirping excited by energetic electrons trapped in a magnetic dipole field experiment [689]. Nonetheless, more experimental and modeling work is required to fully understand the effects of RF-accelerated EPs on AE stability, especially when a synergy between different heating schemes (e.g. ICRF and NBI) can be expected. This remains an open area of research, especially considering the external heating mix planned for ITER. More specifically, phase-space engineering solutions can be employed, by exploiting the tuning of RF resonances in such a way that it can have the effect of decorrelating the EPs from the AE resonances, thereby extinguishing dangerous AE-induced transport. Guiding-center- or full-orbit-following codes can be specially helpful for that purpose, to find scenarios that maximize the RF effect.

The ability to predict, for a given plasma background, the nature of Alfvénic oscillations (fixed-frequency, leading to diffusive losses, or chirping/avalanching, leading to convective losses) can be of considerable advantage for measures aiming at the mitigation of EP transport. Spherical tokamaks tend to exhibit Alfvénic chirping and avalanching, accompanied by wave amplitude bursting, while conventional tokamaks tend to have Alfvénic waves oscillating with a nearly fixed frequency and a quasi-steady amplitude. To be able to explain this puzzling observation, a criterion for the likelihood of chirping oscillations was developed based on the theory of driven, kinetic instabilities near threshold with dissipation [931, 934] and evaluated for a number of NSTX, DIII-D and TFTR discharges [694, 907] using the stability code NOVA-K. It has been predicted [907] and verified experimentally [458, 695, 1132, 1133] that microturbulence can be a strong mediator between the mode transition from fixed-frequency to chirping and vice versa, due to an enhancement of the EP stochasticity. In spherical tokamaks, particles spend more time on the good curvature region and experience higher relative rotation shear. Therefore, spherical tokamaks naturally exhibit lower anomalous transport compared to conventional tokamaks. For example, on NSTX the total thermal ion diffusivity has been found to be of order of the neoclassical level [1134]. These distinct turbulence features have been found to explain why chirping instabilities are rare in conventional tokamaks and common in spherical tokamaks. Predictions for baseline ELMy, reversed-shear and hybrid scenarios of experiments planned for ITER have also been recently explored [695] and shown to be near the borderline between the fixed-frequency and the chirping regimes when collisional and microturbulence effects are accounted for. For scenarios in which other resonance decorrelating mechanisms are important, the TAEs and RSAEs would then be expected to exhibit a steady response with no frequency excursions. Experiments with reduced turbulence in DIII-D (using negative triangularity) [458] and in AUG (through impurity accumulation in the core) [1132] observed more prevalence of chirping than in usual operational configurations. The turbulence acts to effectively increase the scattering experienced by the resonant EPs [838] and therefore prevents the chirping and avalanching responses, resulting in diffusive transport. An example of the emergence of chirping correlating with low turbulence is shown in figure 85. It was also found recently that microturbulence may affect AE amplitudes [837], supported by expensive numerical simulations which are available for estimates.

When microturbulence is accounted for, diffusive losses can dominate the transport and quasilinear theory is expected to be sufficient to capture the essence of the self-consistent evolution of the EP distribution function. Quasilinear frameworks have been developed [1135] and have been applied to Alfvénic oscillations [906, 1136, 1137]. Recently, the
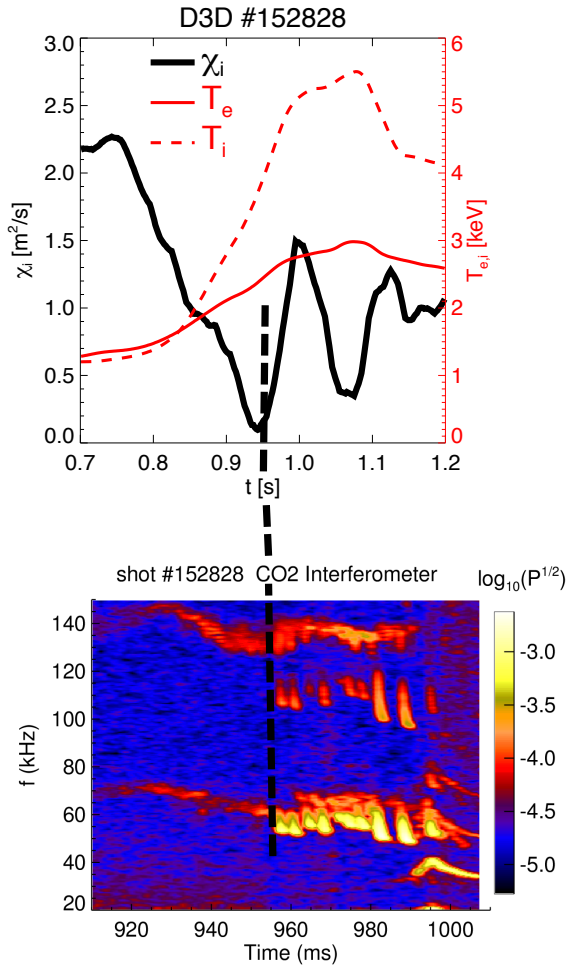
Figure 85. Correlation of Alfvénic chirping onset with a marked reduction of turbulence, as inferred by the ion heat conductivity calculated by TRANSP. Reproduced from [907].

quasilinear framework was extended to the case of a single mode [912], without any resonance overlap, when stochastic processes dominate the wave dynamics over the characteristic wave growth time and make the dynamics increasingly more time-local [910, 911]. The resonance (or window) function that weights the resonance strength in the EP diffusion coefficient was derived self-consistently in [912]. Such a resonance function is shown in figure 86 for the cases of scattering (blue) and Krook (red) collisions. Remarkably, the quasilinear theory that uses the analytically derived window functions has been demonstrated [912] to replicate the same saturation levels of the more complex nonlinear theory near threshold [914]. The resonance function has also been extended to account for dynamical friction [913] and has been applied to the dynamics of self-gravitating systems [1138].

One way of prescribing the microturbulence scattering is through the changes in ion canonical toroidal angular momentum P_ϕ through the change in
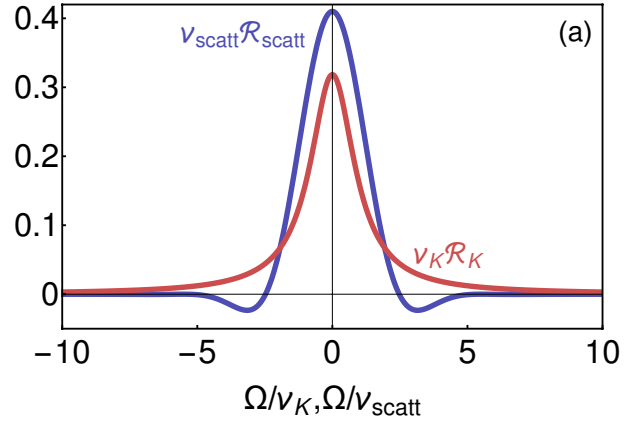

Figure 86. Plots of the self-consistently derived resonance functions $\mathcal{R}$ in quasilinear theory for the case of scattering (blue) and Krook (red) collisions. In the absence of broadening, the resonance function becomes simply a δ-function at $\Omega = 0$. Reproduced from [912].

the radial position of the EP. Additionally, the classical Coulomb collisions can modify P_ϕ directly through the pitch $\chi = v_\parallel / v$. The quasilinear frameworks of [694, 906] have been recently adopted to build a 2D realistic RBQ model with relaxation along the canonical momentum and the energy variables [908, 917]. In a 1D case, shown here for simplicity, RBQ evolves the EP distribution function as

$$\frac{\partial f}{\partial t} \simeq \sum_{k,p} \frac{\partial}{\partial P_\phi} D_{kp}(P_\phi; t) \frac{\partial}{\partial P_\phi} f$$

$$+ \left\langle [1 + R_{Dh}] \frac{\partial P_\phi}{\partial \chi} \frac{\partial}{\partial P_\phi} \nu_{\chi\chi} \frac{\partial P_\phi}{\partial \chi} \right\rangle \frac{\partial (f - f_0)}{\partial P_\phi} \quad (97)$$

where the diffusion coefficients due to AEs are $D_{kp}(P_\phi; t) \sim \delta B_\theta^2 \mathcal{R}(\Omega_{kp})$ and $\nu_{\chi\chi} = \nu_\perp (1 - \chi^2)$ for the case of Coulomb collisions with $\nu_\perp$ being the 90° scattering rate [894]. The second term on the right-hand side of equation (97) represents pitch angle scattering due to classical Coulomb collisions ('1' in the square brackets) and and due to anomalous scattering due to microturbulence (R_{Dh} in the square brackets) [838]. If $R_{Dh} \gg 1$, the diffusion is dominated by microturbulence, and if $R_{Dh} \ll 1$, it is dominated by collisions. The resonance window function $\mathcal{R}(\Omega_{kp})$ prescribes the weight of the resonant interaction on a P_ϕ grid. In the absence of collisions and modes, it is a delta function taken at the perturbative resonance, i.e. $\mathcal{R}(\Omega_{kp}) \to \delta(\Omega_{kp})$. It broadens within a certain window across the resonance with collisions and mode amplitude. The shape of $\mathcal{R}(\Omega_{kp})$ can be analytically computed self-consistently [912] (see also Ref. [1139]), provided that the degree of marginality makes the resonant dynamics increasingly local in time [910].

In RBQ simulations, equation (97) is supplemented by an equation governing AE amplitude evolution $dC_k^2(t)/dt = 2(\gamma_{L,k}(t) + \gamma_{d,k})C_k^2(t)$, where

growth rates, $\gamma_{L,k}(t)$, are computed at each time t using the distribution function f, whereas the damping rate, $\gamma_{d,k}$, is fixed in time but needs to be corrected non-perturbatively, so the damping may change as the mode evolves. During the development of the RBQ model, rigorous verification studies were proposed, including the analytically expected amplitude of a saturated mode [820], the dependence of the mode amplitude on the effective pitch angle scattering frequency, and computations of different marginally unstable cases [917].

The scattering window function $\mathcal{R}_{\mathrm{scatt}}$ (blue curve of figure 86) has been shown to be critical for realistic modeling of EP relaxation due to AEs. Earlier, a comparison between the quasilinear approach in a model geometry [1137] and the BOT code had been performed using a heuristic, flat-top broadening function. In the BOT code, the Vlasov equation was solved fully nonlinearly in 1D for one resonance in Fourier space [915]. Although the quasilinear and the BOT simulations can agree qualitatively fairly well, they agree quantitatively only in a limited parameter range. RBQ simulations employing the self-consistent resonance window function [912] in tokamak geometry were compared with BOT [837]. The most important difference between the two simulations, which are qualitatively very similar, is the recovery time between the peaks which is about 30 to 50% larger in RBQ than in the BOT code for the same scattering frequency. The experimental point lies near the threshold of existence and non-existence of steady-state regimes in both RBQ and BOT simulations whereas the AE amplitudes are in a steady-state regime in the DIII-D discharge of interest [860]. Figure 87 illustrates BOT and RBQ results where the DIII-D parameters for an RSAE mode of interest correspond to the red curve, showing that the normalized nonlinear bounce frequency, ω_b, was consistent between the RBQ and BOT simulations. Both models agree fairly well in near-threshold regimes.

Recently, a comprehensive stability analysis of ITER steady-state plasma was performed using the ideal MHD code NOVA, its drift kinetic extension NOVA-C and the 2D quasilinear code RBQ with a novel methodology [572]. Within that study a potentially important effect of AEs on EP confinement was identified which is due to EP density depletion near the plasma center. This effect is connected with the beam-ion and alpha current drive which will be also depleted near the center so that the generation of current drive is required for whole-device modeling (WDM) simulations. A self-consistent analysis of a plasma discharge including this effect is needed to evaluate its consequences on the plasma scenario.

The beam ions injected at 1 MeV lead to stronger AE growth rates in comparison with fusion alpha particles, which are born isotropically. This was not the case in earlier studies of ITER baseline scenario [31] where NBI injected fast ions have much smaller (around ten times smaller) beta. On the other hand, the background microturbulence can enhance EP losses in ITER plasmas, which deserves careful consideration. Present applications of RBQ and NUBEAM to the ITER steady-state case have shown a weak loss of fast ions to the wall at the level of a few percent [572].
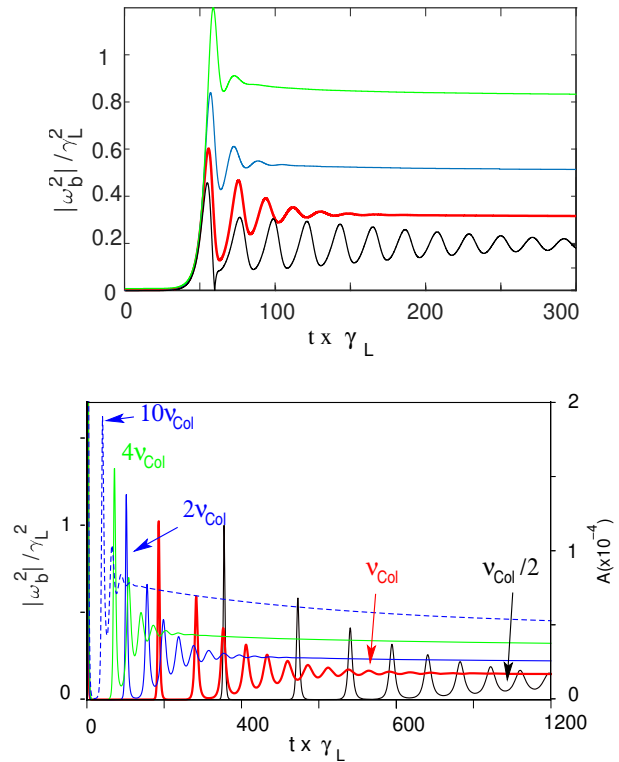

Figure 87. AE amplitude (shown in terms of the nonlinear bounce frequency) vs. time from RBQ1D and BOT for different levels of collisionality, modeling a DIII-D plasma. (Top panel) BOT has the effective frequency rates (going from the bottom figure up) $0.49\gamma_{\mathrm{L}}, 0.618\gamma_{\mathrm{L}}, 0.778\gamma_{\mathrm{L}}$ and $0.98\gamma_{\mathrm{L}}$. They correspond to the RBQ scattering rates $\nu_{\mathrm{Col}}/2, \nu_{\mathrm{Col}}, 2\nu_{\mathrm{Col}}$ and $4\nu_{\mathrm{Col}}$ of the nominal scattering frequency $\nu_{\mathrm{Col}} = 8.9s^{-1}$ computed by NOVA-K (bottom panel). Both figures have the same color coding for the corresponding scattering frequencies, i.e. the red curve is the nominal (collisional) scattering frequency. A much larger value of the scattering frequency curve, $10\nu_{\mathrm{Col}}$, is added for RBQ simulations as blue dashed like. Reproduced from [837].

10. EP current drive and scenario optimization by EP phase-space control

EPs can be very attractive to enhance the performance of fusion reactors by phase-space control and optimization. In this section, several such phase-space control possibilities involving EPs are discussed which have been demonstrated either experimentally or theoreti-

cally. Here we understand the term *control* to denote strategies to steer a discharge towards a higher performance by means of actuators affecting either the EPs directly, or indirectly by mediating EP-driven instabilities. There are two possible avenues to suppress or mitigate such instabilities, which both aim for separation of the mode locations and the locations with steep EP gradients: 1) modify the EP distribution to flatten the gradients at the mode location, and 2) modify the background plasma profiles to move eigenmodes away from the region with steep EP gradient (or high EP density). Both avenues have been explored in recent years on several tokamaks and stellarators [121,546,1140–1142]. Promising actuators to this end are variable NBI and ICRF sources that change the gradients in the EP distribution, localized ECRF heating affecting the slowing down of EPs, localized ECCD to change the helicity of the magnetic equilibrium and hence the existence criteria and damping of AEs, and externally applied 3D magnetic perturbations to change the EP distribution and hence the wave drive [1142]. In this section, these phase-space control schemes are considered from the perspective of their effects on AEs and on EP confinement as well as on the overall fusion reactor performance with the goal to optimize plasma scenarios in burning plasma conditions. We start by reviewing EP current drive, since it can make an important contribution to the overall current drive and can be an important control knob for scenario optimization.

10.1. EP current drive

In addition to the essential role of EPs in heating burning plasmas, they can also generate noninductive current drive [20]. Different noninductive current drive schemes have been reviewed in [1143]. Fully noninductive discharges at high pressure are being studied extensively at EAST [1144]. The ITER NBI system [1145] has two heating NBIs with the possibility to add a third. Heating NBIs also drive current and introduce plasma rotation due to the oblique NBI beam path with respect to the magnetic field. Additional current drive schemes planned in ITER are ICCD and ECCD.

To calculate the EP current drive (NBCD or ICCD) for the purpose of scenario optimization accurately, we need to know the EP phase-space distribution function, which may or may not be captured accurately in whole device models (WDMs) such as TRANSP. The EP current drive is found from the first moment of the phase-space distribution function on the equilibrium timescale, which is much longer than the timescale associated with the Alfvén wave period. Thus, the current density is related to the phase-space distribution functions of all species in

the plasma, including the EPs, according to

$$\boldsymbol{J} = \sum_{\mathrm{s}} Z_{\mathrm{s}} e \int (\boldsymbol{v}_{\parallel} + \boldsymbol{v}_{\mathrm{dr}}) f_{\mathrm{s}} \frac{2\pi B}{\sqrt{2m^3(\mathcal{E} - \mu B)}} \mathrm{d}\mu \mathrm{d}\mathcal{E}, \quad (98)$$

where $2\pi B/\sqrt{2m^3(\mathcal{E} - \mu B)}$ is the Jacobian.

The calculation of the EP current drive should include the screening effect by thermal electrons which is not trivial since the electron gyromotion needs to be resolved. For example, the EP current screening by thermal electrons leads to so-called Ohkawa current [1147] which depends on the effective plasma charge Z_{eff} and modifies only the parallel component of the EP current. However, the parallel currents do not appear in the Grad–Shafranov equation used to calculate plasma equilibria, and thus the Ohkawa current does not enter the calculation of plasma equilibria explicitly.

Equation (98) suggests that the most useful and straightforward way to compute the EP current drive is to compute the EP distribution function in COM space. The representation of EP phase-space distributions in various coordinate system is not trivial since the COM space Jacobian diverges at the trapped-passing boundary [1148, 1149]. The current drive is quite sensitive to the details of the distribution function [1150], so it needs to be accurate enough in at least the following three requirements. First, the model needs to accurately represent the balance between the passing and trapped EPs since the bounce average of the trapped-EP contribution to the parallel component of the current is much smaller than the passing-EP contribution. Second, the model needs to accurately represent the balance between the low- and high-energy EPs, since high-energy EPs cause more current than low-energy EPs. Third, the model needs to accurately represent the Ohkawa current [1147] in the calculation of the parallel component of EP current drive, as already mentioned.

As an example of the effects of these requirements, a recent study fitted the radial dependence of the current drive by adjusting the radial diffusion [1146]. Although the fit only partially satisfies our three requirements for the diffusion coefficients, it shows how sensitive the current drive is to the magnitude of the radial diffusion. This study varied the *ad hoc* diffusion coefficient, which is fairly moderate, uniformly over velocity space for two discharge with different NBI power levels. For the high power discharge, anomalous diffusion at a moderate level ($D_{\mathrm{b}} \sim 0.3\,\mathrm{m}^2/\mathrm{s}$) was used to fit the current drive to the reconstructed NBI current profile (figure 88 (b)). The fitted diffusion magnitude already provides some constraints for the choice of the distribution function parametrization.

However, for the AE-induced relaxation of EP distribution function and similar wave-particle interactions, the multidimensionality of the problem should not be overlooked. The current drive was
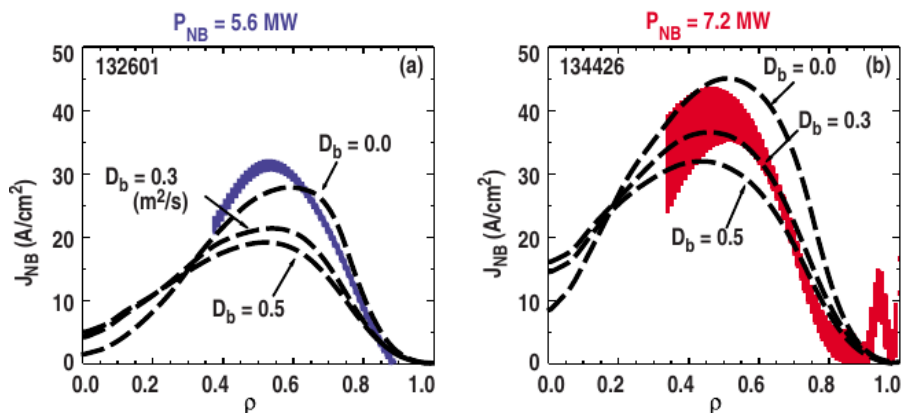
Figure 88. Effects of *ad hoc* anomalous EP diffusion on off-axis NBCD profiles at DIII-D. The measured NBCD profile fits best with the theoretical calculation with $D_b = 0$ and $0.3\,\mathrm{m^2/s}$ at (a) $P_{NB} = 5.6\,\mathrm{MW}$ and (b) $7.2\,\mathrm{MW}$, respectively. Reproduced from [1146].

later simulated using the kick model which includes both the diffusive and convective motion of all EPs in the presence of MHD instabilities (see section 7). The internal kink-like mode and several TAEs with mode numbers $n = 1$ to $n = 6$ were included. Figure 89 illustrates that the kicks in COM space are substantially different for the kink mode and the TAEs. The figure suggests that the uniform *ad hoc* diffusion [1146] may not be appropriate to describe the current drive because a mode with a given frequency interacts differently with the various groups of EPs, which have different characteristic orbital frequencies.

An important question on the path to burning plasma operations is how to optimize plasma discharges to achieve optimum burning plasma conditions. The EP contribution to this goal could be critical due to the effects of AEs and other modes on the current drive efficiency. Given the importance of the current drive for the plasma scenario and the availability of the power from fusion products, NBI or ICRF, the benefits of current drive control could be significant for the overall reactor performance.

The difficulty of the current drive problem in the presence of EPs lies in both its accurate diagnostic and its accurate modeling. The EP current density in the plasma center from NBI heating was measured by velocity-space tomography based on FIDA measurements at EAST [217]. The modeling tools need to accurately resolve the EP distribution function in COM space and in time which can be addressed by initial value simulations but not necessarily by the reduced models. To a large extent, EP current drive is not properly calculated by present common models which needs to be addressed for integration into the whole device modeling tools such as TRANSP [895] for predictive simulations of future burning plasma devices.

10.2. Actuators changing linear stability properties

AEs in burning plasmas could produce significant transport of the EP population to the wall, which could degrade the fusion performance and could cause localized heat loads from EP impact. External actuators to control AEs in burning plasmas are being developed in present fusion devices to mitigate this risk. These can act on the gradients in the EP distribution affecting the mode drive, or on the magnetic helicity affecting the Alfvén continuum damping and the existence of AEs in the Alfvén continuum. In practice, these control strategies are interrelated and cannot be changed individually. For example, changes in the kinetic profiles (T_e, n_e) directly change both the wave drive and the damping. Changes in the q-profile affect not only the Alfvén continuum and hence the continuum damping but also the EP distribution and hence the wave drive. Experiments in present tokamaks and stellarators together with numerical simulations allow us to develop control techniques applicable to future burning plasmas, which we will review in the following [1142]: variable ICRF and NBI, ECRF, ECCD, and RMPs.

10.2.1. Toroidally asymmetric ICRF waves. As discussed in section 2, the changes in particle toroidal canonical angular momentum and energy of a particle interacting with an ICRF wave are related by $\Delta P_\phi = (n/\omega)\Delta\mathcal{E}$. ICRF heating increases the energy of EPs, so we always have $\Delta\mathcal{E} > 0$. The mode number can be large for ICRF heating ($n \sim 30$), and the spatial transport can be significant despite the high wave frequency. This allows flattening of the spatial profiles or moving steep gradients away from the mode location. Toroidally asymmetric waves can have positive or negative toroidal mode numbers n. The particles can thus be transported either
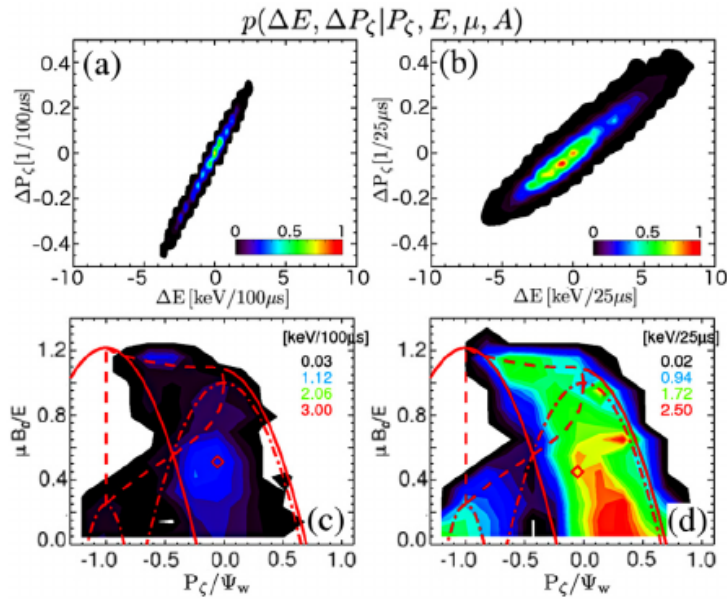
Figure 89. Illustration that EP transport in different parts of phase space depends on the instability. The probability density function $p(\Delta\mathcal{E}, \Delta P_\zeta)$ for "kicks" in energy and canonical angular momentum resulting from (a) a kink-like mode and (b) TAEs for fast particles with energy $\mathcal{E} = 80\,\text{keV}$, $P_\zeta = 0$ and $\Lambda = \mu B_0/\mathcal{E} = 0.5$. (c)–(d) Root mean square of energy kicks for (c) kinks and (d) TAEs at $\mathcal{E} = 80\,\text{keV}$ in different parts of phase space. Reproduced from [1150].

in the positive or in the negative direction of P_ϕ, corresponding to inward or outward transport in the poloidal flux coordinate ψ [1151–1153]. This control knob on the transport of ICRF-accelerated EPs has been demonstrated on JET where the energetic ^{3}He density profile could be modified selectively. Measured γ-ray emission profiles showed clearly that peaked EP profiles were obtained for ICRF waves with $+90°$ phasing, corresponding to an inward EP transport, and flattened EP profiles were obtained for ICRF heating with $-90°$ phasing, corresponding to an outward EP transport. Toroidally asymmetric waves can further be used to induce plasma rotation, which may be of significant interest for scenario optimization [1154].

10.2.2. Variable NBI. As discussed in section 2, NBI heating generates highly anisotropic EP distributions. As the operational parameters of the various NBI sources can be controlled, the EP population from NBI heating can be changed quite substantially. This allows, e.g., changing the gradients in the EP population or changing the EP phase-space densities at the wave-particle resonances that cause the AE drive, which has been experimentally demonstrated by varying the heating power, voltage, and torque [1155, 1156], the toroidal rotation shear [1157], the energy and pitch of the injected particles [581,604] and the spatial gradients of the EP distribution [545,1158].

For example, experiments in NSTX-U changed the AE activity by using either inboard or outboard

NBI heating, significantly modifying phase-space distribution of the NBI ions [604]. Whereas the in-board NBI heating at NSTX-U typically excites GAEs, the outboard (more tangential) NBI stabilizes GAEs [604] as figure 90 demonstrates. Resonant EPs are stabilizing for $k_\perp \rho_{\text{Lf}} < 1.9$ but destabilizing for $1.9 < k_\perp \rho_{\text{Lf}} < 3.9$ according to the Doppler-shifted ion cyclotron resonance model. The stabilization is thought to be due to an increase in the phase-space density of low pitch, deeply passing particles with small Larmor radii as suggested by analytic theory, experiments, and kinetic-MHD simulations with the HYM code [1159]. The kinetic-MHD simulations carried out with the HYM code [1160] suggest that stabilization is due to the reduction of the anisotropy of the NBI ion distribution function by the increase in the passing particle population.

10.2.3. Electron cyclotron current drive. ECCD is a promising tool to control AEs as it can locally change the magnetic shear and hence the AE damping. The AE activity observed in tokamaks and stellarators depends on the Alfvén continuum with its gaps given by the magnetic equilibrium and the thermal plasma profiles [32]. In tokamaks, TAEs do not exist if the plasma pressure gradient is larger than a threshold given by the magnetic shear S, the aspect ratio ϵ, and the Shafranov shift Δ' according to

$$\alpha = -R_0 q^2 \frac{\text{d}\beta}{\text{d}r} > \alpha_{\text{crit}} = (\epsilon + 2\Delta') + S^2. \quad (99)$$
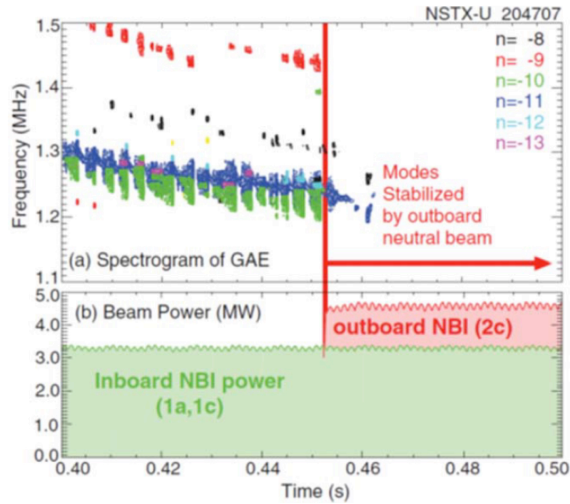
Figure 90. a) Mirnov coil color-coded spectrogram showing counter-propagating GAE activity at NSTX-U. Dominant modes are n=-10 (green) and n=-11 (blue). b) Power of on-axis (green) and off-axis (red) NBIs. Reproduced from [604].
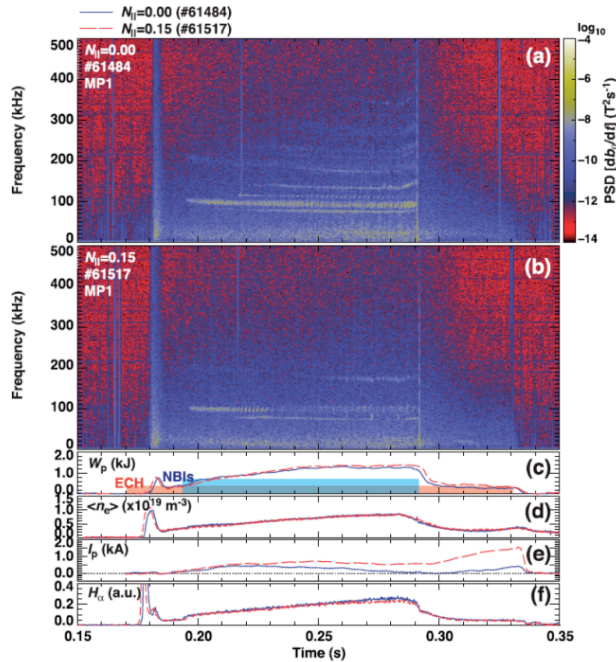

Figure 91. Temporal evolution of the magnetic activity in Heliotron J as measured by a magnetic pick-up coil in a discharge without ECCD, i.e. $N_\parallel = 0$ (a) and with ECCD and $N_\parallel = 0.15$ (b). Temporal evolution of plasma stored energy (c), line-averaged electron density (d), plasma current (e), and Lyman α line for the case with $N_\parallel = 0$ (red) and $N_\parallel = 0.15$ (blue) (f). Reproduced from [1161].

The tokamak confinement principle requires large plasma currents, which makes it rather difficult to change the local magnetic shear by targeted, localized ECCD. Additionally, ECCD also heats the plasma, and the effects of heating and current drive are difficult to

distinguish. Stellarators, on the contrary, have small plasma currents, so ECCD can generate a significant part of the total plasma current, which makes the effect of ECCD on AE activity readily observable. In Heliotron J, ECCD with $N_\parallel = 0.15$ fully suppressed GAEs driven by NBIs as figure 91 shows [1161]. In fact, the basic physics mechanisms for mitigation or suppression of EP-driven modes have been confirmed in several experiments in non-axisymmetric devices, e.g. in TJ-II, Heliotron J and LHD [1162–1164]. In those studies, either NBI or ECCD were used to modify the current profile and local pressure, shifting the mode frequencies into the Alfvén continuum.

10.2.4. ECRF heating. ECRF heating has been used to affect AE dynamics in different ways in tokamaks [121, 292, 900, 1142]. ECRF heating is a highly localized form of heating and allows targeted heating in a narrow region around the ECRF resonance, so individual modes can be targeted. ECRF heating changes the kinetic plasma profiles very locally, and many different types of interaction can be exploited. Since AEs are highly sensitive to the q-profile, the electron density profile and the temperature profile, ECRF has a strong impact on the AE drive and damping and hence on the stability. This idea was corroborated in experiments in DIII-D and AUG. In discharges with early NBI heating and elevated, reversed q-profiles, ECRF heating mitigated [1165] or even suppressed RSAEs [121, 1166]. The localized ECRF power deposition profile was varied in several otherwise nominally identical shots to investigate the impact on the RSAE activity at DIII-D. The power was deposited in the plasma center near the magnetic axis (figure 92a), at the q_{min} position (figure 92b), or at the outer mid-plasma radius. The AE activity was strong for ECRF heating near the magnetic axis, whereas it was fairly weak for ECRF heating at the q_{min} location, and RSAEs were almost suppressed (figure 92). The RSAEs were completely suppressed when ECRF heating is applied at the q_{min} location at AUG, in agreement with the DIII-D results.

It is important to remember that the demonstrated control of RSAE activity by ECRF heating at AUG and DIII-D comes from several simultaneous effects, which are interrelated. The localized ECRF heating has an impact on the mode drive, on the damping, and on the ideal eigenmode itself. The AE stability depends on different damping mechanisms such as electron collisional damping [482] and electron Landau damping [428], as well as on continuum damping [1167] through changes to the modes and the continuum induced by changes in the pressure or plasma rotation [1157, 1168]. The mode drive is also affected since the electron drag on EPs depends on T_e, mod-
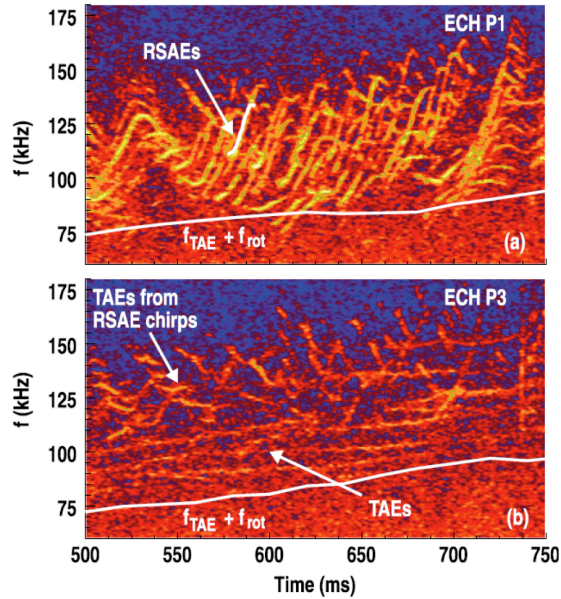
101

Figure 92. Windowed crosspower spectra of vertical and radial CO_2 interferometer data at DIII-D for 1.9 MW ECRF heating deposition at (a) the plasma center #128564, (b) at q_{min} #128560. Overlayed white curves are a typical RSAE and the local TAE frequency plus toroidal rotation frequency at q_{min}. Reproduced from [1165].

ifying the gradients in the EP distribution. Finally, the AEs themselves are affected via coupling to sound waves due to changes in T_e or T_i [1169].

In experiments at DIII-D, the ECRF power deposition, the current ramp rate, the ECRF injection timing, and NBI power were varied to study any changes in the RSAE activity [292]. The impact of ECRF heating on the AE activity was found to be sensitive to all these parameters. RSAEs were even observed to be more unstable for ECRF heating near q_{min} in some cases, which is in contrast to the observations in the original experiments, where they were more unstable for ECRF heating near the magnetic axis. The existence of RSAEs that sweep in frequency strongly depends on the ratio of the minimum frequency of the RSAEs (including a pressure-dependent upshift from the GAM frequency at q_{min}) to the TAE frequency. When these frequencies are similar, no RSAEs are found, whereas TAEs still exist. Typical frequency-sweeping RSAEs are highly sensitive to gradients in the plasma pressure, and may no longer be an eigenmode of the system. When the electron beta increases due to ECRF heating, the RSAE frequency increases and may exceed the characteristic TAE frequency so that RSAEs can no longer sweep, resulting in reduced EP transport. Finite pressure effects can explain many of these observations [292], but they cannot account for the strong impact of ECRF heating on NBI-driven AEs in AUG and DIII-D.

Furthermore, additional factors are found to be important and must be experimentally characterized further. For example, modulated ECRF heating which leads to rapid modulations of TAEs [468]. A second example is that RSAEs are absent in a discharge after T_e profiles have relaxed so that the plasma is apparently similar to that in another discharge where RSAEs were observed [1170].

A plasma scenario of particular interest for steady-state, high-performance discharges is the so-called high-q_{min} scenario, in which the minimum safety factor profile value remains near or above $q_{min} \sim 2$. This prevents the development of potentially disruptive tearing modes [1171]. As a downside, a higher q_{min} can make the scenario more susceptible to AEs for which the growth rate increases as q_{min}^2. Such scenarios can lead to a deterioration of the overall plasma performance [1171, 1172].

Recent experiments on DIII-D [121, 292, 1141, 1173], AUG [1142] and KSTAR [900, 1174] have further demonstrated the potential of AE mitigation/suppression strategies for improving the overall plasma performance.

As an example, low-frequency AE mitigation/suppression schemes for plasma scenario optimization have been extensively tested in DIII-D experiments [1140, 1141] (figure 93).

Another study was aimed at developing scenarios where the q_{min} location is shifted away from the core toward the plasma mid-radius or slightly higher, e.g. using the off-axis NBI as an external actuator to tailor the current density profile [1140]. The idea in those experiments is that the unstable modes, that are potentially detrimental for core EP confinement (e.g. RSAEs), are pushed towards the plasma edge in regions with lower EP density, which quenches the associated EP loss channel. A significant reduction in AE driven EP transport was found and agreed with predictions of critical gradient models discussed in section 7 [1140].

A stabilizing effect of ECRF heating was observed on TJ-II, which was attributed to an increased damping at higher temperatures, but the reason was not obvious [1170]. Experiments on TCV showed an increase in mode activity with increasing ECRF heating and NBI [1175], which in that case was attributed to an increase in the slowing-down time of NBI ions resulting in an increase in EP density. As a general conclusion, those effects are usually well captured by codes such as TRANSP, and competition between drive and damping can be investigated through AE stability codes.

It should be noted that ECRF heating could affect AE activity via other mechanisms. First, ECRF heating has an impact on microturbulence which is
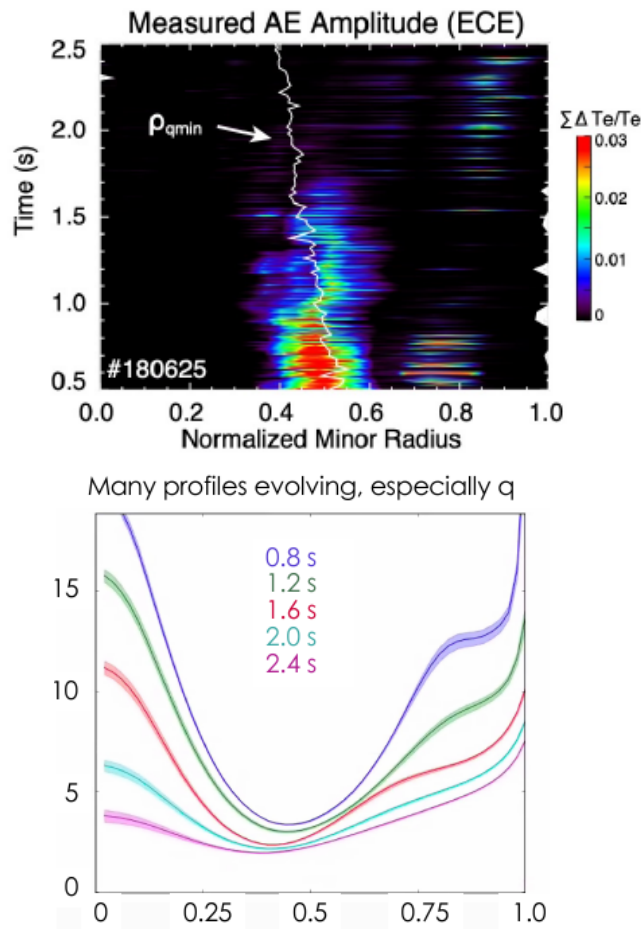
Figure 93. DIII-D scenario optimization shot to mitigate AE excitation and improve plasma performance by applying core ECCD, along with off-axis NBI, to move q_{min} inward to the location of reduced beam pressure gradient. Reproduced from [1141].

thought to affect the AE saturation and the impact on the EP profile [830]. Second, ECRF heating can have an impact on the horizontal polarization of flux surfaces which can form a potential hill for RSAEs, eliminating RSAEs at fairly low ECRF power [1176,1177]. Since the effect depends on changes in the electron distribution function, RSAE were suppressed for timescales similar to the electron-electron collision time. Hence, the AE response to ECRF heating modulation [468] as well as to wave polarization should be studied further.

For ITER and future fusion reactors, the feasibility of AE control schemes through ECRF heating is intriguing. The ITER ECRF heating system is primarily designed for heating, current drive, and NTM control [1178, 1179]. At present, no active investigations on the use of ECRF heating or ECCD for AE mitigation control have been performed, and it is unclear if the timescales and hardware capabilities for mirror steering of the ECRF heating
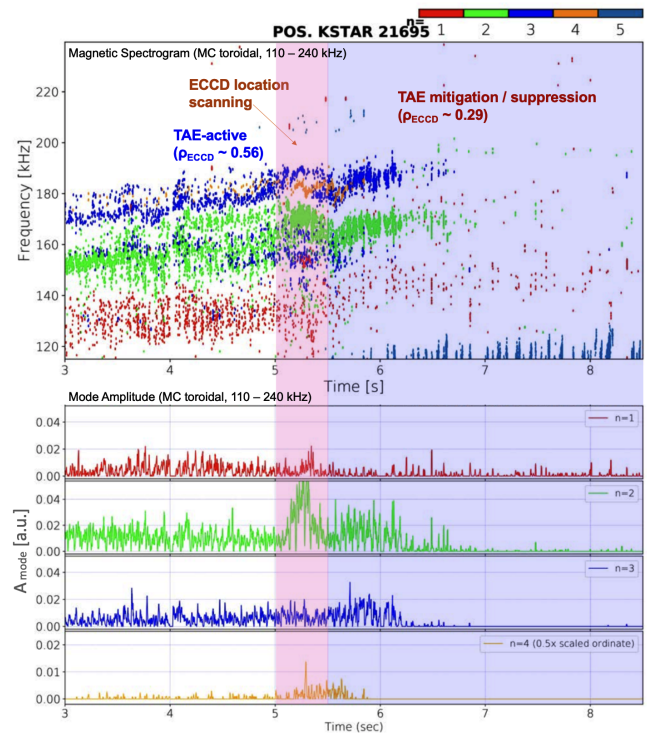

Figure 94. Example of AE mitigation and suppression by ECRF heating on KSTAR. The top panel shows the toroidal mode number spectrum from Mirnov coils at the vessel wall. The ECCD power deposition location is varied from $\rho = 0.56$ to $\rho = 0.29$ between 5 s and 5.5 s, resulting to suppression of TAEs after ≈ 6.5 s. The bottom panels show the evolution of mode amplitude for $n = 1 - 4$, with negligible amplitude detected in the TAE frequency range after 6.5 s. Reproduced from [1174].

system are compatible with such demanding, multi-task operations at ITER [1180].

10.2.5. Externally applied RMPs. Externally applied RMPs are routinely used in tokamaks to stabilize the plasma against MHD activity such as ELMs [1181–1183] or RWMs [408] as discussed in section 8. Externally applied RMPs have been used in NSTX to mitigate TAEs and GAEs by modifying the EP phase-space distribution [970, 1184]. Perturbations of size $\delta B/B \approx 0.01$ at the plasma boundary reduced the mode amplitude, increased the mode bursting frequency, and decreased the frequency chirp. Furthermore, the magnetic perturbation can modify weakly bursting modes temporarily to a saturated continuous mode. Figure 95 shows the impacts of RMP blips on the GAE activity in an NBI heated discharge. Experiments at AUG have corroborated that RMPs can be used to control strong TAEs driven by NBIs.

10.2.6. Sensors for real-time control For real-time control, accurate rapid detection of AEs or fast-ion properties are required. Various methods to detect

unstable AEs have been tested on DIII-D using ECE [1185–1187] and interferometer [1188, 1189] signals. Real-time control of neutral-beam populations based on calculations using the RABBIT code [922] are being developed on AUG [923, 924] and DIII-D.
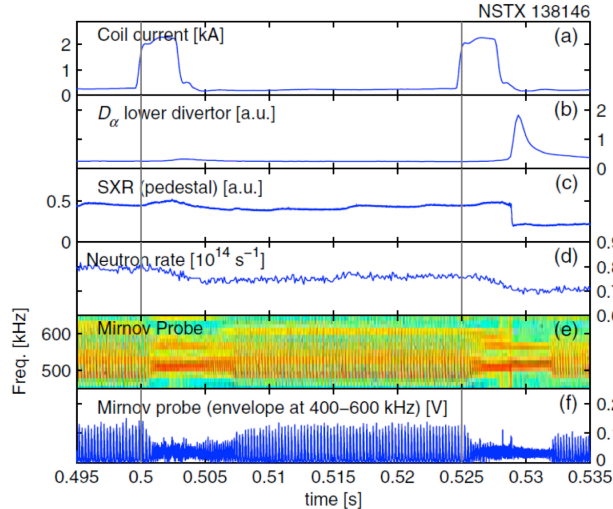

Figure 95. AE mitigation at NSTX via externally applied 3D fields. (a) RMP coil current per turn, (b) D_α-light, (c) SXR emission from the plasma pedestal, (d) neutron rate, (e) spectrogram of Alfvén activity from a magnetic pick-up coil and (f) bandpass filtered magnetic pick-up coil signal. Reproduced from [970].

10.3. Scenario optimization exploiting low- and high-frequency AEs

The basic relation between changes in energy and canonical toroidal angular momentum $n\Delta\mathcal{E} = \omega\Delta P_\phi$ suggests the we can target transport in energy and in P_ϕ selectively through low- or high-frequency waves. EP-driven Alfvénic instabilities with frequencies well below the ion cyclotron frequency transport EPs primarily along the P_ϕ direction with $\Delta\mathcal{E}$ relatively small. For usual EP energies the magnetic flux term of P_ϕ dominates, so $P_\phi \propto \Psi_{\rm pol}$ suggests transport in the radial direction. Conversely, at higher frequencies, $n\Delta\mathcal{E} = \omega\Delta P_\phi$ suggests that $\Delta\mathcal{E}$ is now large whereas the change in P_ϕ can be small for small mode numbers n.

As a result, the low-frequency AEs are mostly driven by the EP radial density gradients whereas high-frequency AEs are mostly driven by the EP energy gradients. Furthermore, the low-frequency AEs lead to primarily radial redistribution of EPs, leading to relaxed EP drive from spatial gradients, whereas the high-frequency AEs lead to primarily energy redistribution of EPs, leading to relaxed drive from energy gradients. Nevertheless, as already discussed, asymmetric ICRF waves with $n \sim 30$ can still cause

significant radial transport. These considerations lead to avenues of scenario optimization via high- and low-frequency AEs.

The high-frequency Alfvénic modes on the order of the ion cyclotron frequency can tap into the EP energy and to a lesser extent the EP toroidal momentum, which is proportional to approximately the square of the minor radius of the confined ion position. Given that both the high-frequency CAE and high-frequency GAE type of instabilities reach primarily the EP kinetic energy, they can provide a opportunities to improve the plasma performance by influencing the EP velocity distribution function. This in turn modifies the stability of EP-driven modes. The linear properties of high-frequency instabilities were discussed in section 6. High-frequency GAEs [598] and CAEs [1160] can channel their energy to the plasma through the excitation of kinetic Alfvén waves (KAW). Such channeling is important in particular for the ICE problem, i.e. it provides an additional damping mechanism not considered earlier. KAW excitation leads to CAE damping through the electron Landau damping by inducing $E_\parallel$ due to the small perpendicular wavelength of KAWs. This particular damping mechanism is new and had not been accounted for in ICE theory [573, 574]. However, these mechanisms exploiting high- and low-frequency AEs need to be better understood and verified for the active plasma optimization of a fusion reactor.

10.4. Alpha channeling

From the point of view of optimizing the plasma discharge, an interesting idea is to utilize the so-called alpha-channeling effect [616, 1190]. As proposed originally, the alpha-channeling diverts energy from energetic alphas to plasma waves that are damped on thermal ions in order to shortcut collisional slowing down on electrons. It is preferable that the alpha energy directly heats the fuel ions, which mostly determine the fusion reactivity, or that the alpha energy is used to amplify the plasma waves that drive current. If successful, alpha-channeling could result in a more economical DT fusion reactor. Simulations and experiments on TFTR support certain separate building blocks that, when taken together, might produce the desired effect [1191, 1192].

Some analyses based on the solution of the steady-state Fokker-Planck equation for the alpha distribution in slab [1193] and full toroidal [1194] geometries indicated that significant extraction of alpha energy using alpha-channeling might be possible, provided there is sufficient control over Alfvénic turbulence to remove the helium ash. However, the practical feasibility of alpha-channeling in an ITER-like plasma is still debated [1195]. Simulations were performed

using a mode with resonances in the ion cyclotron range to extract energy from the alphas and using either a low-frequency mode or microturbulence for ash removal. It was found that any combination of mode amplitudes and diffusion by microturbulence capable of extracting energy from the alphas and ejecting ashes also causes significant alpha energy fluxes to the walls. Despite these discouraging results, alpha-channeling remains an intriguing subject for improving the performance of fusion reactors, requiring further experimental and modeling work.

Alpha-channeling can also be considered in a broader sense, i.e. in order to optimize the plasma discharge by using the fusion-born charged products not only for plasma heating. For example, it was suggested to use Alfvénic instabilities to redistribute EPs in order to reduce the central magnetic shear [1196]. In that case, the formed steady-state internal transport barrier can be sustained as was demonstrated in DIII-D experiments. Another possibility for alpha channeling is EGAM channeling discussed in subsection 9.2.

11. EPs in ITER reduced-field scenarios before DT

The 2016 ITER baseline configuration and research plan foresaw a fairly long operation period in hydrogen and helium plasmas heated by NBI, ICRF and ECRF. This non-nuclear period minimized the activation of the machine by DD fusion neutrons in the early operational phases [4, 5]. In the new 2024 ITER baseline, this period has been significantly shortened and only RF heating will be applied [6]. After a brief period of hydrogen and helium operations, ITER will commence deuterium operations.

The new start-up phase will demonstrate L-mode operation at full magnetic field and full current (5.3 T, 15 MA). H-mode access is easier to achieve at reduced fields and will be attempted at half field and current (2.65 T, 7.5 MA), or possibly even at 1/3 field, 1/3 current, (1.8 T, 5 MA) in ITER. It would be advantageous to attempt H-mode access in deuterium since the L-H transition power threshold is lower than in hydrogen, but deuterium should be avoided in the start-up phase to minimize the activation of the machine. The reduced-field scenarios are further discussed in chapter 6 of this volume [18].

The plasmas in the early operation phases of ITER will be heated mostly by ECRF heating with an additional 10 MW ICRF heating which can generate EPs. As NBI heating had a prominent role in the non-nuclear phase of the original 2016 ITER baseline, the EP related work for these scenarios has had its focus on NBI heating. Therefore, the review in this section

pays much attention to NBI physics, which will play a lesser role in the new plan but will be nevertheless be important just before the DT phase where obviously safe operations is also required, despite the brevity of operation phase.

At reduced field and current, the EP confinement will be worse than at full field and current due to the wider drift orbit widths. Furthermore, the reduced fields cause a relatively stronger magnetic field ripple. Additionally, the lower current leads to lower plasma density, which increases NBI shinethrough that can lead to localized power loads on the plasma-facing components and, in the worst case, result in local melting.

We will first discuss NBI shinethrough and then EP confinement in MHD-quiescent plasmas with external 3D perturbations and various MHD modes, as well as ICRF heating scenarios at reduced field. Microturbulence is not expected to be a particular concern for half-field scenarios (see section 9). Finally, conclusions based on existing results are given and needs for more detailed studies are identified.

11.1. NBI shinethrough power loads in reduced-field scenarios

ITER will have two heating NBIs and one diagnostic beam. The heating NBIs will each inject 16.5 MW at 870 keV for hydrogen and at 1 MeV for deuterium (see section 2). In addition to heating, they also drive current and plasma rotation. The diagnostic beam will operate with hydrogen and inject up to 2 MW at up to 100 keV.

Empirical scaling relationships suggest that H-mode access will be easier at the lower densities of the reduced field scenarios. To reduce shinethrough, the NBI injection energy needs to be decreased from the nominal energy of 1 MeV, which also decreases the available NBI power according to the perveance relationship $P_{\mathrm{NBI}} \propto \mathcal{E}_{\mathrm{inj}}^{2.5}$. In addition, the injected species plays a significant role: the shinethrough is stronger for hydrogen NBIs than for helium NBIs for the same NBI parameters. To consider worst-case scenarios, shinethrough studies have therefore mainly considered hydrogen beams and plasmas.

Most of the shinethrough hits four special panels designed to withstand extra power loads in horizontal rows 15S and 16S (figure 96). The computed shinethrough power on these panels has been found to be within the allowed power limits even at low densities. However, a small portion of the shinethrough can pass through the 10 mm wide horizontal gap between the rows and can hit blanket shield block 16DS [1145, 1198]. Since the shield blocks are not designed to be replaced during the lifetime of ITER, it is crucial to ensure benign shinethrough loads in this
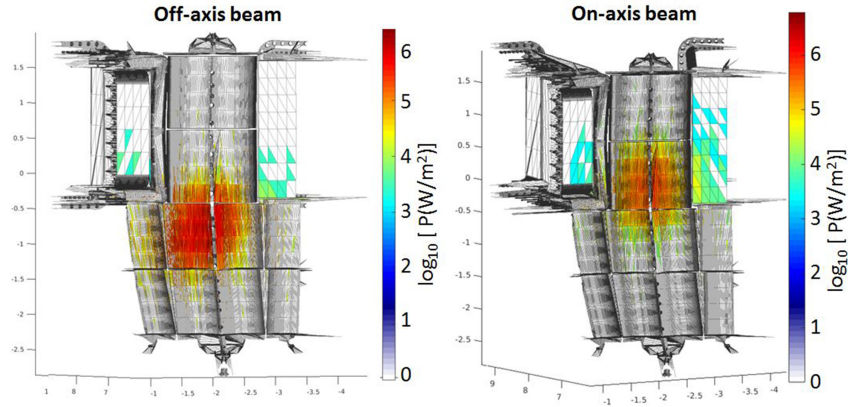
Figure 96. Power densities of NBI shinethrough losses from 9.4 MW, 530 keV beams off-axis beams (left figure) and on-axis beams(right figure) in 5 MA and 1.8 T hydrogen plasmas, as calculated by BBNBI/ASCOT. The power is the total power from the two beam boxes. Reproduced from [1197].

gap ($<$0.8 MW/m^2).

Early work on wall load patterns was based on an analytic beam model [1145]. Later, more detailed simulations using the beamlet-based NBI code BBNBI [1199] were performed for the 1/3-field hydrogen plasma scenario for two different kinetic profiles [1197, 1200]. One was at 50% of the Greenwald density ($0.5\,n_{\mathrm{GW}}$) with temperature profiles corresponding to about 40 MW auxiliary heating, and the other at $0.9\,n_{\mathrm{GW}}$ with over 50 MW of auxiliary heating. At $0.5\,n_{\mathrm{GW}}$, the NBI injection energy had to be reduced to 530 keV, which gives a beam power of 4.7 MW. At $0.9\,n_{\mathrm{GW}}$, the NBIs can be injected at 745 keV [1145], which gives a beam power of 11.15 MW.

At $0.5\,n_{\mathrm{GW}}$, the highest power loads of about 1 MW/m^2 were found predominantly on the shinethrough panels in row 15S for the on-axis beam and on the shinethrough panels in row 16S for the off-axis beam. The high-power shinethrough footprint is smaller for the on-axis beam. The load on the critical horizontal gap is benign at about 0.2 MW/m^2. The structures adjacent to shinethrough panels in row 15S also receive a benign shinethrough load of tens of kilowatts. At $0.9\,n_{\mathrm{GW}}$, the high-power shinethrough footprint from the on-axis beam and the off-axis beams become similar in size. This results in higher loads on both the TBM frame and on the diagnostic port, reaching up to 100 kW/m^2. The power density on the sensitive horizontal gap between rows 15S and 16S then approaches the power limit of 0.8 MW/m^2.

A helium plasma in the 1/3-field scenario at $n = 0.4\,n_{\mathrm{GW}}$ with hydrogen injection at various power levels and corresponding changes in the injection energy was studied in [1201]. Both the total and peak shinethrough power loads were found to have the same dependence on the injection energy, $P_{\mathrm{shinethrough}} \propto \mathcal{E}_{\mathrm{inj}}^4$, which is stronger than the perveance relation

$P_{\mathrm{NBI}} \propto \mathcal{E}_{\mathrm{inj}}^{2.5}$. These larger loads for higher energy particles are explained by their higher probability to pass through the plasma without ionization. The total shinethrough power fraction is 19% (2.3 MW) for the nominal injection energy of 580 keV and power of 12 MW. While the peak power loads on the dedicated shinethrough panels remained well below the design limit of 4.7 MW/m^2, the distribution of the load was not confined to these panels. The peak power limit, 0.3 MW/m^2, for the adjacent TBM port (to the left of shinethrough panels in figure 96) and the diagnostic port (to the right) was reached for the diagnostic port just due to the shinethrough.

The same study also considered the half-field scenario with a helium plasma at $n = 0.4\,n_{\mathrm{GW}}$ with hydrogen injection at 16.5 MW at 870 keV. The total shinethrough power fraction was only slightly higher than in the 1/3-field case at 21% (3.5 MW), and the power load distribution was very similar both qualitatively and quantitatively. More recently, shinethrough was studied for a wider plasma parameter range, for hydrogen injection into hydrogen and helium plasmas, and the shinethrough fraction was fitted as a function of the plasma parameters [1202]. Since its impact on the shinethrough is different for on-axis and off-axis beam configurations, this work considered also the density peaking factor as a variable. Further work is needed to investigate the shinethrough of deuterium NBI on deuterium plasmas.

11.2. EP confinement in MHD-quiescent reduced-field scenarios with external perturbations

In the non-nuclear phase, the EPs are generated by auxiliary heating only. ICRF heating can produce EPs in the plasma core, and NBIs can produce co-going EPs. Despite the wider drift orbits in the low-current

scenarios, prompt losses are still expected to be small assuming axisymmetry. Neoclassical transport is also expected to be benign. However, the EP transport and loss channels due to 3D effects and MHD activity are expected to be stronger in the half-field scenarios than in the full-field scenarios. In this subsection, we will discuss the effect of the unavoidable magnetic field ripple in the half- and 1/3-field scenarios, including the wall power loads.

EPs in the standard ITER magnetic configurations with 3D effects have been discussed in section 8. The ITER 15 MA baseline scenario is close to axisymmetric due to the ferritic inserts optimized for that scenario: the TF ripple at the outboard midplane separatrix is reduced to 0.3%, except for near the NBI ports (0.6%). However, while the ferritic inserts compensate the TF ripple at the full field, the ferritic material saturates already at magnetic fields below 2 T. Therefore, the ferritic inserts overcompensate the TF ripple at the lower fields, so that their effect can turn into ripple enhancement. Indeed, in the 1/3-field scenario, the TF ripple phase is reversed, and the ripple strength at the outboard midplane separatrix can reach $\sim$1.3%, which is larger than the unmitigated ripple in the baseline scenario ($\sim$1.1%) [1197] and could compromise the good EP confinement. The maximum TF ripple for the half-field and full-field scenarios are similar, but the phase of the ripple relative to the position of the inserts is also reversed.

Therefore, while the EP confinement is predicted to be very good in the main operating phases (15 MA baseline, 12.5 MA hybrid, and 9 MA "advanced tokamak" scenarios) [1011], it was less clear in the half- and 1/3-field scenarios. Nevertheless, EP losses in ITER due to TF ripple mitigated by ferritic inserts in reduced field scenarios have been found to be acceptable [1203]. The ferritic inserts reduce both the total power loss and the peak power flux to the wall by an order of magnitude both in full-field and in the half-field scenario compared to a case without ferritic inserts.

The losses of hydrogen beam ions in hydrogen plasma in the 1/3-field scenario were estimated in ASCOT simulations at $n = 0.4\,n_{\mathrm{GW}}$ and at $n = 0.9\,n_{\mathrm{GW}}$ [1200]. For the 735 keV beams at $n = 0.9\,n_{\mathrm{GW}}$, only 65 kW of the beam power of nearly 20 MW was lost (0.3%). For the 530 keV beams at $n = 0.4\,n_{\mathrm{GW}}$, 270 kW of the beam power of 9.4 MW was lost (3%).

The effect of the three pairs of TBMs (recently reduced to two pairs) on the 3D magnetic field and the EP confinement was assessed by including a numerical model for the magnetization of the European helium-cooled pebble bed TBMs [1007]. The initial study addressed beam ions and alphas in the ramp-up and flat-top phases of the 15 MA baseline scenario, where the losses with and without TBMs were compared. While the wall load increased by about a factor three, it was still benign at only tens of kW. The divertor loads remained unaffected. No evidence for non-diffusive channelling, possibly leading to hot spots, was found. Instead, the diffusive loss channels were intensified due to the TBM perturbation, allowing ions from deep in the plasma to escape. The TBMs caused no significant changes in the slowing-down density profiles.

The fusion alpha results in the study indicated that the presence of TBMs enhances the ripple diffusion of banana particles, but the increase is less than an order of magnitude. ICRF-heated ions were not included in this study, but the effect should be similar to the part of the alpha population on similar orbit types.

The effect of ELM control coil perturbation was assessed at several full-field scenarios and the half-field scenario [941]. Introducing the ELM control coils was found to decrease the beam-ion confinement even for the 15 MA baseline scenario. The power loads increased by an order of magnitude which can be attributed to the field line stochasticity penetrating deeper than the pedestal top. In contrast to the TBM perturbation, ELM control coils mainly affect the power loads on the divertor. Including the plasma response was found to intensify the losses in the plasma periphery, where both the baseline and half-field scenarios feature the largest number of beam ions. Up to 4% of the beam power could be lost. This power load increased due to a new loss channel for marginally trapped ions [1012].

11.3. Effects of MHD modes on EPs in reduced-field scenarios

The interaction between EPs and thermal-plasma driven MHD modes was described in section 5. For ITER, such studies have considered the main operating scenarios and fusion alphas, e.g. [353] and [354], where the latter included also the 3D structure of the magnetic field.

Nevertheless, a recent study [483] assessed the excitation of TAEs by beam ions for reduced field and current, together with the effect of these modes on the EP transport (figure 97). Due to lower field and still relatively high beam energies, the beam ions are super-Alfvénic. NOVA-K simulations found that modes with a wide range of toroidal mode numbers n are excited, and that the most unstable ones were around $n = 20$. These modes reduce the computed mainly beam-target neutron production (which is proportional to the EP density) by up to 30% as a result of beam ion redistribution. It thus appears that, in these conditions, TAEs will be a concern.
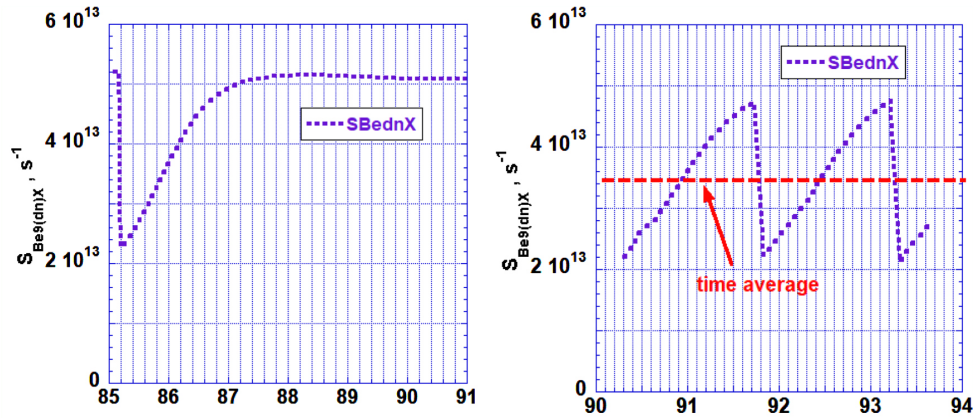
Figure 97. Impact of (a) sawtooth- and (b) TAE-induced mixing of EPs on the neutron rate for an ITER 7.5 MA/2.65 T helium H-mode plasma at $n/n_{\mathrm{G}} = 0.5$ with 33 MW of H_0-NBI and 20 MW of ECRF heating with $c_{\mathrm{Be}} = 10\%$. Reproduced from [483].

The study also considered how a sawtooth redistributes EPs in helium plasmas. A monster sawtooth in these plasmas has a sawtooth period of around 10 s. Although there is a significant drop in the neutron production after a monster sawtooth crash, the time average of the neutron production is not significantly altered. This is because the EP distribution rapidly recovers between two sawtooth crashes.

Regarding the EP-driven modes, a significant change is expected due to the inclusion of novel ICRF three-ion schemes (section 3). In particular, instabilities will be driven by ICRF-heated ions which, in JET, has resulted in a rich spectrum of modes [38].

11.4. ICRF heating scenarios at half field

During the early operational phases at ITER, the ICRF system will focus on demonstrating ion cyclotron wall cleaning (ICWC), evaluating ICRF coupling, and testing the compatibility of ICRF with a full-tungsten first wall. Additionally, it may be used for early studies of EP physics, modeling, and EP diagnostics, particularly targeting AEs and the impact of MeV-range EPs. Key AE characteristics for modeling, such the as toroidal mode number and the location of the mode, can be obtained from Mirnov coils and ECE measurements. If additional diagnostics, such as gamma-ray measurements, are available, they could strongly improve benchmarking modeling against EP measurement data, in support of future ITER experiments involving alphas.

A range of efficient ICRF scenarios based on plasma mix and magnetic field is available at ITER. Hydrogen minority heating in deuterium plasmas, suitable for a half-field ITER operation ($B_0 = 2.65$T, $f \approx 40$ MHz, $n_{\mathrm{H}}/n_{\mathrm{e}} \approx 2 - 5\%$), is particularly robust for testing ICRF heating in H-mode plasmas

at half-field. By changing the hydrogen minority concentration, one can change the ratio of electron-to-bulk-ion heating, test RF coupling and assess impurity production, critical for evaluating the potential to extend ICRF power to 20 MW in future ITER phases.

However, the 10 MW of ICRF power available during the early operational phases may be insufficient to destabilize AEs with hydrogen minority heating in ITER, unless targeting very low density plasmas. JET experiments typically require at least 4-5 MW of ICRF power to destabilize AEs with H minority heating. Given the large size of ITER compared to JET, optimizing the absorbed RF power per resonant ion is crucial for driving AEs with EP generated by ICRF heating. This goal can be achieved using three-ion ICRF scenarios, validated on various tokamaks, which are effective in generating MeV-range EPs and destabilizing AEs. Unlike typical minority heating scenarios that require resonant ion concentrations of a few percent, three-ion scheme scenarios can be tailored to channel ICRF power to a very small population of resonant ions with concentrations below ∼0.5%.

11.5. Future work on ITER reduced-field scenarios

In this section, we have summarized the work dedicated to EPs in operating scenarios with reduced field and current. The beam shinethrough has been analyzed in detail to guarantee the integrity of the device for NBI heated plasmas. The confinement of beam ions can be assumed to be very good in the absence of MHD and external perturbations such as ELM control coils. The corresponding neutron rates have been estimated [483].

However, much of the existing work needs to be updated following the changes in the ITER baseline, requiring further EP studies at reduced field and current. Effects of ELM mitigation coils and various low-frequency modes on EP confinement need to be

studied in detail, as well as effects of EP-driven modes, e.g. using the three-ion scheme or NBI-ICRF heating synergistic effects. With the new ITER baseline, shinethrough of deuterium NBIs should also be assessed. The beam power is not necessarily critical for accessing H-mode due to the increase of ECRF power, but for the sake of safe operation of the NBI system in the reduced-field scenarios, its shinethrough limits should be assessed.

Furthermore, control strategies or possible actuators to affect instabilities have never been addressed for half- or 1/3-field scenarios. The non-nuclear phase with its reduced field and current gives a good test platform to test the actuators planned for nuclear phase. In particular, one of the candidates to mitigate AEs is ECCD. This approach relies on the ability to modify the q-profile (section 10), which ought to be easier for reduced current and high ECRF heating power. A numerical assessment of this would be highly desirable in the near future.

12. Runaway electrons

Runaway electrons (RE) have long been a spotlight topic in plasma research. They now attract increased attention as a part of ITER mission considerations. The toroidal current and the associated magnetic energy are greater in ITER than in any present-day tokamak. It is, therefore, of grave concern when highly energetic runaway electrons become the dominant carriers of the current. This concern pertains immediately to the disruption events in which the unmitigated runaways can produce significant localized melting of plasma-facing components.

The disruptions are commonly described macroscopically in the framework of MHD that needs amendments to cover the runaways. The presence of runaways brings kinetic physics into the problem and calls for a kinetic-MHD approach that combines the MHD treatment of the bulk plasma with kinetic modeling of the runaway population in a self-consistent way. The construction of such an integrated model is an overarching goal of the ongoing theoretical and experimental studies of runaway physics. This section describes the status of these studies with an emphasis on recent advances.

The latest review paper on runaway electrons highlights the prevailing physics themes of the last 20 years [36]: the hot-tail mechanism of runaway production, RE interaction with impurity ions, the role of synchrotron radiation in runaway kinetics, RE transport in presence of magnetic fluctuations, micro-instabilities driven by REs in magnetized plasmas, and vertical stability of the plasma with REs. It also includes a discussion of the runaway issues for ITER

and the strategy of RE mitigation.

The need to minimize the impact of RE on ITER motivates the continuous development of new numerical tools (especially for synthetic diagnostic). This effort complements the dedicated experimental work on the present-day tokamaks such as JET [241], ASDEX [1204, 1205], MST [1206], COMPASS [1207, 1208], EAST [1209], DIII-D [240], and J-TEXT [1210]. It is unfortunate that the results of the ongoing experiments themselves are not immediately scalable to next-generation tokamaks, which raises concerns regarding capabilities of disruption mitigation systems (DMS) and runaway control, as summarized in [1211, 1212]. Nevertheless, these results are essential as a testbed for the theoretical conjectures, phenomenological extrapolations and code validation. Diagnostics of runaway electrons in present tokamaks and burning plasmas in ITER is discussed in section 4, and impact of runaway electrons on MHD stability is discussed in chapter 4 of this volume [16].

12.1. RE formation during disruptions

Runaway electron formation during disruption is of grave concern for ITER. The disruption event involves a thermal quench (TQ), a current quench (CQ), and, sometimes, a runaway plateau. The TQ refers to the rapid loss of the plasma kinetic energy, the CQ to the decay of the plasma current, and the runaway plateau is a regime when runaway electrons carry most of the current.

12.1.1. Thermal Quench. Reference [1213] offers a thorough statistical analysis of the TQ triggerings in JET. Two phenomena can cause rapid electron cooling: global MHD events that enhance heat transport via stochastization of magnetic field lines and impurity influx resulting in strong radiative losses. Cooling of bulk electrons reduces the plasma conductivity whereas the toroidal current cannot change significantly on the fast TQ timescale. A strong inductive electric field builds-up as a result. In a post-TQ plasma, this field is up to three orders of magnitude greater than the critical Connor-Hastie field for runaway production. Note that, in the absence of ongoing heat losses, Ohmic reheating after the TQ precludes RE production [36]. Such events were observed in tokamaks [1214].

A so-called hot-tail mechanism of RE generation is the prevailing candidate for primary RE generation during TQ in ITER. It considers partial survival and acceleration of the hot pre-TQ plasma electrons [1215]. Its first analytic descriptions involved an assumption that the distribution of plasma electrons remains Maxwellian during the cooling process [1216, 1217]. This assumption, however, does not hold for a *rapidly* cooling plasma. A more appropriate model,

which assumes collisional drag on a cold background to dominate the evolution of the pre-TQ electron distribution function, was suggested in [1218]. This model is referred to as the "hot-tail model" and has been used to make predictions for ITER (for example [1219]) or to analyse recent experiments [1220, 1221].

The hot-tail RE generation has been modeled numerically in [1222–1224] based on the electron kinetic equation. In [1222], the evolution of the hot-tail distribution function was calculated self-consistently with the inductive electric field and the energy balance of the cold background, assuming that the impurity line-radiation is the dominant energy loss mechanism. The trends observed in [1222] are in general agreement with [1218]. Reference [1224] provides a more recent numerical study of the analytic model [1218] with an improved description of runaway electron scattering.

For a significant hot-tail population, [1222] predicts a 'prompt conversion' regime, in which super-thermal electrons carry most of the current with minimal friction. That limits the inductive electric field. A distinctive feature of this regime is the absence of multi-MeV electrons. A detailed comparison of the model [1222] with experimental observations of the prompt conversion in DIII-D has been reported in [1225]. Reference [1226] reports experimental observation of super-thermal electron populations in DIII-D in comparison with the kinetic hot-tail simulations as well. While the theoretical predictions agree with the observations qualitatively, the calculated hot-tail generation is one to two orders of magnitude lower than the one inferred from experiments. These disagreements are likely due to incompleteness of the physics models used for the hot-tail calculations - a complete model should include the effects of radial transport and inhomogeneities of material injection that triggered the TQ. Kinetic modeling of RE generation in AUG plasma also suggests lack of essential physics in these simplified models [1227], in particular - the radial transport. This calls for self-consistent RE-kinetics and MHD calculations.

12.1.2. Strong avalanche during current quench. The plasma becomes more resistive during TQ. The plasma current then decays during the CQ on the $\tau = \frac{L}{R}$ timescale, where $L \approx 2\pi A l_i / c^2$ is the plasma inductance, A is the major radius, and l_i is the internal plasma inductance coefficient (typically of order unity), and R - is the plasma resistance. Because the "wall time" in ITER is very long - 0.5 s, only the poloidal magnetic field energy inside the wall can dissipate faster than 0.5 s. The plasma current will then be taken over by the wall.

Avalanche generation of RE can slow down the current decay in ITER. Reference [1228] provides the following simplified expression for the avalanche growth rate in a very strong electric field:

$$\frac{1}{j_{\mathrm{re}}} \frac{\partial j_{\mathrm{re}}}{\partial t} \approx \frac{1}{\sqrt{Z+5} \ln \Lambda} \frac{eE}{mc}, \tag{100}$$

where j_{re} is the RE current density, E is the electric field and $\ln \Lambda$ and Z are the Coulomb logarithm and the effective charge as "seen" by the relativistic particles. The inductive electric field E during disruption can be estimated as $E = -\frac{L}{2\pi A} \dot{I}$, where I is the total current.

Integrating equation (100) using the above expression for E provides a relation for the ultimate RE current $I_{\mathrm{re}}(\infty)$ as long as it is smaller than the initial plasma current $I(0)$ [1229],

$$\ln \frac{I_{\mathrm{re}}(\infty)}{I_{\mathrm{re}}(0)} = \frac{l_i}{\sqrt{Z+5} \ln \Lambda} \frac{I(0) - I_{\mathrm{re}}(\infty)}{I_A}, \tag{101}$$

where $I_A = \frac{4\pi mc}{e\mu_0} = 17\,\mathrm{kA}$ is the Alfvén current. A very large initial plasma current $I(0) = 15\,\mathrm{MA}$ in ITER yields a very strong amplification (a few tens of e-folds) of the initial RE current $I_{\mathrm{re}}(0)$. Equation (101) shows that large amplification of the RE current is insensitive to the CQ scenario and its details such as duration or plasma resistivity evolution.

Note that the avalanche theory proposed in [1228] does not treat the effect of partially ionised impurities in detail. It simply uses the sum of free electron density and half of the bound electron density in the definition of the critical electric field to account for the bound electrons (see section 3.2.2 in [36]). This simplification underestimates the avalanche growth rate. Reference [1230] suggests two improvements: to separately evaluate collisional frequencies (i.e. Coulomb logarithms) for free and bound electrons and to count both free and bound electrons in the description of knock-on collisions. The resulting modified avalanche formula is given by equation (30) in [1230]. Yet, the Coulomb logarithms used in [1230] and subsequently in [1219] for collisions with free electrons and scattering are inaccurate because they are based on a fully classical model (see the discussion in section 3.1 in [1231]). More accurate collisional rates based on the Thomas-Fermi model are given in [1232] (see also sections 3.2 and 3.3 in [36]). A further refinement has been discussed in [1233, 1234], where the collision frequencies have been evaluated using the density functional theory. The derived frequencies agree with the Thomas-Fermi model within the range of their validity, i.e. for atoms with $\alpha Z \ll 1$, where $\alpha \approx 1/137$. Section 4 of [1234] shows a reasonable agreement of the results with those of [1219] when the ambient plasma characteristics are similar (i.e. the ambient temperature is taken to be constant as in [1219]). In particular, at sufficiently high deuterium density ($\sim 4 \cdot 10^{21} \mathrm{m}^{-3}$) the generation

of runaways is found to be fully suppressed. This result is in agreement with the original estimate for the RE suppression density given in [1228] (i.e. "Rosenbluth density" $n_{\mathrm{DT}} = 3 - 5 \cdot 10^{21} \mathrm{m}^{-3}$).

In addition, recombination increases the avalanche rate due to the increase of the $n_{\mathrm{bound}}/n_{\mathrm{free}}$ ratio [1234]. However, the ionization balance in [1234] relies on the collisional-radiative model [1235] that implies the plasma to be Maxwellian and transparent to line-radiation. Reassessment of the ionization balance in [1236] gives increased ionization levels for the plasma with minority runaways.

There are some effects of the finite aspect ratio and plasma shaping on the avalanche rate, but none of them appears to be of primary importance. As shown in the seminal work [1228], toroidicity reduces the avalanche rate by a neoclassical factor $(1 + 1.46\sqrt{\varepsilon} + 1.72\varepsilon)^{-\frac{1}{2}}$, where ε is the aspect ratio. Reference [1237], however, suggests that poloidal asymmetry of the electric field enhances the avalanche rate when the inductive field is sufficienty strong, which counteracts the reduction of the avalanche rate with the aspect ratio. References [1238, 1239] report a small reduction of the avalanche rate due to plasma elongation. Reference [1240] discusses parametric dependence of avalanche on radial transport. A newly developed numerical framework [1241] should permit further improvements in such studies. Reference [1242] studies spatial transport in axisymmetric configurations and concludes that it is most important in small to mid size devices, and become insignificant in larger tokamaks. Reference [1243] highlights the critical role of the avalanche source on the surface heating of plasma facing components due to deconfined runaway electrons.

12.2. Plateau and Mitigation

When REs overtake most of the current, the electric field drops to the near-threshold value for the RE avalanche. This phase of RE evolution and the value of the threshold electric field deserve special attention because they correspond to the long-term RE current decay [1244].

The RE spectrum now peaks at very high energies where radiative processes such as synchrotron and bremsstrahlung play a significant role. Because of that, the threshold electric field exceeds the critical Connor-Hastie electric field E_{c} [1245] determined by the purely collisional slowing-down. Refs. [1246–1248] consider bremsstrahlung as a limiting mechanism for RE energy gain. Bremsstrahlung can be significant in the presence of high-Z impurities. However, the combined effect of pitch angle-scattering and synchrotron radiation leads to faster energy losses in ITER-like disruption scenarios [1249–1252].

Synchrotron losses cause accumulation of the pre-existing runaways around the stable phase-space attractor when the electric field eventually drops to the near-threshold level [1249, 1253]. Figure (98) shows an example of such a quasi steady-state distribution function. This distribution function has a leak into
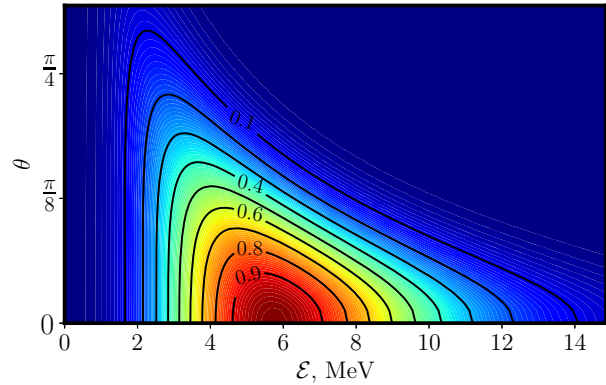

Figure 98. Example of RE distribution function in the near-threshold regime. Parameters correspond to $E/E_{\mathrm{c}} = 4$, $Z = 10$, and the ratio of radiation to collisional times is $\nu_{\mathrm{drag}}\tau_{\mathrm{rad}} = 5$. The avalanche generation is switched off. Reproduced from [36].

the cold bulk. The resulting decay time depends exponentially on the strengths of the inductive electric field. This feature and the exponential growth of the population at higher electric fields ensure that the inductive electric field remains close to the threshold during the entire RE current decay. Experimental observation of such a non-monotonic distribution function in DIII-D was reported in [1254].

A rigorous kinetic treatment [36, 1249, 1253] provides the following estimate for the threshold electric field in the limit of small "over-criticality" parameter α:

$$\frac{E_0}{E_{\mathrm{c}}} \approx 1 + \frac{\alpha\sqrt{2}}{\sqrt[6]{1 + 8\alpha^2}}, \tag{102}$$

where $\alpha \equiv (Z_{\mathrm{eff}} + 1)/\sqrt{\nu_{\mathrm{drag}}\tau_{\mathrm{rad}}}$, ν_{drag} is the collisional frequency at the characteristic momentum, and $E_{\mathrm{c}} = \frac{mc}{|e|}\nu_{\mathrm{drag}}$ equals the Connor-Hastie field when the plasma is fully ionized. References [1255, 1256] confirm the threshold using the adjoint Fokker-Planck equation method. Reference [1257] also reports an agreement with the threshold equation (102). It uses a fully conservative knock-on operator that enables an accurate calculation of the avalanche growth rate in this near-threshold regime. References [1242, 1252, 1258–1260] are consistent with the above results. They highlight the vortex structure in the momentum phase space around the attractor. The resulting threshold electric field value is reported to agree with [1256] as well [1260].

111

In presence of high-Z impurities, $Z_{\rm eff}$ and $\nu_{\rm drag}$ should be calculated accordingly (see discussion in section 12.1.2). Reference [1261], in which this threshold field is called "effective critical field", considers the effect of partially ionized impurities carefully. It also includes the effect of bremsstrahlung losses. A good agreement between the results of [1261] and equation (102) is reported in section 7 of [36] for ITER-relevant impurity densities. At very high densities, such as $10^{21}{\rm m}^{-3}$, bremsstrahlung needs to be taken into account, and equation (102) becomes inaccurate.

12.2.1. Benign termination. Plasma current decay during CQ can trigger vertical displacement events (VDEs) in ITER. These events create damaging stresses on the plasma facing components. The current decay rate during the VDE is roughly

$$\frac{{\rm d}I}{{\rm d}t} \approx \frac{2\pi R}{L_{\rm i}} E_0. \tag{103}$$

Inductive coupling between the plasma and the vessel relates the plasma current to the vertical position of the plasma [36, 1262]. Evolution of the current profile during VDEs often leads to MHD instabilities [1263–1266]. In a plateau regime with high background density, these instabilities can cause fast and *localized* loss of RE to the wall. It is highly desirable to avoid this scenario in ITER because of the potential damage the localized RE losses can cause to the wall.

Recent experiments on JET and DIII-D demonstrate benign termination of large runaway beams [241, 1263, 1267, 1268]. In these experiments, a megaampère runaway beam terminates without excessive heat loads onto the plasma facing components.

The key to the harmless termination scenarios is a massive deuterium injection into the runaway beam. This technique promotes recombination and expulsion of the high-Z material from the plasma [1269]. The enhanced heat conduction with D_2 drops the bulk electron temperature below the ionization threshold to allow recombination. The ambient plasma density then falls below the measurable value ($\approx 10^{18}{\rm m}^{-3}$). The subsequent MHD event has a short Alfvén time. Infrared camera observations [1268] and modeling [1265] show that such instability scatters REs on a large area, minimizing the localized damage to the wall. When REs are lost, the thermal plasma carries the current. The low impurity content in such plasmas precludes the regeneration of REs, and the plasma current decays resistively. Currently, not all aspects of this benign termination scenario are well understood, and further research is needed to assess the feasibility of such a technique in ITER.

12.2.2. Synchrotron emission. The diagnostic techniques for RE include measurements of soft x-ray emission, hard x-ray emission, and synchrotron emission. The latter has received increased attention in recent years. The numerical codes SOFT (Synchrotron-detecting Orbit Following Tool) [1270] and KORC (Kinetic Orbit Runaway electron Code) [1271] have been developed for synthetic diagnostic and comparison of the simulations with experimental data. The SOFT code follows guiding center orbits whereas KORC has a full orbit capability. Synchrotron emission provides information about the runaway beam position, energy spectrum and pitch-angle distribution of the runaway electrons. Synthetic diagnostic is essential for analyzing experimental data because it is yet unfeasible to infer the runaway parameters from the data via an inversion procedure. In Alcator C-Mod [1272], ten-channel motional Stark effect (MSE) diagnostic detected synchrotron radiation. In TCV [1273], visible images were recorded using the multispectral imaging system Multi-Cam that distributes incoming light over four channels with different narrowband filters. In DIII-D [1274], polarized full cross section images were recorded. Although the collected data are not sufficiently complete for accurate reconstruction of the runaway electron distribution function, the observed polarization of synchrotron emission indicates that the characteristic pitch-angles of the runaway electrons exceed those predicted by theory in the absence of runaway scattering by collective modes. Synchrotron emission was used in [1275] for the reconstruction of the runaway electron current profile in DIII-D post-disruption plateau plasmas.

12.3. Waves for RE mitigation

There are ongoing attempts to use perturbed fields in plasmas to control runaway electrons. The perturbations can be generated by external antennas or by the runaways themselves (via kinetic instabilities). Depending on spatial scales and frequencies of the perturbed fields, these fields can either cause radial transport of the runaways to the wall or enhance pitch-angle scattering of the runaway electrons. The potential benefit from enhanced scattering is the enhancement of runaway energy losses via synchrotron radiation.

The radial transport of the runaways is predominantly due to the low-frequency perturbed fields (below the electron gyrofrequency). In this case, the guiding center approximation holds for the runaways. The unperturbed guiding center orbits in a tokamak have three constants of motion $(P_\phi, \mathcal{E}, J_\perp)$ and are characterized by the toroidal and poloidal frequencies $\omega_\phi(P_\phi, \mathcal{E}, J_\perp)$ and $\omega_\theta(P_\phi, \mathcal{E}, J_\perp)$. The perturbed field

112

resonates resonances with these frequencies when

$$\omega - n\omega_\phi(P_\phi; \mathcal{E}; J_\perp) - l\omega_\theta(P_\phi; \mathcal{E}; J_\perp) = 0, \qquad (104)$$

where ω is the perturbation frequency, n is the toroidal mode number and l is an integer. This resonance condition suggests what particles are most sensitive to perturbations. However, such particles still do not move far from their equilibrium orbits unless the resonances overlap [721] to give rise to global diffusion.

The frequencies of MHD perturbations are commonly much smaller than $\omega_\phi(P_\phi, \mathcal{E}, J_\perp)$ and $\omega_\theta(P_\phi, \mathcal{E}, J_\perp)$ for relativistic electrons. These nearly static perturbations do not change the particle energy significantly. They change the toroidal angular momentum P_ϕ, and they thereby transport particles across the equilibrium magnetic surfaces. The resonances given by equation (104) are closely related to rational magnetic surfaces, but not exactly due to the drift-orbit excursions. Consequently, stochastic diffusion of magnetic field lines does not necessarily cause the same diffusion of the fast electrons. As shown in [1276], the drift-orbit-averaged diffusion coefficient for passing particles is formally a sum of delta-functions located at discrete resonances, which precludes global transport of particles unless nonlinearity of the perturbed motion mixes the resonances into a continuous array [721]. However, the resonances with low to moderate n and l often require impractically large perturbations to overlap. Such resonances form isolated phase space islands separated by KAM surfaces. The resulting transport is then a combination of convection within the islands and diffusion across the KAM surfaces. The corresponding advection-diffusion transport model [1277] can reasonably replicate the results of direct numerical simulations, but the free parameters in this model limit its predictive capability.

Depending on input parameters, one finds global stochasticity or co-existence of stochastic areas and nested magnetic surfaces [1278]. The co-existence of destroyed and undestroyed magnetic surfaces suggests that the electrons may escape in short pulses through statistically formed 'turnstiles' [1279]. That complicates predictions of the REs losses even when the codes simulate saturated regimes of plasma instabilities rather than just pre-specified perturbations.

Simulations of existing experiments with nonlinear MHD codes NIMROD [1280, 1281] and JOREK [1025] indicate that the MHD modes do produce high-order resonances needed to randomize magnetic surfaces globally [1265]. However, it is still unfeasible for the existing codes to simulate the randomized field directly, because of severe resolution requirements and the need for a kinetic rather than MHD description of the emerging short scales. This difficulty motivates numerous sensitivity studies of the fast electron

transport to prescribed fluctuations [833, 1277, 1282–1290]. Such studies involve Monte Carlo simulations with either guiding center codes such as ANTS [1284], ASCOT [1291] or, more recently, a full orbit code KORC [614] and MARS-F [1292]. One of the topics of interest is whether resonant magnetic perturbations produced by external coils can be used to facilitate runaway losses [1284, 1293]. This is a viable option for medium-size or small machines, such as DIII-D [1294], AUG [1295], TEXTOR [1296] or COMPASS [1297], but does not look practical for an ITER-size device in which the required short scale perturbations decay too quickly with the distance from the coils.

Besides the externally imposed resonant magnetic perturbations and those resulting from bulk plasma instabilities, the guiding center resonance equation (104) appears to be responsible for the excitation of recently observed low-frequency CAEs by the runaways themselves [1298]. Excitation of these modes signifies that the driving electrons have the pitch-angles characteristic of trapped particles and that their distribution over parallel momentum has a positive slope. It is unlikely that these electrons carry most of the runaway current, and it is, therefore, difficult to expect a great benefit from enhancing their radial losses, but it is conceivable that they can serve as a diagnostic tool in the spirit of MHD-spectroscopy [1299] that proved very informative for energetic ions.

12.3.1. Self-excited waves. Pitch-angle scattering and synchrotron losses of the runaways can raise the critical electric field for runaway multiplication and limit the runaway energy gain (see subsection 12.2). It is, therefore, natural to consider micro-instabilities to enhance the scattering rate. Strongly anisotropic distribution of the REs is prone to high frequency and short wavelength kinetic instabilities. These instabilities are generally tractable within the WKB approximation, in which case the wave frequency satisfies a local dispersion relation, and the wave-particle resonance condition is

$$\omega - k_\parallel v_\parallel - \frac{N\omega_c}{\gamma} = 0, \qquad (105)$$

where N is an integer. The dominant resonances for the runaway electrons are the Cherenkov resonance ($N = 0$) and the anomalous Doppler resonance ($N = 1$).

Excitation of whistler modes via anomalous Doppler resonance is of particular interest. These modes change primarily the electron pitch-angles rather than the radial positions. The resulting losses of runaway energies can be faster than the runaway transport to the walls.

In the early tokamaks, such as TM-3, T-6, TFR and others, the "fan" instability [1300, 1301]

113

was observed frequently in the presence of runaway electrons. More recently, observations of runaway-driven instabilities were reported in Refs. [688, 1302–1304]. Linear stability theory reveals that collisional damping is essential for the modes of interest [1305]. This damping precludes excitation of kinetic instabilities by REs for post-disruption ITER parameters with electron temperature less than about 20 eV. Such instability can however develop at higher temperatures and lower plasma densities as in the recent DIII-D experiments [1302]. Although the importance of collisional damping is already seen from local analysis, an experimentally relevant stability assessment must be non-local because the wave packets perform multiple bounces within the plasma during their amplification. A ray-tracing code COIN (convective instability) [1305] addresses this aspect, which enables runaway stability assessment for present day machines as well as for ITER. The resulting instability thresholds have been confirmed in [379] with the use of a ray tracing code GENRAY [1306,1307].

Related to potential benefits from kinetic instabilities is the idea of injecting ECRF waves for RE mitigation [1308]. The obstacles in implementation of this idea are the cutoff frequency issue and the collisional dissipation of the injected waves. Also, the spectrum of the injected waves needs to be sufficiently broad to resonate with (affect) a large fraction of runaway electrons.

Nevertheless, the injection of ECRF waves tends to be beneficial even without their direct impact on runaway electrons. First, high-power ECRF heating may help to keep the bulk electrons sufficiently warm to alleviate drastic drop of the Spitzer conductivity during thermal quench. Second, the ECCD may help to prevent the runaway build-up because the thermal quench and the resulting drop in Spitzer conductivity would not necessarily create a very strong inductive electric field in the presence of ECCD. The population of current-carrying electrons tends to be super-thermal in the presence of ECCD, and the collisional slowing down force for these electrons is therefore relatively insensitive to the bulk electron temperature. There are encouraging experimental results [1309, 1310] in support of this concept.

Experimental observations of runaway-driven micro-instabilities always exhibit nonlinear behavior of the excited waves rather than their linear growth. Intermittent bursts of the waves and chirping phenomena seen in the experiments [688] are beyond the scope of linear analysis. These phenomena are reminiscent of nonlinear scenarios for kinetic instabilities driven by energetic ions, and they are likely to have interesting diagnostic applications. Recent quasi-linear simulations within an idealized spatially uniform model [1311]

exhibit a strong effect of the excited waves on the RE electron spectrum. This model predicts an increase of the avalanche threshold field above the Connor–Hastie value, which is qualitatively consistent with DIII-D observations. However, the nonlinear theory is not yet ready for predictive modeling of ITER conditions.

13. Summary and Outlook

The era of burning plasma physics is approaching with the construction of the ITER tokamak as well as the design or construction of several other devices that currently aim at operating burning plasmas: CFETR, SPARC, STEP, and BEST. Burning plasmas are by definition predominantly self-heated by energetic alphas, leading to a high degree of plasma self-organization. Scenario optimization in future burning plasma devices for fusion power generation hence calls for a clear understanding of the physics of alphas, and more generally of EPs. The recent DT campaigns on JET have provided an opportunity for testing some of the most important diagnostics and validating the modeling aspects of fusion-born alphas and alpha-driven instabilities [39–53].

The interactions between EPs and a zoology of thermal-plasma-driven and EP-driven instabilities, EPMs, turbulence and 3D effects need to be understood in the qualitatively new regime of burning plasmas. Even in present devices containing non-active or weakly burning plasmas, our predictive capabilities of wave drive and damping and EP transport are challenged when several modes are concurrently destabilized and when synergistic interactions take place. In addition to the ongoing work on these topics on present devices, we will need to carefully diagnose the wave drive and damping as well as EP transport and losses in the future large-scale devices capable of sustaining burning plasmas, both in their non-active and active phases. Such experiments in tokamaks able to sustain burning plasmas will provide the experimental basis to validate our increasingly sophisticated simulation and modeling tools that will be used to guide and even accelerate future research programmes towards their mission goals, as well as to design and optimize future fusion power plants. High fidelity physics models will capture the scientific community's knowledge of EP behaviour, whilst reduced or surrogates models, perhaps constructed with the help of Machine Learning (ML), will bring super-computer modeling capabilities to desktop computers and enable rich EP physics effects to be included in routine predictive simulations and interpretive analysis.

On the EP diagnostics frontier, substantial progress has been made since the last update

114

of the ITER Physics Basis [20]. Several high-resolution EP diagnostics have been developed that can provide a wealth of experimental data. These include EP diagnostics sensitive to the EP phase-space distribution function as well as fluctuation diagnostics sensitive to modes interacting with the EPs. Advances in fast digitization techniques and techniques to exploit fast digitization have significantly improved fluctuation diagnostics on major tokamaks and will be available at ITER. An example is the two-color toroidal interferometer and polarimeter (TIP) which has demonstrated high-resolution spectra of several AEs and low-frequency modes such as NTMs. The TIP to be installed on ITER will be able to detect AEs even in the plasma core and will likely be the workhorse of fluctuation diagnostics on ITER. ECE diagnostics, microwave reflectometry, and magnetic pick-up coils will also provide high-resolution fluctuation measurements at ITER.

Several high-resolution confined and lost EP diagnostics can now give us detailed experimental access to the EP phase-space distribution. For example, gamma-ray emission from nuclear reactions can now not only identify what reaction is taking place by identifying peaks in the spectra, but can also resolve the Doppler broadening of these peaks, giving diagnostic access to the velocities causing the Doppler broadening. Diamond NES detectors can provide high-resolution measurements of energy spectra of DT neutrons, directly characterizing the fusion reaction. As for fluctuation diagnostics, fast digitization methods have increased the time resolution and the spectral resolution of CTS measurements substantially. FIDA, INPA, FILD, and ICE diagnostics have been deployed on several medium-sized tokamaks and stellarators and provide high-resolution measurements on confined and lost EP populations. The ICE detectors are hoped to provide the experimental basis needed to understand the relation between EPs and ICE emission. For example, accurate measurements of the polarization of the ICE are needed, as well as a forward model that can predict when ICE occurs as well as the ICE spectrum. Understanding ICE is particularly important in view of the limited set of EP diagnostics foreseen for ITER. At ITER, CTS and GRS are the only foreseen diagnostics to measure confined alphas, and FILD and possibly ICE could diagnose lost alphas.

The leading tokamaks have been, or are being, equipped with rich sets of high-resolution EP diagnostics which have motivated the development of tomographic inversion procedures, allowing the measurement of 2D EP velocity distribution functions. Multi-view sets of high-resolution EP diagnostics with more than 20-30 installed lines-of-sight have even allowed the measurement of 3D EP phase-space distribution

functions. Such measurements will be improved in the coming years through the installation of new EP diagnostics aided by physics-based prior information, such as collisional physics and wave-particle interaction physics. The final goal in this direction is the development of integrated data analysis procedures that combine information from many diagnostics, including those for EPs, perhaps even including fluctuation diagnostics, to obtain a more holistic determination of the plasma state, including EPs. This data-led approach, including prior assumptions, provides the experimental basis to continually challenge our codes and physics understanding. For ITER, such an approach allows the maximum amount of information to be extracted from the restricted set of EP diagnostics installed. Whilst such approaches often make use of sampling techniques and are computationally expensive, the use of neural networks trained as part of the many evaluations necessary to infer the plasma state, together with increased exploitation of accelerator technologies such as GPUs, is expected to allow more and more routine use of such advanced data interpretation techniques. Further supporting the execution of research programmes conducted around the world as part of the common focus on the realisation of fusion as an energy source.

On the EP physics theory frontier, there has been significant progress and increased sophistication in both the modeling and simulation of EP-driven phenomena and in the validation of these models with experiments. As fusion research gravitates towards the burning plasma regime, the dependence on modeling becomes even more critical since the EP characteristics of future devices do not generally overlap with those of current experiments, and there will be a significant gap in time before validation becomes possible in DT burning plasma devices.

There are several future directions in EP simulation efforts in preparation for this new era. First, existing models need to continue to improve both in physics fidelity and computational efficiency. Some of the new physics topics that need to be explored include: coupling between core plasma microturbulence, EP-driven turbulence, and zonal flows; introduction of multiple EP species (e.g., beams, alphas, ICRF tails) and study of the synergistic interactions between them; extension of nonlinear simulations to longer timescales where alpha and external EP source variations become important; inclusion of 3D equilibrium effects in the EP instability models and exploration of optimization possibilities; and a more detailed modeling of the effects of EP deposition on plasma-facing components.

A second avenue is the incorporation of full EP turbulence and physics models into integrated modeling frameworks. The practical motivation for this is the need for a more self-consistent physics design

115

of future devices and reliable prediction of regimes where EP heat loads on plasma-facing components will become problematic. Additionally, interfaces to EP analysis tools will increasingly need to be accessible to non-experts in EP physics. Integrated full discharge simulations will also be needed to evaluate the range of regimes that the plasma must pass through during startup and shutdown. If regimes are encountered on startup with strong EP instability and poor confinement, then more external power will be required for startup; this can significantly increase the cost of a reactor in comparison to the case where more optimal EP turbulence minimizing startup trajectories are followed. During shutdown the plasma will likewise pass through multiple parameter regimes; care will be needed to control this phase to avoid sudden and intense EP losses to the wall. The scientific motivation is that while EP physics has often in the past been compartmentalized and focused on just a few time slices from carefully curated discharges, the reality is that EP phenomena are continuously evolving and are coupled to and affected by the surrounding plasma environment. Taking this into account is likely to lead to new insights and correlations with the dynamics of the surrounding plasma that have not been noticed in the more focused approaches that are currently in use. To support integrated modeling frameworks, there will be a continuing need to evaluate trade-offs between the computationally efficient reduced EP models vs. computationally intensive high fidelity EP models.

Fortunately, two trends will help with this challenge. One is the advent of GPUs (graphics processing units) and the associated progress in massively parallel scientific computations. The other is the increasing use of machine learning/artificial intelligence methods which allow the construction and training of rapidly evaluated surrogate models that can encapsulate the results from the more computationally intensive high fidelity EP models in a form that will be of use within the integrated plasma simulation frameworks. In future devices such as ITER, the dominance of alpha heating, the lack of direct external control over the alpha source, and the limited number of diagnostics available in a nuclear environment will lend substantial value to continued development of high-fidelity EP physics simulation tools.

The experimental and simulation tools need to be used in concert to comprehensively map out the physics of EPs, including wave-particle interactions and synergistic interactions among modes and between modes and turbulence, as well as the associated EP transport. The most important thermal-plasma-driven instabilities interacting with EPs are currently thought to be sawteeth, NTMs, KBMs, ELMs, and RWMs. The most important EP-driven instabilities are the zoology of AEs, ranging from the high-frequency modes in the ion cyclotron frequency range (e.g., GAEs or CAEs), via the intermediate-frequency modes in Alfvén frequency range (e.g., TAEs, EAEs, or RSAEs), down to low-frequency modes in the diamagnetic frequency range (e.g., BAEs, BAAEs, LFAMs, or EGAMs) and their kinetically modified branches. At high EP pressure, these EP-driven modes can overcome continuum damping and form distinct EPM branches with properties depending on the EP population. Simulations with predictive capabilities call for global, nonlinear kinetic models and codes, which are being developed, but also for reduced modeling based on the progress of our EP physics understanding. Whereas the behavior of isolated EP-driven modes is fairly well understood, their interplay when several modes are active, their nonlinear evolution, and their interaction with turbulence, in particular synergistic effects between turbulence and EP-driven instabilities, are clear targets for future research. Additionally, 3D effects due to deviations from axisymmetry need to be accounted for in linear and nonlinear modeling and simulation.

It is sometimes advantageous to operate burning plasma devices at reduced plasma current and magnetic field in their early operational phases, e.g. to reduce electromagnetic loads due to disruptions. Such reduced-field and current scenarios require careful consideration due to the possibilities of enhanced NBI shine-through at low density and EP losses associated with larger orbit widths. This is one of the many aspects that must be taken into account when commissioning devices to full operation and will need to be reflected in the ITER Research Plan as well as those of other future devices.

It has become recognized that EPs form an integral part of plasma scenario optimization for burning plasmas. Plasma scenarios can be optimized by means of actuators modifying either the EP distribution function itself or the existence, drive or damping of EP-driven modes, thereby modifying the EP transport. EP phase-space modification has been demonstrated using ECRF heating, ECCD, ICRF heating, ICCD, NBI heating, NBCD, and RMPs as actuators, with varying degrees of understanding and control. Synergistic effects in the plasma such as the interaction between AEs and turbulence or the suppression of turbulence by means of EPs have also been explored. Various ICRF schemes can selectively heat electrons or ions or accelerate EPs into the MeV-range, such as the novel three-ion scheme, 2nd or 3rd harmonic heating, or minority heating. Experiments have also demonstrated that EP current drive can be a significant actuator for scenario optimization. However, while there are several external actuators

116

to control AEs in present devices and some of them might be applicable to control AEs in burning plasmas, systematic studies in present devices as well as integrated prospective modeling activities for future burning plasmas are still needed. Demonstrating that any of these control schemes has the efficacy and efficiency to be useful in ITER and other burning plasmas remains at the forefront of current research.

Finally, runaway electrons driven and accelerated during the current quench phase of disruptions are an area of concern for ITER and constitute an existential threat to the tokamak concept. ITER must necessarily approach regime in which runaways may appear with caution, and new capabilities such as shattered pellet injection, disruption prediction and avoidance based on machine learning, high-power ECRF and ECCD actuators, and diagnostics for runaway electrons are being prepared. In similarity with alpha particle physics, runaway electron physics in ITER will enter new regimes that cannot be fully tested on existing tokamak experiments. In the runaway simulation and modeling area, comprehensive models have been developed based on classical physics, but the effects of the variety of instabilities that strong runaway beams are likely to drive have not yet been consistently integrated into the predictive modeling paradigm. Since runaway-electron instabilities may provide mitigating effects through enhanced scattering of runaways, improved understanding of their role will be an important future development in the continuing search for runaway electron control mechanisms.

In this review, we have outlined our current understanding of EP physics on the path to burning plasmas. We have discussed what we currently consider the most significant EP research topics on that path, summarized the state-of-the-art, and called for future research. Progressing on these current research topics will require pushing the frontier of our understanding of EP physics deeper into yet uncharted territory, by developing new theoretical understanding, by more powerful simulations, and by better controlled and diagnosed experiments in present devices and in future burning plasma devices.

Acknowledgments

Acronyms

AC	Alfvén continuum
AE	Alfvén eigenmode
AITG	Alfvénic ion temperature gradient mode
ALE	abrupt large event
AUG	ASDEX Upgrade
BAAE	beta-induced Alfvén-acoustic eigenmode
BAE	beta-induced Alfvén eigenmode
BGK	Bernstein-Greene-Kruskal
CAE	compressional Alfvén eigenmode
c.c.	complex conjugate
CD	current drive
CGL	Chew, Goldberger and Low
CGM	critical gradient model
CTS	collective Thomson scattering
COM	constants of motion

CQ	current quench
CXRS	charge-exchange recombination spectroscopy
DD	deuterium-deuterium
DMS	disruption mitigation system
DT	deuterium-tritium
EAE	ellipticity-induced Alfvén eigenmode
e-BAE	electron-driven beta-induced Alfvén eigenmode
EC	electron cyclotron
ECE	electron cyclotron emission
ECEI	electron cyclotron emission imaging
ECRF	electron cyclotron radio-frequency
ECCD	electron cyclotron current drive
EGAM	energetic-particle-driven geodesic acoustic mode
eEGAM	energetic-electron-driven geodesic acoustic mode
ELM	edge-localized mode
EP	energetic particle
EPM	energetic particle mode
ERTL	edge resonant transport layer
EWM	energetic-particle-driven wall modes
DIP	dispersion interferometer polarimeter
FFCW	fixed-frequency continuous wave
FIDA	fast-ion D-alpha
FILD	fast-ion loss detector
FLR	finite Larmor radius
FMCW	frequency-modulated continuous wave
FW	fast magnetosonic wave
FWI	fast wave interferometer
GAE	global Alfvén eigenmode
GAM	geodesic acoustic mode
GGAM	global geodesic acoustic mode
GPU	graphics processing unit
GRS	gamma-ray spectroscopy
HAE	helicity-induced Alfvén eigenmode
HFSR	how-field-side reflectometer
H-mode	High-confinement mode
HpGe	high-purity germanium
HXR	hard x-ray
i-BAE	ion-driven beta-induced Alfvén eigenmode
IC	ion cyclotron
ICCD	ion cyclotron current drive
ICE	ion cyclotron emission
ICRF	ion cyclotron range of frequencies
IIH	ion-ion hybrid
IMAS	integrated modelling and analysis suite
ITB	internal transport barrier
ITER	International Thermonuclear Experimental Reactor
ITG	ion-temperature gradient
ITPA	International Tokamak Physics Activity
KAM	Kolmogorov-Arnold-Moser

KAW	kinetic Alfvén wave
KBM	kinetic ballooning mode
KTAE	kinetic toroidal Alfvén eigenmode
LaBr	lanthanum bromide
LFAM	low-frequency Alfvén mode
LFSR	low-field-side reflectometer
LH	low-confinement to high-confinement
L-mode	low-confinement mode
MAE	mirror-induced Alfvén eigenmode
m-BAE	magnetic-island-driven beta-induced Alfvén eigenmode
MES	motional Stark effect
NAE	non-circular triangularity-induced Alfvén eigenmode
NGAE	non-conventional global Alfvén eigenmode
NES	neutron emission spectroscopy
NBCD	neutral beam current drive
NBI	neutral beam injection
NNBI	negative-ion neutral beam injection
NPA	neutral particle analyzer
MHD	magnetohydrodynamic
NTM	neoclassical tearing mode
PIC	particle in cell
PNBI	positive-ion neutral beam injection
PoPola	poloidal polarimeter
RBQ	resonance broadening quasilinear
RE	runaway electrons
RF	radio-frequency
RMP	resonant magnetic perturbation
RSAE	reversed-shear Alfvén eigenmode
RWM	resistive wall mode
SAW	shear Alfvén wave
SAWC	shear Alfvén wave continuum
SSNPA	solid-state neutral particle analyzer
SW	slow magnetosonic wave
SXR	soft x-ray
TAE	toroidicity-induced Alfvén eigenmode
TBM	test blanket module
TEM	trapped electron mode
TF	toroidal field
TIP	toroidal interferometer and polarimeter
TM	tearing mode
TQ	thermal quench
Q	power amplification factor
VDE	vertical displacement event
WDM	whole-device model
WKB	Wentzel–Kramers–Brillouin
ZC	zonal current
ZF	zonal flow
ZFS	zonal field structure
ZS	zonal state

References

[1] Bigot B. 2019 *Nucl. Fusion* **59** 112001
[2] Bigot B. 2022 *Nucl. Fusion* **62** 042001

[3] Salewski M. *et al* 2018 *Nucl. Fusion* **58** 096019
[4] ITER Organization 2018 *2018 ITER Research Plan within the Staged Approach (Level III – Provisional version) Tech. Rep. ITR-18-003 ITER Organization St. Paul Lez Durance Cedex, France*
[5] ITER Organization 2024 *2024 ITER Research Plan within the Staged Approach (Level III – Final Version) Tech. Rep. ITR-24-005 ITER Organization St. Paul Lez Durance Cedex, France*
[6] Barabaschi P. 2023 *ITER Progress on ITER manufacturing, construction, commissioning and plans 29th IAEA Fusion Energy Conference – Programme, Contributions and Conference Material (Vienna: International Atomic Energy Agency (IAEA)) pp OV 1–3*
[7] Keilhacker M. *et al* 1999 *Nucl. Fusion* **39** 209–234
[8] Wenninger R. *et al* 2015 *Nucl. Fusion* **55** 063003
[9] Creely A. J. *et al* 2020 *J. Plasma Phys.* **86** 865860502
[10] Muldrew S. I. *et al* 2024 *Fusion Eng. Des.* **201** 114238
[11] Meyer H. 2024 *Phil. Trans. Royal Soc A* **382** 20230406
[12] Zhuang G. *et al* 2019 *Nucl. Fusion* **59** 112010
[13] Campbell D. J. *et al* 2025 *Nucl. Fusion* Chapter 1: Overview and Summary
[14] Yoshida M. *et al* 2025 *Nucl. Fusion* Chapter 2: Transport and confinement
[15] Fenstermacher M. *et al* 2025 *Nucl. Fusion* Chapter 3: Pedestal and edge physics
[16] Bandyopadhyay I. *et al* 2025 *Nucl. Fusion* Chapter 4: MHD, disruptions and control
[17] Krieger K. *et al* 2025 *Nucl. Fusion* Chapter 5: Scrape–off layer and divertor physics
[18] Na Y.-S. *et al* 2025 *Nucl. Fusion* Chapter 6: Integrated operation scenarios
[19] Mazon D. *et al* 2025 *Nucl. Fusion* Chapter 8: Diagnostics
[20] Fasoli A. *et al* 2007 *Nucl. Fusion* **47** S264
[21] ITER Physics Expert Group on Energetic Particles, Heating and Current Drive and ITER Physics Basis Editors 1999 *Nucl. Fusion* **39** 2471
[22] Heidbrink W. W. and Sadler G. J. 1994 *Nucl. Fusion* **34** 535–615
[23] Wong K.-L. 1999 *Plasma Phys. Contol. Fusion* **41** R1
[24] Zweben S. J. *et al* 2000 *Nucl. Fusion* **40** 91
[25] Eriksson L.-G. and Porcelli F. 2001 *Plasma Phys. Control. Fusion* **43** R145
[26] Chen L. and Zonca F. 2007 *Nucl. Fusion* **47** S727
[27] Heidbrink W. W. 2008 *Phys. Plasmas* **15** 055501
[28] Breizman B. N. and Sharapov S. E. 2011 *Plasma Phys. Control. Fusion* **53** 054001
[29] Lauber P. 2013 *Phys. Rep.* **533** 33–68
[30] Gorelenkov N., Pinches S. and Toi K. 2014 *Nucl. Fusion* **54** 125001
[31] Pinches S. D. *et al* 2015 *Phys. Plasmas* **22** 021807
[32] Chen L. and Zonca F. 2016 *Rev. Mod. Phys.* **88** 015008
[33] McClements K. G. and Fredrickson E. D. 2017 *Plasma Phys. Control. Fusion* **59** 053001
[34] Todo Y. 2019 *Rev. Mod. Plasma Phys.* **3** 1
[35] Moseev D., Salewski M., Garcia-Muñoz M., Geiger B. and Nocente M. 2018 *Rev. Mod. Plasma Phys.* **2**(1) 7
[36] Breizman B. N., Aleynikov P., Hollmann E. M. and Lehnen M. 2019 *Nucl. Fusion* **59** 083001
[37] Heidbrink W. W. and White R. B. 2020 *Phys. Plasmas* **27** 30901–30925
[38] Kazakov Y. O. *et al* 2021 *Phys. Plasmas* **28** 020501
[39] Maslov M. *et al* 2023 *Nucl. Fusion* **63** 112002
[40] Fitzgerald M. *et al* 2023 *Nucl. Fusion* **63** 112006
[41] Sharapov S. *et al* 2023 *Nucl. Fusion* **63** 112007
[42] Oliver H. *et al* 2023 *Nucl. Fusion* **63** 112008
[43] Mantsinen M. *et al* 2023 *Nucl. Fusion* **63** 112015
[44] Nocente M. *et al* 2022 *Rev. Sci. Instrum.* **93** 093520

[45] Kiptily V. G. *et al* 2023 *Phys. Rev. Lett.* **131**(7) 075101
[46] Bonofiglo P. *et al* 2024 *Nucl. Fusion* **64** 096038
[47] Kiptily V. *et al* 2024 *Nucl. Fusion* **64** 086059
[48] Kirov K. *et al* 2024 *Nucl. Fusion* **64** 086011
[49] Järleblad H. *et al* 2024 *Nucl. Fusion* **64** 026015
[50] Mailloux J. *et al* 2022 *Nucl. Fusion* **62** 042026
[51] Maggi C. *et al* 2023 *Nucl. Fusion* **63** 110201
[52] Garcia J. *et al* 2024 *Nat. Commun.* **15** 7846
[53] Maggi C. F. *et al* 2024 *Nucl. Fusion* **64** 112012
[54] Northrop T. G. and Teller E. 1960 *Phys. Rev.* **117** 215–225
[55] Hastie R. J., Taylor J. B. and Haas F. A. 1967 *Annals of Physics* **41** 302–338
[56] Kruskal M. D. and Kulsrud R. M. 1958 *Phys. Fluids* **1** 265–274
[57] Fitzgerald M. 2024 *Solution of the linear wave-particle kinetic equation for global modes of arbitrary frequency in a tokamak, in preparation*
[58] Eriksson L.-G., Mantsinen M. J., Hellsten T. and Carlsson J. 1999 *Phys. Plasmas* **6** 513–518
[59] Zhang R., Fu G., White R. and Wang X. 2015 *Nucl. Fusion* **55** 122002
[60] Chen X. *et al* 2013 *Phys. Rev. Lett.* **110**(6) 065004
[61] Järleblad H. *et al* 2024 *Comp. Phys. Com..* **294** 108930
[62] Brizard A. J. 2011 *Phys. Plasmas* **18** 022508
[63] Helander P. and Sigmar D. J. 2005 *Collisional Transport in Magnetized Plasmas* (Cambridge University Press) ISBN 9780521020985
[64] Hinton F. L. and Hazeltine R. D. 1976 *Rev. Mod. Phys.* **48**(2) 239–308
[65] Catto P. J. 1978 *Plasma Phys.* **20** 719–722
[66] Fisch N. J. 1987 *Rev. Mod. Phys.* **59**(1) 175–234
[67] De Vries P. C. *et al* 2008 *Nucl. Fusion* **48** 035007
[68] Sharapov S. E. *et al* 2008 *Fusion Sci. Technol.* **53** 989–1022
[69] Canik J. M. *et al* 2010 *Nucl. Fusion* **50** 034012
[70] Kaye S. M. *et al* 2005 *Nucl. Fusion* **45** S168
[71] Scott S. D. *et al* 2020 *J. Plasma Phys.* **100**(5) 865860508
[72] Tinguely (MIT) R. A. and Scott (CFS) S. 2022 *private comm.*
[73] Siccinio M. *et al* 2022 *Fusion Eng. Des.* **176** 113047
[74] Ren Z.-Z. *et al* 2023 *Nucl. Fusion* **64** 016008
[75] Xu Y., Zhang D., Chen J. and Zhong F. 2022 *Plasma Sci. Tech.* **24** 105101
[76] Trubnikov B. A. 1965 *Rev. Plasma Phys.* **1**
[77] Gaffey J. D. 1976 *J. Plasma Phys.* **16** 149
[78] Stix T. H. 1972 *Plasma Phys.* **14** 367–384
[79] Connor J. W. *et al* 1994 Non-ideal effects on Toroidal Alfven Eigenmode stability *21st EPS Conf. Control. Fusion Plasma Phys.* (Montpellier, France)
[80] Brambilla M. 1998 *Kinetic Theory of Plasma Waves* (Oxford University Press) ISBN 9780198559566
[81] Petty C. *et al* 1995 *Nucl. Fusion* **35** 773
[82] Dumont R. and Zarzoso D. 2013 *Nucl. Fusion* **53** 13002
[83] Pinsker R. I. 1998 *Plasma Phys. Control. Fusion* **40** A215–A229
[84] Noterdaeme J.-M. *et al* 2005 *Fusion Eng. Des.* **74** 191–198
[85] Porkolab M. 1994 *AIP Conf. Proc.* **314** 99–127
[86] ITER Physics Expert Group on Energetic Particles, Heating and Current Drive and ITER Physics Basis Editors 1999 *Nucl. Fusion* **39** 2495
[87] Salewski M. *et al* 2017 *Nucl. Fusion* **57** 056001
[88] Wilson J. R. and Bonoli P. T. 2014 *Phys. Plasmas* **22** 021801
[89] Ongena J. *et al* 2017 *Plasma Phys. Control. Fusion* **59** 054002
[90] Hosea, Joel 2017 *EPJ Web Conf.* **157** 02003
[91] Lin Y., Wright J. C. and Wukitch S. J. 2020 *J. Plasma*

Phys. **86** 865860506

[92] Schneider M. *et al* 2016 *Nucl. Fusion* **56** 112022

[93] Sharapov S. *et al* 2016 *Nucl. Fusion* **56** 112021

[94] Mantsinen M. J. *et al* 2002 *Phys. Rev. Lett.* **88**(10) 105002

[95] Mantsinen M., Eriksson L.-G., Gondhalekar A. and Hellsten T. 1999 *Nucl. Fusion* **39** 459

[96] Wilson J. R. *et al* 1995 *Phys. Rev. Lett.* **75**(5) 842–845

[97] Wilson J. R. *et al* 1996 *AIP Conf. Proc.* **355** 3–6

[98] Start D. F. H. 1998 *Plasma Phys. Control. Fusion* **40** A87

[99] Start D. *et al* 1999 *Nucl. Fusion* **39** 321

[100] Jacquet P. *et al* 2023 *AIP Conf. Proc.* **2984** 030003

[101] Stix T. H. 1975 *Nucl. Fusion* **15** 737

[102] Lerche E. *et al* 2016 *Nucl. Fusion* **56** 036022

[103] Kazakov Y. *et al* 2020 *Nucl. Fusion* **60** 112013

[104] Kazakov Y., Eester D. V., Dumont R. and Ongena J. 2015 *Nucl. Fusion* **55** 032001

[105] Ongena J. *et al* 2017 *EPJ Web Conf.* **157**

[106] Brambilla M. and Bilato R. 2009 *Nucl. Fusion* **49** 085004

[107] Kazakov Y. O. *et al* 2017 *Nat. Phys.* **13** 973–978

[108] Campbell D. J. *et al* 1988 *Phys. Rev. Lett.* **60**(21) 2148–2151

[109] Phillips C. *et al* 1992 *Phys. Fluids B* **4** 2155–2164

[110] Chapman I. T. *et al* 2007 *Plasma Phys. Control. Fusion* **49** B385

[111] Sauter O. *et al* 2002 *Phys. Rev. Lett.* **88** 105001

[112] Graves J. P. *et al* 2012 *Nat. Commun.* **3** 624

[113] Lennholm M. *et al* 2009 *Phys. Rev. Lett.* **102** 115004

[114] Lennholm M. *et al* 2009 *Fusion Sci. Technol.* **55** 45

[115] Lennholm M. *et al* 2011 *Nucl. Fusion* **51** 073032

[116] Graves J. *et al* 2000 *Phys. Rev. Lett.* **84** 1204–1207

[117] Graves J., Chapman I., Coda S., Eriksson L.-G. and Johnson T. 2009 *Phys. Rev. Lett.* **102** 065005

[118] Graves J. P. *et al* 2014 *Plasma Phys. Control. Fusion* **57** 014033

[119] Lennholm M. *et al* 2015 *Nucl. Fusion* **56** 016008

[120] Snipes J. A. *et al* 2000 *Plasma Phys. Control. Fusion* **42** 381

[121] Sharapov S. E. *et al* 2018 *Plasma Phys. Control. Fusion* **60** 14026

[122] Dumont R. J. *et al* 2018 *Nucl. Fusion* **58** 082005

[123] Snipes J. A. *et al* 2005 *Phys. Plasmas* **12** 056102

[124] Kramer G. *et al* 2000 *Nucl. Fusion* **40** 1383

[125] Mantsinen M. J. *et al* 2002 *Plasma Phys. Control. Fusion* **44** 1521

[126] Oliver H. J. C., Sharapov S. E., Breizman B. N. and Zheng L.-J. 2017 *Phys. Plasmas* **24** 122505

[127] Hellesen C. *et al* 2018 *Nucl. Fusion* **58** 056021

[128] Nabais F. *et al* 2022 *Nucl. Fusion* **62** 104001

[129] Kiptily V. *et al* 2020 *Nucl. Fusion* **60** 112003

[130] Kiptily V. *et al* 2021 *Nucl. Fusion* **61** 114006

[131] Kiptily V. G. *et al* 2022 *Plasma Phys. Control. Fusion* **64** 064001

[132] Dreval M. *et al* 2022 *Nucl. Fusion* **62** 056001

[133] Mazzi S. *et al* 2022 *Nature Phys.* **18**(7) 776–782

[134] Loarte A. *et al* 2024 The new ITER Baseline, Research Plan and Open R&D issues *50th EPS Conf. Plasma Physics*

[135] Lamalle P. *et al* 2013 *Fusion Eng. Des.* **88** 517–520

[136] Schneider M. *et al* 2017 *EPJ Web Conf.* **157** 03046

[137] Schneider M. *et al* 2017 Heating scenarios for the new staged-approach of the ITER research plan *44th EPS Conf. Control. Fusion Plasma Physics* p P5.153

[138] Van Eester D. *et al* 2017 *EPJ Web Conf.* **157** 03061

[139] Kazakov Y. O. *et al* 2023 *AIP Conf. Proc.* **2984** 020001

[140] Kazakov Y. O. *et al* 2018 *Proc. 45th EPS Conf. Control. Fusion Plasma Physics* P5.1047

[141] Van Eester D., Louche F. and Koch R. 2002 *Nucl.*

[142] Kazakov Y. O. *et al* 2015 *Phys. Plasmas* **22** 082511

[143] Song C. *et al* 2020 *Phys. Scr.* **96** 025603

[144] Stagner L. *et al* 2022 *Nucl. Fusion* **62** 026033

[145] Gin D. *et al* 2014 *AIP Conf. Proc.* **1612** 149–152

[146] Chugunov I. *et al* 2011 *Nucl. Fusion* **51** 083010

[147] Nocente M. *et al* 2017 *Nucl. Fusion* **57** 076016

[148] Korsholm S. B. *et al* 2022 *Rev. Sci. Instrum.* **93** 103539

[149] Rasmussen J. *et al* 2019 *Plasma Phys. Contol. Fusion* **61** 095002

[150] Rasmussen J. *et al* 2019 *Nucl. Fusion* **59** 096051

[151] Salewski M. *et al* 2009 *Nucl. Fusion* **49** 025006

[152] Salewski M. *et al* 2009 *Plasma Phys. Control. Fusion* **51** 035006

[153] Afanasyev V. *et al* 2010 *Nucl. Instrum. Methods Phys. Res. A* **621** 456–467

[154] Scholz M. *et al* 2019 *Nucl. Fusion* **59** 065001

[155] Källne J. *et al* 2000 *Phys. Rev. Lett.* **85**(6) 1246–1249

[156] Afanasyev V. *et al* 2022 *J. Instrum.* **17** C07001

[157] Kiptily V. G., Cecil F. E. and Medley S. S. 2006 *Plasma Phys. Control. Fusion* **48** R59

[158] Nocente M. *et al* 2019 *Plasma Phys. Control. Fusion* **62** 014015

[159] Nocente M. *et al* 2020 *Nucl. Fusion* **60** 124006

[160] Nocente M. *et al* 2021 *Rev. Sci. Instrum.* **92** 043537

[161] Tardocchi M. *et al* 2011 *Phys. Rev. Lett.* **107** 205002

[162] Kiptily V. *et al* 2010 *Nucl. Fusion* **50** 084001

[163] Eriksson J. *et al* 2015 *Nucl. Fusion* **55** 123026

[164] Eriksson J. *et al* 2018 *Plasma Phys. Control. Fusion* **61** 014027

[165] Nocente M. *et al* 2013 *IEEE Transact. Nucl. Sci.* **60** 1408–1415

[166] Nocente M. *et al* 2016 *Rev. Sci. Instrum.* **87** 11E714

[167] Salewski M. *et al* 2010 *Nucl. Fusion* **50** 035012

[168] Salewski M. *et al* 2011 *Nucl. Fusion* **51** 083014

[169] Meo F. *et al* 2008 *Rev. Sci. Instrum.* **79** 10E501

[170] Furtula V. *et al* 2012 *Rev. Sci. Instrum.* **83** 013507

[171] Nielsen S. K. *et al* 2015 *Plasma Phys. Control. Fusion* **57** 035009

[172] Rasmussen J. *et al* 2015 *Plasma Phys. Control. Fusion* **57** 075014

[173] Stejner M. *et al* 2010 *Rev. Sci. Instrum.* **81** 10D515

[174] Nishiura M. *et al* 2014 *Nucl. Fusion* **54** 023006

[175] Nielsen S. K. *et al* 2017 *Phys. Scripta* **92** 024001

[176] Moseev D. *et al* 2019 *Rev. Sci. Instrum.* **90** 013503

[177] DeGrandchamp G. *et al* 2022 *Nucl. Fusion* **62** 106033

[178] McClements K. *et al* 2015 *Nucl. Fusion* **55** 043013

[179] Ichimura M. *et al* 2008 *Nucl. Fusion* **48** 035012

[180] Sato S. *et al* 2010 *Plasma and Fusion Research* **5** S2067

[181] D'Inca R. 2014 *Ph.D thesis, Max Planck Inst. Plasma Phys.*

[182] Ochoukov R. *et al* 2019 *Nucl. Fusion* **59** 086032

[183] Ochoukov R. *et al* 2020 *Nucl. Fusion* **60** 126043

[184] Liu L. *et al* 2020 *Nucl. Fusion* **61** 026004

[185] Thatipamula S. G. *et al* 2016 *Plasma Phys. Control. Fusion* **54** 065003

[186] Chapman B. *et al* 2018 *Nucl. Fusion* **58** 096027

[187] Fredrickson E. D. *et al* 2019 *Phys. Plasmas* **26** 032111

[188] Thome K. E. *et al* 2019 *Nucl. Fusion* **59** 086011

[189] Liu L. *et al* 2020 *Nucl. Fusion* **60** 044002

[190] Liu L. *et al* 2023 *Plasma Phys. Control. Fusion* **66** 015007

[191] Saito K. *et al* 2013 *Plasma Sci. Technol.* **15** 209

[192] Reman B. C. G. *et al* 2022 *Plasma Phys. Control. Fusion* **64** 085008

[193] Moseev D. *et al* 2021 *Rev. Sci. Instrum.* **92** 033546

[194] Heidbrink W. W. *et al* 2007 *Plasma Phys. Control. Fusion* **49** 1457

[195] Salewski M. *et al* 2014 *Plasma Phys. Control. Fusion* **56** 105005

Fusion **42** 310

[196] Jacobsen A. *et al* 2015 *Nucl. Fusion* **55** 053013

[197] Jacobsen A. S. *et al* 2017 *Rev. Sci. Instrum.* **88** 073506

[198] Salewski M. *et al* 2015 *Nucl. Fusion* **55** 093029

[199] Salewski M. *et al* 2016 *Nucl. Fusion* **56** 046009

[200] Galdon-Quiroga J. *et al* 2018 *Plasma Phys. Control. Fusion* **60** 105005

[201] Schmidt B. S. *et al* 2024 *Plasma Phys. Control. Fusion* **66** 045004

[202] Heidbrink W. W., Garcia A., Boeglin W. and Salewski M. 2021 *Plasma Phys. Control. Fusion* **63** 055008

[203] Schmidt B. S. *et al* 2021 *Rev. Sci. Instrum.* **92** 053528

[204] Schmidt B. S. *et al* 2023 *Phys. of Plasmas* **30** 092109

[205] Rueda-Rueda J. *et al* 2024 *Plasma Phys. Control. Fusion* **66** 065025

[206] Stagner L. and Heidbrink W. W. 2017 *Phys. Plasmas* **24** 092505

[207] Järleblad H. *et al* 2021 *Rev. Sci. Instrum.* **92** 043526

[208] Järleblad H. *et al* 2022 *Nucl. Fusion* **62** 112005

[209] Rud M. *et al* 2024 *Nucl. Fusion* **64** 036007

[210] Kiptily V. G. *et al* 2004 *Phys. Rev. Lett.* **93** 115001

[211] Kiptily V. *et al* 2005 *Nucl. Fusion* **45** L21

[212] Salewski M. *et al* 2012 *Nucl. Fusion* **52** 103008

[213] Salewski M. *et al* 2014 *Nucl. Fusion* **54** 023005

[214] Salewski M. *et al* 2016 *Nucl. Fusion* **56** 106024

[215] Salewski M. *et al* 2013 *Nucl. Fusion* **53** 063019

[216] Jacobsen A. S. *et al* 2016 *Plasma Phys. Control. Fusion* **58** 042002

[217] Madsen B. *et al* 2020 *Plasma Phys. Control. Fusion* **62** 115019

[218] Weiland M. *et al* 2016 *Plasma Phys. Control. Fusion* **58** 025012

[219] Weiland M. *et al* 2017 *Nucl. Fusion* **57** 116058

[220] Jacobsen A. S. *et al* 2016 *Plasma Phys. Control. Fusion* **58** 045016

[221] Rasmussen J. *et al* 2016 *Nucl. Fusion* **56** 112014

[222] Salewski M. *et al* 2018 *Fusion Sci. Tech.* **74** 23–36

[223] Madsen B. *et al* 2018 *Rev. Sci. Instrum.* **89** 10D125

[224] Madsen B. *et al* 2020 *Nucl. Fusion* **60** 066024

[225] Su J. *et al* 2021 *Plasma Sci. Technol.* **23** 095103

[226] Geiger B. *et al* 2017 *Plasma Phys. Control. Fusion* **59** 115002

[227] Rud M. *et al* 2024 *Nucl. Fusion* **64** 076018

[228] Salewski M. 2019 *Dr. techn. thesis, Tech. Univ. Denmark*

[229] Salewski M. *et al* 2019 *J. Instrum.* **14** C05019

[230] Schmidt B. *et al* 2023 *Nucl. Fusion* **63** 076016

[231] Rud M. *et al* in preparation *Fast-ion phase-space tomography with wave-particle interactions in the ion cyclotron frequency range as prior*

[232] Schmidt B. S. *et al* 2024 *submitted*

[233] Garcia-Munoz M. *et al* 2016 *Rev. Sci. Instrum.* **87** 11D829

[234] García-Muñoz M. *et al* 2008 *Phys. Rev. Lett.* **100**(5) 055005

[235] García-Muñoz M. *et al* 2010 *Phys. Rev. Lett.* **104**(18) 185002

[236] Galdon-Quiroga J. *et al* 2018 *Phys. Rev. Lett.* **121**(2) 025002

[237] Nocente M. *et al* 2018 *Rev. Sci. Instrum.* **89** 10I124

[238] Molin A. D. *et al* 2023 *Meas. Sci. Tech.* **34** 085501

[239] Jaspers R., Lopes Cardozo N. J., Donné A. J. H., Widdershoven H. L. M. and Finken K. H. 2001 *Rev. Sci. Instrum.* **72** 466–470

[240] Lvovskiy A. *et al* 2020 *Nucl. Fusion* **60** 056008

[241] Reux C. *et al* 2022 *Plasma Phys. Control. Fusion* **64** 034002

[242] Shevelev A. *et al* 2021 *Nucl. Fusion* **61** 116024

[243] Zhou R. J. *et al* 2019 *Rev. Sci. Instrum.* **90** 123510

[244] Shevelev A. E. *et al* 2013 *Nucl. Fusion* **53** 123004

[245] Jaspers R. *et al* 1995 *J. Nucl. Mater.* **220** 682–687

[246] Paz-Soldan C. *et al* 2014 *Phys. Plasmas* **21** 022514

[247] Zhou R. J. *et al* 2013 *Plasma Phys. Control. Fusion* **55** 055006

[248] Cheon M., Kim J., An Y., Seo D. and Kim H. 2016 *Nucl. Fusion* **56** 126004

[249] Carbajal L. and Del-Castillo-Negrete D. 2017 *Plasma Phys. Control. Fusion* **59** 124001

[250] Hoppe M. *et al* 2018 *Nucl. Fusion* **58** 026032

[251] Pandya S. P. *et al* 2018 *Phys. Scr.* **93** 115601

[252] Sharapov S. *et al* 2001 *Phys. Lett. A* **289** 127–134

[253] Donné A. *et al* 2007 *Nucl. Fusion* **47** S337

[254] Van Zeeland M. A. *et al* 2018 *Rev. Sci. Instrum.* **89** 10B102

[255] Carlstrom T. N., Snider R. T., Baxi C. B., Rettig C. L. and Peebles W. A. 1998 *Diagnostics Exp. Thermonucl. Fusion React. 2, Ed. by Stott* al., *Plenum Press. New York* 193

[256] Van Zeeland M. A. *et al* 2013 *Rev. Sci. Instrum.* **84**(4) 043501

[257] Van Zeeland M. A. *et al* 2017 *Plasma Phys. Control. Fusion* **59** 125005

[258] Irby J. H., Marmar E. S., Sevillano E. and Wolfe S. M. 1988 *Rev. Sci. Instrum.* **59**(8) 1568–1570

[259] Carlstrom T. N., Ahlgren D. R. and Crosbie J. 1988 *Rev. Sci. Instrum.* **59**(7) 1063–1066

[260] Kawano Y., Nagashima A., Hatae T. and Gunji S. 1996 *Rev. Sci. Instrum.* **67**(4) 1520–1528

[261] Innocente P., Martini S., Canton A. and Tasinato L. 1997 *Rev. Sci. Instrum.* **68**(1) 694–697

[262] Gil C. *et al* 2008 *Rev. Sci. Instrum.* **79** 10E710

[263] Mlynek A. *et al* 2010 *Rev. Sci. Instrum.* **81**(3) 033507

[264] Van Zeeland M. A. *et al* 2006 *Nucl. Fusion* **46** S880

[265] Van Zeeland M. A. *et al* 2005 *Plasma Phys. Control. Fusion* **47** L31

[266] Brower D. L. *et al* 2001 *Rev. Sci. Instrum.* **72**(1 II) 1077–1080

[267] Van Zeeland M. A. *et al* 2006 *Phys. Rev. Lett.* **97**(13) 135001

[268] Heidbrink W. W., Fasoli A., Borba D. and Jaun A. 1997 *Phys. Plasmas* **4**(10) 3663–3666

[269] Udintsev V. S. *et al* 2006 *Plasma Phys. Control. Fusion* **48** L33

[270] Sharapov S. E. *et al* 2002 *Phys. Plasmas* **9**(5) 2027–2036

[271] Austin M. E. *et al* 2007 *Electron Cyclotron Emission and Electron Cyclotron Resonance Heating (EC-15)* 170 – 177

[272] Garcia-Munoz M. *et al* 2011 *Nucl. Fusion* **51** 103013

[273] Kramer G. I., Sips A. C. C. and Cardozo N. J. L. 1993 *Plasma Phys. Control. Fusion* **35** 1685

[274] Elfimov A. *et al* 2006 *Nucl. Fusion* **46** S722

[275] Wang G. *et al* 2006 *Nucl. Fusion* **46** S708

[276] Hacquin S. *et al* 2007 *Plasma Phys. Control. Fusion* **49** 1371

[277] Crocker N. *et al* 2017 *Nucl. Fusion* **58** 016051

[278] Nazikian R. *et al* 1998 *Phys. Plasmas* **5** 1703–1711

[279] Bretz N. 1992 *Phys. Fluids B: Plasma Phys.* **4** 2414–2422

[280] Fanack C. *et al* 1996 *Plasma Phys. Control. Fusion* **38** 1915

[281] Mazzucato E. and Nazikian R. 1991 *Plasma Phys. Control. Fusion* **33** 261

[282] Muscatello C. *et al* 2020 *Nucl. Fusion* **60** 066005

[283] Muscatello C. M. *et al* 2021 *Rev. Sci. Instrum.* **92** 033524

[284] Silva A. *et al* 1999 *Rev. Sci. Instrum.* **70** 1072–1075

[285] Hicks N. K. *et al* 2010 *Fusion Sci. Tech.* **57** 1–9

[286] Ma Y. 2017 (private communication) *ITER_D_P9J7XG System Design Description (DDD) 55.AJ HF*

Sensors

[287] Akiyama T., Yasuhara R., Kawahata K., Okajima S. and Nakayama K. 2014 *Rev. Sci. Instrum.* **85** 11D301

[288] Piovesan P. *et al* 2008 *Nucl. Fusion* **48** 065001

[289] Barnsley R. 2012 (private communication) *ITER_D_6y2ASR System Design Description (DDD) 55.E7 Radial X-Ray Camera*

[290] Watson G. and Heidbrink W. W. 2003 *Rev. Sci. Instrum.* **74** 1605–1608

[291] Akiyama T. *et al* 2022 *J. Instrum.* **17** C01052

[292] Van Zeeland M. A. *et al* 2016 *Nucl. Fusion* **56** 112007

[293] Berk H. L., Borba D. N., Breizman B. N., Pinches S. D. and Sharapov S. E. 2001 *Phys. Rev. Lett.* **87**(18) 185002

[294] Breizman B. N., Berk H. L., Pekker M. S., Pinches S. D. and Sharapov S. E. 2003 *Phys. Plasmas* **10** 3649–3660

[295] Cai H. and Li D. 2022 *National Sci. Rev.* **9** nwac019

[296] Buttery R. J. *et al* 2008 *Phys. Plasmas* **15** 056115

[297] Fietz S. *et al* 2013 *Plasma Phys. Control. Fusion* **55** 085010

[298] Gerhardt S. P. *et al* 2009 *Nucl. Fusion* **49** 032003

[299] Anderson J. K. *et al* 2013 *Phys. Plasmas* **20** 056102

[300] Heidbrink W. W. *et al* 2018 *Nucl. Fusion* **58** 082027

[301] Hegna C. C. and Bhattacharjee A. 1990 *Phys. Fluids B: Plasma Phys.* **2** 1804–1814

[302] Takahashi R., Brennan D. P. and Kim C. C. 2009 *Phys. Rev. Lett.* **102** 135001

[303] Cai H. 2021 *Nucl. Fusion* **61** 126012

[304] Cai H. and Fu G. 2012 *Phys. Plasmas* **19** 072506

[305] Liu Y., Hastie R. J. and Hender T. C. 2012 *Phys. Plasmas* **19** 092510

[306] Cai H., Li D. and Cao J. 2015 *Phys. Plasmas* **22** 102512

[307] Halfmoon M. R. and Brennan D. P. 2017 *Phys. Plasmas* **24** 062501

[308] Zhang X., Cai H. and Wang Z.-X. 2019 *Phys. Plasmas* **26** 062505

[309] Cai H. 2016 *Nucl. Fusion* **56** 126016

[310] Yang J., Fredrickson E. D., Podestà M. and Poli F. M. 2022 *Plasma Phys. Control. Fusion* **64** 095005

[311] Cai H., Cao J. and Li D. 2017 *Nucl. Fusion* **57** 056006

[312] Cai H. and Cao J. 2018 *Nucl. Fusion* **58** 036008

[313] Tang X. *et al* 2020 *Phys. Plasmas* **27** 032508

[314] Fredrickson E. D. 2002 *Phys. Plasmas* **9** 548–559

[315] Sesnic S., Günter S., Gude A., Maraschek M. and ASDEX Upgrade Team 2000 *Phys. Plasmas* **7** 935

[316] Li E. *et al* 2016 *Plasma Phys. Control. Fusion* **58** 045012

[317] Chen W. *et al* 2019 *Nucl. Fusion* **59** 096037

[318] Marchenko V. S. and Lutsenko V. V. 2001 *Phys. Plasmas* **8** 4834–4838

[319] Zhu X.-L., Chen W., Wang F. and Wang Z.-X. 2020 *Nucl. Fusion* **60** 046023

[320] Zhang X., Gao B., Cai H., Zheng S. and Wang Z.-X. 2020 *Plasma Phys. Control. Fusion* **62** 085010

[321] Cai H., Wang S., Xu Y., Cao J. and Li D. 2011 *Phys. Rev. Lett.* **106** 075002

[322] Brennan D., Kim C. and Haye R. L. 2012 *Nucl. Fusion* **52** 033004

[323] Podesta M. *et al* 2019 *Nucl. Fusion* **59** 106013

[324] Furth H. P., Killeen J. and Rosenbluth M. N. 1963 *Phys. Fluids* **6** 459

[325] Furth H. P., Rutherford P. H. and Selberg H. 1973 *Phys. Fluids* **16** 1054

[326] Qu W. X. and Callen J. D. 1985 Univ. Wisconsin Report No. UWPR-85-5

[327] Hirshman S. and Sigmar D. 1981 *Nucl. Fusion* **21** 1079

[328] Carrera R., Hazeltine R. D. and Kotschenreuther M. 1986 *Phys. Fluids* **29** 899–902

[329] Wilson J. W., Connor J. W., Hastie R. J. and Hegna C. C. 1996 *Phys. Plasmas* **3** 248

[330] Smolyakov A. I., Hirose A., Lazzaro E., Re G. B. and Callen J. D. 1995 *Phys. Plasmas* **2** 1581–1598

[331] Liu D. *et al* 2020 *Nucl. Fusion* **60** 112009

[332] Sen A., Chandra D. and Kaw P. 2013 *Nucl. Fusion* **53** 053006

[333] Chandra D. *et al* 2015 *Nucl. Fusion* **55** 053016

[334] Wang H., Todo Y., Ido T. and Osakabe M. 2015 *Phys. Plasmas* **22** 092507

[335] Ren Z. *et al* 2020 *Plasma Sci. Technol.* **22** 065102

[336] Sakamoto Y. *et al* 2005 *Nucl. Fusion* **45** 574–580

[337] Yang J. *et al* 2023 *Plasma Phys. Control. Fusion* **65** 064004

[338] Fu G. Y. *et al* 2006 *Phys. Plasmas* **13** 052517

[339] Cao J. *et al* 2016 *Phys. Plasmas* **23** 012301

[340] Gao B., Cai H., Gao X. and Wan Y. 2021 *Nucl. Fusion* **61** 116070

[341] Gao B., Cai H., Wang F., Gao X. and Wan Y. 2021 *Phys. Plasmas* **28** 12104

[342] Forest C. *et al* 1997 *Phys. Rev. Lett.* **79** 427

[343] Carolipio E., Heidbrink W., Forest C. and White R. 2002 *Nucl. Fusion* **42** 853

[344] Mynick H. E. 1993 *Phys. Fluids B* **5** 1471

[345] Mynick H. E. 1993 *Phys. Fluids B* **5** 2460

[346] García-Muñoz M. *et al* 2007 *Nucl. Fusion* **47** L10–L15

[347] García-Muñoz M. *et al* 2009 *Nucl. Fusion* **49** 085014

[348] Poli E., García-Muñoz M., Fahrbach H.-U. and Günter S. 2008 *Phys. Plasmas* **15** 032501

[349] Zhao J. *et al* 2022 *Phys. Plasmas* **29** 082502

[350] Zarzoso D., del Castillo-Negrete D., Lacroix R., Bernard P.-E. and Touzet S. 2022 *Plasma Phys. Control. Fusion* **64** 044003

[351] Strumberger E., Günter S., Schwarz E., Tichmann C. and the ASDEX Upgrade Team 2008 *New J. Phys.* **10** 023017

[352] Bardóczi L., Podestà M., Heidbrink W. W. and Van Zeeland M. A. 2019 *Plasma Phys. Control. Fusion* **61** 055012

[353] Kurki-Suonio T. *et al* 2011 *Nucl. Fusion* **51** 083041

[354] Snicker A., Hirvijoki E. and Kurki-Suonio T. 2013 *Nucl. Fusion* **53** 093028

[355] Porcelli F. 1991 *Plasma Phys. Control. Fusion* **33** 1601

[356] Kiptily V. 2009 *Nucl. Fusion* **49** 065030

[357] Chapman I. *et al* 2010 *Nucl. Fusion* **50** 102001

[358] Nave M. F. F. *et al* 2006 *Phys. Plasmas* **13** 014503

[359] Chapman I. *et al* 2006 *Nucl. Fusion* **46** 1009

[360] Chapman I. *et al* 2008 *Nucl. Fusion* **48** 035004

[361] Liu D. *et al* 2022 *Nucl. Fusion* **62** 112009

[362] Nave M. *et al* 2002 *Nucl. Fusion* **42** 281

[363] Porcelli F., Boucher D. and Rosenbluth M. N. 1996 *Plasma Phys. Control. Fusion* **38** 2163

[364] Kolesnichenko Y., Lutsenko V., White R. and Yakovenko Y. 2000 *Nucl. Fusion* **40** 1325–1341

[365] Muscatello C. M. *et al* 2012 *Plasma Phys. Control. Fusion* **54** 025006

[366] Stratton B. C. *et al* 1996 *Nucl. Fusion* **36** 1586

[367] Sadler G. J. *et al* 1990 *Fusion Technol.* **18** 556–572

[368] Marcus F. B. *et al* 1994 *Nucl. Fusion* **34** 687

[369] Pace D. *et al* 2011 *Nucl. Fusion* **51** 043012

[370] Nielsen S. *et al* 2011 *Nucl. Fusion* **51** 063014

[371] Geiger B. *et al* 2015 *Nucl. Fusion* **55** 083001

[372] Jaulmes F. *et al* 2016 *Nucl. Fusion* **56** 112012

[373] Liu D. *et al* 2018 *Nucl. Fusion* **58** 082028

[374] Kim D., Podestà M., Liu D. and Poli F. M. 2018 *Nucl. Fusion* **58** 082029

[375] Kim D. *et al* 2019 *Nucl. Fusion* **59** 086007

[376] Cecconello M. and Sperduti A. 2018 *Plasma Phys. Control. Fusion* **60** 055008

[377] Cecconello M. and Sperduti A. 2019 *Plasma Phys. Control. Fusion* **61** 129501

[378] Jackson A. R., Jacobsen A. S., McClements K. G., Michael C. A. and Cecconello M. 2020 *Nucl. Fusion* **60** 126035
[379] Liu C. *et al* 2018 *Nucl. Fusion* **58** 096030
[380] Mironov M. I. *et al* 2018 *Nucl. Fusion* **58** 082030
[381] Moseev D. *et al* 2024 *Nucl. Fusion* **64** 066028
[382] Podestà M. *et al* 2022 *Plasma Phys. Control. Fusion* **64** 025002
[383] Bonofiglo P. J. *et al* 2022 *Nucl. Fusion* **62** 026026
[384] Teplukhina A. *et al* 2021 *Nucl. Fusion* **61** 116056
[385] Bonofiglo P. J. *et al* 2022 *Nucl. Fusion* **62** 112002
[386] Murari A., Craciunescu T., Peluso E., Lerche E. and Gelfusa M. 2017 *Nucl. Fusion* **57** 126057
[387] Lennholm M. *et al* 2017 *Fusion Eng. Des.* **123** 535
[388] Lerche E. *et al* 2017 *Nucl. Fusion* **57** 036027
[389] Lerche E. *et al* 2020 *Nucl. Fusion* **60** 126037
[390] Tsang K. T. and Sigmar D. J. 1981 *Nucl. Fusion* **21** 1227
[391] Cooper W. A. 1982 *Nucl. Fusion* **22** 835
[392] Rosenbluth M. N., Tsai S. T., Van Dam J. and Engquist M. G. 1983 *Phys. Rev. Lett.* **51** 1967
[393] Wang X.-H., Bhattacharjee A., Mauel M. and Van Dam J. 1988 *Phys. Fluids* **31** 332
[394] Yamagishi T. 1991 *Nucl. Fusion* **31** 1540
[395] Spong D. A., Sigmar D. J., Cooper W. A., Hastings D. E. and Tsang K. T. 1985 *Phys. Fluids* **28** 2494
[396] Spong D. A. *et al* 1987 *Phys. Scr.* **1987** 18
[397] Van Dam J. W. and Fu G. 1988 *Fusion Technology* **13** 423
[398] Spong D. A., Holmes J. A., Leboeuf J.-N. and Christenson P. J. 1990 *Fusion Technology* **18** 496
[399] Biglari H. and Chen L. 1991 *Phys. Rev. Lett.* **67** 3681
[400] Tsai S.-T. and Chen L. 1993 *Phys. Fluids B, Plasma Phys.* **5** 3284
[401] Yamagishi T. 1990 *J. Phys. Soc. Jpn.* **59** 138
[402] Yamagishi T. 1991 *J. Phys. Soc. Jpn.* **60** 3351
[403] Chen L. 1994 *Phys. Plasmas* **1** 1519
[404] Gorelenkov N., Cheng C. and Tang W. 1998 *Phys. Fluids* **5** 3389
[405] Snyder P. *et al* 2002 *Phys. Plasmas* **9** 2037
[406] Hu B., Betti R. and Manickam J. 2005 *Phys. Plasmas* **12** 057301
[407] Strait E. J. *et al* 1995 *Phys. Rev. Lett.* **74**(13) 2483–2486
[408] Sabbagh S. A. *et al* 2006 *Phys. Rev. Lett.* **97**(4) 045004
[409] Garofalo A. M. *et al* 1999 *Phys. Rev. Lett.* **82**(19) 3811–3814
[410] Reimerdes H. *et al* 2006 *Phys. Plasmas* **13** 056107
[411] Reimerdes H. *et al* 2007 *Phys. Rev. Lett.* **98**(5) 055001
[412] Chapman I. T. *et al* 2009 *Plasma Phys. Control. Fusion* **51** 055015
[413] Liu Y., Chu M. S., Chapman I. T. and Hender T. C. 2008 *Phys. Plasmas* **15** 112503
[414] Liu Y., Chu M., Chapman I. and Hender T. 2009 *Nucl. Fusion* **49** 035004
[415] Liu Y. 2010 *Nucl. Fusion* **50** 095008
[416] Berkery J. W. *et al* 2010 *Phys. Plasmas* **17** 082504
[417] Bai X., Liu Y. and Hao G. 2020 *Phys. Plasmas* **27** 124502
[418] Chapman I. T., Gryaznevich M. P., Howell D. F., Liu Y. Q. and the MAST Team 2011 *Plasma Phys. Control. Fusion* **53** 065022
[419] Chapman I. T. *et al* 2012 *Phys. Plasmas* **19** 052502
[420] Hao G. *et al* 2011 *Phys. Plasmas* **18** 032513
[421] Berkery J. W. *et al* 2010 *Phys. Rev. Lett.* **104**(3) 035003
[422] Reimerdes H. *et al* 2011 *Phys. Rev. Lett.* **106**(21) 215002
[423] Garcia-Munoz M. *et al* 2013 *Nucl. Fusion* **53** 123008
[424] Galdon-Quiroga J. *et al* 2019 *Nucl. Fusion* **59** 066016
[425] Rivero-Rodriguez J. *et al* 2023 *Nucl. Fusion* **63** 086028
[426] Dominguez-Palacios J. *et al* 2024 *accepted in Nat. Phys.*
[427] Fu G. Y. 2008 *Phys. Rev. Lett.* **101** 185002
[428] Candy J. 1996 *Plasma Phys. Control. Fusion* **38** 795–801
[429] Mett R. and Mahajan S. 1992 *Phys. Fluids B: Plasma Phys.* **4** 2885–2893
[430] Chen L., Vaclavik J. and Hammett G. W. 1988 *Nucl. Fusion* **28** 389–398
[431] Kolesnichenko Y. I. *et al* 2016 *Plasma Phys. Control. Fusion* **58** 045024
[432] Fitzgerald M. *et al* 2022 *Nucl. Fusion* **62** 106001
[433] Sharapov S. E. *et al* 2004 *Phys. Rev. Lett.* **93** 165001
[434] Li Y. M., Mahajan S. M. and Ross D. W. 1987 *Phys. Fluids* **30** 1466–1484
[435] Mikhailovsky A. B. 1973 *Nucl. Fusion* **13** 259–269
[436] Turnbull A. D. *et al* 1993 *Phys. Fluids B: Plasma Phys.* **5** 2546–2553
[437] Heidbrink W. W., Strait E. J., Chu M. S. and Turnbull A. D. 1993 *Phys. Rev. Lett.* **71** 855–858
[438] Zonca F. and Chen L. 1996 *Phys. Plasmas* **3** 323–343
[439] Zonca F. and Chen L. 2008 *Europhys. Lett.* **83** 35001
[440] Winsor N., Johnson J. L. and Dawson J. M. 1968 *Phys. Fluids* **11** 2448–2450
[441] van der Holst B., Beliën A. J. C. and Goedbloed J. P. 2000 *Phys. Plasmas* **7** 4208–4222
[442] Gorelenkov N. N., Berk H. L., Fredrickson E., Sharapov S. E. and JET EFDA Contributors 2007 *Phys. Lett. A* **370** 70–77
[443] Gorelenkov N. N. *et al* 2007 *Plasma Phys. Control. Fusion* **49** B371
[444] Falessi M. and et al 2020 *J. Plasma Phys.* **86** 84580501
[445] Chavdarovski I. and Zonca F. 2009 *Plasma Phys. Control. Fusion* **51** 115001
[446] Chavdarovski I. and Zonca F. 2014 *Phys. Plasmas* **21** 052506
[447] Rodrigues P. and Cella F. 2021 *Nucl. Fusion* **61** 096001
[448] Chen L. and Zonca F. 2017 *Phys. Plasmas* **24** 072511
[449] Cheng C. Z., Kramer G. J., Podesta M. and Nazikian R. 2019 *Phys. Plasmas* **26** 082508
[450] Kramer G. J., Cheng C. Z., Podestà M. and Nazikian R. 2020 *Plasma Phys. Control. Fusion* **62** 075012
[451] Gorelenkov N. N. and Berk H. L. 2021 *Phys. Plasmas* **28** 074701
[452] Zonca F., Chen L., Santoro R. A. and Dong J. Q. 1998 *Plasma Phys. Control. Fusion* **40** 2009
[453] Lauber P. *et al* 2009 *Plasma Phys. Control. Fusion* **51** 124009
[454] Lauber P. and Lu Z. 2018 *J. Phys. Conf. Ser.* **1125** 12015
[455] Li Y., Hu S., Zheng W. and Xiao Y. 2020 *Phys. Plasmas* **27** 062505
[456] Ma R., Qiu Z., Li Y. and Chen W. 2021 *Nucl. Fusion* **61** 036014
[457] Fesenyuk O. P., Kolesnichenko Y. I. and Yakovenko Y. V. 2013 *Phys. Plasmas* **20** 122503
[458] Van Zeeland M. A. *et al* 2019 *Nucl. Fusion* **59** 086028
[459] Gao Z., Peng L., Wang P., Dong J. and Sanuki H. 2009 *Nucl. Fusion* **49** 045014
[460] Curran D., Lauber P., Carthy P. J. M., da Graça S. and Igochine V. 2012 *Plasma Phys. Control. Fusion* **54** 055001
[461] Lauber P. *et al* 2019 *22nd Energ. Part. Phys. TG ITPA Meet. Rovaniemi, Finland*
[462] Fu G. Y. and Van Dam J. W. 1989 *Phys. Fluids B* **1** 1949–1952
[463] Fu G. Y. and Cheng C. Z. 1992 *Phys. Fluids B: Plasma Phys.* **4** 3722–3734
[464] Heidbrink W. W. 2002 *Phys. Plasmas* **9** 2113–2119
[465] Weller A. *et al* 2001 *Phys. Plasmas* **8** 931–956

123

[466] Tobias B. J. *et al* 2011 *Phys. Rev. Lett.* **106** 075003
[467] Classen I. *et al* 2011 *Plasma Phys. Control. Fusion* **53** 124018
[468] van Zeeland M. A. *et al* 2009 *Nucl. Fusion* **49** 065003
[469] Kolesnichenko Y., Tykhyy A. and White R. 2020 *Nucl. Fusion* **60** 112006
[470] Crocker N. A. *et al* 2011 *Plasma Phys. Control. Fusion* **53** 105001
[471] Tobias B. *et al* 2012 *Nucl. Fusion* **52** 103009
[472] Heidbrink W. W., Hansen E., Austin M. E., Kramer G. J. and Van Zeeland M. A. 2022 *Nucl. Fusion* **62** 066020
[473] Abel I., Breizman B., Sharapov S., Contributors J.-E. *et al* 2009 *Phys. Plasmas* **16** 102506
[474] Heidbrink W., Austin M., Spong D. A., Tobias B. and Van Zeeland M. 2013 *Phys. Plasmas* **20** 082504
[475] Du X. *et al* 2024 *Phys. Rev. Lett.* **132**(21) 215101
[476] Wang Z. *et al* 2013 *Phys. Rev. Lett.* **111** 145003
[477] Todo Y., Van Zeeland M. A., Bierwage A., Heidbrink W. W. and Austin M. E. 2015 *Nucl. Fusion* **55** 073020
[478] Heidbrink W. *et al* 2008 *Nucl. Fusion* **48** 084001
[479] Hu W. *et al* 2017 *Nucl. Fusion* **58** 096032
[480] Chen L. 2008 *Plasma Phys. Control. Fusion* **50** 124001
[481] Betti R. and Freidberg J. P. 1992 *Phys. Fluids B: Plasma Phys.* **4** 1465–1474
[482] Gorelenkov N. N. and Sharapov S. E. 1992 *Phys. Scr.* **45** 163
[483] Polevoi A. R. *et al* 2021 *Nucl. Fusion* **61** 076008
[484] Hasegawa A. and Chen L. 1976 *Phys. Fluids* **19** 1924–1934
[485] Breizman B. N. and Sharapov S. E. 1995 *Plasma Phys. Control. Fusion* **37** 1057–1074
[486] Jaun A., Fasoli A. and Heidbrink W. W. 1998 *Phys. Plasmas* **5** 2952–2955
[487] Fasoli A., Jaun A. and Testa D. 2000 *Phys. Lett. A* **265** 288–293
[488] Lauber P., Günter S. and Pinches S. D. 2005 *Phys. Plasmas* **12** 122501
[489] Lauber P. 2021 Kinetic Alfven waves in tokamak plasmas *Top. Plenary talk, 5th Asia Pacific Conf. Plasma Phys. 26. Sept. - 1, Oct.*
[490] Fasoli A. *et al* 1997 *Plasma Phys. Control. Fusion* **39** B287
[491] Tinguely R. *et al* 2021 *Nucl. Fusion* **61** 026003
[492] Fasoli A. *et al* 1995 *Phys. Rev. Lett.* **75** 645
[493] Testa D. *et al.* 2007 *Proc. 34th EPS Conf. Control. Fusion Plasma Phys.*
[494] Klein A., Testa D., Snipes J., Fasoli A. and Carfantan H. 2007
[495] Klein A. *et al.* 2008 *Proc. 35th EPS Conf. Control. Fusion Plasma Physics, Heraklion*
[496] Panis T. *et al* 2009 *11th IAEA TCM Energ. Part. Magn. Confin. Syst. Kyiv*
[497] Panis T. *et al* 2010 5th ITPA Topical Group Meeting on Energetic Particles, Seoul (Korea)
[498] Panis T. *et al* 2010 *Nucl. Fusion* **50** 084019
[499] Testa D. *et al* 2010 *Nucl. Fusion* **50** 084010
[500] Testa D. *et al* 2010 *Europhys. Lett.* **92** 50001
[501] Testa D. *et al* 2011 *Fusion Eng. Des.* **86** 381–392
[502] Panis T., Fasoli A., Testa D. and Contributors J.-E. 2012 *Nucl. Fusion* **52** 023013
[503] Panis T., Fasoli A., Testa D. and Contributors J.-E. 2012 *Nucl. Fusion* **52** 023014
[504] Testa D., Panis T., Blanchard P. and Fasoli A. 2012 *Nucl. Fusion* **52** 094006
[505] Panis T. *et al* 2010 *5th ITPA Top. Gr. Meet. Energ. Part. Seoul (Korea), 18-20 Oct. 2010.*
[506] Testa D. *et al* 2010 *EXW/P7-27, 23rd IAEA Fusion Energy Conf. Daejeon, Repub. Korea, 11-16 Oct.* 2010.
[507] Testa D. *et al* 2011 *Nucl. Fusion* **51** 043009
[508] Testa D. *et al* 2011 *JET, Contrib. Oral Pap. 12th IAEA TCM Energ. Part. Magn. Confin. Syst. Austin*
[509] Testa D., Blanchard P., Panis T. and Contributors J. 2015 *Nucl. Fusion* **55** 123010
[510] Lauber P. and al E. 2010 *23rd IAEA FEC, Daejeon, Repub. Korea, 11-16 Oct. 2010)* **THW/P7-08**
[511] Nabais F. *et al* 2018 *Nucl. Fusion* **58** 082007
[512] Popovich P., Cooper W. A. and Villard L. 2006 *Comput. Phys. Commun.* **175** 250–263
[513] Mellet N. and al E. 2011 *Comput. Phys. Commun.* **182** 570–589
[514] Lauber P., Günter S., Könies A. and Pinches S. 2007 *J. Comp. Phys.* **226** 447 – 465
[515] Woskov P. *et al.* 2012 *Proc. 54th Annu. Meet. APS Div. Plasma Phys.*
[516] Debelle T. *et al.* 2013 *11th Int. Symp. Fusion Nucl. Technol. (ISFNT), 16-20 Sept. 2013, Barcelona*
[517] Puglia P. *et al* 2015 *14th IAEA TCM Energ. Part. Magn. Confin. Syst.*
[518] Puglia P. *et al* 2016 *Nucl. Fusion* **56** 112020
[519] Puglia P. *et al* 2017 *Proc. 59th Annu. Meet. APS Div. Plasma Phys. 23-27 Oct. 2017, Milwaukee (USA).*
[520] Dowson S. *et al* 2019 *Fusion Eng. Des.* **146** 2639–2643
[521] Aslanyan V. *et al.* 2016 *Proc. 58th Annu. Meet. APS Div. Plasma Physics, Oct. 31st –November 4th 2016, San José (USA).*
[522] Aslanyan V. *et al.* 2017 *US-TTF Meet. April 2017*
[523] Fil N. *et al.* 2018 *Proc. 60th Annu. Meet. APS Div. Plasma Physics, 5-9 Novemb. 2018, Portl. (USA).*
[524] Aslanyan V. *et al* 2018 *Nucl. Fusion* **59** 026008
[525] Tinguely R. *et al* 2020 *28th IAEA Fusion Energy Conf. Nice (FR), 12-17 Oct. 2020*
[526] Tinguely R. A. *et al* 2020 *Plasma Phys. Control. Fusion* **62** 115002
[527] Tinguely R. A. *et al* 2022 *Nucl. Fusion* **62** 076001
[528] Fasoli A. *et al* 2010 *Plasma Phys. Control. Fusion* **52** 075015
[529] Snipes J. A., Gorelenkov N. N. and Sears J. A. 2006 *Nucl. Fusion* **46** 1036
[530] Vannini F. *et al* 2020 *Phys. Plasmas* **27** 042501
[531] Lu Z. X., Zonca F. and Cardinali A. 2012 *Phys. Plasmas* **19** 042104
[532] Falessi M. V., Carlevaro N., Fusco V., Vlad G. and Zonca F. 2019 *Phys. Plasmas* **26** 082502
[533] Könies A. *et al* 2018 *Nucl. Fusion* **58** 126027
[534] Wang H., Todo Y. and Kim C. C. *et al.* 2013 *Phys. Rev. Lett.* **110** 155006
[535] Lu Z. X., Wang X., Lauber P. and Zonca F. 2018 *Nucl. Fusion* **58** 082021
[536] Lu Z. X. *et al* 2019 *Plasma Phys. Control. Fusion* **61** 044005
[537] Meng G., Lauber P., Lu Z. X. and Wang X. 2020 *Nucl. Fusion* **60** 056017
[538] MENG G., LAUBER P., WANG X. and LU Z. 2022 *Plasma Science and Technology* **24** 025101
[539] Spong D. A. *et al* 2012 *Phys. Plasmas* **19** 082511
[540] Zhang W., Holod I., Lin Z. and Xiao Y. 2012 *Phys. Plasmas* **19** 022507
[541] Zhang H. S. *et al* 2013 *Phys. Plasmas* **20** 12510
[542] Kramer G. J., Tobias B. J., Turnbull A. and Bass E. M. 2019 *Nucl. Fusion* **59** 094001
[543] Fredrickson E. D. *et al* 2007 *Phys. of Plasmas* **14** 102510
[544] Taimourzadeh S. *et al* 2019 *Nucl. Fusion* **59** 066006
[545] Heidbrink W. *et al* 2013 *Nucl. Fusion* **53** 093006
[546] Van Zeeland M. A. *et al* 2021 *Nucl. Fusion* **61** 066028
[547] Van Zeeland M. *et al* 2024 *Nucl. Fusion* **64** 056033
[548] Deng W. *et al* 2012 *Nucl. Fusion* **52** 043006

124

[549] Dong G. *et al* 2017 *Phys. Plasmas* **24** 081205
[550] Wang H., Todo Y., Osakabe M., Ido T. and Suzuki Y. 2020 *Nucl. Fusion* **60** 112007
[551] Rizvi H., Ryu C. and Lin Z. 2016 *Nucl. Fusion* **56** 112016
[552] He H. *et al* 2018 *Nucl. Fusion* **58** 126023
[553] Schneller M. *et al* 2013 *Nucl. Fusion* **53** 123003
[554] Vannini F. *et al* 2021 *Phys. Plasmas* **28** 072504
[555] Fil N. *et al* 2021 *Phys. Plasmas* **28** 102511
[556] Polevoi A. R. *et al* 2002 *J. Plasma Fusion Res.* **5** 82–87
[557] Todo Y. and Bierwage A. 2014 *Plasma and Fusion Research* **9** 3403068
[558] Waltz R. E. and Bass E. M. 2014 *Nucl. Fusion* **54** 104006
[559] Lauber P. 2015 *Plasma Phys. Control. Fusion* **57** 054011
[560] Schneller M., Lauber P. and Briguglio S. 2015 *Plasma Phys. Control. Fusion* **58** 014019
[561] Rodrigues P. *et al* 2015 *Nucl. Fusion* **55** 083003
[562] Figueiredo A. *et al* 2016 *Nucl. Fusion* **56** 076007
[563] Fitzgerald M., Sharapov S. E., Rodrigues P. and Borba D. 2016 *Nucl. Fusion* **56** 112010
[564] Isaev M. Y., Medvedev S. Y. and Cooper W. A. 2017 *Plasma Phys. Reports* **43** 109–118
[565] Hayward-Schneider T., Lauber P., Bottino A. and Lu Z. X. 2021 *Nucl. Fusion* **61** 036045
[566] Vlad G., Briguglio S., Fogaccia G., Zonca F. and Schneider M. 2005 *Nucl. Fusion* **46** 1–16
[567] Gorelenkov N. *et al* 2008 *PPPL Report 4287*
[568] Lanti E. *et al* 2020 *Comp. Phys. Comm.* **251** 107072
[569] Pinches S. *et al* 1998 *Comp. Phys. Comm.* **111** 133–149
[570] Popa V.-A. *et al* 2023 *Nucl. Fusion* **63** 126008
[571] Lin Z. *et al* 2023 Prediction of energetic particle confinement in ITER operation scenarios *Proc. 29th IAEA Fusion Energy Conf. London, UK* pp IAEA–CN–316–2295 URL https://conferences.iaea.org/event/316/contributions/27785/
[572] Gorelenkov N., Duarte V., Gorelenkova M., Lin Z. and Pinches S. 2024 *Nucl. Fusion* **64** 076061
[573] McClements K. *et al* 2015 *Nucl. Fusion* **55** 043013
[574] Gorelenkov N. 2016 *New J. Phys.* **18** 105010–105013
[575] Appel L. C. *et al* 2008 *Plasma Phys. Control. Fusion* **50** 115011
[576] Gryaznevich M. *et al* 2008 *Nucl. Fusion* **48** 084003
[577] Fredrickson E. D., Gorelenkov N. N. and Menard J. 2004 *Phys. Plasmas* **11** 3653–3659
[578] Fredrickson E. D. *et al* 2006 *Phys. Plasmas* **13** 056109
[579] Heidbrink W. W., Fredrickson E. D., Gorelenkov N. N., Rhodes T. L. and Van Zeeland M. A. 2006 *Nucl. Fusion* **46** 324
[580] Ochoukov R. *et al* 2023 *Nucl. Fusion* **63** 046001
[581] Fredrickson E. *et al* 2014 *Nucl. Fusion* **54** 093007
[582] Mikhailovskii A. B. 1986 *Rev. Plasma Phys.* **9** 103–265
[583] Coppi B., Cowley S., Kulsrud R., Detragiache P. and Pegoraro F. 1986 *Phys. Fluids* **29** 4060–4070
[584] Gorelenkov N. N. and Cheng C. Z. 1995 *Nucl. Fusion* **35** 1743–1752
[585] Gorelenkov N. N., Cheng C. Z. and Fredrickson E. 2002 *Phys. Plasmas* **9** 3483–3488
[586] Smith H., Fülöp T., Lisak M. and Anderson D. 2003 *Phys. Plasmas* **10** 1437–1442
[587] Gorelenkov N. N. *et al* 2006 *Nucl. Fusion* **46** S933—-S941
[588] Fredrickson E. D. *et al* 2001 *Phys. Rev. Lett.* **87** 145001–145004
[589] Fredrickson E. D. *et al* 2013 *Phys. Plasmas* **20** 042112
[590] Gorelenkov N. N. *et al* 2003 *Nucl. Fusion* **43** 228–233
[591] Tang S. X. *et al* 2021 *Phys. Rev. Lett.* **126**(15) 155001
[592] Lestz J., Belova E. and Gorelenkov N. 2021 *Nucl. Fusion* **61** 086016
[593] Kolesnichenko Y., Fülöp T., Lisak M. and Anderson D. 1998 *Nucl. Fusion* **38** 1871
[594] Gorelenkov N. N. and Cheng C. Z. 1995 *Phys. Plasmas* **2** 1961–1971
[595] Goedbloed J. P. 1975 *Phys. Fluids* **18** 1258–1268
[596] de Chambrier A. *et al* 1982 *Plasma Physics* **24** 893
[597] Appert K., Gruber R., Troyon F. and Vaclavik J. 1982 *Plasma Phys.* **24** 1147–1159
[598] Kolesnichenko Y. I. *et al* 2005 *Phys. Rev. Lett.* **94** 165004
[599] Crocker N. *et al* 2013 *Nucl. Fusion* **53** 043017
[600] Fredrickson E. *et al* 2018 *Nucl. Fusion* **58** 082022
[601] Belova E., Crocker N. A., Lestz J. and Fredrickson E. 2022 *Nucl. Fusion* **62** 106016
[602] Lestz J. B., Gorelenkov N. N., Belova E. V., Tang S. X. and Crocker N. A. 2020 *Phys. Plasmas* **27** 022512
[603] Belova E. V., Fredrickson E. D., Lestz J. B., Crocker N. A. and Team N.-U. 2019 *Phys. Plasmas* **26** 092507
[604] Fredrickson E. D. and al E. 2017 *Phys. Rev. Lett.* **118** 265001
[605] Lestz J. B., Belova E. V. and Gorelenkov N. N. 2018 *Phys. Plasmas* **25** 042508
[606] Dendy R. O., Lashmore-Davies C. N., McClements K. G. and Cottrell G. A. 1994 *Phys. Plasmas* **1** 1918–1928
[607] Reman B. *et al* 2021 *Nucl. Fusion* **61** 066023
[608] Cottrell G. *et al* 1993 *Nucl. Fusion* **33** 1365
[609] Cottrell G. A. 2000 *Phys. Rev. Lett.* **84**(11) 2397–2400
[610] Stegmeir A., Conway G., Poli E. and Strumberger E. 2011 *Fusion Eng. Des.* **86** 2928–2942
[611] Crocker N. A. *et al* 2022 *Nucl. Fusion* **62** 026023
[612] Fredrickson E. *et al* 2021 *Nucl. Fusion* **61** 086007
[613] Chapman B. *et al* 2020 *Plasma Phys. Control. Fusion* **62** 055003
[614] Carbajal L., Del-Castillo-Negrete D., Spong D., Seal S. and Baylor L. 2017 *Phys. Plasmas* **24** 042512
[615] McClements K. *et al* 2018 *Nucl. Fusion* **58** 096020
[616] Herrmann M. C. and Fisch N. J. 1997 *Phys. Rev. Lett.* **79**(8) 1495–1498
[617] Zonca F. and Chen L. 2014 *Phys. Plasmas* **21** 072121
[618] Shi P. *et al* 2019 *Nucl. Fusion* **59** 066015
[619] Nguyen C. *et al* 2009 *Plasma Phys. Control. Fusion* **51** 095002
[620] Heidbrink W. *et al* 2021 *Nucl. Fusion* **61** 066031
[621] Heidbrink W. *et al* 2021 *Nucl. Fusion* **61** 106021
[622] Chena W. *et al* 2010 *Nucl. Fusion* **50** 084088
[623] Ma R., Qiu Z., Li Y. and Chen W. 2020 *Nucl. Fusion* **60** 056019
[624] Buratti P. *et al* 2005 *Nucl. Fusion* **45** 1446
[625] Chen W. *et al* 2012 *Plasma Fusion Res.* **7** 2402079
[626] Xu M. *et al* 2018 *Nucl. Fusion* **58** 124004
[627] Liu L. *et al* 2019 *Nucl. Fusion* **59** 126022
[628] Heidbrink W. *et al* 2020 *Nucl. Fusion* **61** 016029
[629] Wang X., Zonca F. and Chen L. 2010 *Plasma Phys. Control. Fusion* **52** 115005
[630] Ma R., Chavdarovski I., Ye G. and Wang X. 2014 *Phys. Plasmas* **21** 062120
[631] Ma R., Zonca F. and Chen L. 2015 *Phys. Plasmas* **22** 092501
[632] Zhang H. S. and al E. 2016 *Phys. Plasmas* **23** 042510
[633] Biancalani A., Bottino A., Lauber P., Mishchenko A. and Vannini F. 2020 *J. Plasma Phys.* **86** 825860301
[634] Hole M. J. *et al* 2013 *Plasma Phys. Control. Fusion* **55** 045004
[635] Lauber P. *et al* 2012 *Nucl. Fusion* **52** 094007
[636] Shi P.-W., Chen W. and Duan X.-R. 2021 *Chinese Phys. Lett.* **38** 035202
[637] Bierwage A. and Lauber P. 2017 *Nucl. Fusion* **57** 116063

[638] Gorelenkov N. N. *et al* 2009 *Phys. Plasmas* **16** 056107
[639] Ma R., Chen L., Zonca F., Li Y. and Qiu Z. 2022 *Plasma Phys. Control. Fusion* **64** 035019
[640] Liu Y., Lin Z., Zhang H. and Zhang W. 2017 *Nucl. Fusion* **57** 114001
[641] Choi G. J. *et al* 2021 *Nucl. Fusion* **61** 066007
[642] Hirose A. and Elia M. 1996 *Phys. Rev. Lett.* **76** 628–631
[643] Zonca F. *et al.* 1999 *Phys. Plasmas* **6** 1917–1924
[644] Zonca F. *et al* 2009 *Nucl. Fusion* **49** 085009
[645] Du X. D. *et al* 2021 *Phys. Rev. Lett.* **127**(2) 025001
[646] Berk H. L. and Zhou T. 2010 *Nucl. Fusion* **50** 035007
[647] Qiu Z., Zonca F. and Chen L. 2010 *Plasma Phys. Control. Fusion* **52** 095003
[648] Sasaki M., Itoh K. and Itoh S.-I. 2011 *Plasma Phys. Control. Fusion* **53** 085017
[649] Zarzoso D., Garbet X., Sarazin Y., Dumont R. and Grandgirard V. 2012 *Phys. Plasmas* **19** 022102
[650] Zarzoso D. *et al* 2014 *Nucl. Fusion* **54** 103006
[651] Girardo J.-B. *et al* 2014 *Phys. Plasmas* **21** 092507
[652] Qu Z. S., Hole M. J. and Fitzgerald M. 2016 *Phys. Rev. Lett.* **116** 095004
[653] Sasaki M. *et al* 2016 *Phys. Plasmas* **23** 102501
[654] Ren H. 2016 *Nucl. Fusion* **57** 16023
[655] Qu Z. S., Hole M. J. and Fitzgerald M. 2017 *Plasma Phys. Control. Fusion* **59** 055018
[656] Sasaki M. *et al* 2017 *Scientific Reports* **7**(1) 16767
[657] Ren H. and Wang H. 2018 *Nucl. Fusion* **58** 046005
[658] Nazikian R. *et al* 2008 *Phys. Rev. Lett.* **101**(18) 185001
[659] Fisher R. K. *et al* 2012 *Nucl. Fusion* **52** 123015
[660] Lin D. J. *et al* 2022 *Nucl. Fusion* **62** 112010
[661] Toi K. *et al* 2010 *Phys. Rev. Lett.* **105** 145003
[662] Ido T. *et al* 2011 *Nucl. Fusion* **51** 073046
[663] Ido T. *et al* 2015 *Nucl. Fusion* **55** 083024
[664] Chen W. *et al* 2013 *Nucl. Fusion* **53** 113010
[665] Chen W. *et al* 2013 *Phys. Lett. A* **377** 387–390
[666] Horváth L. *et al* 2016 *Nucl. Fusion* **56** 112003
[667] Lauber P. *et al* 2020 Energetic Particle Dynamics Induced by Off-axis Neutral Beam Injection on ASDEX-Upgrade, JT-60SA and ITER *28th IAEA Fusion Energy Conf. (FEC 2020)*
[668] Berk H. *et al* 2006 *Nucl. Fusion* **46** S888
[669] Boswell C. J. *et al* 2006 *Phys. Lett. A* **358** 154–158
[670] Zarzoso D. *et al* 2013 *Phys. Rev. Lett.* **110**(12) 125002
[671] Zarzoso D., Migliano P., Grandgirard V., Latu G. and Passeron C. 2017 *Nucl. Fusion* **57** 072011
[672] Zarzoso D. *et al* 2018 *Nucl. Fusion* **58** 106030
[673] Biancalani A., Bottino A., Lauber P. and Zarzoso D. 2014 *Nucl. Fusion* **54** 104004
[674] Novikau I. *et al* 2020 *Phys. Plasmas* **27** 042512
[675] Di Siena A. *et al* 2018 *Nucl. Fusion* **58** 106014
[676] Chen Y. *et al* 2020 *Chinese Physics Letters* **37** 095201
[677] Van Zeeland M. A. *et al* 2010 *Nucl. Fusion* **50** 084002
[678] Grandgirard V. *et al* 2016 *Comp. Phys. Comm.* **207** 35–68
[679] Jolliet S. *et al* 2007 *Comp. Phys. Comm.* **177** 409–425
[680] Jenko F., Dorland W., Kotschenreuther M. and Rogers B. N. 2000 *Phys. Plasmas* **7** 1904
[681] Heidbrink W. W. 1995 *Plasma Phys. Control. Fusion* **37** 937–949
[682] Gryaznevich M. P. and Sharapov S. E. 2004 *Plasma Phys. Control. Fusion* **46** S15
[683] Berk H. L., Breizman B. N. and Petviashvili N. V. 1997 *Phys. Lett. A* **6** 213
[684] Berk H. L., Breizman B. N., Candy J., Pekker M. and Petviashvili N. V. 1999 *Phys. Plasmas* **6** 3102
[685] Petviachvili N. 1999 *Coherent structures in nonlinear plasma dynamics* (The University of Texas at Austin)
[686] Vann R. G. L., Dendy R. O., Rowlands G., Arber T. D. and D'Ambrumenil N. 2003 *Phys. Plasmas* **10** 623–630

[687] Pinches S. D., Berk H. L., Gryaznevich M. P., Sharapov S. E. and Contributors J.-E. *et al.* 2004 *Plasma Phys. Control. Fusion* **46** S47
[688] Lvovskiy A. *et al* 2019 *Nucl. Fusion* **59** 124004
[689] Maslovsky D., Levitt B. and Mauel M. E. 2003 *Phys. Rev. Lett.* **90** 185001
[690] Maslovsky D., Levitt B. and Mauel M. E. 2003 *Phys. Plasmas* **10** 1549–1555
[691] Heidbrink W. W. *et al* 2006 *Plasma Phys. Control. Fusion* **48** 1347
[692] Fredrickson E. *et al* 2014 *Nucl. Fusion* **55** 013012
[693] Podesta M. *et al* 2012 *Nucl. Fusion* **52** 094001
[694] Duarte V. N. *et al* 2017 *Phys. Plasmas* **24** 122508
[695] Duarte V. N. *et al* 2018 *Nucl. Fusion* **58** 082013
[696] Gryaznevich M. P. and Sharapov S. E. 2006 *Nucl. Fusion* **46** S942
[697] Podestà M., Fredrickson E. D. and Gorelenkova M. 2018 *Nucl. Fusion* **58** 082023
[698] Fredrickson E. D. *et al* 2016 *26th IAEA Fusion Energy Conf. (Oct. 17-21, 2016), Kyoto, Japan* EX/P4–41
[699] Poloskei P. *et al.* 2017 *P5.179 44th EPS Conf. Plasma Phys. 26 - 30 June 2017*
[700] Lauber P. *et al* 2018 *EX/1-1 Proc. 27th IAEA FEC, 22-27 Oct. 2018, Gandhinagar Gujarat, India.*
[701] Vlad G. *et al* 2021 *Nucl. Fusion* **61** 116026
[702] Rettino B. *et al* 2022 *Nucl. Fusion* **62** 076027
[703] Qu Z. S., Fitzgerald M. and Hole M. J. 2014 *Plasma Phys. Control. Fusion* **56** 075007
[704] Hole M. J., von Nessi G., Fitzgerald M., McClements K. G. and Svensson J. 2011 *Plasma Phys. Control. Fusion* **53** 074021
[705] Zwingmann W., Eriksson L.-G. and Stubberfield P. 2001 *Plasma Phys. Control. Fusion* **43** 1441
[706] Salewski M. *et al* 2018 *Nucl. Fusion* **58** 036017
[707] Hole M. J. *et al* 2020 *Nucl. Fusion* **60** 112010
[708] Moseev D. and Salewski M. 2019 *Phys. Plasmas* **26** 020901
[709] Clemente R. A. 1994 *Plasma Phys. Control. Fusion* **36** 707
[710] Fitzgerald M., Hole M. J. and Qu Z. S. 2015 *Plasma Phys. Control. Fusion* **57** 025018
[711] Gorelenkov N. and Zakharov L. 2018 *Nucl. Fusion* **58** 082031
[712] Kruskal M. D. and Oberman C. R. 1958 *Phys. Fluids* **1** 275–280
[713] Qu Z. S., Hole M. J. and Fitzgerald M. 2015 *Plasma Phys. Control. Fusion* **57** 095005
[714] Chew G. F., Goldberger M. L. and Low F. E. 1956 *Proc. R. Soc. London. Ser. A. Math. Phys. Sci.* **236** 112–118
[715] Bernstein I. B., Frieman E. A., Kruskal M. D., Kulsrud R. M. and Chandrasekhar S. 1958 *Proc. Royal Soc. London A. Math. Phys. Sci.* **244** 17–40
[716] Rosenbluth M. N. and Rostoker N. 1959 *Phys. Fluids* **2** 23–30
[717] Chust T. and Belmont G. 2006 *Phys. Plasmas* **13** 1–21
[718] Layden B., Qu Z. S., Fitzgerald M. and Hole M. J. 2016 *Nucl. Fusion* **56** 112017
[719] Brunetti D., Ham C. J., Graves J. P., Wahlberg C. and Cooper W. A. 2020 *Plasma Phys. Control. Fusion* **62** 115005
[720] Evangelias A. and Throumoulopoulos G. N. 2016 *Plasma Phys. Control. Fusion* **58** 045022
[721] Chirikov B. V. 1979 *Phys. Rep.* **52** 263–379
[722] McGuire K. *et al* 1983 *Phys. Rev. Lett.* **50** 891–895
[723] Kiptily V. *et al* 2018 *Nucl. Fusion* **58** 014003
[724] Gude A., Günter S. and Sesnic S. 1999 *Nucl. Fusion* **39** 127
[725] Nave M. *et al* 2003 *Nucl. Fusion* **43** 179
[726] Arcis N. and Sharapov S. E. 2008 *Phys. Lett. A* **372**

5807–5810

[727] Shi T. *et al* 2013 *Plasma Phys. Control. Fusion* **55** 055007
[728] Igochine V. *et al* 2019 *Nucl. Fusion* **59** 066038
[729] Okabayashi M. *et al* 2011 *Phys. Plasmas* **18** 056112
[730] Joffrin E. 2007 *Plasma Phys. Control. Fusion* **49** B629
[731] Chen L., White R. B. and Rosenbluth M. N. 1984 *Phys. Rev. Lett.* **52** 1122–1125
[732] Ödblom A., Breizman B. N., Sharapov S. E., Hender T. C. and Pastukhov V. P. 2002 *Phys. Plasmas* **9** 155–166
[733] Coppi B. and Porcelli F. 1986 *Phys. Rev. Lett.* **57** 2272–2275
[734] Coppi B., Migliuolo S. and Porcelli F. 1988 *Phys. fluids* **31** 1630–1648
[735] Coppi B. and Porcelli F. 1988 *Fusion Technol.* **13** 447–452
[736] Todo Y., Van Zeeland M. A., Bierwage A. and Heidbrink W. W. 2014 *Nucl. Fusion* **54** 104012
[737] Wang F., Fu G. and Shen W. 2016 *Nucl. Fusion* **57** 016034
[738] Shen W. *et al* 2017 *Nucl. Fusion* **57** 116035
[739] Brochard G. *et al* 2024 *Phys. Rev. Lett.* **132**(7) 075101
[740] Hao G., Wang A., Liu Y. and Qiu X. 2011 *Phys. Rev. Lett.* **107** 015001
[741] Hao G. *et al* 2016 *Phys. Plasmas* **23** 062105
[742] Matsunaga G. *et al* 2009 *Phys. Rev. Lett.* **103** 045001
[743] Heidbrink W. W. *et al* 2011 *Plasma Phys. Control. Fusion* **53** 085028
[744] Beiersdorfer P., Kaita R. and Goldston R. 1984 *Nucl. Fusion* **24** 487
[745] Strachan J. *et al* 1985 *Nucl. Fusion* **25** 863
[746] Li H., Todo Y., Wang H., Idouakass M. and Wang J. 2021 *Nucl. Fusion* **62** 026013
[747] Li H., Todo Y., Wang H., Wang J. and Idouakass M. 2023 *Nucl. Fusion* **63** 086012
[748] Hao G. *et al* 2013 *Phys. Plasmas* **20** 062502
[749] Matsunaga G. *et al* 2013 *Nucl. Fusion* **53** 123022
[750] Matsunaga G. *et al* 2013 *Nucl. Fusion* **53** 073046
[751] Frieman E. A. and Chen L. 1982 *Phys. Fluids* **25** 502–508
[752] Sugama H. 2000 *Phys. Plasmas* **7** 466–480
[753] Brizard A. J. and Hahm T. S. 2007 *Reviews of Modern Physics* **79** 421–468
[754] Grad H. 1969 *Phys. Today* **22 (12)** 34
[755] Hasegawa A. and Chen L. 1975 *Phys. Rev. Lett.* **35** 370
[756] Chen L. and Zonca F. 2011 *Europhys. Lett.* **96** 35001
[757] Chen L. and Zonca F. 2013 *Phys. Plasmas* **20** 055402
[758] Chen L., Zonca F. and Lin Y. 2021 *Rev. Mod. Plasma Phys.* **5** 1
[759] Zonca F. and Chen L. 2014 *Phys. Plasmas* **21** 072120
[760] Zonca F., Chen L., Falessi M. V. and Qiu Z. 2021 *J. Phys. Conf. Ser.* **1785** 12005
[761] Zonca F. *et al* 2015 *New J. Phys.* **17** 13052
[762] Falessi M. V. and Zonca F. 2019 *Phys. Plasmas* **26** 022305
[763] Falessi M. V., Chen L., Qiu Z. and Zonca F. 2023 *New J. Phys.* **25** 123035
[764] Alfvén H. 1942 *Nature* **150** 405–406
[765] Walén C. 1944 *Arkiv för Matematik, Astronomi och Fysik* **30A** 1
[766] Alfvén H. 1950 *Cosmical Electrodynamics* (Oxford, UK: Clarendon)
[767] Zonca F., Romanelli F., Vlad G. and Kar C. 1995 *Phys. Rev. Lett.* **74** 698
[768] Chen L., Zonca F., Santoro R. A. and Hu G. 1998 *Plasma Phys. Control. Fusion* **40** 1823
[769] Chen L. and Zonca F. 2012 *Phys. Rev. Lett.* **109** 145002
[770] Hahm T. S. and Chen L. 1995 *Phys. Rev. Lett.* **74** 266
[771] Qiu Z., Chen L. and Zonca F. 2019 *Nucl. Fusion* **59**

066024

[772] Cheng C. Z., Chen L. and Chance M. S. 1985 *Annals of Physics* **161** 21–47
[773] Qiu Z., Chen L. and Zonca F. 2016 *Nucl. Fusion* **56** 106013
[774] Qiu Z., Chen L., Zonca F. and Ma R. 2020 *Plasma Phys. Control. Fusion* **62** 105012
[775] Wei S., Wang T., Chen N. and Qiu Z. 2021 *J. Plasma Phys.* **87** 905870505
[776] Chen L., Lin Z. and White R. B. 2000 *Phys. Plasmas* **7** 3129
[777] Diamond P. H., Itoh S.-I., Itoh K. and Hahm T. S. 2005 *Plasma Phys. Control. Fusion* **47** R35–R161
[778] Zonca F. *et al* 2015 *Plasma Phys. Control. Fusion* **57** 014024
[779] Rosenbluth M. N. and Hinton F. L. 1998 *Phys. Rev. Lett.* **80** 724
[780] Heidbrink W. *et al* 2007 *Phys. Rev. Lett.* **99** 245002
[781] Qiu Z., Chen L. and Zonca F. 2017 *Nucl. Fusion* **57** 056017
[782] Qiu Z., Chen L. and Zonca F. 2016 *Phys. Plasmas* **23** 090702
[783] Todo Y., Berk H. L. and Breizman B. N. 2010 *Nucl. Fusion* **50** 084016
[784] Biancalani A. *et al* 2021 *Plasma Phys. Control. Fusion* **63** 065009
[785] Zonca F., Chen L. and Santoro R. A. 1996 *Plasma Phys. Control. Fusion* **38** 2011–2028
[786] Qiu Z., Chen L. and Zonca F. 2013 *Europhys. Lett.* **101** 35001
[787] Qiu Z., Chen L., Zonca F. and Chen W. 2018 *Phys. Rev. Lett.* **120** 135001
[788] Qiu Z., Chen L., Zonca F. and Chen W. 2019 *Nucl. Fusion* **59** 066031
[789] Sagdeev R. Z. and Galeev A. A. 1969 *Nonlinear Plasma Theory* (W. A. Benjamin Inc.)
[790] Wang T. *et al* 2018 *Phys. Plasmas* **25** 062509
[791] Chen L. 1999 *J. Geophys. Res.* **104** 2421–2428
[792] Hahm T. S. 2015 *Plasma Sci. Technol.* **17** 534–538
[793] Lauber P. *et al* 2024 *Nucl. Fusion* **64** 096010
[794] Meng G., Lauber P., Lu Z., Bergmann A. and Schneider M. 2024 *Nucl. Fusion* **64** 096009
[795] Brizard A. J. 2004 *Phys. Plasmas* **11** 4429–4438
[796] Abel I. G., Barnes M., Cowley S. C., Dorland W. and Schekochihin A. A. 2008 *Phys. Plasmas* **15** 122509
[797] Burby J. W., Brizard A. J. and Qin H. 2015 *Phys. Plasmas* **22** 100707
[798] Sugama H. 2017 *Rev. Mod. Plasma Phys.* **1** 9
[799] Bottino A. *et al* 2022 *J. Phys.: Conf. Ser.* **2397** 012019
[800] Zonca F., Tao X. and Chen L. 2021 *Rev. Mod. Plasma Phys.* **5** 8
[801] Vedenov A. A., Velikhov E. P. and Sagdeev R. Z. 1961 *Nucl. Fusion* **1** 82–95
[802] Drummond W. E. and Pines D. 1962 *Nucl. Fusion Suppl. Pt.* **3** 1049
[803] Galeev A. A., Karpman V. I. and Sagdeev R. Z. 1965 *Sov. Phys. Dokl.* **9** 681
[804] Al'tshul' L. M. and Karpman V. I. 1966 *Sov. Phys. JETP* **22** 361
[805] Wang X. *et al* 2022 *Phys. Plasmas* **29** 032512
[806] Wang X. *et al* 2023 *Plasma Phys. Control. Fusion* **65** 074001
[807] Vlad G. *et al* 2016 *New J. Phys.* **18** 105004
[808] Brochard G. *et al* 2020 *Nucl. Fusion* **60** 126019
[809] White R. B. *et al* 1983 *Phys. Fluids* **26** 2958–2965
[810] Brochard G. *et al* 2024 Saturation of fishbone instability through zonal flows driven by energetic particle transport in tokamak plasmas (*Preprint* 2402.03797) URL https://arxiv.org/abs/2402.03797
[811] Lee W. W. 1983 *Phys. Fluids* **26** 556–562

[812] Mishchenko A., Cole M., Kleiber R. and Könies A. 2014 *Phys. Plasmas* **21** 052113

[813] Cole M. D. J. *et al* 2017 *Phys. Plasmas* **24** 022508

[814] Cole M. D. J., Borchardt M., Kleiber R., Könies A. and Mishchenko A. 2018 *Phys. Plasmas* **25** 012301

[815] Di Siena A., Görler T., Doerk H., Poli E. and Bilato R. 2018 *Nucl. Fusion* **58** 054002

[816] Hatzky R. *et al* 2019 *J. Plasma Phys.* **85** 905850112

[817] Mishchenko A., Könies A., Kleiber R. and Cole M. 2014 *Phys. Plasmas* **21** 092110

[818] Kleiber R., Hatzky R., Könies A., Mishchenko A. and Sonnendrücker E. 2016 *Phys. Plasmas* **23** 032501

[819] Slaby C., Könies A., Kleiber R. and Garcia-Regaña J. M. 2018 *Nucl. Fusion* **58** 082018

[820] Gorelenkov N. N., Duarte V. N., Podesta M. and Berk H. L. 2018 *Nucl. Fusion* **58** 082016

[821] O'Neil T. M., Winfrey J. H. and Malmberg J. H. 1971 *The Physics of Fluids* **14** 1204–1212

[822] Liu P. *et al* 2022 *Phys. Rev. Lett.* **128**(18) 185001

[823] Chen Y., Fu G. Y., Collins C., Taimourzadeh S. and Parker S. E. 2018 *Phys. Plasmas* **25** 032304

[824] Lin Z., Hahm T. S., Lee W. W., Tang W. M. and White R. B. 1998 *Science* **281** 1835–1837

[825] Dimits A. M. and al E. 2000 *Phys. Plasmas* **7** 969–983

[826] Lin Z., Chen L. and Zonca F. 2005 *Phys. Plasmas* **12** 056125

[827] Liu P. *et al* 2024 *Nucl. Fusion* **64** 076007

[828] Spong D. A., Carreras B. A. and Hedrick C. L. 1994 *Phys. Plasmas* **1** 1503–1510

[829] Spong D. *et al* 2021 *Nucl. Fusion* **61** 116061

[830] Bass E. M. and Waltz R. E. 2010 *Phys. Plasmas* **17** 112319

[831] Liu P. *et al* 2023 *Rev. Mod. Plasma Phys.* **7** 15

[832] Vlad G. *et al* 2018 *Nucl. Fusion* **58** 082020

[833] Hauff T., Pueschel M., Dannert T. and Jenko F. 2009 *Phys. Rev. Lett.* **102**

[834] Zhang H. S. *et al* 2010 *Phys. Plasmas* **17** 112505

[835] Albergante M. *et al* 2011 *Plasma Phys. Control. Fusion* **53** 054002

[836] Zhang W., Lin Z. and Chen L. 2008 *Phys. Rev. Lett.* **101** 095001

[837] Gorelenkov N. and Duarte V. 2021 *Phys. Lett. A* **386** 126944

[838] Lang J. and Fu G.-Y. 2011 *Phys. Plasmas* **18** 055902

[839] Bierwage A. *et al* 2018 *Nature Communications* **9** 1–11

[840] Zhang H. S., Lin Z. and Holod I. 2012 *Phys. Rev. Lett.* **109**(2) 025001

[841] Bierwage A., White R. B. and Duarte V. N. 2021 *Plasma and Fusion Research* **16** 1403087

[842] Park W. *et al* 1992 *Phys. Fluids B: Plasma Phys.* **4** 2033–2037

[843] Park W. *et al* 1999 *Phys. Plasmas* **6** 1796–1803

[844] Spong D. A., Carreras B. A. and Hedrick C. L. 1992 *Phys. Fluids B: Plasma Phys.* **4** 3316–3328

[845] Briguglio S., Vlad G., Zonca F. and Kar C. 1995 *Phys. Plasmas* **2** 3711–3723

[846] Todo Y. and Sato T. 1998 *Phys. Plasmas* **5** 1321–1327

[847] Kim C. C. and Team N. 2008 *Phys. Plasmas* **15** 072507

[848] Vlad G. *et al* 2013 *Nucl. Fusion* **53** 083008

[849] Briguglio S. *et al* 2017 *Nucl. Fusion* **57** 072001

[850] Belova E. V. *et al* 2017 *Phys. Plasmas* **24** 042505

[851] Du X. D. *et al* 2021 *Phys. Rev. Lett.* **127**(23) 235002

[852] Chen Y., White R. B., Fu G.-Y. and Nazikian R. 1999 *Phys. Plasmas* **6** 226–237

[853] Chen Y. *et al* 2013 *Phys. Plasmas* **20** 12109

[854] Mishchenko A. *et al* 2017 *Phys. Plasmas* **24** 081206

[855] Bass E. M. and Waltz R. E. 2020 *Nucl. Fusion* **60** 016032

[856] Van Zeeland M. A. *et al* 2011 *Phys. Plasmas* **18** 056114

[857] Van Zeeland M. A. *et al* 2012 *Nucl. Fusion* **52** 094023

[858] White R. B., Gorelenkov N., Heidbrink W. W. and Van Zeeland M. A. 2010 *Plasma Phys. Control. Fusion* **52** 045012

[859] White R. B., Gorelenkov N., Heidbrink W. W. and Van Zeeland M. A. 2010 *Phys. Plasmas* **17** 056107

[860] Collins C. S. *et al* 2016 *Phys. Rev. Lett.* **116** 095001

[861] Heidbrink W. W. *et al* 2017 *Phys. Plasmas* **24** 056109

[862] Collins C. *et al* 2017 *Nucl. Fusion* **57** 086005

[863] Todo Y., Van Zeeland M. A. and Heidbrink W. W. 2016 *Nucl. Fusion* **56** 112008

[864] Todo Y. 2019 *Nucl. Fusion* **59** 096048

[865] Todo Y., Berk H. L. and Breizman B. N. 2003 *Phys. Plasmas* **10** 2888

[866] Shinohara K. *et al* 2001 *Nucl. Fusion* **41** 603

[867] Fredrickson E. D. *et al* 2009 *Phys. Plasmas* **16** 122505

[868] Podesta M. *et al* 2009 *Phys. Plasmas* **16** 056104

[869] Ishikawa M. *et al* 2006 *Nucl. Fusion* **46** S898

[870] Heidbrink W. *et al* 2016 *Nucl. Fusion* **56** 056005

[871] Briguglio S. *et al* 2007 *Phys. Plasmas* **14** 055904

[872] Bierwage A., Todo Y., Aiba N. and Shinohara K. 2014 *Nucl. Fusion* **54** 104001

[873] Liu D. *et al* 2015 *Phys. Plasmas* **22** 042509

[874] Varela J., Spong D. A. and Garcia L. 2019 *Nucl. Fusion* **59** 076036

[875] Briguglio S., Zonca F. and Vlad G. 1998 *Phys. Plasmas* **5** 3287–3301

[876] Wang X. *et al* 2011 *Phys. Plasmas* **18** 052504

[877] Briguglio S. *et al* 2014 *Phys. Plasmas* **21** 112301

[878] Carlevaro N., Falessi M., Montani G. and Zonca F. 2015 *J. Plasma Phys.* **81** 495810515

[879] Carlevaro N., Montani G. and Falessi M. V. 2020 *J. Plasma Phys.* **86** 845860401

[880] Wang X., Briguglio S., Lauber P., Fusco V. and Zonca F. 2016 *Phys. Plasmas* **23** 012514

[881] Wang X. and Briguglio S. 2016 *New J. Phys.* **18** 085009

[882] Hammett G. W. and Perkins F. W. 1990 *Phys. Rev. Lett.* **64** 3019

[883] Varela J., Spong D. and Garcia L. 2017 *Nucl. Fusion* **57** 046018

[884] Bao J. *et al* 2023 *Nucl. Fusion* **63** 076021

[885] Sheng H., Waltz R. E. and and G. M. Staebler 2017 *Phys. Plasmas* **24** 072305

[886] Bass E. M. and Waltz R. E. 2017 *Phys. Plasmas* **24** 122302

[887] Staebler G. M., Kinsey J. E. and Waltz R. E. 2005 *Phys. Plasmas* **12** 102508

[888] Varela J. *et al* 2024 *Frontiers in Physics - Fusion Plasma Physics, accepted for publication*

[889] Varela J. *et al* 2023 *Plasma Phys. Control. Fusion* 125004

[890] Varela J. *et al* 2022 *Nucl. Fusion* 126020

[891] Poli F. M. 2018 *Phys. Plasmas* **25** 055602

[892] Pereverzev G. V. and Yushmanov P. N. 2002 *IPP Report 5/98*

[893] Coster D. P. *et al* 2010 *IEEE Trans. Plasma Sci.* **38** 2085–2092

[894] Goldston R. *et al* 1981 *J. Comp. Phys.* **43** 61–78

[895] Pankin A., McCune D., Andre R., Bateman G. and Kritz A. 2004 *Comput. Phys. Commun.* **159** 157–184

[896] Podesta M., Gorelenkova M. and White R. B. 2014 *Plasma Phys. Control. Fusion* **56** 055003

[897] Podestà M., Gorelenkova M., Gorelenkov N. N. and White R. B. 2017 *Plasma Phys. Control. Fusion* **59** 095008

[898] White R. B. t. and Chance M. S. 1984 *Phys. fluids* **27** 2455–2467

[899] Cheng C. 1992 *Phys. Rep.* **211** 1–51

[900] Kang J. *et al* 2020 *Nucl. Fusion* **60** 126023

[901] Yang J., Podestà M. and Fredrickson E. D. 2021 *Plasma Phys. Control. Fusion* **63** 045003

[902] Heidbrink W. W., Liu D., Luo Y., Ruskov E. and Geiger B. 2011 *Comm. Comp. Phys.* **10** 716–741

[903] Geiger B. *et al* 2020 *Plasma Phys. Control. Fusion* **62** 105008

[904] Podesta M. *et al* 2022 *Nucl. Fusion* **62** 126047

[905] Teplukhina A. A. *et al* 2023 *Nucl. Fusion* **65** 035023

[906] Berk H. L., Breizman B. N., Fitzpatrick J. and Wong H. V. 1995 *Nucl. Fusion* **35** 1661

[907] Duarte V. N. *et al* 2017 *Nucl. Fusion* **57** 054001

[908] Duarte V. N. 2017 *Quasilinear and nonlinear dynamics of energetic-ion-driven Alfvènic eigenmodes* Ph.D. thesis Universidade de São Paulo

[909] Duarte V. N. 2020 *APS Division of Plasma Physics Meeting*

[910] Duarte V. N. and Gorelenkov N. N. 2019 *Nucl. Fusion* **59** 044003

[911] Lestz J. B. and Duarte V. N. 2021 *Phys. Plasmas* **28** 062102

[912] Duarte V. N., Gorelenkov N. N., White R. B. and Berk H. L. 2019 *Phys. Plasmas* **26** 120701

[913] Duarte V., Lestz J., Gorelenkov N. and White R. 2023 *Phys. Rev. Lett.* **130** 105101

[914] Berk H. L. *et al* 1996 *Phys. Plasmas* **3** 1827–1838

[915] Lilley M. K., Breizman B. N. and Sharapov S. E. 2010 *Phys. Plasmas* **17** 092305

[916] White R. B., Duarte V. N., Gorelenkov N. N. and Meng G. 2019 *Phys. Plasmas* **26** 032508

[917] Gorelenkov N. N., Duarte V. N., Collins C. S., Podestà M. and White R. B. 2019 *Phys. Plasmas* **26** 072507

[918] Waltz R. E., Bass E. M., Heidbrink W. W. and Van Zeeland M. A. 2015 *Nucl. Fusion* **55** 123012

[919] Gorelenkov N. N. *et al* 2016 *Nucl. Fusion* **56** 112015

[920] Candy J. and Waltz R. 2003 *J. Comp. Phys.* **186** 545–581

[921] Zou Y. *et al* 2019 *Nucl. Fusion* **59** 066005

[922] Weiland M. *et al* 2018 *Nucl. Fusion* **58** 082032

[923] Weiland M. *et al* 2023 *Nucl. Fusion* **63** 066013

[924] Weiland M. *et al* 2024 *Nucl. Fusion* **64** 056002

[925] Polevoi A., Ivanov A. and S.Yu. Medvedev e. a. 2020 *Nucl. Fusion* **60** 096024

[926] Spong D. A. *et al* 2023 *IAEA 2023 Fusion Energy Conference* IAEA–CN–316–1775

[927] Bass E. 2023 *IAEA 2023 Fusion Energy Conference* IAEA–CN–316–2327

[928] Bhatnagar P. L., Gross E. P. and Krook M. 1954 *Phys. Rev.* **94**(3) 511–525

[929] Berk H. L., Horton Jr W., Rosenbluth M. N. and Rutherford P. H. 1975 *Nucl. Fusion* **15** 819

[930] Breizman B. N. *et al* 1997 *Phys. Plasmas* **4** 1559

[931] Lilley M. K., Breizman B. N. and Sharapov S. E. 2009 *Phys. Rev. Lett.* **102** 195003

[932] Fasoli A. *et al* 1998 *Phys. Rev. Lett.* **81** 5564–5567

[933] Heeter R. F., Fasoli A. F. and Sharapov S. E. 2000 *Phys. Rev. Lett.* **85** 3177–3180

[934] Berk H. L., Breizman B. N. and Pekker M. 1996 *Phys. Rev. Lett.* **76** 1256–1259

[935] Breizman B. N. 2010 *Nucl. Fusion* **50** 084014

[936] Bernstein I. B., Greene J. M. and Kruskal M. D. 1957 *Phys. Rev.* **108** 546

[937] Zonca F., Briguglio S., Chen L., Fogaccia G. and Vlad G. 2005 *Nucl. Fusion* **45** 477

[938] Berk H. L., Breizman B. N. and Ye H. 1992 *Phys. Rev. Lett.* **68** 3563–3566

[939] Shinohara K. *et al* 2007 *Nucl. Fusion* **47** 997

[940] Äkäslompolo S. *et al* 2015 *Fusion Eng. Des.* **98-99** 1039–1043

[941] Kurki-Suonio T. *et al* 2016 *Nucl. Fusion* **56** 112024

[942] Goloborod'ko V. Y., Kolesnichenko Y. I. and Yavorskij V. A. 1987 *Phys. Scr.* **1987** 46

[943] Kirk A. *et al* 2015 *Nucl. Fusion* **55** 043011

[944] Willensdorfer M. *et al* (the ASDEX Upgrade Team) 2017 *Phys. Rev. Lett.* **119**(8) 085002

[945] Paz-Soldan C. *et al* 2015 *Phys. Rev. Lett.* **114**(10) 105001

[946] Spong D. A. 2015 *Phys. Plasmas* **22** 055602

[947] Tobita K. *et al* 1995 *Nucl. Fusion* **35** 1585

[948] Putvinski S. 1998 *Nucl. Fusion* **38** 1275

[949] Hawryluk R. J. *et al* 1998 *Phys. Plasmas* **5** 1577–1589

[950] Zweben S. *et al* 1998 *Nucl. Fusion* **38** 739

[951] Ruskov E. *et al* 1999 *Phys. Rev. Lett.* **82**(5) 924–927

[952] Kawashima H. *et al* 2001 *Nucl. Fusion* **41** 257

[953] Sato M. *et al* 2002 *Nucl. Fusion* **42** 1008

[954] Assas S., Eriksson L.-G., Nguyen F. and Basiuk V. 2003 *Plasma Phys. Control. Fusion* **45** 145

[955] Basiuk V. *et al* 2003 *Nucl. Fusion* **44** 181

[956] Tobita K. *et al* 1997 *Nucl. Fusion* **37** 1583

[957] Tobita K., Ozeki T. and Nakamura Y. 2004 *Plasma Phys. Control. Fusion* **46** S95

[958] Liu S., Liu X., Ma X., Liu C. and Pu Y. 2013 *Fusion Eng. Des.* **88** 675–678

[959] Kramer G. *et al* 2013 *Nucl. Fusion* **53** 123018

[960] Schaffer M. *et al* 2011 *Nucl. Fusion* **51** 103028

[961] Kramer G. *et al* 2011 *Nucl. Fusion* **51** 103029

[962] Shinohara K. *et al* 2009 *Fusion Eng. Des.* **84** 24–32

[963] Van Zeeland M. A. *et al* 2015 *Nucl. Fusion* **55** 073028

[964] Garcia-Munoz M. *et al* 2013 *Plasma Phys. Control. Fusion* **55** 124014

[965] Sanchis L. *et al* 2018 *Plasma Phys. Contol. Fusion* **61** 014038

[966] Galdon-Quiroga J. *et al* 2022 *Nucl. Fusion* **62** 096004

[967] Gage K. *et al* 2023 *Nucl. Fusion* **63** 036002

[968] Chen X. *et al* 2014 *Rev. Sci. Instrum.* **85** 11E701

[969] Chen X. *et al* 2013 *Nucl. Fusion* **53** 123019

[970] Bortolon A. *et al* 2013 *Phys. Rev. Lett.* **110**(26) 265008

[971] Gonzalez-Martin J. *et al* 2023 *Phys. Rev. Lett.* **130**(3) 035101

[972] Heidbrink W. *et al* 2015 *Nucl. Fusion* **55** 083023

[973] Hirshman S. and Whitson J. 1983 *Phys. Fluids* **26** 3553

[974] Chapman I. T. *et al* 2014 *Nucl. Fusion* **54** 083006

[975] Lazerson S. A. and Chapman I. T. 2013 *Plasma Phys. Control. Fusion* **55** 084004

[976] Lazerson S. A. 2014 *Plasma Phys. Control. Fusion* **56** 095006

[977] Schmitt J. C., Bialek J., Lazerson S. A. and Majeski R. 2014 *Rev. Sci. Instrum.* **85** 11E817

[978] Lazerson S. 2015 *Nucl. Fusion* **55** 023009

[979] King J. D. *et al* 2015 *Phys. Plasmas* **22** 072501

[980] Ham C. *et al* 2016 *Nucl. Fusion* **56** 086005

[981] Ham C. J., Chapman I. T., Kirk A. and Saarelma S. 2014 *Phys. Plasmas* **21** 102501

[982] Wingen A. *et al* 2016 *Nucl. Fusion* **57** 016013

[983] Willensdorfer M. *et al* 2017 *Nucl. Fusion* **57** 116047

[984] Kleiner A., Graves J. P., Cooper W. A., Nicolas T. and Wahlberg C. 2018 *Nucl. Fusion* **58** 074001

[985] Hindenlang F. and Maj O. 2020 GVEC prototype, (internal code documentation) Tech. rep. Max-Planck-Institute for Plasmaphysics

[986] Dudt D. W. and Kolemen E. 2020 *Phys. Plasmas* **27** 102513

[987] Strumberger E., Günter S., Merkel P., Schwarz E. and Tichmann C. 2010 *Nucl. Fusion* **50** 025008

[988] Cooper W., Hirshman S., Merazzi S. and Gruber R. 1992 *Comp. Phys. Comm.* **72** 1–13

[989] Cooper W. A. *et al* 2006 *Fusion Sci. Tech.* **50** 245–257

[990] Cooper W. A. *et al* 2012 *Phys. Plasmas* **19** 102503

[991] Harafuji K., Hayashi T. and Sato T. 1989 *J. Comp. Phys.* **81** 169–192

[992] Hayashi T., Sato T. and Takei A. 1990 *Phys. Fluids B: Plasma Phys.* **2** 329–337

[993] Suzuki Y., Nakajima N., Watanabe K. Y., Nakamura Y. and Hayashi T. 2006 *Nucl. Fusion* **46** L19–L24

[994] Suzuki Y. 2017 *Plasma Phys. Control. Fusion* **59** 054008

[995] Reiman A., Ku L., Monticello D., Nuhrenberg C. and Cooper W. 1997 *Plasma Physics Reports* **23** 472

[996] Greenside H., Reiman A. and Salas A. 1989 *J. Comp. Phys.* **81** 102

[997] Drevlak M., Monticello D. and Reiman A. 2005 *Nucl. Fusion* **45** 731

[998] Hirshman S., Sanchez R. and Cook C. 2011 *Phys. Plasmas* **18** 062504

[999] Peraza-Rodriguez H. *et al* 2017 *Phys. Plasmas* **24** 082516

[1000] Cianciosa M., Hirshman S., Seal S. and Shafer M. 2018 *Plasma Phys. Control. Fusion* **60** 044017

[1001] Sugiyama L. *et al* 2001 *Nucl. Fusion* **41** 739–746

[1002] Orain F. *et al* 2016 *Nucl. Fusion* **57** 022013

[1003] Spong D. A. 2011 *Phys. Plasmas* **18** 056109

[1004] Park J.-K., Boozer A. H. and Glasser A. H. 2007 *Phys. Plasmas* **14** 052110

[1005] White R. 2022 *Phys. Plasmas* **29** 092504

[1006] Varje J. *et al* 2019 High-performance orbit-following code ASCOT5 for Monte Carlo simulations in fusion plasmas (*Preprint* 1908.02482)

[1007] Äkäslompolo S. *et al* 2015 *Nucl. Fusion* **55** 093010

[1008] Tobita K. *et al* 1992 *Phys. Rev. Lett.* **69**(21) 3060–3063

[1009] Tobita K., Tani K., Nishitani T., Nagashima K. and Kusama Y. 1994 *Nucl. Fusion* **34** 1097

[1010] Liu Y. *et al* 2016 *Nucl. Fusion* **56** 066001

[1011] Kurki-Suonio T. *et al* 2016 *Plasma Phys. Control. Fusion* **59** 14013

[1012] Särkimäki K., Varje J., Bécoulet M., Liu Y. and Kurki-Suonio T. 2018 *Nucl. Fusion* **58** 076021

[1013] Sanchis L. *et al* 2021 *Nucl. Fusion* **61** 046006

[1014] Kolesnichenko Y. I., Lutsenko V. V., Wobig H., Yakovenko Y. V. and Fesenyuk O. P. 2001 *Phys. Plasmas* **8** 491–509

[1015] Spong D. A., Sanchez R. and Weller A. 2003 *Phys. Plasmas* **10** 3217–3224

[1016] Könies A. and Eremin D. 2010 *Phys. Plasmas* **17** 012107

[1017] Cheng C. Z. and Chance M. S. 1986 *Phys. Fluids* **29** 3695–3701

[1018] Yakovenko Y. V. *et al* 2007 *Plasma Phys. Control. Fusion* **49** 535

[1019] Sovinec C. *et al* 2004 *J. Comp. Phys.* **195** 355–386

[1020] Todo Y. *et al* 2017 *Phys. Plasmas* **24** 081203

[1021] Roberds N. A. *et al* 2016 *Phys. Plasmas* **23** 092513

[1022] Sugiyama L. E. and Strauss H. R. 2010 *Phys. Plasmas* **17** 062505

[1023] Zhou Y., Ferraro N., Jardin S. and Strauss H. 2021 *Nucl. Fusion* **61** 086015

[1024] Hirshman S. P., van Rij W. I. and Merkel P. 1986 *Comp. Phys. Comm.* **43** 143–155

[1025] Hoelzl M. *et al* 2021 *Nucl. Fusion* **61** 065001

[1026] Nikulsin N., Hoelzl M., Zocco A., Lackner K. and Günter S. 2019 *Phys. Plasmas* **26** 102109

[1027] Nikulsin N., Hoelzl M., Zocco A., Lackner K. and and S. G. 2021 *J. Plasma Phys.* **87** 855870301

[1028] Kolesnichenko Y. I., Lutsenko V. V., Wobig H. and Yakovenko V. 2002 *Phys. Plasmas* **9** 517–528

[1029] Paul E. J. *et al* 2022 *Nucl. Fusion* **62** 126054

[1030] Könies A. 2000 *Phys. Plasmas* **7** 1139–1147

[1031] Könies A., Mishchenko A. and Hatzky R. 2008 *AIP Conf. Proc.* **1069** 133–143

[1032] Nührenberg C. 1996 *Phys. Plasmas* **3** 2401–2410

[1033] Nührenberg C. 1999 *Phys. Plasmas* **6** 137–147

[1034] Windisch T. *et al* 2017 *Plasma Phys. Contol. Fusion* **59** 105002

[1035] Kornilov V. 2004 *Global Ion-Temperature-Gradient Driven Instabilities in Stellarator swithin Two-Fluid and Gyrokinetic Descriptions* phd thesis University Greifswald

[1036] Holod I., Zhang W. L., Xiao Y. and Lin Z. 2009 *Phys. Plasmas* **16** 122307

[1037] Cole M. D. J. *et al* 2019 *Phys. Plasmas* **26** 032506

[1038] Wilms F. *et al* 2021 *J. Plasma Phys.* **87** 905870604

[1039] Lin Z. and Chen L. 2001 *Phys. Plasmas* **8** 1447–1450

[1040] Cole M. D. J., Mishchenko A., Bottino A. and Chang C. S. 2021 *Phys. Plasmas* **28** 034501

[1041] Mishchenko A. 2005 *New methods in gyrokinetic particle-in-cell simulations* PhD Greifswald Greifswald

[1042] Hatzky R., Könies A. and Mishchenko A. 2007 *J. Comp. Phys.* **225** 568–590

[1043] Di Siena A. *et al* 2019 *Phys. Plasmas* **26** 052504

[1044] Di Siena A., Bañón Navarro A. and Jenko F. 2020 *Phys. Rev. Lett.* **125**(10) 105002

[1045] Spong D., Holod I., Todo Y. and Osakabe M. 2017 *Nucl. Fusion* **57** 086018

[1046] Kleiber R. *et al* 2019 Global gyrokinetic PIC simulations for stellarators and heliotrons with emphasis on experimentally relevant scenarios *18th European Fusion Theory Conference (EFTC), Ghent, Belgium*

[1047] Mishchenko A. *et al* 2019 Global gyrokinetic PIC simulations for stellarators and heliotrons with emphasis on experimentally relevant scenarios *22nd International Stellarator and Heliotron Workshop, Madison (Wisconsin, USA)*

[1048] Cole M., Mishchenko A., Könies A., Kleiber R. and Borchardt M. 2014 *Phys. Plasmas* **21** 072123

[1049] Cole M. D. J. *et al* 2015 Progress in non-linear electromagnetic gyrokinetic simulations of Toroidal Alfvén Eigenmodes *14th IAEA Technical Meeting on Energetic Particles in Magnetic Confinement Systems.* (Vienna: IAEA) p 1

[1050] Spong D. 2013 *Nucl. Fusion* **53** 053008

[1051] Varela J. *et al* 2020 *Nucl. Fusion* **60** 26016

[1052] Varela J., Spong D. and Garcia L. 2017 *Nucl. Fusion* **57** 126019

[1053] Todo Y. *et al* 2010 *Fusion Sci. Tech.* **58** 277–288

[1054] Wang H., Todo Y., Ido T. and Suzuki Y. 2018 *Phys. Rev. Lett.* **120**

[1055] Wang H., Todo Y., Oasakabe M., Ido T. and Suzuki Y. 2019 *Nucl. Fusion* **59** 096041

[1056] Seki R. *et al* 2020 *J. Plasma Phys.* **86** 905860520

[1057] Dvornova A. 2021 *Hybrid fluid-kinetic MHD simulations of the excitation of Toroidal Alfvén Eigenmodes by fast particles and external antenna* Ph.D. thesis Eindhoven University of Technology, Applied Physics proefschrift.

[1058] Spong D. A., D'Azevedo E. and Todo Y. 2010 *Phys. Plasmas* **17** 022106

[1059] Fehér T. B. 2013 *Simulation of the interaction between Alfvén waves and fast particles* PhD Thesis Greifswald Greifswald

[1060] Könies A. and Kleiber R. 2012 *Phys. Plasmas* **19** 122111

[1061] Bowden G. W., Hole M. J. and Könies A. 2015 *Phys. Plasmas* **22** 092114

[1062] Strumberger E., Merkel P., Sempf M. and Günter S. 2008 *Phys. Plasmas* **15** 056110

[1063] Kerner W., Goedbloed J., Huysmans G., Poedts S. and Schwarz E. 1998 *J. Comp. Phys.* **142** 271–303

[1064] Strumberger E. and Günter S. 2016 *Nucl. Fusion* **57** 016032

[1065] Wesson J. and Campbell D. J. 2011 *Tokamaks* vol 149 (Oxford university press)

[1066] Fredrickson E. *et al* 1995 *Nucl. Fusion* **35** 1457

[1067] Saigusa M. *et al* 1998 *Plasma Phys. Control. Fusion* **40** 1647

[1068] Heidbrink W. W. *et al* 1999 *Nucl. Fusion* **39** 1369

[1069] Bernabei S. *et al* 2000 *Phys. Rev. Lett.* **84**(6) 1212–1215

[1070] Sharapov S. *et al* 2013 *Nucl. Fusion* **53** 104022

[1071] Gassner T. *et al* 2012 *Phys. Plasmas* **19** 032115

[1072] Bernabei S. *et al* 2001 *Nucl. Fusion* **41** 513

[1073] Fu G. Y. 2011 *J. Plasma Phys.* **77** 457–467

[1074] Biancalani A., Carlevaro N., Bottino A., Montani G. and Qiu Z. 2018 *J. Plasma Phys.* **84** 725840602

[1075] Kramer G. J. *et al* 2012 *Phys. Rev. Lett.* **109** 035003

[1076] Zarzoso D. and del Castillo-Negrete D. 2020 *J. Plasma Phys.* **86** 795860201

[1077] Lévy P. 1934 *Annali della Scuola Normale Superiore di Pisa-Scienze Fisiche e Matematiche* **3** 337–366

[1078] Lévy P. 1940 *Compositio mathematica* **7** 283–339

[1079] Paul W. and Baschnagel J. 1999 *From Physics to Finance, Springer, Berlin*

[1080] Biancalani A., Chen L., Pegoraro F. and Zonca F. 2010 *Phys. Rev. Lett.* **105** 095002

[1081] Liu Y. *et al* 2019 *Nucl. Fusion* **59** 106024

[1082] Xu M. *et al* 2021 *Nucl. Fusion* **61** 036034

[1083] Cai H., Gao B., Xu M., Liu A. and Kong D. 2021 *Nucl. Fusion* **61** 036029

[1084] Zhu J., Ma Z. W., Wang S. and Zhang W. 2018 *Nucl. Fusion* **58** 046019

[1085] Riggs G., Koepke M., Heidbrink W., Van Zeeland M. A. and Spong D. 2024 *Phys. Plasmas* **31** 042305

[1086] Groebner R. *et al* 1986 *Nuclear fusion* **26** 543

[1087] Dimits A. M. *et al* 2000 *Phys. Plasmas* **7** 969–983

[1088] Romanelli F. 1989 *Phys. Fluids B: Plasma Phys.* **1** 1018–1025

[1089] Hobirk J. *et al* 2012 *Plasma Phys. Control. Fusion* **54** 095001

[1090] Mantica P. *et al* 2009 *Phys. Rev. Lett.* **102** 175002

[1091] Citrin J. *et al* 2013 *Phys. Rev. Lett.* **111** 155001

[1092] Mantica P. *et al* 2011 *Phys. Rev. Lett.* **107** 135004

[1093] Bonanomi N. *et al* 2018 *Nucl. Fusion* **58** 056025

[1094] McKee G. R. *et al* 2000 *Phys. Plasmas* **7** 1870–1877

[1095] Tardini G. *et al* 2007 *Nucl. Fusion* **47** 280–287

[1096] Beer M. A. *et al* 1997 *Phys. Plasmas* **4** 1792–1799

[1097] Bourdelle C. *et al* 2005 *Nucl. Fusion* **45** 110–130

[1098] Jian X. *et al* 2019 *Nucl. Fusion* **59** 106038

[1099] Di Siena A. *et al* 2021 *Phys. Rev. Lett.* **127** 025002

[1100] Romanelli M., Zocco A. and Crisanti F. 2010 *Plasma Phys. Control. Fusion* **52** 045007

[1101] Citrin J. *et al* 2014 *Nucl. Fusion* **54** 023008

[1102] Garcia J. *et al* 2015 *Nucl. Fusion* **55** 053007

[1103] Doerk H. *et al* 2016 *Plasma Phys. Control. Fusion* **58** 115005

[1104] Wilkie G. *et al* 2018 *Nucl. Fusion* **58** 082024

[1105] Doerk H. *et al* 2018 *Nucl. Fusion* **58** 016044

[1106] Citrin J. *et al* 2015 *Plasma Phys. Control. Fusion* **57** 014032

[1107] Di Siena A. *et al* 2019 *Nucl. Fusion* **59** 124001

[1108] Whelan G. G. *et al* 2019 *Phys. Plasmas* **26** 082302

[1109] Di Siena A. *et al* 2018 *Phys. Plasmas* **25** 042304

[1110] Mazzi S. *et al* 2020 *Nucl. Fusion* **60** 046026

[1111] Nishiura M. *et al* 2024 *Phys. Plasmas* **31** 062505

[1112] Garcia J., Görler T. and Jenko F. 2018 *Phys. Plasmas* **25** 055902

[1113] Ghizzo A. and Del Sarto D. 2023 *Nucl. Fusion* **63** 104002

[1114] White R. B. and Mynick H. E. 1989 *Phys. Fluids B: Plasma Phys.* **1** 980–982

[1115] Estrada-Mila C., Candy J. and Waltz R. E. 2006 *Phys. Plasmas* **13** 112303

[1116] Hauff T. and Jenko F. 2007 *Phys. Plasmas* **14** 092301

[1117] Dannert T. *et al* 2008 *Phys. Plasmas* **15** 062508

[1118] Angioni C. and Peeters A. G. 2008 *Phys. Plasmas* **15** 052307

[1119] Angioni C. *et al* 2009 *Nucl. Fusion* **49** 055013

[1120] Peeters A. G. *et al* 2009 *Comput. Phys. Commun.* **180** 2650–2672

[1121] Kotschenreuther M., Rewoldt G. and Tang W. M. 1995 *Comput. Phys. Commun.* **88** 128–140

[1122] Dorland W., Jenko F., Kotschenreuther M. and Rogers B. N. 2000 *Phys. Rev. Lett.* **85** 5579

[1123] Zhang W., Lin Z. and Chen L. 2011 *Phys. Rev. Lett.* **107** 239501

[1124] Jenko F., Hauff T., Pueschel M. J. and Dannert T. 2011 *Phys. Rev. Lett.* **107** 239502

[1125] Suzuki T. *et al* 2011 *Nucl. Fusion* **51** 083020

[1126] Heidbrink W. *et al* 2009 *Phys. Rev. Lett.* **103** 175001

[1127] Pace D. C. *et al* 2013 *Phys. Plasmas* **20** 056108

[1128] Zhou S. *et al* 2010 *Phys. Plasmas* **17** 092103

[1129] Zhou S. *et al* 2011 *Phys. Plasmas* **18** 082104

[1130] Bovet A., Fasoli A., Ricci P., Furno I. and Gustafson K. 2015 *Phys. Rev. E* **91** 041101

[1131] Wong K. L. *et al* 1997 *Phys. Plasmas* **4** 393–404

[1132] Lauber P. *et al* 2018 Strongly non-linear energetic particle dynamics in ASDEX Upgrade scenarios with core impurity accumulation *27th IAEA Fusion Energy Conf.*

[1133] Duarte V. N. *et al* 2023 *Nucl. Fusion* **63** 036018

[1134] Kaye S. M. *et al* 2007 *Nucl. Fusion* **47** 499–509

[1135] Kaufman A. N. 1972 *J. Plasma Phys.* **8** 1–5

[1136] Fitzpatrick J. A. 1996 *A numerical model of wave-induced fast particle transport in a fusion plasma* (University of California, Berkeley)

[1137] Ghantous K., Berk H. L. and Gorelenkov N. N. 2014 *Phys. Plasmas* **21** 032119

[1138] Hamilton C., Tolman E. A., Arzamasskiy L. and Duarte V. N. 2023 *Astrophys. J.* **954** 12

[1139] Catto P. J. 2020 *J. Plasma Phys.* **86** 815860302

[1140] Kramer G. *et al* 2017 *Nucl. Fusion* **57** 056024

[1141] Collins C. and Van Zeelandand E.M. Bass M. A. 2021 Improving Fast-Ion Confinement and Performance by Reducing Alfvén Eigenmodes in the $qmin > 2$, Steady-State Scenario *Proceedings 28th IAEA Fusion Energy Conf. Eur.* IAEA-CN-286/EX/8-2

[1142] Garcia-Munoz M. *et al* 2019 *Plasma Phys. Control. Fusion* **61** 054007

[1143] Kolesnichenko Y. I., Parail V. V. and Pereverzev G. V. 1992 Generation of non-inductive current in a tokamak *Rev. Plasma Phys.* vol 17 ed Kadomtsev B. B. (Consultants Bureau, New York) pp 1–192

[1144] Huang J. *et al* 2020 *Nucl. Fusion* **60** 016002

[1145] Singh M. J., Boilson D., Polevoi A. R., Oikawa T. and Mitteau R. 2017 *New J. Phys.* **19** 055004

[1146] Park J. M. *et al* 2009 *Phys. Plasmas* **16** 092508

[1147] Ohkawa T. 1970 *Nucl. Fusion* **10** 185–197

[1148] Bierwage A. *et al* 2022 *Comp. Phys. Comm.* **275** 108305

[1149] Benjamin S. *et al* 2023 *Comp. Phys. Comm.* **292** 108893

[1150] Podestà M. *et al* 2015 *Nucl. Fusion* **55** 053018

[1151] Eriksson L.-G. and al E. 1998 *Phys. Rev. Lett.* **81** 1231–1234

[1152] Sharapov S. *et al* 2000 *Nucl. Fusion* **40** 1363

[1153] Mantsinen M. J. *et al* 2002 *Phys. Rev. Lett.* **89**(11) 115004

[1154] Eriksson L.-G. *et al* 2004 *Phys. Rev. Lett.* **92**(23) 235001

[1155] Pace D. C. *et al* 2016 *Nucl. Fusion* **57** 014001

[1156] Pace D. *et al* 2018 *Phys. Plasmas* **25**

[1157] Podestà M. *et al* 2010 *Phys. Plasmas* **17** 122501

[1158] Turnyanskiy M. and al E. 2013 *Nucl. Fusion* **53** 053016

[1159] Belova E. V., Gorelenkov N. N. and Cheng C. Z. 2003 *Phys. Plasmas* **10** 3240–3251

[1160] Belova E. V., Gorelenkov N. N., Fredrickson E. D.,

　　　　Tritz K. and Crocker N. A. 2015 *Phys. Rev. Lett.* **115**(1) 015001

[1161] Yamamoto S. *et al* 2017 *Nucl. Fusion* **57** 126065

[1162] Cappa Á. *et al* 2021 *Nucl. Fusion* **61** 066019

[1163] Varela J. *et al* 2020 *Nucl. Fusion* **60** 046013

[1164] Yamamoto S. *et al* 2020 *Nucl. Fusion* **60** 066018

[1165] Van Zeeland M. A. *et al* 2008 *Plasma Phys. Control. Fusion* **50** 035009

[1166] Garcia-Munoz M. *et al* 2015 *IAEA TM Energ. Part. Magn. Confin. Syst. (IAEA HQ, Vienna, 4–7 Sept.*

[1167] Berk H. L., Van Dam J. W., Guo Z. and Lindberg D. M. 1992 *Phys. Fluids B: Plasma Phys.* **4** 1806–1835

[1168] Saigusa M. *et al* 1997 *Nucl. Fusion* **37** 1559

[1169] Chu M. S. and al E. 1992 *Phys. Fluids B: Plasma Phys.* **4** 3713–3721

[1170] Nagaoka K. *et al* 2013 *Nucl. Fusion* **53** 072004

[1171] Heidbrink W. W. *et al* 2014 *Plasma Phys. Control. Fusion* **56** 095030

[1172] Holcomb C. T. *et al* 2015 *Phys. Plasmas* **22** 055904

[1173] Collins C. S., Holcomb C. T., Van Zeeland M. A. and al. E. 2021 *FEC IAEA preprint 0933*

[1174] Kim J. *et al* 2022 *Nucl. Fusion* **62** 026029

[1175] Geiger B. *et al* 2020 *Plasma Phys. Control. Fusion* **62** 095017

[1176] Hsu J. Y., Chan V. S., Harvey R. W., Prater R. and Wong S. K. 1984 *Phys. Rev. Lett.* **53**(6) 564–567

[1177] Marchenko V. S. and Baschenko O. S. 2013 *Plasma Phys. Control. Fusion* **55** 052002

[1178] Henderson M. *et al* 2015 *Phys. Plasmas* **22** 021808

[1179] Farina D., Henderson M., Figini L., Ramponi G. and Saibene G. 2012 *Nucl. Fusion* **52** 033005

[1180] Poli F. *et al* 2017 *Nucl. Fusion* **58** 016007

[1181] Evans T. E. *et al* 2006 *Nature Phys.* **2** 419–423

[1182] Loarte A. 2006 *Nature Phys.* **2** 369–370

[1183] Suttrop W. *et al* 2011 *Phys. Rev. Lett.* **106**(22) 225004

[1184] Kramer G. J. *et al* 2016 *Plasma Phys. Control. Fusion* **58** 085003

[1185] Hu W. *et al* 2018 *Nucl. Fusion* **58** 124001

[1186] Jalalvand A. *et al* 2021 *Nucl. Fusion* **62** 026007

[1187] Kaptanoglu A. A. *et al* 2022 *Nucl. Fusion* **62** 106014

[1188] Garcia A. V. *et al* 2023 *Nucl. Fusion* **63** 126039

[1189] Garcia A. V. *et al* 2023 Alfvén eigenmode detection using Long-Short Term Memory Networks and CO 2 Interferometer data on the DIII-D National Fusion Facility *2023 International Joint Conference on Neural Networks (IJCNN)* (IEEE) pp 1–8

[1190] Fisch N. J. and Rax J.-M. 1992 *Phys. Rev. Lett.* **69**(4) 612–615

[1191] Fisch N. J. 2000 *Nucl. Fusion* **40** 1095

[1192] Fisch N. J. 2015 *AIP Conf. Proc.* **1689** 020001

[1193] Cianfrani F. and Romanelli F. 2018 *Nucl. Fusion* **58** 076013

[1194] Cianfrani F. and Romanelli F. 2019 *Nucl. Fusion* **59** 106005

[1195] White R. B., Romanelli F., Cianfrani F. and Valeo E. 2021 *Phys. Plasmas* **28** 012503

[1196] Wong K. L. *et al* 2004 *Phys. Rev. Lett.* **93**(8) 085002

[1197] Schneider M. *et al* 2019 *Nucl. Fusion* **59** 126014

[1198] Polevoi A. R. *et al* 2013 *Nucl. Fusion* **53** 123026

[1199] Asunta O. *et al* 2015 *Comput. Phys. Commun.* **188** 33–46

[1200] Kurki-Suonio T. *et al* 2018 Beam ion performance and power loads in the ITER pre-fusion power operating scenarios (PFPO) with reduced field and current *Prepr. 2018 IAEA Fusion Energy Conf* pp p—-TH

[1201] Snicker A., Särkimäki K., Varje J., Schneider M. and Polevoi A. 2018 *EPS Conference Proceedings*

[1202] Vincenzi P., Schneider M. and Snicker A. 2024 *Fusion Eng. Des.* **200** 114178

[1203] Kurki-Suonio T. *et al* 2009 *Nucl. Fusion* **49** 095001

[1204] Pautasso G. *et al* 2020 *Nucl. Fusion* **60** 086011

[1205] Linder O., Fable E., Jenko F., Papp G. and Pautasso G. 2020 *Nucl. Fusion* **60** 096031

[1206] Munaretto S. *et al* 2020 *Nucl. Fusion* **60** 046024

[1207] Mlynar J. *et al* 2019 *Plasma Phys. Control. Fusion* **61** 14010

[1208] Ficker O. *et al* 2019 *Nucl. Fusion* **59** 096036

[1209] Tang T. *et al* 2021 *Nucl. Fusion* **61** 076003

[1210] Lin Z. F. *et al* 2019 *Plasma Phys. Control. Fusion* **61** 024005

[1211] Boozer A. H. 2017 *Nucl. Fusion* **57** 056018

[1212] Boozer A. H. 2018 *Nucl. Fusion* **58** 036006

[1213] de Vries P. C. *et al* 2014 *Phys. Plasmas* **21** 056101

[1214] de Vries P. C. *et al* 2012 *Plasma Phys. Control. Fusion* **54** 124032

[1215] Harvey R. W. *et al* 2000 *Phys. Plasmas* **7** 114590

[1216] Helander P., Smith H., Fulop T. and Eriksson L.-G. 2004 *Phys. Plasmas* **11** 5704

[1217] Smith H., Helander P., Eriksson L.-G. and Fulop T. 2005 *Phys. Plasmas* **12** 122505

[1218] Smith H. M. and Verwichte E. 2008 *Phys. Plasmas* **15** 072502

[1219] Martin-Solis J. R., Loarte A. and Lehnen M. 2017 *Nucl. Fusion* **57** 066025

[1220] Linder O., Papp G., Fable E., Jenko F. and Pautasso G. 2021 *J. Plasma Phys.* **87** 905870301

[1221] Insulander Björk K. *et al* 2021 *Plasma Phys. Control. Fusion* **63** 085021

[1222] Aleynikov P. and Breizman B. N. 2017 *Nucl. Fusion* **57** 046009

[1223] Stahl A., Embreus O., Papp G., Landreman M. and Fülöp T. 2016 *Nucl. Fusion* **56** 112009

[1224] Petrov Y. V., Parks P. B. and Harvey R. W. 2021 *Plasma Phys. Control. Fusion* **63** 035026

[1225] Paz-Soldan C. *et al* 2020 *Nucl. Fusion* **60** 056020

[1226] Hollmann E. M. *et al* 2021 *Nucl. Fusion* **61** 016023

[1227] Insulander Björk K. *et al* 2020 *J. Plasma Phys.* **86** 855860401

[1228] Rosenbluth M. N. and Putvinski S. V. 1997 *Nucl. Fusion* **37** 1355–1362

[1229] Martin-Solis J. R., Loarte A. and Lehnen M. 2015 *Phys. Plasmas* **22** 082503

[1230] Martin-Solis J. R., Loarte A. and Lehnen M. 2015 *Phys. Plasmas* **22** 092512

[1231] Breizman B. N. and Aleynikov P. B. 2017 *Nucl. Fusion* **57** 125002

[1232] Zhogolev V. and Konovalov S. 2014 *VANT Ser. Nucl. Fusion* **37**

[1233] Hesslow L., Embréus O., Vallhagen O. and Fülöp T. 2019 *Nucl. Fusion* **59** 084004

[1234] Vallhagen O., Embreus O., Pusztai I., Hesslow L. and Fülöp T. 2020 *J. Plasma Phys.* **86** 475860401

[1235] Summers H. P., O'Mullane M. G., Whiteford A. D., Badnell N. R. and Loch S. D. 2007 *AIP Conf. Proc.* **901** 239–248

[1236] Garland N. A. *et al* 2022 *Phys. Plasmas* **29** 12504

[1237] McDevitt C. J. and Tang X.-Z. 2019 *EPL (Europhysics Lett.)* **127** 045001

[1238] Fülöp T. *et al* 2020 *J. Plasma Phys.* **86** 474860101

[1239] Liu Y., Li L., Paz-Soldan C., Parks P. B. and Lao L. L. 2021 *Nucl. Fusion* **61** 066038

[1240] Svensson P. *et al* 2021 *J. Plasma Phys.* **87** 905870207

[1241] Hoppe M., Embreus O. and Fülöp T. 2021 *Comput. Phys. Commun.* **268** 108098

[1242] McDevitt C. J., Guo Z. and Tang X.-Z. 2019 *Plasma Phys. Control. Fusion* **61** 024004

[1243] Beidler M. *et al* 2024 *Nucl. Fusion* **64** 076038

[1244] Breizman B. N. 2014 *Nucl. Fusion* **54** 072002

[1245] Connor J. W. and Hastie R. J. 1975 *Nucl. Fusion* **15** 415–424

[1246] Bakhtiari M., Kramer G. J. and Whyte D. G. 2005 *Phys. Plasmas* **12** 102503

[1247] Bakhtiari M. *et al* 2005 *Phys. Rev. Lett.* **94** 215003

[1248] Embréus O., Stahl A. and Fülöp T. 2016 *New J. Phys.* **18** 093023

[1249] Aleynikov P. and Breizman B. N. 2015 *Phys. Rev. Lett.* **114** 155001

[1250] Stahl A., Hirvijoki E., Decker J., Embréus O. and Fulop T. 2015 *Phys. Rev. Lett.* **114** 115002

[1251] Decker J. *et al* 2016 *Plasma Phys. Control. Fusion* **58** 025016

[1252] Guo Z., Tang X.-Z. and McDevitt C. J. 2017 *Phys. Plasmas* **24** 112508

[1253] Fontanilla A. K. and Breizman B. N. 2017 *Phys. Plasmas* **24** 112509

[1254] Paz-Soldan C. *et al* 2017 *Phys. Rev. Lett.* **118** 255002

[1255] Liu C., Brennan D. P., Bhattacharjee A. and Boozer A. H. 2016 *Phys. Plasmas* **23** 010702

[1256] Liu C., Brennan D. P., Boozer A. H. and Bhattacharjee A. 2016 *Plasma Phys. Control. Fusion* **59** 024003

[1257] Embréus O., Stahl A. and Fülöp T. 2018 *J. Plasma Phys.* **84** 905840102

[1258] Guo Z., McDevitt C. J. and Tang X.-Z. 2017 *Plasma Phys. Control. Fusion* **59** 044003

[1259] Guo Z., McDevitt C. and Tang X. 2019 *Phys. Plasmas* **26** 082503

[1260] McDevitt C. J., Guo Z. and Tang X. Z. 2019 *Plasma Phys. Control. Fusion* **61** 054008

[1261] Hesslow L., Embréus O., Wilkie G. J., Papp G. and Fülöp T. 2018 *Plasma Phys. Control. Fusion* **60** 074010

[1262] Kiramov D. I. and Breizman B. N. 2017 *Phys. Plasmas* **24** 100702

[1263] Paz-Soldan C. *et al* 2019 *Plasma Phys. Control. Fusion* **61** 054001

[1264] Zhao C., Liu C., Jardin S. C. and Ferraro N. M. 2020 *Nucl. Fusion* **60** 126017

[1265] Bandaru V. *et al* 2021 *Plasma Phys. Control. Fusion* **63** 035024

[1266] Li L. *et al* 2021 *Nucl. Fusion* **61** 096034

[1267] Reux C. *et al* 2021 *Phys. Rev. Lett.* **126** 175001

[1268] Paz-Soldan C. *et al* 2021 *Nucl. Fusion* **61** 116058

[1269] Hollmann E. M. *et al* 2020 *Phys. Plasmas* **27** 042515

[1270] Hoppe M., Embreus O., Paz-Soldan C., Moyer R. A. and Fulop T. 2018 *Nucl. Fusion* **58** 082001

[1271] Del-Castillo-Negrete D., Carbajal L., Spong D. and Izzo V. 2018 *Phys. Plasmas* **25** 056104

[1272] Tinguely R. A., Hoppe M., Granetz R. S., Mumgaard R. T. and Scott S. 2019 *Nucl. Fusion* **59** 096029

[1273] Hoppe M. *et al* 2020 *Nucl. Fusion* **60** 094002

[1274] Popović Ž. *et al* 2021 *Phys. Plasmas* **28** 082510

[1275] Marini C. *et al* 2024 *Nucl. Fusion* **64** 076039

[1276] Myra J. R., Catto P. J., Mynick H. E. and Duvall R. E. 1993 *Phys. Fluids B: Plasma Phys.* **5** 1160–1163

[1277] Särkimäki K., Hirvijoki E., Decker J., Varje J. and Kurki-Suonio T. 2016 *Plasma Phys. Control. Fusion* **58** 125017

[1278] Boozer A. H. 2019 *Plasma Phys. Control. Fusion* **61** 024002

[1279] Boozer A. H. and Punjabi A. 2016 *Phys. Plasmas* **23** 102513

[1280] Izzo V. A. 2006 *Nucl. Fusion* **46** 541–547

[1281] Izzo V. A. *et al* 2008 *Phys. Plasmas* **15** 056109

[1282] Särkimäki K., Embreus O., Nardon E. and Fülöp T. 2020 *Nucl. Fusion* **60** 126050

[1283] Yoshino R. and Tokuda S. 2000 *Nucl. Fusion* **40** 1293

[1284] Papp G., Drevlak M., Fulop T. T. and Pokol G. I. 2012 *Plasma Phys. Control. Fusion* **54** 125008

[1285] Izzo V. A., Humphreys D. A. and Kornbluth M. 2012 *Plasma Phys. Control. Fusion* **54** 095002

[1286] Abdullaev S. 2014 *Magnetic Stochasticity in Magnetically Confined Fusion Plasmas* (Springer International Publishing)

[1287] Papp G., Drevlak M., Pokol G. I. and Fülöp T. 2015 *J. Plasma Phys.* **81** 475810503

[1288] Sommariva C. *et al* 2018 *Nucl. Fusion* **58** 016043

[1289] Liu Y. *et al* 2022 *Nucl. Fusion* **62** 066026

[1290] Carbajal L., Del-Castillo-Negrete D. and Martinell J. J. 2020 *Phys. Plasmas* **27** 032502

[1291] Hirvijoki E. *et al* 2014 *Comput. Phys. Commun.* **185** 1310–1321

[1292] Liu Y. Q., Parks P. B., Paz-Soldan C., Kim C. and Lao L. L. 2019 *Nucl. Fusion* **59** 126021

[1293] Aleynikov P. B. *et al* 2010 Simulations of runaway electron transport under MHD perturbations in ITER *37th EPS Conf. Plasma Phys. 2010, EPS 2010* vol 1 pp 281–284 ISBN 9781622763313

[1294] Beidler M. T., Del-Castillo-Negrete D., Baylor L. R., Shiraki D. and Spong D. A. 2020 *Phys. Plasmas* **27** 112507

[1295] Gobbin M. *et al* 2021 *Nucl. Fusion* **61** 066037

[1296] Lehnen M., Bozhenkov S. A., Abdullaev S. S. and Jakubowski M. W. 2008 *Phys. Rev. Lett.* **100** 255003

[1297] Liu Y. *et al* 2020 *Phys. Plasmas* **27** 102507

[1298] Liu C. *et al* 2021 *Nucl. Fusion* **61** 036011

[1299] Fasoli A. *et al* 2002 *Plasma Phys. Control. Fusion* **44** B159—-B172

[1300] Alikaev V. V., Razumova K. A. and Sokolov Y. A. 1975 *Sov. J. Plasma Phys.(Engl. Transl.);(United States)* **1**

[1301] Vlasenkov V. S., Leonov V. M., Merezhkin V. G. and Mukhovatov V. S. 1973 *Nucl. Fusion* **13** 509–516

[1302] Spong D. A. *et al* 2018 *Phys. Rev. Lett.* **120** 155002

[1303] Heidbrink W. W. *et al* 2019 *Plasma Phys. Control. Fusion* **61** 014007

[1304] Buratti P. *et al* 2021 *Plasma Phys. Control. Fusion* **63** 095007

[1305] Aleynikov P. and Breizman B. 2015 *Nucl. Fusion* **55** 043014

[1306] Smirnov A., Harvey R. and Kupfer K. 1994 *Bull Amer. Phys. Soc* **39** 1626

[1307] Smirnov A. P. and Harvey R. W. 2003 *The GENRAY Ray Tracing Code* URL http://www.compxco.com/Genray_manual.pdf

[1308] Guo Z., McDevitt C. J. and Tang X.-Z. 2018 *Phys. Plasmas* **25** 032504

[1309] Reinke M. L. *et al* 2019 *Nucl. Fusion* **59** 066003

[1310] Decker J. *et al* 2024 *arXiv preprint arXiv:2404.09900*

[1311] Liu C. *et al* 2018 *Phys. Rev. Lett.* **120** 265001